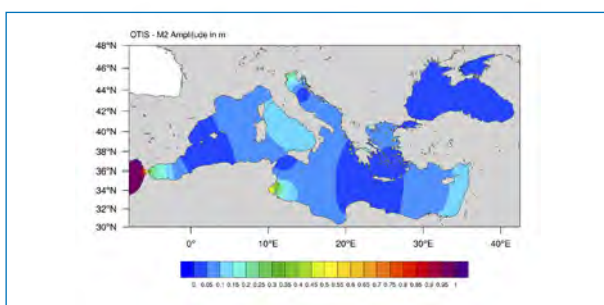
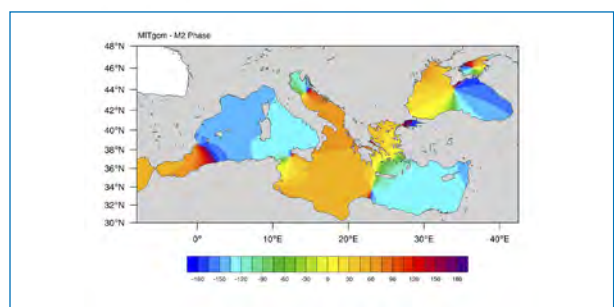
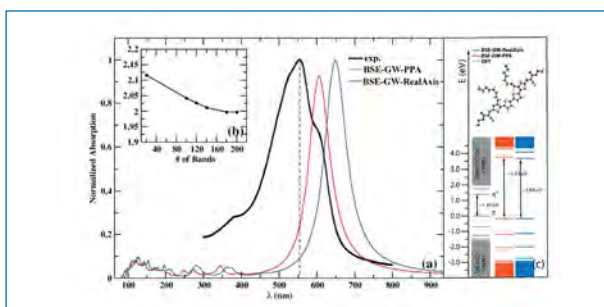
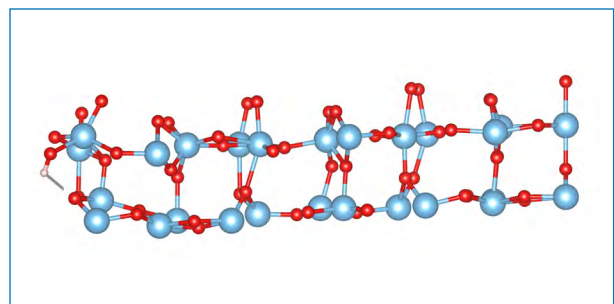
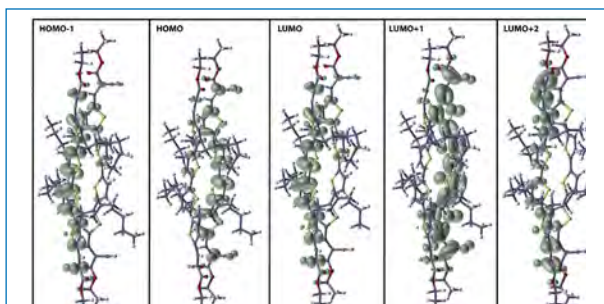


High Performance Computing on CRESCO infrastructure: research activities and results 2016



**High Performance Computing on CRESCO Infrastructure:
research activities and results 2016**

Contributions provided by a selection of users of the CRESCO infrastructure

Scientific Editor: *Michele Gusso*, ENEA, DTE-ICT-HPC, Brindisi Research Centre

Acknowledgements: We wish to thank *Gianclaudio Ferro* for providing the Reporter system (<http://hdl.handle.net/10840/5791>) to collect the contributions and to build the Volume

Cover: *Amedeo Trolese*, ENEA, DTE-ICT-PRA, Frascati Research Centre

ISBN: 978-88-8286-362-3

Contents

<i>Foreword</i>	5
<i>M-TraCE: the development of a new tool in CRESCO-HPC environment for high resolution elaboration of backward trajectories</i>	
<i>L. Vitali, M. D'Isidoro, G. Cremona, E. Petralia, A. Piersanti, G. Righini</i>	6
<i>Atmospheric pollution trends simulated for the period 1990–2010 in Europe: EURODELTA - Trends project</i>	
<i>M. Adani, G. Briganti, A. Cappelletti, M. D'Isidoro, M. Mircea</i>	10
<i>The I/O benchmarking methodology of EoCoE project</i>	
<i>S. Luehrs, A. Funel, M. Haefele, F. Ambrosino, G. Bracco, A. Colavincenzo, G. Guarnieri, M. Gusso, G. Ponti</i>	16
<i>The effect of hydrostatic pressure on the structural and superconducting properties of A15 Nb₃Sn</i>	
<i>R. Loria, G. De Marzi</i>	23
<i>Organocatalytic Coupling of Bromo-Lactide with Cyclic Ethers and Carbonates</i>	
<i>L. Cavallo, L. Caporaso, L. Falivene, R. Credendino</i>	29
<i>Ab initio formation energy of hydrogenated graphene oxides</i>	
<i>F. Buonocore, N. Lisi</i>	33
<i>The role of plant phenology in stomatal ozone flux modelling</i>	
<i>A. Anav, A. De Marco</i>	40
<i>Calibration of the high resolution regional earth system model (RegESM) over the Med-CORDEX domain</i>	
<i>M. V. Struglia, S. Calmanti, A. Carillo, A. Dell'Aquila, E. Lombardi, G. Sannino</i>	43
<i>A neural network for molecular dynamics simulations of hydrogenated amorphous silicon</i>	
<i>M. Gusso, J. Behler</i>	47
<i>Inter-layer synchronization in non-identical multilayer networks</i>	
<i>I. Sendina-Nadal, I. Leyva, R. Sevilla-Escoboza, R. Gutiérrez, J. M. Buldú, S. Boccaletti</i>	52
<i>FARO2.0 - A renewed gateway to ENEAGRID resources</i>	
<i>A. Mariano, G. D'Amato, F. Ambrosino, G. Aprea, F. Buonocore, M. Celino, A. Colavincenzo, M. Fina, A. Funel, S. Giusepponi, G. Guarnieri, F. Palombi, S. Pierattini, G. Ponti, G. Santomauro, G. Bracco, S. Migliori</i>	60

<i>Cloud infrastructure for scalability and high availability in business ICT applications</i> <i>A. Mariano, F. Beone, A. Scalise</i>	66
<i>Analysis of diffraction pattern for cadmium sulfide nanocluster by using Debye scattering equation</i> <i>E. Burresti, M. Celino, L. Tapfer</i>	72
<i>Theory and modeling of energetic particle driven instabilities</i> <i>S. Briguglio, G. Fogaccia, V. Fusco, G. Vlad, X. Wang, T. Wang</i>	78
<i>Neutron Transport analysis in DEMO in-vessel components</i> <i>R. Villari, D. Flammini, F. Moro</i>	86
<i>Electronic excitations in small oligothiophene molecules</i> <i>F. Gala, G. Zollo</i>	90
<i>Monte Carlo simulations supporting safety studies of PWR's and irradiation tests in TAPIRO research reactor</i> <i>P. Console Camprini, K. W. Burn</i>	100
<i>Nuclear responses in the ITER IVVS port cell</i> <i>D. Flammini, F. Moro, R. Villari</i>	105
<i>Edge modeling with SOLEDGED2-EIRENE code in RFX-mod and TCV fusion devices</i> <i>P. Innocente</i>	109
<i>Ab-initio study of the c-Si/a-Si:H interface for PV technology</i> <i>S. Giusepponi, M. Celino, M. Gusso, U. Aeberhard, P. Czaja</i>	113
<i>Molecular dynamics of GeO₂: Car-Parrinello simulations in the range 10-4000 K</i> <i>G. Mancini, M. Celino, A. Di Cicco</i>	117
<i>Development of the new circulation forecast model for the Mediterranean Sea</i> <i>G. Sannino, A. Carillo, A. Bargagli, E. Lombardi</i>	122
<i>Computational design and validation of a reconfigurable three-dimensional DNA nanostructure</i> <i>F. Iacovelli, M. Falconi</i>	126
<i>Calculation of correction factors for solid-state detectors in radiotherapy photon beams</i> <i>M. Pimpinella, L. Silvi</i>	133
<i>Hydrogen interaction with TiO₂ surface</i> <i>R. Vujanin, B. Paskaš Mamula, J. Grbovic Novakovic, N. Novakovic</i>	137

<i>An alternative use of prompt-Self Powered Neutron Detectors: spectral-deconvolution for monitoring high-intensity neutron fluxes</i>	
<i>L. Lepore, R. Remetti, A. Pietropaolo</i>	141
<i>Neutronic analyses in support of the WCLL DEMO design development</i>	
<i>F. Moro, D. Flammini, R. Villari</i>	149
<i>Report on CFD simulations of LOVA (Loss of vacuum accident) with ANSYS CFX 17.0 EUROfusion engineering grant safety analysis</i>	
<i>F. Tieri</i>	154
<i>Quantitative in situ gamma spectrometry in contaminated soil</i>	
<i>M. Altavilla</i>	158
<i>Influence of mass media in the Naming Game</i>	
<i>F. Palombi, S. Ferriani, S. Toti</i>	161
<i>Forces exerted by a solitary wave on horizontal cylinder</i>	
<i>L. Gurnari, P. Filianoti</i>	167
<i>High pressure premixed CH₄/H₂-Air flames</i>	
<i>D. Cecere, E. Giacomazzi, N. Arcidiacono, F. R. Picchia</i>	172
<i>Definition of a figure of merit for the optimization of ENEA NAI device</i>	
<i>R. Remetti, G. Gandolfo, L. Lepore, N. Cherubini</i>	179
<i>Structure of metal oxide nanoclusters from ab-initio computation</i>	
<i>R. Grena</i>	185
<i>Smagorinsky dynamic model for large-eddy simulation of turbulence</i>	
<i>G. Rossi, D. Cecere, E. Giacomazzi, N. M. S. Arcidiacono, F. R. Picchia, B. Favini</i>	189
<i>Characterization of MCL1 inhibition via Fast Switching Double annihilation technology on the CRESCO3 cluster</i>	
<i>P. Procacci</i>	195
<i>DPPC biomembrane solubilization by Triton TX-100: a computational study</i>	
<i>A. Pizzirusso, A. De Nicola, G. J. A. Sevink, A. Correa, M. Cascella, T. Kawakatsu, M. Rocco, Y. Zhao, M. Celino, G. Milano</i>	202
<i>Variant discovery for Triticum durum variety identification</i>	
<i>G. Aprea, A. Fiore, P. Pallara, G. Giuliano</i>	207
<i>Molecular dynamics simulations of peptide-TiO₂ interfaces</i>	
<i>M. Polimeni, L. Petridis, J. C. Smith, C. Arcangeli</i>	211

<i>Materials for energy in the framework of the european center of excellence EoCoE</i>	
<i>M. Celino, S. Giuseppeponi, M. Gusso, U. Aeberhard, A. Walker, S. Islam, D. Borgis, X. Blase, M. Salanne, M. Burbano, T. Deutsch, L. Genovese, M. Athenes, M. Levesque, P. Pochet</i>	216
<i>Cavity design for a cyclotron auto-resonance maser (CARM) radiation at high frequency</i>	
<i>S. Ceccuzzi, G. Dattoli, E. Di Palma, G. L. Ravera, E. Sabia, I. Spassovsky</i>	222
<i>First principle studies of materials for energy conversion and storage</i>	
<i>M. Pavone, A. B. Munoz-Garcia, E. Schiavo</i>	227
<i>Role of the Sub-surface Vacancy in the amino-acids adsorption on the (101) Anatase TiO₂ surface: A first-principles study</i>	
<i>L. Maggi, F. Gala, G. Zollo</i>	233
<i>LES of heat transfer in an asymmetric rib-roughened duct: influence of rotation</i>	
<i>D. Borello, A. Salvagni, F. Rispoli</i>	238
<i>SOLEEDGE2D-EIRENE simulations of the reference scenario of the M15-20 JET experiment</i>	
<i>G. Rubino</i>	242

Foreword

During the year 2016, CRESCO high performance computing clusters have provided about 43 million hours of “core” computing time, at a high availability rate, to more than one hundred users, supporting ENEA research and development activities in many relevant scientific and technological domains. In the framework of joint programs with ENEA researchers and technologists, computational services have been provided also to academic and industrial communities.

This report, the eighth of a series started in 2008, is a collection of 45 papers illustrating the main results obtained during 2016 using CRESCO/ENEAGRID HPC facilities. The significant number of contributions testifies the importance of the interest for HPC facilities in ENEA research community. The topics cover various fields of research, such as materials science, efficient combustion, climate research, nuclear technology, plasma physics, biotechnology, aerospace, complex systems physics, renewable energies, environmental issues, HPC technology. The report shows the wide spectrum of applications of high performance computing, which has become an all-round enabling technology for science and engineering.

Since 2008, the main ENEA computational resources is located near Naples, in Portici Research Centre. This is a result of the CRESCO Project (Computational Centre for Research on Complex Systems), co-funded, in the framework of the 2001-2006 PON (European Regional Development Funds Program), by the Italian Ministry of Education, University and Research (MIUR).

The Project CRESCO provided the resources to set up the first HPC x86_64 Linux cluster in ENEA, achieving a computing power relevant on Italian national scale (it ranked 126 in the HPC Top 500 June 2008 world list, with 17.1 Tflops and 2504 cpu cores). It was later decided to keep CRESCO as the signature name for all the Linux clusters in the ENEAGRID infrastructure, which integrates all ENEA scientific computing systems, and is currently distributed in six Italian sites. CRESCO computing resources were later upgraded in the framework of PON 2007-2013 with the project TEDAT and the cluster CRESCO4, 100 Tflops computing power. In 2016 the ENEAGRID computational resources consist of about 8500 computing cores (in production) and a raw data storage of about 1400 TB.

The success and the quality of the results produced by CRESCO stress the role that HPC facilities can play in supporting science and technology for all ENEA activities, national and international collaborations, and the ongoing renewal of the infrastructure provides the basis for an upkeep of this role in the forthcoming years.

In this context, 2015 is also marked by the signature of an agreement between ENEA and CINECA, the main HPC institution in Italy, to promote joint activities and projects. In this framework, CINECA and ENEA participated successfully to a selection launched by EUROfusion, the European Consortium for the Development of Fusion Energy, for the procurement of a several Pflops HPC system, beating the competition of 7 other institutions. The new system MARCONI-FUSION started operation in July 2016 at 1 Pflops computation power level which has been increased to 5 Pflops in the summer of 2017. The ENEA-CINECA agreement is a promising basis for the future development of ENEA HPC resources in the coming years. A new CRESCO6 cluster of 0.7 Pflops is planned to be installed before the end of the current year, 2017.

Dipartimento Tecnologie Energetiche,
Divisione per lo Sviluppo Sistemi per l'Informatica e l'ICT - CRESCO Team

M-TRACE: THE DEVELOPMENT OF A NEW TOOL IN CRESCO-HPC ENVIRONMENT FOR HIGH RESOLUTION ELABORATION OF BACKWARD TRAJECTORIES

Lina Vitali^{1*}, Massimo D'Isidoro¹, Giuseppe Cremona¹, Ettore Petralia¹, Antonio Piersanti¹
and Gaia Righini¹

¹ENEA SSPT-MET-INAT, Via Martiri di Monte Sole 4, 40129, Bologna, Italy

ABSTRACT. This work describes a new tool for the calculation and the statistical elaboration of backward trajectories. In order to take advantage of the high resolution meteorological database of the Italian national air quality model MINNI, stored in CRESCO-HPC environment, a dedicated set of procedures was implemented, in same environment, under the name of M-TraCE, MINNI module for **T**rajectories **C**alculation and statistical **E**laboration.

1 Introduction

Backward trajectory analysis is commonly used in a variety of atmospheric analyses [1]. In particular it is meaningful interpreting air composition measurements with respect to air mass origin and path through the atmosphere [2]. Backward trajectories are helpful for the interpretation of a single local event [3, 4], or can be processed through statistical analysis in order to provide information on the main directions of air masses fluxes and so on the region of influence of a site of interest [5]. Inter-comparison studies [6, 7] between different back trajectory models have shown that model performances are mainly determined by the quality and the spatial and temporal resolution of the underlying meteorological dataset, especially when complex terrain is involved [8, 9].

Here, the development of a new tool for backward trajectory analysis on the Italian territory is presented. Being the Italian peninsula characterized by complex orography, the usage of high resolution fields is mandatory to adequately describe the meteorological features. Italian National AMS-MINNI [10] meteorological database, at 4 km spatial resolution, has been used for this purpose. Furthermore, in some cases, additional *ad-hoc* meteorological simulations have been carried out at higher resolution (1 km) in order to better describe local meteorological features nearby the site of interest.

2 Methodology

2.1 Implemented procedures

M-TraCE is a package of procedures for high resolution computation and statistical elaboration of backward trajectories. M-TraCE is grouped into three main modules:

- ~ CORE: the core of the code, written in NCL [11], which calculates a single trajectory arriving at the site of interest at a selected time
- ~ LOOP: the procedure which allows looping to automatically calculate multiple trajectories
- ~ STAT: the procedure for the statistical processing of a sample of trajectories.

*Corresponding author. E-mail: lina.vitali@enea.it.

The core of the code is inspired by the HYSPLIT [12] model. In particular the method of Petterssen [13], a discrete numerical integration scheme based on simple Euler steps, is used to calculate air masses movements.

The result is the three-dimensional pathway of the trajectory provided both as graphical display and text file (Fig. 1).

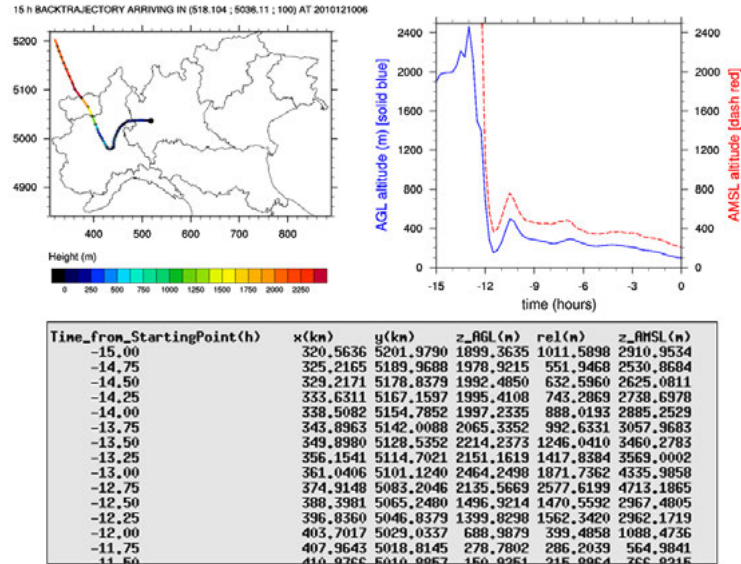


Fig.1: The three-dimensional pathway of the trajectory: graphical display (top) and text file (bottom).

When the LOOP procedure is selected, the core code is recursively run on multiple cases; the output is a broad set of trajectories suitable for statistical analysis through the STAT procedure. In particular the following set of statistical parameters, are processed at the same horizontal resolution of the ingested wind field:

- ~ trajectories transits number in order to identify the main circulation patterns (e.g., Fig. 2);
- ~ the residence time (time spent by air mass in each spatial cell), for assessing regions of influence;
- ~ the average transport time, for the delimitation of the maximum extension of the area of spatial representativeness, according to [14];
- ~ information on the height of air masses falling into each cell (minimum, maximum and average).

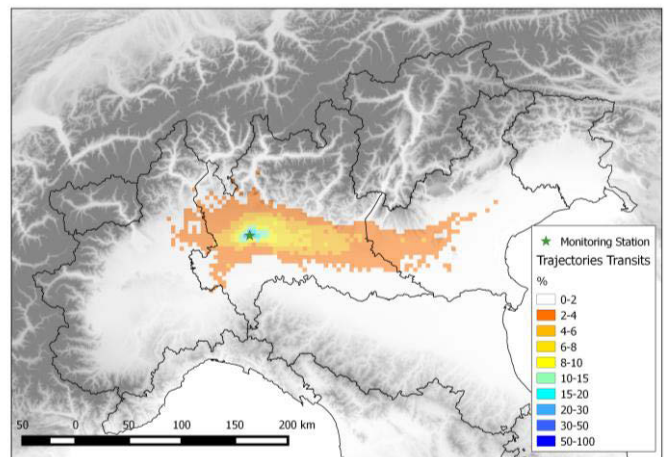


Fig.2: An example of statistical analysis: number in percent of trajectories transits.

2.2 MINNI meteorological database

Wind fields for M-TraCE trajectories calculation are supplied by AMS-MINNI meteorological database, produced and stored in CRESCO-HPC environment, using the prognostic non-hydrostatic meteorological model RAMS [15].

RAMS is highly customizable for a wide range of applications, specifically for different spatial scales. In particular a multiple grid nesting scheme allows for the solution of model equations simultaneously on any number of interacting computational meshes of differing spatial resolution. The highest resolution meshes are used to model small scale atmospheric features, whereas coarse meshes are used to simulate large scale atmospheric systems that interact with the smaller scale ones. These features make RAMS suitable for high-resolution simulations, especially in case of complex terrain environments.

A comprehensive validation of the calculated AMS-MINNI meteorological fields is systematically carried out through the comparison with independent observations [16].

Actually, M-TraCE relies on an official, high spatial and time resolution, validated database and its development and usage represent a new further valorisation of the MINNI products availability.

Table 1 summarizes the features of AMS-MINNI meteorological database, stored in CRESCO-HPC environment, including typical computation resources employed for meteorological simulation at different spatial resolutions.

Table 1: Features of the AMS-MINNI meteorological database and hardware usage.

Year	Domain	Resolution (km)	Storage	Num. Cores	Computational time
2003	Italy	4	~600GB per year	304	~15 days per year
2005					
2007					
2010					
2015					
2016	Campania	1	~150GB	320	~11 days
2015					
2010					
2010	Areas in Northern Italy	1	~250GB	376	~10 days
2010	Areas in Central and Southern Italy	1	~200GB	256	~12 days

3 Applications and current works

A preliminary version of M-TraCE, i.e. the module for single backward trajectory computation, was used to interpret in situ vertical profiles of aerosol physical properties [9]. The complete and upgraded version of the tool, including routines for statistical elaboration, was applied for the first time to the sites of the Italian Network of Special Purpose Monitoring Stations, designed and maintained by the Italian Ministry of the Environment, Land and Sea [17].

Recently M-TraCE has been used to support source apportionment assessment in the neighbourhood of industrial areas in Southern Italy and currently it is used for the interpretation of air quality monitoring data, in the frame of the “Campania Trasparente” project (<http://www.campaniatrasparente.it/>), an integrated plan for the comprehensive monitoring of different environmental and biological media throughout Campania Region.

References

- [1] I.A. Pérez, F. Artuso, M. Mahmud, U. Kulshrestha, M.L. Sánchez, M.Á. García. Applications of Air Mass Trajectories. *Advances in Meteorology*, **2015**, Article ID 284213, (2015).
- [2] E. Brattich, M.A. Hernández-Ceballos, G. Cinelli, L. Tositti. Analysis of ^{210}Pb peak values at Mt. Cimone (1998–2011). *Atmospheric Environment*, **112**, pp. 136-147, (2015).
- [3] G. Pace, D. Meloni, A. di Sarra. Forest fire aerosol over the Mediterranean basin during summer 2003. *Journal of Geophysical Research*, **110**, D21202, (2005).
- [4] E. Remoundaki, A. Papayannis, P. Kassomenos, E. Mantas, P. Kokkalis, M. Tsezo. Influence of saharan dust transport events on PM_{2.5} concentrations and composition over Athens. *Water Air and Soil Pollution*, **224**, 1373, (2013).
- [5] D. Folini, P. Kaufmann, S. Uhl, S. Henne. Region of influence of 13 remote European measurement sites based on modeled CO mixing ratios. *Journal of Geophysical Research*, **114**, D8 (2009).
- [6] A. Stohl, L. Haimberger, M. Scheele, H. Wernli. An intercomparison of results from three trajectory models. *Meteorological Applications*, **8**, pp. 127–135, (2001).
- [7] J. Harris, R. Draxler, S. Oltman. Trajectory model sensitivity to differences in input data and vertical transport method. *Journal of Geophysical Research*, **110**, D14109, (2005).
- [8] M.A. Hernández-Ceballos, C.A. Skjøth, H. García-Mozo, J.P. Bolívar, C. Galán. Improvement in the accuracy of back trajectories using WRF to identify pollen sources in southern Iberian Peninsula. *International Journal of Biometeorology*, **58**, pp. 2031-2043, (2014).
- [9] G. Pace, W. Junkermann, L. Vitali, A. di Sarra, D. Meloni, M. Cacciani, G. Cremona, A. Iannarelli, G. Zanini. On the complexity of the boundary layer structure and aerosol vertical distribution in the coastal Mediterranean regions: a case study. *Tellus B*, **67**, 27721, (2015).
- [10] M. Mircea, L. Ciancarella, G. Briganti, G. Calori, G. Cappelletti, I. Cionni, M. Costa, G. Cremona, M. D'Isidoro, S. Finardi, G. Pace, A. Piersanti, G. Righini, C. Silibello, L. Vitali, G. Zanini. Assessment of the AMS-MINNI system capabilities to simulate air quality over Italy for the calendar year 2005. *Atmospheric Environment*, **84**, pp. 178-188, (2014).
- [11] NCAR Command Language (Version 6.3.0) [Software]. Boulder, Colorado: UCAR/NCAR/CISL/TDD, (2015).
- [12] R.R. Draxler and G.D. Rolph. HYSPLIT (HYbrid Single-Particle Lagrangian Integrated Trajectory) Model access via NOAA ARL READY Website (<http://ready.arl.noaa.gov/HYSPLIT.php>). NOAA Air Resources Laboratory, Silver Spring, MD, (2015).
- [13] S. Petterssen. Weather analysis and forecasting. McGraw-Hill Book Company, New York, (1954), pp 221-223.
- [14] W. Spangl, J. Schneider, L. Moosmann, C. Nagl. Representativeness and classification of air quality monitoring stations – Final Report. Umweltbundesamt report, Umweltbundesamt, Vienna, (2007).
- [15] W. R. Cotton, R. A. Pielke, R. L. Walko, G. E. Liston, C. J. Tremback, H. Jiang, R. L. McAnelly, J. Y. Harrington, M. E. Nicholls, G. G. Carrio, J. P. McFadden. RAMS 2001: Current status and future directions. *Meteorology and Atmospheric Physics*, **82**, pp. 5-29, (2003).
- [16] L. Vitali, S. Finardi, G. Pace, A. Piersanti, G. Zanini. Validation of simulated atmospheric fields for air quality purposes in Italy. *Proceedings of the 13th International Conference on Harmonisation within Atmospheric Dispersion Modelling for Regulatory Purposes*, pp. 609-613, (2010).
- [17] L. Vitali, G. Righini, A. Piersanti, G. Cremona, G. Pace, L. Ciancarella. M-TraCE: a new tool for high-resolution computation and statistical elaboration of backward trajectories on the Italian domain. *Meteorology and Atmospheric Physics*, pp. 1-15, (2016).

ATMOSPHERIC POLLUTION TRENDS SIMULATED FOR THE PERIOD 1990–2010 IN EUROPE: EURODELTA - TRENDS PROJECT.

Mario Adani², Gino Briganti¹, Andrea Cappelletti¹, Massimo D’Isidoro², Mihaela Mircea²

¹ ENEA - National Agency for New Technologies, Energy and Sustainable Economic Development, Pisa, Italy

² ENEA - National Agency for New Technologies, Energy and Sustainable Economic Development, Bologna, Italy

ABSTRACT. The present paper shows some preliminary results obtained in the project EURODELTA 3 - Trends and, in particular, describes the simulations performed with the atmospheric modelling system AMS - MINNI. The AMS-MINNI is the reference modelling system of Italian Ministry of Environment, developed with the aim to support air quality policy at national and regional level. The simulations were carried out over a 21-year period, from 1990 to 2010, and over the whole Europe. The results show good agreement with those delivered by other participating models and with the measurements.

1 Introduction

The EU Directive 2008/50/EC promotes modelling techniques for assessing spatial distribution of the air pollution. The air quality (AQ) models are essential tools for developing emissions control plans needed to improve air quality levels and to preserve both human health and ecosystems. These models incorporate advection/dispersion drivers coupled with complex gas and aerosol chemistry solvers, and, therefore, require a lot of computational resources; supercomputing architectures, etc., like CRESCO infrastructure developed in ENEA.

This paper describes the work carried out under the “Trends” phase of the EURODELTA 3 (ED3) project with AMS-MINNI modelling system on CRESCO grid [2]. The project provided a framework for European modelling groups to share experiences in addressing policy relevant problems and to get further understanding in modeling air quality in Europe. ED3 is a scientific activity in the framework of EMEP Task Force on Measurement and Modelling [3], under the Convention on Long-range Transboundary Air Pollution.

The focus of EURODELTA 3 - Trends is to assess the efficiency of the Gothenburg protocol in reducing exposure to air pollution in Europe. The exercise aims to disentangle the role of meteorological variability, long range transport (boundary conditions) and emissions over 20 years period. The project consists of three Tiers (Table 1) and the first two were presented in the last CRESCO Report [4].

The third Tier required 38 additional simulations: a) 21-year reference simulations (1990-2010), with meteorology, emissions and boundary conditions specific to each year (3 simulations were already performed during Tier 1 for the years: 1990, 2000 and 2010) and b) 21-year simulations with constant 2010 emissions, in order to investigate the contributions of meteorological variability and of boundary conditions (a total of 20 new simulations were required, since one was already performed in Tier 1).

Tier / # years	Experiment	Key question	Code
REF	R 2010	Reference for 2010	M10B10E10
Tier 1	1A Reference for 1990, 2000, 2010	How do model compare with observation in 1990, 2000, and 2010 ? -> Comparison 1A & OBS	M00B00E00 M90B90E90
5 yrs	1B Meteorology and boundary conditions of 2010 emissions of 1990, 2000	What if no emission change occurred in Europe ? -> Comparison 1A vs. 1B	M10B10E00 M10B10E90
Tier 2	2A Meteorology of 2010 emissions & boundary conditions of 1990, 2000	What if no emission changed beyond Europe ? -> Comparison 2A vs. 1B	M10B00E00 M10B90E90
7 yrs	2B Meteorology & emissions of 2010 modelled boundary conditions of 1990, 2000, 2010	What is the uncertainty related to boundary conditions ? -> Comparison 2A & 2B	M10C10E10 M00C00E00 M90C90E90
	2C Meteorology of 2000, emissions of 1990 and boundary conditions of 2000 and 1990	Additional simulations for decomposition of factors	M00B90E90 M00B00E90
Tier 3	3A 21-yr reference trend	How do model capture the trend in observations ? -> Comparison 3A & OBS	M??B??E??
3B yrs	3B 21-yr trend with 2010 emissions	Does meteorological variability contribute to the AQ trend over the past 20 yrs? -> Comparison 3A & 3B	M??B??E10

Table 1: Summary of model experiments and corresponding key scientific questions[2]. For each tier, the number of simulated years is expressed in addition to the previous tier.

2 Modeling set-up

The modelling setup used for Tier 3 was the same reported in previous Cresco report [4] for Tier 1 and 2. The simulations were conducted with the air quality model FARM (Flexible Regional Atmospheric Model) [5] [6], developed by ARIANET s.r.l. (<http://www.aria-net.it/>) in Fortran 77/90 language. FARM is a three-dimensional Eulerian grid model with K-type turbulence closure that accounts for the transport, chemical reactions and ground deposition of atmospheric pollutants. The version used is 4.7, with SAPRC99 gas phase chemical mechanism [7] and AERO3 aerosol model[8]. This version was recently rewritten to support hybrid MPI-OpenMP parallelization [9]. The characteristics of the computational domain used in FARM simulations are shown in Table 2. Horizontal coordinates are in latitude/longitude, whereas vertical levels are in meters above the ground.

SW corner	(-17°E,32°N)
(NX, NY, NZ)	(143,153,16)
Vertical Z levels [m]	Quasi-logarithmic: 20, 75, 150, 250, 380, 560, 800, 1130, 1570, 2160, 2970, 4050, 5500, 7000, 8500, 10000
(ΔX, ΔY)	(0.4°,0.25°)

Table 2: Characteristics of the computational domain.

Meteorological, boundary condition and emission data were provided to all participants (<http://www.geosci-model-dev-discuss.net/gmd-2016-309/>) and they were processed to be used as input in FARM as is described in the next sections..

All the input/output data of AQ model were stored in the gporq1_minni file system. Table 3 summarizes the settings and the resources employed on the Cresco grid used and , respectively, employed in each step described below. It worth noting that, with respect to previous work [4], only a restricted list of variables were saved, the values corresponding to the level close to the ground, and, therefore, the required storage for the output of each simulated year was reduced by 60%. Emissions

were deleted once the run was completed, only the pre-processed emissions were saved, allowing to free disk space.

The time needed to complete all simulations (38 years) was ca. 2.5 months.

2.1 Boundary and initial conditions

Boundary and initial conditions used in the study were a simplified version of those used for the simulations with the standard EMEP MSC-W model (http://emep.int/mscw/index_mscw.html). These data are based upon climatological observations, except for dust. They were processed to map the chemical species specific to SAPRC99 gas phase chemical scheme and to particulate matter included in AERO3 aerosol model.

The yearly archives were divided in daily files and processed separately by using a scalar job on cresco4_h6 queue. In this way, scalar jobs were parallelized “by hand”. Monthly files with initial conditions contained 14 variables of 3D float type while those with lateral and top boundary conditions contained 14 variables of 2D float type.

Process	Cores	Queues	Elapsed time	Disk space	Total disk space
Boundary conditions	1	cresco4_h6	~ 20'/year	1.6 GB/year	29 GB
Meteorology	-	Local	-	200 GB/year	3.7 TB
SURFPRO	1	cresco4_h144 cresco3_h144	~ 45'/year ~ 1h20'/year	115 GB/year	2 TB
Emission Manager	12	cresco4_h6 cresco3_h144	~ 2h/year ~ 4h/year	400 GB/year	7 TB
FARM	16	cresco4minni_h24	~ 1÷1.5 day/year depending on Grid crowding and other I/O simultaneous processes.	93 GB/year	3.5 TB
Post-processing	1	cresco4_h144 cresco3_h144 cresco4_h6	~ 2÷3 day/year	38 GB/y	1.4 TB

Table 3: Summary of resources employed on Cresco grid.

2.2 Meteorology

Yearly meteorological fields from WRF (www.wrf-model.org) were processed by SURFPRO to estimate boundary layer height and diffusivities and to determine natural emissions such as volatile organic compounds emitted by vegetation, wind-blown dust and sea salt aerosols. Since PBL height is evaluated by means of a prognostic scheme (relaxation method based on 2D diffusion equations), and the calculation of volatile organic compounds requires the average temperature of the previous day, SURFPRO was run in a scalar way, by using both cresco3_h144 and cresco4_h144 queues. Each yearly run were completed in 45' on cresco4_h144 and 1h20' on cresco3_h144 (about 70% slower). Output files had dimension of 323 MB/day, leading to an amount of 115 GB/y storage for the whole period.

Each meteorological file includes 7 variables (3D float type) such as geopotential, wind components, temperature, pressure and vapour content and 4 variables (2D float type) such as orography, sea surface temperature, cloud coverage and precipitation.

SURFPRO files contain 3 variables (3D float) such as geopotential, horizontal and vertical diffusivities and 113 variables such as boundary layer turbulence, natural emissions, etc.

2.3 Emissions

The emissions fields were based on TNO_MACC and EMEP databases and were delivered as total yearly and vertically integrated of NO_x, SO_x, VOCs, PM2.5, PM coarse and CO mass in each 2D grid cell and for each anthropogenic categories of SNAP nomenclature (from 1 to 10). A dedicated software (Emission Manager, EMGR), integrated in the AMS-MINNI modelling system, performed the needed transformations of these 2D fields in 3D+T fields of chemical species considered in the SAPRC99 and AERO3 schemes. The temporal and spatial disaggregation was performed in several the steps:

- Chemical disaggregation of NO_x, SO_x, VOCs and PM2.5 (PM coarse is not speciated in FARM model);
- Vertical distribution according emission category profiles;
- Time modulation according to species and source category modulation coefficients.

Both vertical and time modulation profiles were provided in ED3 project. The natural emissions are computed by MEGAN model in SURFPRO processor.

EMGR is an ensemble of script, makefiles and serial Fortran executables. Due to the non-evolutionary nature of computations, the work can be divided in more than one serial job (12 monthly, or 52 weekly or 365 daily) and submitted to serial queues. Monthly based computations take about 4 hours with cresco3 queues and 2 hours using cresco4 queues.

2.4 FARM air quality model

The concentration fields were calculated for each year with 12 monthly jobs. For each monthly run, a spin-up period of 15 days has been considered. Since domain extension is about 5000 km and mean surface winds about 15 km/h, the spin-up is expected to avoid the inclusion of transitory effects.

The runs were performed with 16 cores and cresco4minni_h24 queue. The choice of employing 16 cores only is for optimizing the elapsed times: it seems to be a good compromise for current availability of resources [4]. The use of MPI or the OpenMP versions of the FARM code did not result in a significant difference in elapsed times.

The simulations require an elapsed time of about 1÷1.5 day/year, depending mainly on other simultaneous I/O processes and grid crowding. Storing a restrict list of variables 2D rather than all variables 3D, allowed to bypass the critical conditions occurring when massive simultaneous I/O operations are in progress [4]. At most, two years were run simultaneously by using the MINNI and other available queues.

3 Discussion

Figure 1 shows an example of particulate matter (PM10 and PM2.5) concentrations trend simulated with the following models: CHIMERE, CMAQ, EMEP, MATCH, MINNI, LOTOS-EUROS, POLAIR, and WRF-CHEM [11]. The analysis was restricted to rural and suburban stations with at least the 75% of data for each year. Simulated and observed monthly averaged data are plotted. Correlation, root mean square errors and biases are also reported under each plot, for each air quality modelling system. It can be noted that all models generally underestimate PM10 while reproduce better PM2.5, showing lower biases and mean errors. On the contrary, correlations are higher for PM10, due to the major contribution of local primary sources, that are better reproduced by models

than the secondary part of particulate matter (PM). Secondary PM represents most of PM_{2.5} and has a non-local origin, being generated by complex photochemical transformations and aerosol processes acting in polluted atmosphere, with time scale up to several hours. MINNI and CHIMERE show the best correlations for both PM₁₀ and PM_{2.5}, with almost identical biases for PM₁₀ (-6 µg/m³). The overall negative bias observed for PM₁₀ is higher in the winter period, when residential heating gives the main contribution and may be underestimated. Focusing on PM_{2.5} trend, it is worth noting that MINNI is capable of reproducing the peaks of monthly PM_{2.5} concentrations. Further analyses are in progress to evaluate model performances and trends for ozone (O₃), nitrogen dioxide (NO₂) and deposition of total oxidized sulphur (SO_x), oxidised nitrogen (NO_x) and reduced nitrogen (NH_x).

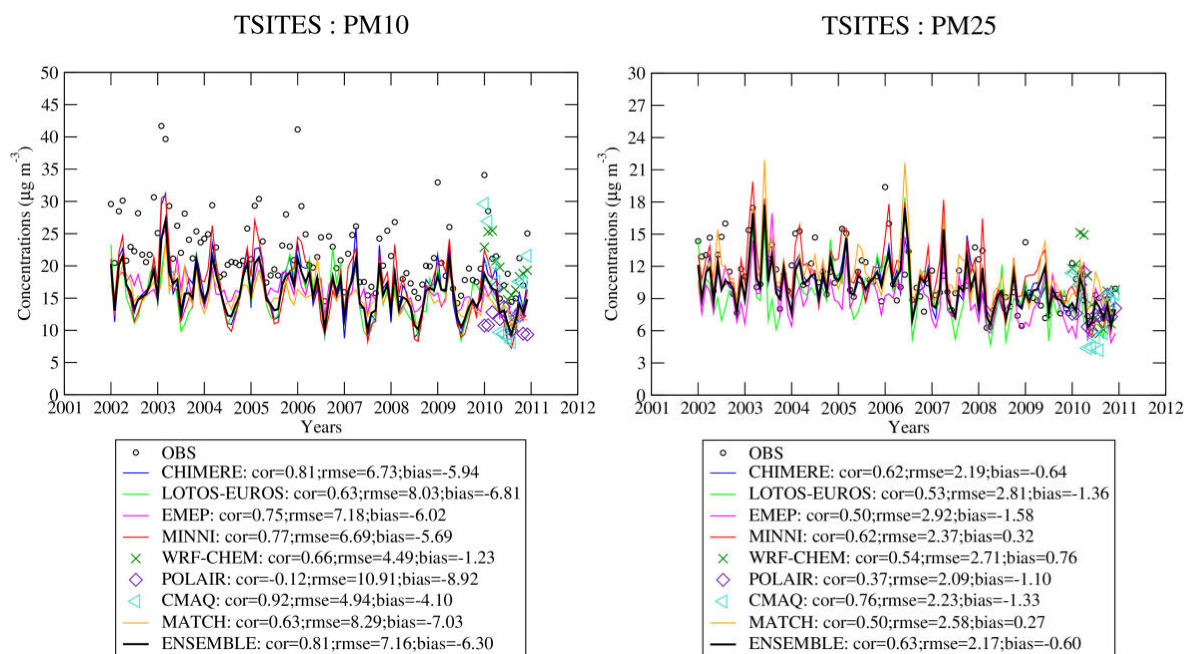


Figure 1: Evolution of monthly PM₁₀ (left) and PM_{2.5} (right) concentrations over the 2002-2010 period for rural and suburban stations, providing at least 75% of measurements each year [11].

References

- [1] ZANINI G., MIRCEA M., BRIGANTI G., CAPPELLETTI A., PEDERZOLI A., VITALI L., PACE G., MARRI P., SILIBELLO C., FINARDI S., CALORI G. “*The MINNI project: an integrated assessment modeling system for policy making*”. International Congress on Modelling and Simulation. Zealand, Melbourne, Australia, 12-15 December 2005, pp. 2005-2011. ISBN: 0-9758400-2-9.
- [2] <https://wiki.met.no/emep/emep-experts/tfmmtrendeuroldelta>
- [3] <http://www.nilu.no/projects/ccc/tfmm/>
- [4] BRIGANTI G., CAPPELLETTI A., MIRCEA M., ADANI M., D'ISIDORO M. (2016). “*Atmospheric Pollution Trends simulated at European Scale in the framework of the EURODELTA 3*”

Project". High Performance Computing on CRESCO infrastructure: research activities and results 2015, ISBN: 978-88-8286-342-5.

[5] SILIBELLO C., CALORI G., BRUSASCA G., CATENACCI G., FINZI G. "*Application of a photochemical grid model to Milan metropolitan area*". Atmospheric Environment **32** (11) (1998) pp. 2025-2038.

[6] GARIAZZO C., SILIBELLO C., FINARDI S., RADICE P., PIERSANTI A., CALORI G., CECINATO A., PERRINO C., NUSIO F., CAGNOLI M., PELLICIONI A., GOBBI, G.P., DI FILIPPO P. "*A gas/aerosol air pollutants study over the urban area of Rome using a comprehensive chemical transport model*". Atmospheric Environment **41** (2007) pp. 7286-7303.

[7] CARTER W.P.L. "*Documentation of the SAPRC-99 chemical mechanism for VOC reactivity assessment*". Final report to California Air Resources Board, Contract no. 92-329, and (in part) 95-308, (2000).

[8] BINKOWSKI F.S., ROSELLE S.J. "*Models-3 community multiscale air quality (CMAQ) model aerosol component- 1. Model description*". Journal of Geophysical Research **108** (2003) p. 4183, <http://dx.doi.org/10.1029/2001JD001409>, D6.

[9] MARRAS G., SILIBELLO C., CALORI G. "*A Hybrid Parallelization of Air Quality Model with MPI and OpenMP*". Recent Advances in the MPI: 19th European MPI Users Group Meeting, EuroMPI 2012, Vienna, Austria, September 23-26. Springer Berlin Heidelberg Editor.

[10] ARIANET S.R.L. "*SURFPRO3 User's guide (SURFace-atmosphere interface PROcessor, Version 3)*". Software manual. Arianet R2011.31.

[11] COLETTE A. et al. (2017). "*Long term air quality trends in Europe Contribution of meteorological variability, natural factors and emissions*". ETC/ACM Technical Paper 2016/7, January 2017.

THE I/O BENCHMARKING METHODOLOGY OF EoCoE PROJECT

S. Lührs^{1*}, A. Funel^{2†}, M. Haefele^{3‡}
F. Ambrosino^{2§}, G. Bracco^{2¶}, A. Colavincenzo^{2||}, G. Guarnieri^{2**}, M. Gusso^{2††}, G. Ponti^{2‡‡}

¹*Jülich Supercomputing Centre, Germany*

²*ENEA, Italy*

³*Maison de la Simulation, France*

ABSTRACT. The Energy oriented Centre of Excellence in computing applications (EoCoE) is one of the 8 centres of excellence in computing applications established within the Horizon 2020 programme of the European Commission. The project gives qualified high performance computing (HPC) support to research on renewable energies. In order to fully exploit the huge computing power of current supercomputers scientific applications need to be optimized for each specific hardware architecture. Often, much of the running time is spent in I/O operations. We present the methodology adopted by EoCoE to detect and remove I/O bottlenecks, and the first results of benchmarking activities obtained on CRESCO4 system at ENEA.

1 The EoCoE project

The Energy oriented Centre of Excellence in computing applications (EoCoE) [1] is one of the 8 centres of excellence in computing applications established within the Horizon 2020 programme of the European Commission. The primary goal of EoCoE is to foster and accelerate the European transition to a reliable and low carbon energy supply by giving high qualified HPC support to research on renewable energy sources. EoCoE project aims to create a new community of HPC experts and scientists working together to achieve advances on renewable energies.

EoCoE project is composed of four pillars: a) meteorology; b) materials modelling to design efficient low cost devices for energy generation and storage; c) water (goethermal energy); d) nuclear fusion; and a transversal basis. The objective of the transversal basis is to overcome bottlenecks in application codes from the pillars. It develops cutting-edge mathematical and numerical methods, and benchmarking tools to optimize application performances on many available HPC platforms. The transversal basis gives support in the following fields: numerical methods and applied mathematics; linear algebra; sys-

*Corresponding author. E-mail: s.luehrs@fz-juelich.de.

†Corresponding author. E-mail: agostino.funel@enea.it.

‡Corresponding author. E-mail: matthieu.haefele@maisondelasimulation.fr.

§Corresponding author. E-mail: fiorenzo.ambrosino@enea.it.

¶Corresponding author. E-mail: giovanni.bracco@enea.it.

||Corresponding author. E-mail: antonio.colavincenzo@enea.it.

**Corresponding author. E-mail: guido.guarnieri@enea.it.

††Corresponding author. E-mail: michele.gusso@enea.it.

‡‡Corresponding author. E-mail: giovanni.ponti@enea.it.

tem tools for HPC; advanced programming methods for exascale; tools and services for HPC. EoCoE is structured around a central Franco- German hub coordinating a pan-European network, gathering a total of eight countries and twenty-two partners. The project is coordinated by Maison de la Simulation (France) [2].

2 The I/O benchmarking methodology

I/O benchmarking is one of the activities of EoCoE project belonging to the transversal basis. Efficient I/O is crucial for a fast execution of a code. It could happen that a code run fast on a HPC platform and slow on another even if the two systems have the same microprocessors. Often the bottleneck is due to poor I/O performance. There are many causes which may degrade I/O performance: inefficient I/O strategy, inappropriate size of I/O buffers, large number of I/O calls, poor file system performance etc. It is very important to use benchmarks to get I/O behavior in a reproducible way to identify bottlenecks. The adopted methodology is outlined below:

- find I/O pattern at runtime;
- simulate the I/O pattern on all available HPC systems to find bottlenecks;
- remove bottlenecks:
 - code changes, optimized libraries
 - code refactoring and integration of optimized libraries.

The I/O pattern at runtime provides information on how a file system is accessed by a program without the need to look at the details of the written code. Among the many available tools we present Darshan [3], a library capable to characterize the I/O behavior at runtime with a minimum overhead. Once obtained the I/O pattern for a given system, it has to be simulated on all available systems in order to find bottlenecks. I/O performance is influenced not only by the strategy used at code level but also by the hardware and software which manage disk storage and file systems. As a consequence, I/O parameters and strategy may be adjusted for a specific HPC system in order to fully exploit its resources. In this work we also present IOR [4], an I/O simulator which can reproduce I/O patterns using various interfaces.

3 Results

In this section we present the first I/O benchmarking results obtained on CRESCO4 [5] system at ENEA [6]. The tools are very flexible and have been applied for the I/O analysis of a high parallel code, the study of the scalability of common parallel I/O libraries, to measure the efficiency of two disk storage systems under heavy workload, and to compare the performance of two parallel file systems with different block size.

3.1 CRESCO4 architecture

CRESCO4 cluster is composed of 304 computing nodes each of which has 2×8 cores Intel E5-2670 (Sandy Bridge), 2.6 GHz and 64 GB RAM for a total of 4864 cores. The interconnect is based on Infini-

Band (IB) QLogic [7] fabric 4×QDR (40 Gb/s). The I/O benchmarks have been executed on parallel file systems GPFS IBM Spectrum Scale (version 4.2.2.0) [8] configured with 6 NSD I/O servers.

3.2 Darshan

Darshan is a library designed to capture at runtime the I/O behavior of applications, even running on large HPC systems, including pattern of access within files. The library is scalable and lightweight in the sense that the overhead introduced during measurements, in terms of running execution time, is small compared to the case where measurements are absent. In order to collect I/O information applications have to be instrumented before execution. Darshan supports instrumentation of static and dynamic executables and captures both MPIIO and POSIX file access, and limited information about HDF5 [9] and PnetCDF [10] access.

In fig. 1 is shown an example of I/O pattern captured by Darshan for a CFD (external aerodynamics) simulation with 1024 cores. This example shows that the huge number of I/O accesses (~830000) and the small I/O size (~KB) are hints for a bottleneck.

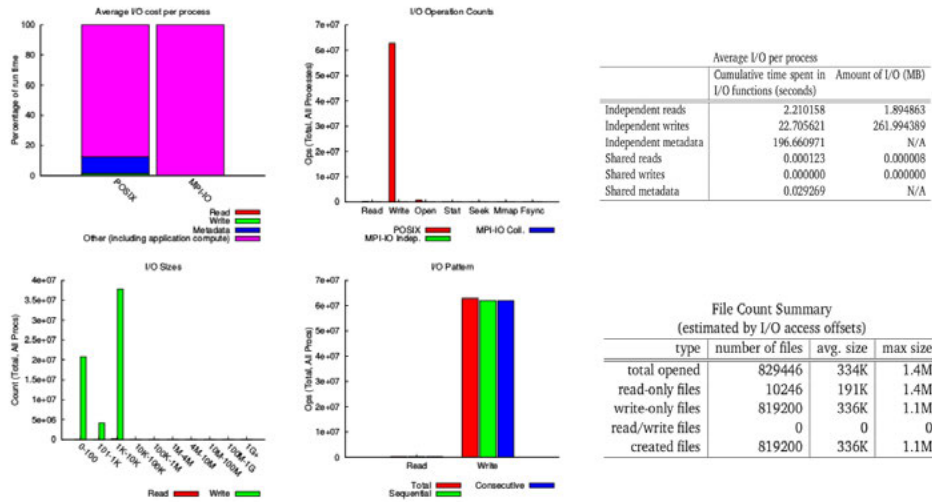


Figure 1: An example of I/O pattern captured by Darshan for a CFD (external aerodynamics) simulation with 1024 cores on CRESCO4 supercomputer at ENEA.

3.3 IOR

IOR can be used to test the performance of parallel file systems using various interfaces (MPIIO, HDF5, PnetCDF, POSIX) and access patterns. IOR uses MPI for process synchronization. An important feature of IOR is that it can simulate two basic parallel I/O strategies: shared file and one-file per process. In the shared file case all processes read/write to a single common file, while in the one-file per process each process reads/writes its own file. In fig. 2 is illustrated the IOR file structure in the case of a write operation to a single shared file. An IOR file is as a sequence of segments which represent the application data (for example a HDF5 or PnetCDF dataset). Each processor holds a part of the segment called a block. Each block, in turn, is divided in chunks called transferSize. The transferSize is the amount of data transferred from the processor to the disk storage in a single I/O function call. IOR manages the blocks and collect them into segments to make a file. The IOR file structure in the case of one-file per

process is the same except that each processor reads/writes its own file. The benchmark comes with a rich variety of options which can be passed as command line arguments to the executable. IOR is a versatile benchmark and can be used in many contexts. We present results concerning the scalability of most common I/O interface libraries, the measure of the efficiency of disk storage systems, and the comparison of the performance of two GPFS file systems configured with different block size.

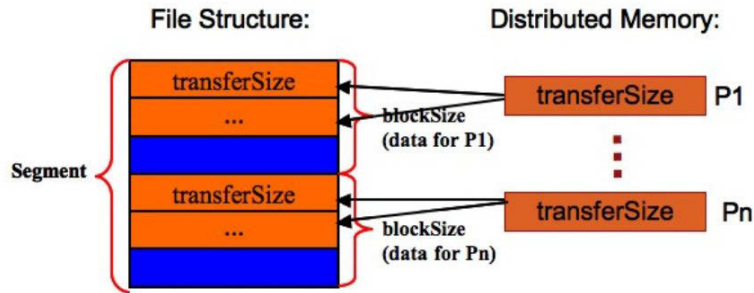


Figure 2: The IOR file structure.

The study of I/O scalability of common used libraries (MPIIO, HDF5, PnetCDF, POSIX) provides hints to users on how to setup their codes. Sometimes, the best number of tasks for I/O management and/or the I/O strategy (master- slave, single shared file, one file per task etc.) can only be found experimentally. The IOR benchmark tool is used to simulate I/O intensive jobs up to 256 cores. Each core is assigned an I/O task. Results show (see fig. 3) that for the three tested interfaces (MPIIO, HDF5, POSIX) the best configuration is with 64 tasks reading/writing a common shared file.

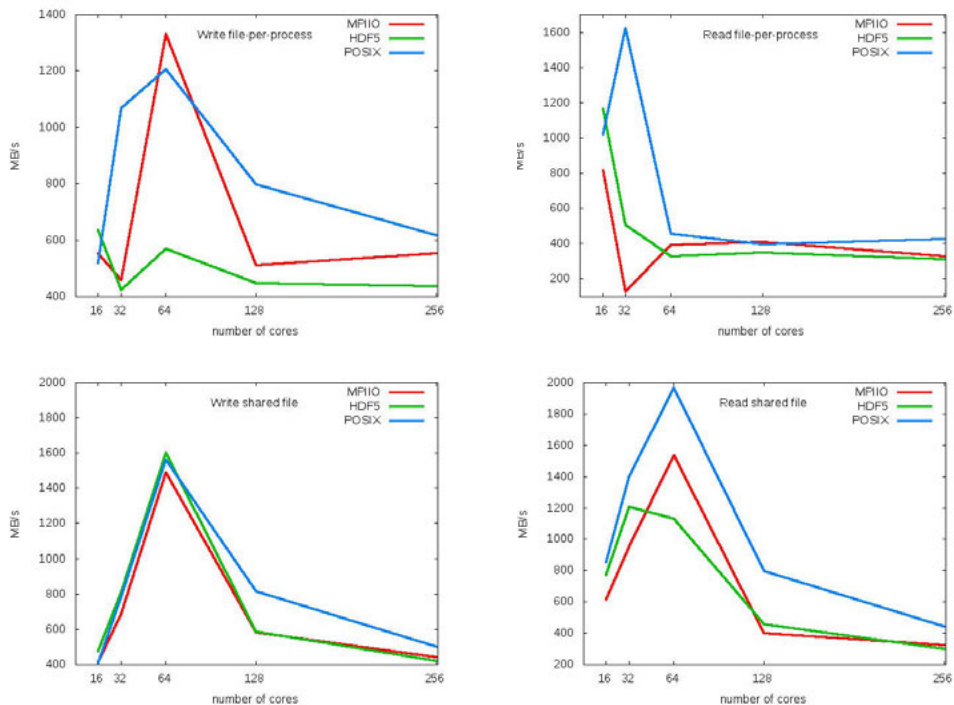


Figure 3: Scalability analysis results of MPIIO, HDF5 and POSIX I/O interfaces.

Sometimes a computing center can provide many kind of hardware disk storage systems. Depending of the needed I/O performance, it can be useful to dedicate some systems to intensive I/O workloads and others to low performance/long term storage. We present results concerning an experiment whose purpose is to measure the efficiency of two different DDN [11] disk storage systems under the same heavy I/O workload by using IOR benchmark. The efficiency of a system is obtained by measuring how much the I/O performance differs from its maximum peak. Efficiency gives an idea on how a storage technology is evolving. In fig. 4 is shown the experimental apparatus.

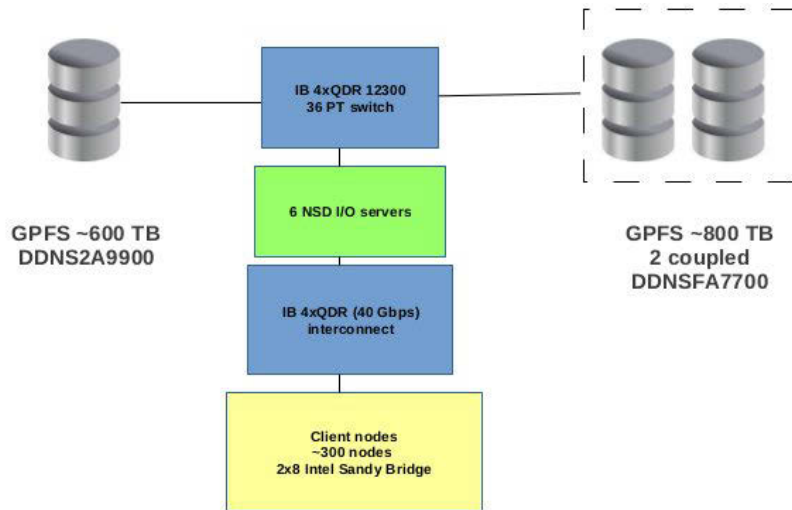


Figure 4: The two disk storage systems whose efficiency has been measured by using IOR benchmark. Left: DDNS2A9900 of ~ 600 TB. Right: two coupled DDNSFA7700 of ~ 800 TB. Each storage is accessed by a GPFS file system with the same software configuration.

In this experiment two GPFS file systems with 1 MB blocksize and 6 I/O servers over an IB 4xQDR (40 Gb/s) network are used to access two storage systems: (A) a DDNS2A9900 of ~ 600 TB and (B) two coupled DDNSFA7700 hosting ~ 800 TB. The maximum available I/O throughput is ~ 6 GB/s and ~ 18 GB/s for (A) and (B) respectively. Each I/O client node has 16 cores Intel Sandy Bridge (E5- 2670 2.6 GHz). To simulate a heavy workload each core executes an I/O task which reads/writes 1 GB and in this situation the 16 tasks on each client share the bandwidth of the network card. Results (see fig. 5) show that in the case of full load the efficiency is $\sim 8\%$ for system (A) and $\sim 30\%$ for (B).

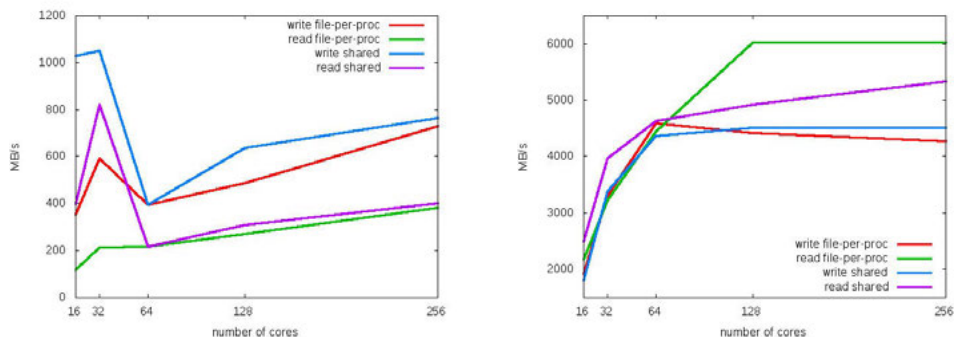


Figure 5: Measure of I/O throughput for a (A) DDNS2A9900 (left) and (B) two coupled DDNSFA7700 (right) disk storage systems. Under full load the efficiency is $\sim 8\%$ for system (A) and $\sim 30\%$ for (B).

IOR benchmark can be used to find optimal setting parameters of a file system. In the next experiment we want to compare the I/O performance of two GPFS file systems with 1 MB and 256 KB block size. We use a striping IOR configuration in which $\text{blockSize}=\text{transferSize}=\{128, 256\}$ KB and $\{1, 4, 256\}$ MB to simulate small, medium and large I/O. Runs are executed on a single computing node of CRESCO4. Each core is assigned an I/O task and all tasks write/read a common shared file. The aggregate amount of data for each run is 256 MB. For this experiment (see fig. 6) results show that 1 MB block size file system performs better than 256 KB.

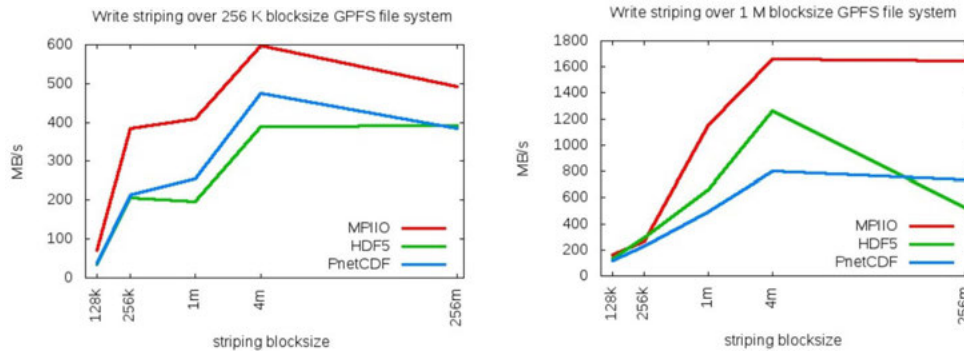


Figure 6: I/O performance of two GPFS file systems with 256 KB and 1 MB block size obtained by using IOR. The test is executed on a single node of CRESCO4 with 16 cores Intel Sandy Bridge (E5-2670 2.6 GHz) 64 GB RAM.

4 Conclusions

We have presented the I/O benchmarking methodology of EoCoE project and some experimental results obtained with Darshan and IOR on the ENEA HPC system CRESCO4. We have found these open source software very useful and used together with other tools allow to optimize the I/O on large HPC systems both at code and hardware level.

5 Acknowledgments

Work supported by the Energy oriented Centre of Excellence for computing applications (EoCoE), grant agreement no. 676629, funded within the Horizon 2020 framework of the European Union.

References

- [1] www.eocoe.eu/.
- [2] www.maisondelasimulation.fr/.
- [3] www.mcs.anl.gov/research/projects/darshan/.
- [4] <https://github.com/l1nl/ior>.
- [5] www.cresco.enea.it/.

- [6] www.enea.it/.
- [7] www.qlogic.com/.
- [8] www.ibm.com/support/knowledgecenter/en/stxkqy_4.2.2.
- [9] <https://support.hdfgroup.org/hdf5/>.
- [10] <https://trac.mcs.anl.gov/projects/parallel-netcdf>.
- [11] www.ddn.com/.

THE EFFECT OF HYDROSTATIC PRESSURE ON THE STRUCTURAL AND SUPERCONDUCTING PROPERTIES OF A15 Nb₃Sn

Rita Loria¹, and Gianluca De Marzi^{2*}

¹“Roma Tre” University, Department of Science, Via della Vasca Navale 84,00146, Rome, Italy

²ENEA, C. R. Frascati, Via Enrico Fermi 45, 00044 Frascati, Italy

ABSTRACT. We report on investigations of the structural and superconducting properties of Nb₃Sn in the GPa range by first-principle calculations based on Density Functional Theory (DFT). *Ab-initio* calculated lattice parameter of Nb₃Sn as function of pressure has been used as input for the calculations of the phonon dispersion curves and the electronic band structures along different high symmetry directions in the Brillouin zone. The critical temperature has been calculated as a function of the hydrostatic pressure by means of the Allen-Dynes modification of the McMillan formula: its behaviour as a function of hydrostatic pressure shows that the electronic contributions play a dominant role if compared to the phonon contributions; however, the anomalies found below 6 GPa are clearly ascribed to lattice instabilities. Finally, these theoretical results are compared with the experimental data obtained by using x-rays from a synchrotron radiation source. The experimental Equation of State obtained at room temperature and at pressures up to ~ 50 GPa reveals an anomaly in the P-V plot in the region 5-10 GPa, in agreement with theoretical predictions. These findings are a clue that Nb₃Sn could have some structural instability with impact on its superconducting properties when subjected to a pressure of a few GPa and represent an important step to understand and optimize the performances of Nb₃Sn materials under the hard operational conditions of the high field superconducting magnet.

1 Introduction

The A15 phase Nb₃Sn compound [1] is the present most widely used high field superconductor in science and industrial applications employing high-field superconducting magnets, like the International Thermonuclear Experimental Reactor (ITER) [2] and the CERN LHC Luminosity Upgrade [3]. In such applications, the superconducting coils of the high-field magnets are subject to large mechanical loads caused by the thermal contractions during the cooling down and the strong Lorentz forces due to the electromagnetic field. These novel and exceptional requirements renewed the interest in this supposedly well-known compound, opening the way for further insights into the dependence of the superconducting properties on the mechanical stress.

* Corresponding author. E-mail: gianluca.demarzi@enea.it.

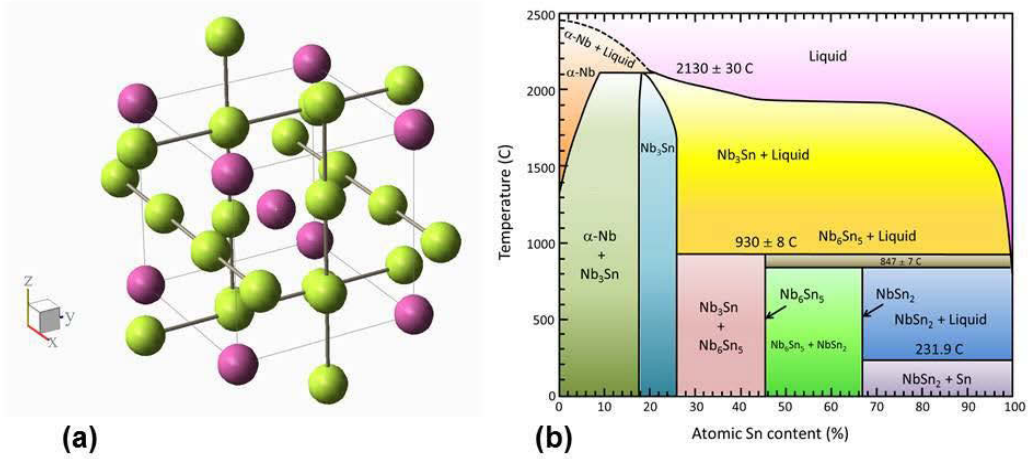


Fig.1: (a) The unit cell of the A15 structure of the Nb_3Sn compound: Sn atoms (in purple) form a bcc lattice and Nb (in green) atoms form three mutually orthogonal chains parallel to the edges of the unit cell; (b) Equilibrium phase diagram for the $\text{Nb}_{1-\beta}\text{Sn}_\beta$ binary system [4].

At atmospheric pressure Nb_3Sn shows a cubic β -W type crystal structure with a Pm-3m (no. 223) space group. In this structure, depicted in Fig. 1a, the Sn atoms form a body centered cubic lattice while the Nb atoms form three mutually orthogonal chains that lie parallel to the edges of the unit cell. The binary phase diagram of $\text{Nb}_{1-\beta}\text{Sn}_\beta$ is depicted in Fig. 1b: the brittle Nb_3Sn phase can exist over a wide composition range from about $0.18 \leq \beta \leq 0.25$ at.% Sn. The superconducting properties of Nb_3Sn are sensitive to an externally applied strain in a detrimental way [5], [6], [7]. Several studies have explored the degradation of the critical current density and critical temperature by an applied axial stress on technological wires, but little is known about the effect of a hydrostatic pressure on technological specimen.

In this work the structural, electronic and vibrational properties of the material have been investigated by means of ab-initio calculations based on Density Functional Theory (DFT). DFT models allow to calculate the elastic constant and to model the evolution of T_c as a function of pressure highlighting separately the electronic and phonon contributions. The results are compared to XRD experimental data obtained on Nb_3Sn technological wires [8].

2 *Ab initio* calculations

First-principles calculations were performed using plane-wave Density Functional Theory (DFT) [9] as implemented in the QUANTUM-ESPRESSO code (QE) [10]. The DFT scheme here employed adopts a Generalized Gradient Approximation (GGA) of the electron exchange and correlation energy using Perdew-Wang formula (PW91) [11]. The electron-ion interactions have been modelled with ultra-soft pseudopotentials (US-PPs) in the context of a plane wave expansion basis set. US-PPs have allowed the usage of an energy cut-off of 40 Ry for the wave functions and 400 Ry for the electron density. An artificial thermal broadening (*smearing*) and a $8 \times 8 \times 8$ Monkhorst-Pack k -point grid [12] for the Brillouin zone sampling have been employed for the simple cubic cell, whereas k -points convergence tests were performed in order to determine the amount of k -points necessary to perform accurate calculations. The ground state configurations have been obtained via the Broyden-Fletcher-Goldfarb-Shanno algorithm [13]. The phonon dispersion curves, $\omega_n(\mathbf{q})$, have been computed in the framework of Density-Functional Perturbation Theory [9] with QE, whereas a $2 \times 2 \times 2$ \mathbf{q} -point uniform grid, previously tested to be sufficient for convergence, has been employed

to calculate the entire phonon spectra. A denser k -mesh of $24 \times 24 \times 24$ was used for the calculation of the electron-phonon (*el-ph*) coupling constant λ at each given pressure. All lattice parameters have been calculated by relaxing a cubic cell in the whole range of pressure.

Fig. 2a shows the calculated volumes up to 50 GPa together with the XRD results. The calculated P-V curve has been fitted to the Rydberg-Vinet Equation of States (EoS) [14] for isotropic compression. From the fit we obtain $V_0 = 149.65 \text{ \AA}^3$, $K_0 = 167.92 \text{ GPa}$ and $K'_0 = 4.23$, in fair agreement with the experimental values ($V_0 = 148.73 \text{ \AA}^3$, $K_0 = 167.76 \text{ GPa}$ and $K'_0 = 3.58$ [8]; V_0 = volume at atmospheric pressure, K_0 = bulk modulus, and K'_0 = pressure derivative of K_0).

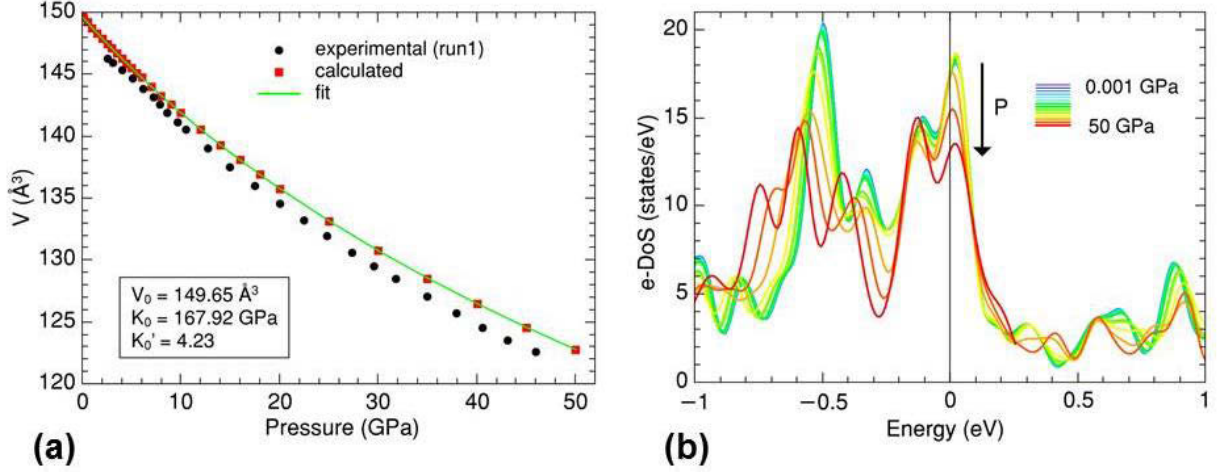


Fig. 2: (a) Calculated volume of Nb_3Sn as a function of pressure, compared with XRD data [8] (black markers); (b) Electronic density of states (e-DOS) as a function of pressure: at the Fermi level (conventionally set to zero) the e-DOS decreases with pressure.

Also, our calculations slightly overestimate the volume values ($\Delta V \cong 1.5 \text{ \AA}^3$). However the observed discrepancies in the volume are unlikely to be ascribed to the role of impurities in Nb_3Sn : with the atomic Sn content in the range from 18 to 25 % a variation of only 0.6% in the cell volume has been observed [15]. Moreover, Ta addition would increase the cell volume, contrary to the comparison shown in Fig. 2a. In fact, the discrepancies might originate from the pseudopotential used for the calculations: several authors ([16] and references therein) observed that GGA may overestimate the volume for 4d and 5d metals. Nevertheless, our calculated lattice parameter at atmospheric P, $a = 5.309 \text{ \AA}$, is in good agreement with results obtained with previous DFT calculations [6], [17].

The obtained lattice parameters have been used as inputs for the calculations of both the phonon dispersion curves and electronic band structures along several high-symmetry directions in the Brillouin zone. We computed the Electron Density of States (e-DoS) for different values of pressure: this is plotted in Fig. 2b. It is clear that the e-DoS at the Fermi level $N(E_F)$ decreases as pressure is increased. Thus, squeezing the cell alters $N(E_F)$. This quantity has particular relevance to evaluate T_c : indeed it is proportional to the electron-phonon coupling parameter λ which appears in the Allen-Dynes modification of the McMillan formula for T_c [18, 19]:

$$T_c = \frac{\hbar\omega_{\text{ln}}}{1.20} \exp\left(-\frac{1.04(1+\lambda)}{\lambda(1+0.62\lambda)}\right) \quad (1)$$

where ω_{ln} is a weighted logarithmically averaged phonon frequency. The parameter μ^* represents the effective Coulomb-repulsion parameter which describes the interaction between electrons can be calculated at each pressure using the expression $\mu^* = 0.26 \cdot N(E_F)/(1+N(E_F))$ [20].

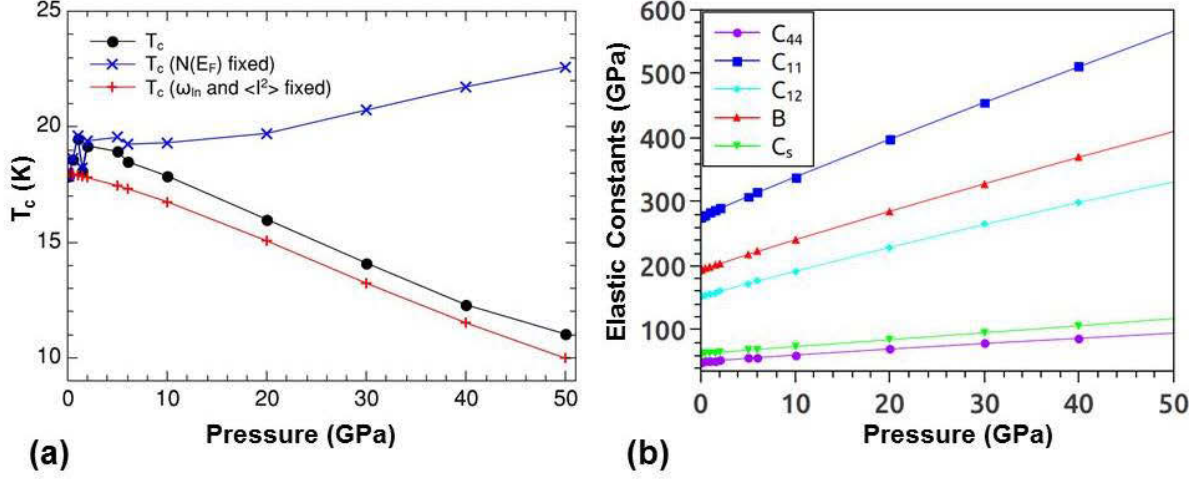


Fig. 3: (a) The critical temperature T_c calculated as a function of hydrostatic pressure (black line). The electronic and vibrational contributions have been separated by fixing ω_{ln} and $\langle I^2 \rangle$ (red line) or $N(E_F)$ (blue line) at their atmospheric pressure values; (b) The behaviour of the elastic constants in cubic Nb_3Sn as a function of hydrostatic pressure.

In Fig. 3a, a plot of T_c as a function of pressure is reported. Several oscillations are present in T_c at low pressure, in the range 0-6 GPa. The plot contains also T_c calculated by fixing ω_{ln} or λ at their atmospheric pressure values. It is clear that the overall behavior of T_c is mainly dictated by electronic contribution, whereas the oscillating behavior at low pressure seems to be mainly related to phononic anomalies, therefore must be closely related to lattice stresses and squeezing. This finding, also in comparison with XRD results [8], confirms that something at the structural level happens on Nb_3Sn at low pressure and room temperature. Above 10 GPa, calculations show that T_c decreases linearly with pressure at a rate of $\cong -1.5 \text{ K GPa}^{-1}$, in agreement with the value of -1.4 K GPa^{-1} reported in literature for a single crystal of Nb_3Sn in the tetragonal phase [21].

We also studied the pressure effects on elastic constants. From the phonon dispersion curves, one can infer information about the elastic constants. In fact, in a perfect crystal the elastic constants can be directly obtained from the slopes of the acoustic branches in the long wavelength limit ($|q| \rightarrow 0$). The relation between the sound velocity v_s along a given direction and the corresponding elastic constant C_{ij} is $C_{ij} = \rho v_s^2$, where ρ is the density of the crystal. For a cubic lattice, the expressions for C_{ij} associated to the phonon branches are reported in Table 1; in particular, for C_{11} and C_{44} the following relations hold:

$$C_{11} = \rho \left(\lim_{|\xi| \rightarrow 0} \frac{\partial v_{|\xi 0 0 L}(q)}{\partial |\xi|} a_0 \right)^2 = \rho v_{s,|\xi 0 0 L}^2 \quad (4a)$$

$$C_{44} = \rho \left(\lim_{|\xi| \rightarrow 0} \frac{\partial v_{|\xi 0 0 T}(q)}{\partial |\xi|} a_0 \right)^2 = \rho v_{s,|\xi 0 0 T}^2 \quad (4b)$$

where $v_{s,|\xi 0 0|L}$ and $v_{s,|\xi 0 0|T}$ are the longitudinal and transverse velocity of sound in the $[\xi 0 0]$ direction, ξ is the phonon wave vector coordinate renormalized by a factor $a_0/2\pi$, a_0 being the lattice parameter of the cubic cell, and ρ is the mass density of the material. The calculated elastic moduli at different pressures are shown in Fig. 3b. From the plot it is clear that values of elastic constants increase linearly with pressure. The slope of C_{11} and C_{44} are respectively 5.98 and 0.91: the effect of pressure is more pronounced in C_{11} than in C_{44} , as recently pointed out by Reddy *et al.* [22]. It is known that the martensitic transition observed at 43 K and atmospheric pressure is associated with a softening of the elastic modulus C_{44} and a vanishing of $C_{11} - C_{12}$ when the transition is approached from high temperature [23, 24]. However, our calculated elastic constants do not show anomalies ascribable to a similar structural phase transition.

Phononic Branch	$C_{ij} =$
$[\xi \xi \xi]L$	$\frac{1}{3}(C_{11} + 2C_{12} + 4C_{44})$
$[\xi \xi \xi]T_1$	$\frac{1}{3}(C_{11} - C_{12} + C_{44})$
$[\xi \xi \xi]T_2$	$\frac{1}{3}(C_{11} - C_{12} + C_{44})$
$[\xi \xi 0]L$	$\frac{1}{2}(C_{11} + C_{12} + 2C_{44})$
$[\xi \xi 0]T_1$	C_{44}
$[\xi \xi 0]T_2$	$\frac{1}{2}(C_{11} - C_{12})$
$[\xi 0 0]L$	C_{11}
$[\xi 0 0]T$	C_{44}

Table 1: The correspondence between the acoustic branches and elastic constants for a cubic crystal. T = degenerate transverse modes; T_i= non-degenerate transverse modes; and L = longitudinal modes. $[\xi \xi \xi]$ denotes the directions in the reduced Brillouin Zone.

3 Conclusions

In summary, we studied the structural and superconducting properties of Nb₃Sn under hydrostatic pressure. The numerical predictions showed that the calculated elastic constants increase with pressure, without showing anomalies, whereas T_c decreases with pressure with concomitant phonon-driven anomalies in the range 0-6 GPa. Finally, this work suggests that even if no evident structural phase transition occurs, a possible structural change as a result of an applied pressure for Nb₃Sn can take place.

References

- [1] B. T. Matthias. Transition temperatures of superconductors, *Phys. Rev.* **92**, pp. 874-876, (1953).
- [2] A. Vostner, and E. Salpiero. Enhanced critical current densities in Nb₃Sn superconductors for large magnets, *Supercond. Sci. Technol.* **19**, pp. S90-S95, (2006).
- [3] L. Bottura, G. de Rijk, L. Rossi, and E. Todesco. Advanced accelerator magnets for upgrading the LHC, *IEEE Trans. Appl. Supercond.* **22**, 4002008 (8pp), (2012).
- [4] A. Godeke. A review of the properties of Nb₃Sn and their variation with A15 composition, morphology and strain state, *Supercond. Sci. Technol.* **19**, R68-R80, (2006).
- [5] J. V. Ekin. Strain scaling law for flux pinning in practical superconductors, *Cryogenics* **20**, pp. 611-624, (1980).

-
- [6] G. De Marzi, L. Morici, L. Muzzi, A. della Corte, and M. Buongiorno Nardelli. Strain sensitivity and superconducting properties of Nb₃Sn from first principles calculations, *J. Phys.: Condens. Matter* **25**, 135702 (7pp), (2013).
- [7] G. De Marzi, and L. Morici. Ab-initio calculation of Nb₃Sn superconducting properties under applied mechanical strain, *High Performance Computing on CRESCO Infrastructure: research activities and results 2012*, pp. 165-172 (ISBN 978-88-8286-302-9, March 2014).
- [8] R. Loria, G. De Marzi, S. Anzellini, L. Muzzi, N. Pompeo, F. Gala, E. Silva, and C. Meneghini. The effect of hydrostatic pressure on the superconducting and structural properties of Nb₃Sn: ab-initio modeling and SR-XRD investigation, *IEEE Trans. Appl. Phys.* **27**, 16606888 (5pp) (2016).
- [9] P. Giannozzi, *et al.* Phonons and related crystal properties from density-functional perturbation theory, *J. Phys.: Condens. Matter* **21**, 395502 (19pp), (2009).
- [10] S. Baroni, S. de Gironcoli, A. Dal Corso, and P. Giannozzi. QUANTUM ESPRESSO: a modular and open-source software project for quantum simulations of materials, *Rev. Mod. Phys.* **73**, pp. 515-562, 2001.
- [11] J. P. Perdew, P. Ziesche, and H. Eschrig. Electronic structure of solids '91, Ed. P. Ziesche and H. Eschrig (Akademie Verlag, Berlin, 1991).
- [12] H. J. Monkhorst, and J. D. Pack. Special points for Brillouin-zone integrations, *Phys. Rev. B* **13**, pp. 5188-5192, 1976.
- [13] S. R. Billeter, A. Curioni, and W. Andreoni. Efficient linear scaling geometry optimization and transition-state search for direct wavefunction optimization schemes in density functional theory using a plane-wave basis, *Comp. Mater. Sci.* **27**, pp. 437-445, (2003).
- [14] P. Vinet, J. Ferrante, J. Rose, and J. Smith. Compressibility of solids, *J. Geophys. Res.* **92**, pp. 9319-9325, (1987).
- [15] A. Godeke. A review of the properties of Nb₃Sn and their variation with A15 composition, morphology and strain state, *Supercond. Sci. Technol.* **19**, R68-R80, (2006).
- [16] A. Dewaele, M. Torrent, P. Loubeyre, and M. Mezouar. Compression curves of transition metals in the Mbar range: Experiments and projector augmented-wave calculations, *Phys. Rev. B* **78**, pp. 104102 (13pp), (2008).
- [17] H. M. Tütüncü, G. P. Srivastava, and S. Bağcı, Theoretical examination of whether phonon dispersion in Nb₃Sn is anomalous", *Phys. Rev. B* **74**, p. 212506 (4pp), (2006).
- [18] W. L. McMillan. Transition temperature of strong-coupled superconductors, *Phys. Rev.* **167**, pp. 331-344, (1968).
- [19] P. B. Allen, and R. C. Dynes. Transition temperature of strong-coupled superconductors reanalyzed, *Phys. Rev. B* **12**, pp. 905-922, (1975).
- [20] K.H. Benemann and J.W. Garland. *Superconductivity in D- and F-B and Metals*, edited by D.H. Douglass (American Institute of Physics, New York, 1971).
- [21] C. W. Chu, and L. J. Vieland. The superconducting transition temperature and its high-pressure behaviour of tetragonal Nb₃Sn, *J. Low Temp. Phys.* **17**, pp. 25-29, (1974).
- [22] P. V. Sreenivasa Reddy, V. Kanchana, G. Vaitheeswaran, P. Modak, and A. K. Verma. Electronic topological transitions in Nb₃X (X=Al, Ga, In, Ge, and Sn) under compression investigated by first principles calculations, *J. Appl. Phys.* **119**, ID 075901 (15pp), (2016).
- [23] L. R. Testardi. Structural instability and superconductivity in A-15 compounds, *Rev. Mod. Phys.* **47**, pp. 637-648, (1975).
- [24] W. Rehwald, M. Rayl, R. W. Cohen, and G. D. Cody. Elastic moduli and magnetic susceptibility of monocrystalline Nb₃Sn, *Phys. Rev. B* **6**, pp. 363-371, (1972).

ORGANOCATALYTIC COUPLING OF BROMO-LACTIDE WITH CYCLIC ETHERS AND CARBONATES

Luigi Cavallo^{1,2*}, Lucia Caporaso¹, Laura Falivene² and Raffaele Credendino^{1,2}

¹*Dipartimento di Chimica e Biologia "A. Zambelli", Università degli Studi di Salerno, Via Giovanni Paolo II 132, 84084 Fisciano, SA, Italy.*

²*Physical Sciences and Engineering Division, King Abdullah University of Science and Technology, KAUST Catalysis Center, Thuwal, 23955-6900, Saudi Arabia*

ABSTRACT. The demand for more sustainable world is pushing chemical industry towards using chemical building blocks from renewable resources or to develop chemical processes better corresponding to the principles of the green chemistry. This goal requires developing new catalytic processes using molecules derived from renewable sources. In this scenario we report here on a computational mechanistic study devoted to clarify the coupling of bromine substituted lactide (Br-LA) with tetrahydrofuran (THF) in presence of a N-heterocyclic carbene (NHC). The computational work clearly indicated that the reaction is catalysed by a bromine anion formed in the initial reactivity of the NHC with Br-LA. Contrary to common knowledge, the NHC is not playing any role in the catalytic cycle.

1 Introduction

Increasing energy demand has often pushed science and technology revolutions. At the beginning of the 20th century, it was the increasing gasoline demand from the emerging automotive market that spurred the transformation of a basically coal economy into the oil economy we still experience. At the beginning of the 21st century it is the energy demand from an increasing world population, together with the increasing levels of atmospheric CO₂, that is pressing science and technology for another revolution. In this context catalysis and chemistry can play a remarkable role towards building a sustainable world. In fact, it has been estimated that catalysis contributes to roughly 30% of the Gross World Product (GWP), and thus developing more sustainable processes by using chemical building blocks from renewable sources, or by developing more efficient and energy less expensive chemical processes, is one of the missions of contemporary chemistry. Among the most promising methodologies is organopolymerization of monomers from renewable sources.

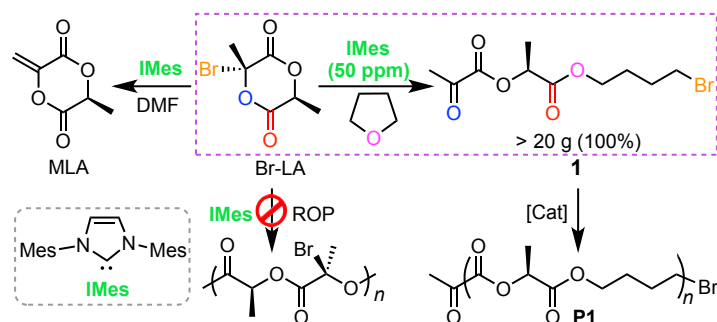


Figure 1: Schematic representation of the reactivity observed when Br-LA is treated in THF in presence of the N-heterocyclic carbene IMes.

Indeed, organopolymerization is today a preferred method for the synthesis of polymers when metal-free products or processes are of primary concern. In this context, the high Brønsted basicity and

nucleophilicity, coupled with good leaving group features, has made catalysts based on N-heterocyclic carbene (NHC) based particularly attractive, due to the unique reactivity and selectivity they promote in different types of organic reactions, including polymerizations. Among the most relevant examples is the ring-opening polymerization (ROP) of lactide [1,2] for the synthesis of relatively high molecular weight biodegradable and biocompatible poly(lactide) (PLA).

Aiming at synthesizing functionalized PLAs with enhanced properties, we started from a Br-substituted L-lactide (Br-LA) presenting a bromine substituent on one of the sp^3 C atoms of LA. While attempting to polymerize Br-LA with N-heterocyclic carbene (NHC) catalysts in tetrahydrofuran (THF), we found that Br-LA undergoes exclusive coupling with the solvent molecule (THF) to form the chiral bromo-diester **1** in Figure 1. This Br-LA + THF coupling reaction is completely selective (in a precisely 1:1 fashion), readily scalable (> 20 g), and extremely efficient (with only 50 ppm NHC catalyst loading). Density functional theory (DFT) calculations at the University of Salerno were performed to clarify the mechanism of this novel coupling reaction of Br-LA with THF [3], in analogy to previous work on the polymerization of polar monomers [4].

2 Methods

Molecular dynamics (MD) simulations were performed to explore the preferential approach between the reactants using the Born–Oppenheimer scheme as implemented in the CP2K Quickstep code [5]. The electronic structure calculations were carried out at the DFT level by using the Perdew–Burke–Ernzerhof exchange and correlation functional. The CP2K program employs a mixed basis set approach with Gaussian-type orbitals (GTO) and plane waves (PWs). An energy cut-off of 300 Ry is used for the plane-waves basis set. A triple- ζ basis set with a double polarization function, in conjunction with the Goedecker–Teter–Hutter pseudopotentials, was used for all the atoms. The systems were introduced in a cubic box of $15 \times 15 \times 15 \text{ \AA}^3$. Distance between reacting atoms was frozen at given values and was used approximate reaction coordinate for short 1ps long MD simulations. Selected structures from the MD simulations were used as starting geometries for static DFT calculations.

The static DFT calculations were performed by using the Gaussian 09 package [6]. Geometries were optimized at the generalized gradient approximation (GGA) level using the BP86 functional and the SVP basis set. The reported free energies were built through single point energy calculations on the BP86/SVP geometries using the hybrid meta GGA M06 functional and the triple- ζ TZVP basis set. Electrostatic and non-electrostatic solvent effects were included with the PCM model using THF as the solvent. Thermal energies and entropy effects were calculated at the BP86 level with a temperature of 298 K and a pressure of 1354 atm. Most of the calculations were performed on the CRESCO platform [7].

3 Results

Initially the general reactivity of a basic and nucleophilic NHC, IMes, towards Br-LA was explored. As for the basic behavior, IMes can remove a proton from the CH group of Br-LA, with a free energy barrier of 10.3 kcal/mol, leading to the ion-pair $[\text{IMesH}]^+\text{Br}^-$ together with the zwitterionic cyclic species **X** (Figure 2). Removing a proton from one of the CH_3 groups to form the ion-pair $[\text{IMesH}]^+\text{Br}^-$ together with MLA is disfavored by 5.6 kcal/mol in terms of free energy, despite the very stable product **Y** is formed. As for the nucleophilic behavior, IMes can interact with both carbonyl groups of Br-LA. The preferential route is for attack to the carbonyl that is less hindered (colored in red, Figure 2) with a *trans* orientation of the attacked C=O and of the Br atom. This corresponds to the concerted ring opening of Br-LA and Br^- elimination from the neighboring C atom with a free energy barrier of 6.9 kcal/mol only. The resulting product is the acylazolium bromide **Z**, 21.4 kcal/mol below reactants. Dissociation of this ion-pair costs 7.4 kcal/mol. Overall,

the results shown in Figure 2 indicate that the easiest reaction pathway corresponds to nucleophilic attack of NHC to the Br-LA with ring-opening of Br-LA and elimination of a free Br⁻ anion.

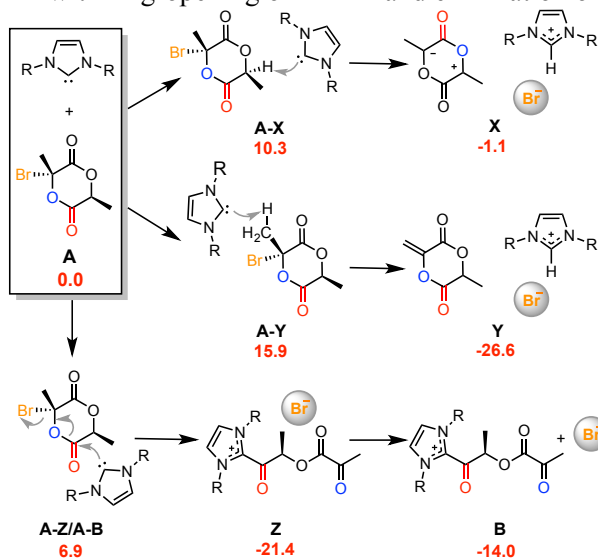


Figure 2. Reactivity of IMes towards Br-LA (numbers in red are free energies in kcal/mol).

In the following step we investigated the reactivity with THF starting from Br⁻, within the “bromide cycle”, as well as from the acylazolium, within the “NHC cycle”, see Figure 3. Within the NHC cycle THF is activated by the acylazolium and it is attacked by Br via transition state **B-C** in Scheme 3, and a free energy barrier of 25.2 kcal/mol. The opening of THF ring leads to the zwitterionic intermediate **C**, followed by regeneration of the free NHC with formation of the coupling product **1** laying nearly 11 kcal/mol below reactants. Within the bromide cycle it is a free Br⁻ anion that acts as the catalyst triggering the opening of the Br-LA ring via transition state **D-E** and a free energy barrier of 17.2 kcal/mol, leading to Br⁻ plus the acyl bromide intermediate **E**, see Figure 3 [3].

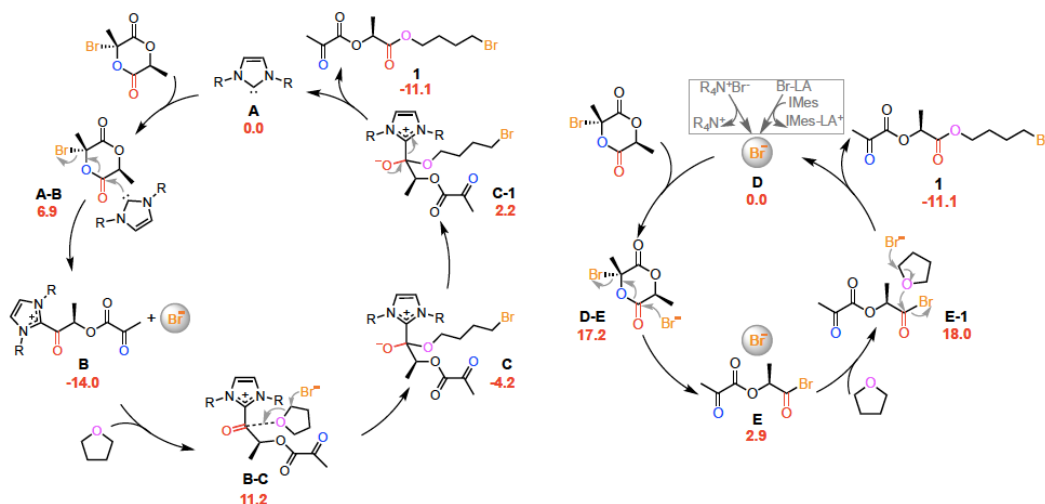


Figure 3. NHC catalytic cycle (left) and bromide catalytic cycle (right) proposed for the coupling of Br-LA with THF. The numbers in red are the free energies of intermediates and transition states relative to the starting species (IMes + THF + Br-LA in the NHC cycle and [IMesH]⁺Br⁻ + THF + Br-LA in the bromine cycle). All free energies are in kcal/mol.

The subsequent reaction of **E** with THF proceeds via transition state **E-1** and a free energy barrier of 15.1 kcal/mol from **E**, leading to the coupling product **1** and liberation of the free Br⁻ anion.

Comparison of the NHC and of the bromide cycles shows that the energy span of the NHC cycle, corresponding to 25.2 kcal/mol from **B** to **B-C**, is 7.2 kcal/mol higher in energy than the largest energy window in the Br⁻ cycle, 18.0 kcal/mol from **D** to **E-1**. This indicated that the real catalyst promoting the observed reactivity is Br⁻, while IMes plays the role of a co-catalyst promoting the liberation of Br⁻ from Br-LA [3].

2 Conclusions

In summary, DFT calculations were fundamental to demonstrate that the coupling reaction of Br-LA and THF proceeds through a catalytic cycle where the real catalyst is the Br⁻ anion, rather than the most intuitive cycle where the NHC is the catalyst. This successful story has required enormous computational resources since: i) Before exploring the Br⁻ catalytic all the more reasonable routes involving the NHC as catalyst were explored; ii) The remarkable conformational flexibility of these systems required very expensive DFT-MD simulations to explore potential approaches of the different molecules before refining the catalytic cycle via standard static DFT methods, typically used to investigate reactivity.

4. References

- [1] K. Fuchise, Y. Chen, T. Satoha and T. Kakuchi. Recent progress in organocatalytic group transfer polymerization. *Polym. Chem.* **4**, 4278, (2013).
- [2] S. Naumann and A. P. Dove. N-Heterocyclic carbenes as organocatalysts for polymerizations: trends and frontiers. *Polym. Chem.* **6**, 3185, (2015).
- [3] J. B. Zhu, X. Y. Tang, L. Falivene, L. Caporaso, L. Cavallo and E. Y.-X. Chen. Organocatalytic Coupling of Bronno-Lactide with Cyclic Ethers and Carbonates to Chiral Bromo-Diesters: NHC or Anion Catalysis?. *ACS Catalysis* **7**, 3929, (2017).
- [4] J. He, Y. Zhang, L. Falivene, L. Caporaso, L. Cavallo and E. X.-Y. Chen. Chain Propagation and Termination Mechanisms for Polymerization of Conjugated Polar Alkenes by Al-Based Frustrated Lewis Pairs. *Macromolecules* **47**, 7765, (2014).
- [5] J. K. M. VandeVondele, F. Mohamed, M. Parrinello, T. Chassaing, J. Hutter. Quickstep: Fast and Accurate Density Functional Calculations Using a Mixed Gaussian and Plane Waves Approach. *J. Comp. Phys. Comm.* **167**, 103, (2005).
- [6] M. Frisch. Gaussian09 Inc., Willingford, Conneticut, USA, (200).
- [7] G. Ponti, F. Palombi, D. Abate, F. Ambrosino, G. Aprea, T. Bastianelli, F. Beone, R. Bertini, G. Bracco, M. Caporicci, B. Calosso, M. Chinnici, A. Colavincenzo, A. Cucurullo, P. Dangelo, M. De Rosa, P. De Michele, A. Funel, G. Furini, D. Giammattei, S. Giusepponi, R. Guadagni, G. Guarnieri, A. Italiano, S. Magagnino, A. Mariano, G. Mencuccini, C. Mercuri, S. Migliori, P. Ornelli, S. Pecoraro, A. Perozziello, S. Pierattini, S. Podda, F. Poggi, A. Quintiliani, A.; Rocchi, C. Scio`, F. Simoni and A. Vita. The role of medium size facilities in the HPC ecosystem: the case of the new CRESCO4 cluster integrated in the ENEAGRID infrastructure. Proceedings of the 2014 International Conference on High Performance Computing and Simulation, HPCS 2014, art. no. 6903807, 1030-1033.

AB INITIO FORMATION ENERGY OF HYDROGENATED GRAPHENE OXIDES

Francesco Buonocore^{1*}, and Nicola Lisi¹

¹ ENEA Italian National Agency for New Technologies, Energy and Sustainable Economic Development, C.R. Casaccia, Via Anguillarese, 301, I-00123 Rome, Italy

ABSTRACT. The ideal structure of graphene oxide should consist of a defectless graphene lattice with oxygen related groups, either epoxide or hydroxyl bonded out of the plane. In experiments however graphene oxide is usually derived from graphite through strongly oxidative chemical reactions. Such chemical route, which is known to produce a material with a defective lattice, it is also expected to add heterogeneous carbon groups that can be only in a non-hydrogenated form. Therefore hydrogenated graphene oxide can only be synthesised by post-processing methods such as hydrogen spillover or plasma functionalization. On the other hand the direct synthesis of hydrogenated graphene oxide by chemical vapour deposition, hence the possibility to insert in the lattice hydrogenated carbon groups during growth, cannot be excluded in principle. Here we have used QUANTUM ESPRESSO package installed on the high performance computer facility CRESCO to perform *ab initio* calculations of the formation energy of hydrogenated and non-hydrogenated graphene oxide derivatives, functionalized with epoxide and hydroxyl groups. We have investigated more than forty configurations and calculated which of them are stable.

1 Introduction

Graphene oxide (GO) is easily obtained by the exfoliation of graphite oxide, using ultrasonic treatment [1] or thermal shocks [2]. It can be easily dispersed in water and exhibits interesting features, such as a sizeable electronic band gap, giant infrared absorption, catalytic activity as well as useful mechanical properties [3-7]. GO is commonly prepared by strongly oxidative chemical routes, such as Hummers' method [8]. GO produced in experiments usually contains several defects which spoil the hexagonal symmetry of the carbon lattice. However, the ideal GO is a functionalized form of graphene that contains only epoxide and hydroxyl functional groups disorderly distributed along a defect-free, two-dimensional carbon lattice [2-11], and therefore covalently-bonded hydrogen is not expected. Nevertheless, using a post-processing techniques, hydrogenated GO, referred hereafter as HGO, can be synthesized [12]. Moreover, one can postulate that an ideal GO (i.e., the hydroxyl- and epoxy-based graphene derivative) could be synthesized via alternative chemical-physical methods that do not involve a strongly oxidative wet chemistry (e.g., by means of a chemical vapor deposition – CVD – process with suitable gas precursors and conditions) eventually adding plasma activation of selected radicals. These methods do not preclude the formation of HGO. By adding the hydrogen and hydroxyl functionalization, the HGO structures proposed in this work would instead allow a fine control of the chemical interface with different solids and liquids. Further, the residual sp^2 , alkene bonds can act as sites available for additional covalent functionalization processes. Several theoretical studies have investigated the periodic as well as the irregular distribution of oxygen species in the two-dimensional carbon geometry [13-18]. However, no one has investigated so far the stability of the HGO structures. In the present report we investigate by *ab initio* calculations the stability of graphene lattices functionalized with oxygen species and hydrogen, in order to find which

are the stable structures, favoured with respect to the competing formation of water by the H and O atoms.

2 Computational details

The computational approach was based on a pseudo-potential plane-wave method using PWSCF code as implemented in the QUANTUM-ESPRESSO package [19], compiled with Intel Fortran compiler, Math Kernel Library (MKL) and Message Passing Interface (MPI) parallelization on the Cresco4 cluster of the high performance computer facility CRESCO [20], with a good scalability up to hundreds of cores. We used the generalized gradient approximation (GGA) with the Perdew, Burke and Ernzerhof (PBE) exchange-correlation functional [21], taking into account spin-polarisation. The pseudo-potential plane-wave calculations were performed using Vanderbilt ultra-soft pseudo-potentials [22]. All geometry optimizations were performed with cut-off for the wave functions of 40 Ry, cut-off for the charge density of 400 Ry and $12 \times 12 \times 1$ Monkhorst-Pack grid. The systems were fully relaxed with a convergence threshold of 0.001 Ryd/Å on the inter-atomic forces. We had previously optimized the unit cell of graphane, a fully hydrogenated graphene structure [23], by imposing that the stress on the cell is less than 0.04 GPa, and we are here using the same cell for each of the functionalized graphene structures. The final self-consistent calculations of the optimized structure properties made use of a cut-off for the wave functions and charge density of 60 and 600 Ry, respectively, allowing a convergence of the total energy below 0.002 eV/atom, compared to calculations with 70 Ry of cut-off and $15 \times 15 \times 1$ Monkhorst-Pack grid. In all of the examined structures, we have added O and/or H atoms to the same carbon honeycomb supercell built by using the in-plane 2×2 unit cell of the graphene which contains 8 C atoms. The vacuum gap between each monolayer and its image was set to 20 Å.

We considered two different kind of functionalization that we distinguish with the symbols G_{OH} and G_O : the G_{OH} structures have all C atoms sp^3 hybridized as in graphane; the G_O structures have a mix of sp^2 and sp^3 hybridization as in partially functionalized graphene. In this way, for instance, $G_{OH}(n_h OH n_{EPO} O)$ indicates that n_h hydroxide and n_{EPO} epoxide groups have been added to the ideal graphene supercell, and then all of the remaining $(8 - n_h - 2n_{EPO})$ C atoms have been hydrogenated; $G_O(n_{EPO} O n_h OH n_{HYD} H)$ indicates that n_h (n_{EPO}) hydroxide (epoxide) groups and n_{HYD} hydrogen atoms (those that are not in the hydroxide group) have been added to C atoms. The functionalized $(n_h + 2n_{EPO} + n_{HYD})$ C atoms are sp^3 hybridized and the remaining $(8 - n_h - 2n_{EPO} - n_{HYD})$ C atoms in the supercell are sp^2 hybridized.

The formation energy per functionalized C atom is defined as:

$$E_F = \left(E_{TOT} - E_G - \frac{1}{2} n_O E_{O_2} - \frac{1}{2} n_H E_{H_2} \right) / n_F \quad (1),$$

where E_{TOT} and E_G are the total electronic energy of the G_{OH} or G_O and graphene systems, n_O and n_H are the number of O and H atoms, n_F is the number of functionalized C atoms and E_{O_2} and E_{H_2} are the total energy of O_2 and H_2 molecules, respectively. The module of formation energy says how much stable or unstable is the system. Low formation energy (i.e. more negative values) corresponds to more stable systems.

We calculated the binding energy per functional group in accord with the following definition:

$$E_B = (E_{TOT} - E_G - n_{EPO} E_O - n_{HYD} E_H - n_h E_{OH}) / (n_{EPO} + n_{HYD} + n_h) \quad (2),$$

where E_G , E_O , E_H and E_{OH} are the total energy of graphene, O atom, H atom and OH group. Following definition (2), negative (positive) binding energy corresponds to bound (unbound) system and its module gives a measure of the average strength of the bonds. Geometry optimization,

formation energy and binding energy have been calculated over a full amount of more than forty atomic configurations.

3 Results and discussion

3.1 Hydrogenated graphene oxide

We have performed a systematic study of hydroxyl functionalized GOH structures, where all of the C atoms not bound to O were passivated with hydrogen so that every C atom is sp^3 hybridized as in graphane. The relaxed geometries are shown in Figure 1 a-h), where the lowest energy structures for each composition, over 25 different configurations examined, are reported. We have found that by substituting the H atoms of graphane by hydroxyl groups the average C-C bond length increases so that the covalent bond gets weaker. On the other side, the increase of the OH-H bond length can be related to the formation of hydrogen bonds when the density of hydroxyl groups increases. Here OH indicates the O atom of the hydroxyl group to avoid any ambiguity with the epoxy O. The average C-OH bond length starts to decrease only when one of the two sides is fully functionalized and then the formation of the hydrogen bonds chain is completed. The absolute value of the binding energy, reported in Figure 2 a), decreases by increasing the number of hydroxyl groups, implying the weakening of the bond strength. Besides, the formation energy, shown in Figure 2 c) (triangle points), decreases by increasing n_h , so that by replacing H atoms with hydroxyl groups the functionalized graphene becomes more stable. We observe that the $G_0H(n_hOH)$ structures are even more stable than graphane, which has the same total number of functionalized C atoms. $G_0H(8OH)$, which is the full passivated by hydroxyl groups structure whose stability has been investigated by Wang [17], is more stable than graphane by as much as 1.23 eV per functionalized C atom. However, we highlight that $G_0H(8OH)$ is the only structure with all C atoms sp^3 hybridized considered in this paper that does not present atomic hydrogen functionalization.

We have also considered the $G_0(OH H)$, $G_0(2OH 2H)$ and $G_0(3OH H)$ structures that are derived from $G_0H(OH)$, $G_0H(2OH)$ and $G_0H(3OH)$ but which contains only the minimal number of H atoms necessary to passivate the C dangling bonds due to unpaired electrons. The resulting structures are passivated by one, two and one H atom, respectively, such that the tri-coordinated C atoms are sp^2 hybridized (as in graphene) and the tetra-coordinated C atoms are sp^3 hybridized (as in graphane). The relaxed structures are shown in Figure 1 i-k). Among these three structures, $G_0(2OH 2H)$ is the one with the shortest average C-OH bond length and the highest absolute value of binding energy. We observe from Figure 2 c) (round points) that the free energy of formation decreases, i.e. stability increases, by rising the number of hydroxyl groups.

In order to study the stability of the structures functionalized both with hydroxyl and epoxy groups we considered the two limit structures $G_0(O OH)$ and $G_0(2O 2OH)$, corresponding to low degree of oxidation and saturated oxidation, respectively. The low energy isomers were investigated, without studying the stability, by Lahaye and co-authors [15]. In this section we investigate the hydrogenated structures $G_0H(O OH)$ and $G_0H(2O 2OH)$, fully covered by adding five and two H atoms, respectively, shown in Figure 1 n,l). Moreover we investigated $G_0(O 4H)$, corresponding to graphene with one epoxy group adsorbed and passivated with four H atoms, where two tri-coordinated C atoms in the $G_0(O 4H)$ structure are sp^2 hybridized. The relaxed structures of $G_0H(2O 2OH)$, $G_0(O 4H)$ and $G_0H(O OH)$ are shown in Figure 1 l-n). $G_0H(O OH)$ has the shortest average C-O bond length and is also the structure with more C atoms hydrogen-passivated. The $G_0H(O OH)$ and $G_0H(2O 2OH)$ are the structures with the lowest value of the binding energy and formation energy of -0.38 and -0.50 eV per functionalized C atom, respectively, as reported in Figures 2 b) and 2 d). However, the two structures, epoxide- and hydroxyl-functionalized, are both found to be less stable than

hydrogenated and hydroxyl-functionalized $G_0H(nhOH)$ structures for $n_h > 1$. On the other side, $G_0(O 4H)$ is less stable with high formation energy.

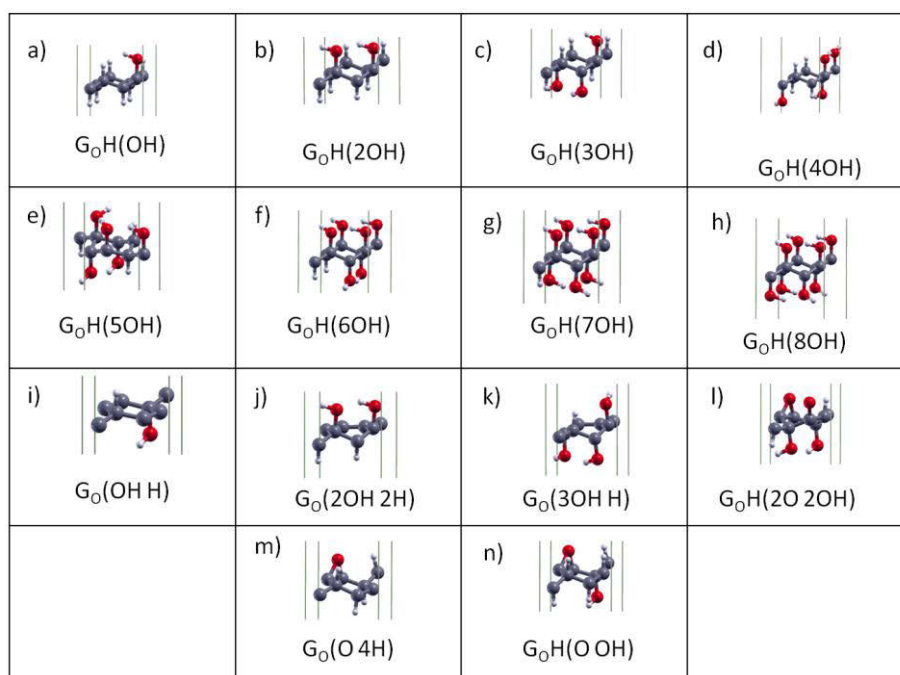


Fig. 1: The relaxed geometries of the most stable hydrogenated graphene oxide configurations are shown.

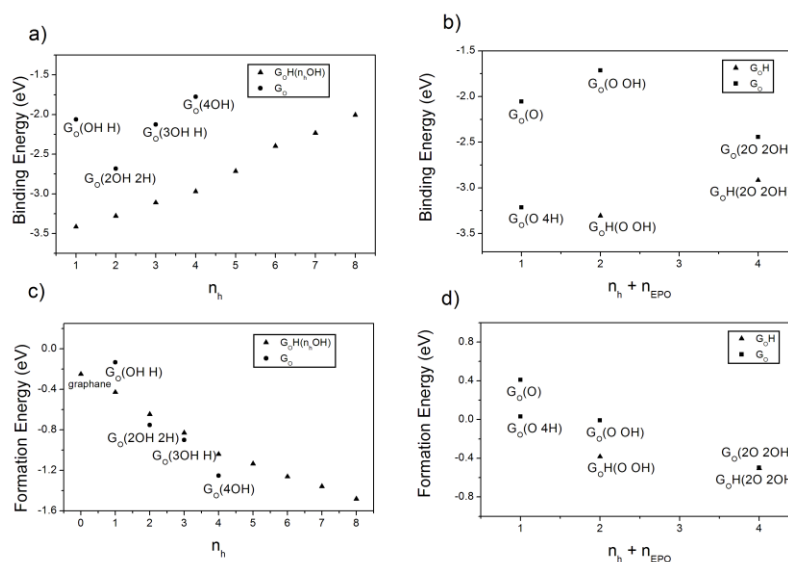


Fig. 2: Binding energy per functional group of a) graphene functionalized with hydrogen atoms and hydroxyl groups and b) graphene functionalized with hydrogen atoms and/or epoxy and hydroxyl groups. In c) and d), respectively, formation energy per functional group of the same structures.

3.2 Non hydrogenated graphene oxide

The non-hydrogenated $G_O(O\ OH)$, $G_O(20\ 2OH)$ and $G_O(O)$ structures were also investigated. The relaxed structures are shown in Figure 3 a-c). The $G_O(20\ 2OH)$ structure have short average C-OH and C-O lengths and it is also the one characterized by the highest absolute value of the binding energy per functionalized C atom. The $G_O(20\ 2OH)$ structure is found to be the most stable among them with formation energy of -0.50 eV per functionalized C atom. On the other hand, the non-hydrogenated $G_O(O\ OH)$ and $G_O(O)$ structures have high formation energy of -0.01 and 0.408 eV per functionalized C atom. In particular, the low stability of $G_O(O\ OH)$ is related to the presence of a single unpaired electron in the unit cell so that it reacts easily with functional groups in the environment. The unpaired electron results in a magnetic moment of 1.0 Bohr magneton per unit cell. The $G_O(n_hOH)$ structures with $n_h= 1, 2, 3, 5, 6$ and 7 , not shown here, obtained from the most stable structures found in the section 3.1 by removing the hydrogen atoms, have unpaired electrons and are very reactive, and so they are unstable. Indeed, the $G_O(n_hOH)$ structures with $n_h= 1, 5$ and 7 exhibit magnetic properties with 1.0 Bohr magneton, i.e., a single unpaired electron, per unit cell of eight carbon atoms. The $G_O(n_hOH)$ structures with $n_h= 2$ and 3 exhibit 1.68 and 0.76 Bohr magneton per unit cell, while $G_O(6OH)$ exhibits 2.0 Bohr magneton per unit cell (i.e. two unpaired electrons localized on two different carbon atoms). Instead $G_O(4OH)$, shown in Figure 3 d), have not unpaired electrons, and the average C-OH bonds are longer, while the binding energies is higher and the formation energy lower than those of $G_OH(4OH)$, as shown in Figures 1 a) and 1 c), respectively.

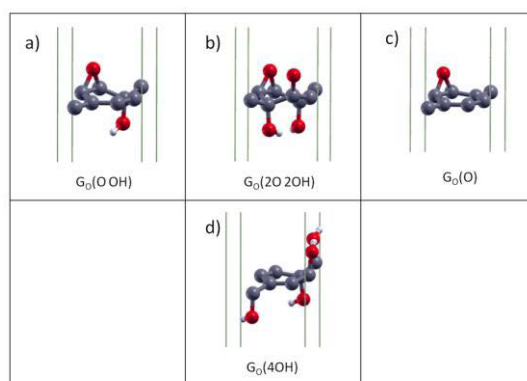


Fig. 3: The relaxed geometries of the graphene oxide structures are shown.

4 Conclusions

In conclusion, By using first principles calculations we have estimated the energy of formation of hydrogenated and not-hydrogenated graphene oxide derivatives, functionalized with epoxide and hydroxyl groups. The graphene oxide derived structures have been modelled by using a periodic cell containing 8 C atoms. We have found that hydrogenation increases the average strength of the bonds and the stability. The formation energy of $G_OH(n_hOH)$ structures with full sp^3 hybridization of C atoms decreases towards more stable configurations by increasing n_h , i.e., by substituting H atoms with hydroxide groups, and $G_OH(8OH)$ results as the most stable. We found that $G_OH(n_hOH)$ structures are the most stable among the investigated systems and that they can be even more stable

than graphane. The hydrogenated graphene oxide structures functionalized with hydroxyl and epoxy groups, $G_0H(O\ OH)$ and $G_0H(2O\ 2OH)$, have low formation energy, but they are less stable than most of $G_0H(n_hOH)$ structures. Among the non-hydrogenated GO structures with mixed sp^2 and sp^3 hybridization of C atoms, $G_0(4OH)$ has low formation energy, as well as $G_0(2O\ 2OH)$.

The use of catalysts could promote the formation of HGO. Indeed, in a recent work [12] the hydrogenation of GO at room temperature has been established using nickel nanoparticles and through in-situ generated hydrogen and enhanced spillover. The present results suggest the structures to be investigated by phase diagram calculations [24], to prove that the direct growth or synthesis of graphene HGO derivatives is experimentally feasible in suitable conditions. In analogy to organic molecules, the HGO structures here proposed could allow a fine control of the chemical interactions and interfacing properties with other molecules, liquids and solids.

The computing resources and the related technical support used for this work have been provided by CRESCO/ENEAGRID High Performance Computing infrastructure and its staff [20]. CRESCO/ENEAGRID High Performance Computing infrastructure is funded by ENEA, the Italian National Agency for New Technologies, Energy and Sustainable Economic Development and by Italian and European research programs, see <http://www.cresco.enea.it/english> for information.

References

- [1] Hernandez, Y.; Nicolosi, V.; Lotya, M.; Blighe, F.M.; Sun, Z.; De, S.; McGovern, I.T.; Holland, B.; Byrne, M.; Gun'ko, Y.K. et al. High-Yield Production of Graphene by Liquid-Phase Exfoliation of Graphite. *Nat. Nanotechnol.* **2008**, *3*, 563-568.,
- [2] Schniepp, H. C.; Li, J.-L.; McAllister, M. J.; Sai, H.; Herrera-Alonson, M.; Adamson, D. H.; Prud'homme, R.K.; Car, R.; Seville, D.A.; Aksay, I.A. Functionalized Single Graphene Sheets Derived from Splitting Graphite Oxide. *J. Phys. Chem. B.* **2006**, *110*, 8535-8539.
- [3] Yan J.-A.; Xian, L, Chou, M.Y.; Structural and Electronic Properties of Oxidized Graphene. *Phys. Rev. Lett.* **2009**, *103*, 086802.
- [4] Acik, M.; Lee, G.; Mattevi, C.; Chhowalla, M.; Cho, K.; Chabal, Y. J. Unusual Infrared-Absorption Mechanism in Thermally Reduced Graphene Oxide. *Nat. Mater.* **2010**, *9*, 840–845.
- [5] Robinson, J. T.; Perkins, F. K.; Snow, E. S.; Wei, Z. Q.; Sheehan, P. E. Reduced Graphene Oxide Molecular Sensors. *Nano Lett.* **2008**, *8*, 3137.
- [6] Park, S.; Lee, K.-S.; Bozoklu, G.; Cai, W.; Nguyen, S. T.; Ruoff, R. S. Graphene Oxide Papers Modified by Divalent Ions—Enhancing Mechanical Properties via Chemical Cross-Linking. *ACS Nano* **2008**, *2*, 572–578.
- [7] Robinson, J. T.; Zalalutdinov, M.; Baldwin, J. W.; Snow, E. S.; Wei, Z.; Sheehan, P.; Houston, B. H. Wafer-scale Reduced Graphene Oxide Films for Nanomechanical Devices. *Nano Lett.* **2008**, *8*, 3441.
- [8] Hummers, W.S.; Offeman, R.E. Preparation of Graphitic Oxide. *J. Am. Chem. Soc.* **1958**, *80*, 1339.
- [9] Dreyer, D. R.; Park, S.; Bielawski, C.W.; Ruoff, R.S. The Chemistry of Graphene Oxide. *Chem. Soc. Rev.* **2010**, *39*, 228–240.
- [10] Szabo, T.; Berkesi, O.; Forgo, P.; Josepovits, K.; Sanakis, Y.; Petridis, D.; Dékány, I. Evolution of Surface Functional Groups in a Series of Progressively Oxidized Graphite Oxides. *Chem. Mater.* **2006**, *18*, 2740–2749.
- [11] Lerf, A.; He, H.; Forster, M.; Klinowski, J. Structure of Graphite Oxide Revisited. *J. Phys. Chem. B* **1998**, *102*, 4477–4482
- [12] Krishna, R.; Titus, E.; Okhay, O.; Gil, J. C.; Ventura, J.; Ramana, E. V.; Gracio, J. J. A., Rapid Electrochemical Synthesis of Hydrogenated Graphene Oxide Using Ni Nanoparticles. *Int. J.*

Electrochem. Sci. **2014**, *9*, 4054 - 4069

- [13] Boukhvalov, W.; Katsnelson, M. I. Modeling of Graphite Oxide. *J. Am. Chem. Soc.* **2008**, *130*, 10697.
- [14] Fonseca, A. F.; Zhang, H.; Cho, K. Formation Energy of Graphene Oxide Structures: A Molecular Dynamics Study on Distortion and Thermal Effects. *Carbon* **2015**, *84*, 365–374.
- [15] Lahaye, R. J. W. E.; Jeong, H. K.; Park, C. Y.; Lee, Y. H. Density Functional Theory Study of Graphite Oxide for Different Oxidation Levels. *Phys. Rev. B* **2009**, *79*, 125435.
- [16] Ghaderi, N.; Peressi, M. First-Principle Study of Hydroxyl Functional Groups on Pristine, Defected Graphene, and Graphene Epoxide. *J. Phys. Chem. C* **2010**, *114*, 21625–21630
- [17] Wang, L.; Sun, Y. Y.; Lee, K.; West, D.; Chen, Z. F.; Zhao, J. J.; Zhang, S. B. Stability of Graphene Oxide Phases from First-Principles Calculations. *Phys. Rev. B* **2010**, *82*, 161406(R).
- [18] Huang, B.; Xiang, H.; Xu, Q.; Wei, S.-H.; Overcoming the Phase Inhomogeneity in Chemically Functionalized Graphene: The Case of Graphene Oxides. *Phys. Rev. Lett.* **2013**, *110*, 085501.
- [19] Giannozzi, P.; Baroni, S.; Bonini, N.; Calandra, M.; Car, R.; Cavazzoni, C.; Ceresoli, D.; Chiarotti, G. L.; Cococcioni, M.; Dabo, I.; et al. QUANTUM ESPRESSO: a modular and open-source software project for quantum simulations of materials. *J. Phys. Condens. Matter* **2009**, *21*, 395502
- [20] Ponti, G.; Palombi, F.; Abate, D.; Ambrosino, F.; Aprea, G.; Bastianelli, T.; Beone, F.; Bertini, R.; Bracco, G.; Caporicci, M.; et al. The Role of Medium Size Facilities in the HPC Ecosystem: the Case of the New CRESCO4 Cluster Integrated in the ENEAGRID Infrastructure. *IEEE HPCS* **2014**, *6903807*, 1030–1033. Ecosystem: the Case of the New CRESCO4 Cluster Integrated in the ENEAGRID Infrastructure. *IEEE HPCS* **2014**, *6903807*, 1030–1033.
- [21] Perdew, J. P.; Burke, K.; Ernzerhof, M. Generalized Gradient Approximation Made Simple. *Phys. Rev. Lett.* **1996**, *77*, 3865.
- [22] Vanderbilt, D. Soft self-consistent pseudopotentials in a generalized eigenvalue formalism. *Phys. Rev. B* **1990**, *41*, 7892.
- [23] Sofo, J. O.; Chaudhari, A. S.; Barber, G. D. Graphane: A two-dimensional hydrocarbon. *Phys. Rev. B* **2007**, *75* 153401.
- [24] Buonocore, F.; Capasso, A.; Lisi, N. An ab initio study of hydroxylated graphane. *J. Chem. Phys.* **2017**, *147* 104705.

THE ROLE OF PLANT PHENOLOGY IN STOMATAL OZONE FLUX MODELLING

Alessandro Anav^{1*}, Alessandra De Marco¹

¹ *Italian National Agency for New Technologies, Energy and the Environment (ENEA), C.R. Casaccia, S. Maria di Galeria, Italy.*

ABSTRACT. Plant phenology plays a pivotal role in the climate system as it regulates the gas exchange between the biosphere and the atmosphere. The uptake of ozone by forest is estimated through several meteorological variables and a specific function describing the beginning and the termination of plant growing season; actually, in many risk assessment studies, this function is based on a simple latitude and topography model. In this study, using two satellite datasets, we apply and compare six methods to estimate the start and the end dates of the growing season across a large region covering all Europe for the year 2011. Results show a large variability between the green-up and dormancy dates estimated using the six different methods, with differences greater than one month. However, interestingly, all the methods display a common spatial pattern in the uptake of ozone by forests with a marked change in the magnitude, up to 1.9 TgO₃ yr⁻¹, and corresponding to a difference of 25% in the amount of ozone that enters the leaves. Our results indicate that improved estimates of ozone fluxes require a better representation of plant phenology in the models used for O₃ risk assessment.

1 Introduction

Plant phenology is usually defined as the timing of periodic events in the life cycle of plants. For any given biome, phenology events, such as bud-burst, flowering, leaf unfolding, and leaf coloration, depend primarily on the climatic conditions. On the other hand, plant phenology influences climate, defining the biosphere-atmosphere boundary conditions which influence surface albedo and terrestrial water cycle dynamics, as well as the atmospheric chemistry through the exchange of several compounds. Therefore, reliable phenological models are needed to correctly quantifying gas exchanges between terrestrial vegetation and the atmosphere.

The past decade has seen a particularly rapid increase in the number of launched satellites, as well as an improvement in both spatial and temporal resolution of the data they produce. In this regard, remote sensing is a valuable tool for plant phenology estimation. In fact, the seasonal cycle of the normalized difference vegetation index (NDVI) as well as time evolution of the leaf area index (LAI) have been widely used to estimate the timing of phenological events.

In this frame, this work aims to assess how much the stomatal O₃ flux changes when different phenological models are used to estimate the start and the end of growing season. Here, using a regional climate model and a chemistry transport model, we compare for the year 2011 the stomatal O₃ fluxes computed using different algorithms and methodologies to estimate the green-up and dormancy dates over a large region extending from Northern Africa to the Scandinavian region and part of the Russia.

2 Models description

Meteorological data are simulated through the Weather Research and Forecasting (WRF3.6); it is a limited-area, non-hydrostatic, terrain-following eta-coordinate mesoscale model. The model domain covers almost all Europe (except northern Scandinavia and Iceland) and part of North Africa (550x340 grid points) with a spatial resolution of 16 km [1].

To simulate gas-phase chemistry, aerosol formation, transport and deposition at regional scale we used the chemistry-transport model CHIMERE (version 2013b). The model was forced by WRF output and anthropogenic emissions, at the same spatial resolution of the atmospheric model.

Both models are parallel and have been compiled with the intel compiler and ran over CRESCO3 with 144 CPUs; the domain decomposition has been achieved with MPI.

Satellite retrievals have been processed using IDL and MATLAB, while NCL has been used to map the stomatal uptake of ozone.

3 Results

Using two satellite datasets and six widely used methods to extract the start and the end of the growing season, our results indicate a common spatial pattern in the cumulated stomatal uptake of O₃, although the magnitude of the fluxes slightly differs (**Figure 1**). This finding suggests that, on regional scale, climate is the main driver of the uptake of gases from the atmosphere to the vegetation [1]

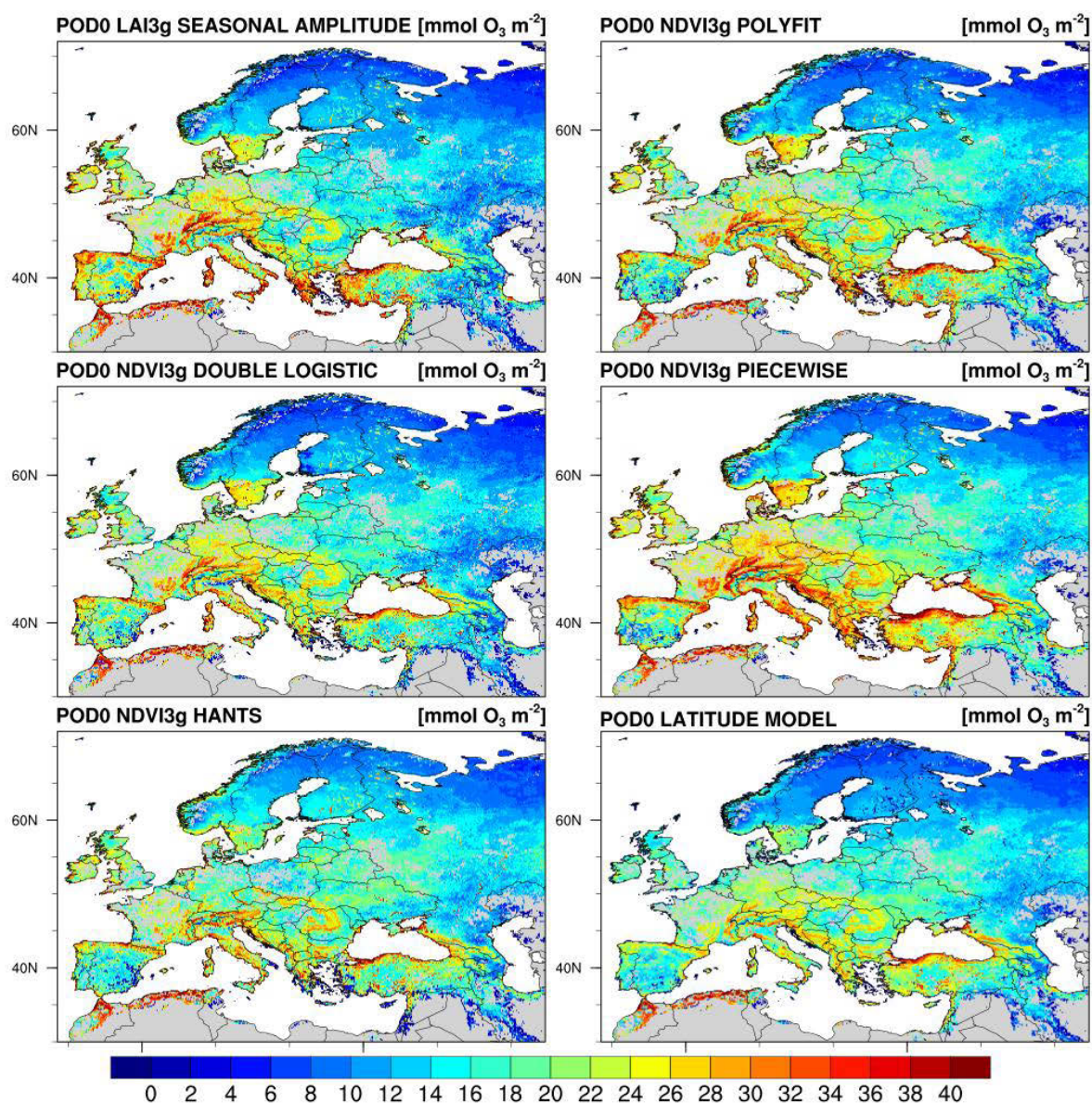


Fig.1: Spatial distribution of stomatal O₃ fluxes (i.e. POD0) computed using different methods to estimate the beginning and the end of the growing season.

References

- [1] A. Anav et al. The role of plant phenology in stomatal ozone flux modelling. *Global Change Biology* in press, (2017).

CALIBRATION OF THE HIGH RESOLUTION REGIONAL EARTH SYSTEM MODEL (REGESM) OVER THE MED-CORDEX DOMAIN

Struglia M.V.^{1*}, Calmanti S.¹, Carillo A.¹, Dell'Aquila A.¹, E. Lombardi¹, Sannino G.¹

¹*ENEA SSPT-MET-CLIM, Italian National Agency for New Technologies, Energy and Sustainable Economic Development, 00123 Roma, Italy*

ABSTRACT. Preliminary results are presented from the calibration of a high resolution Regional Earth System Model (RegCM4) for the Mediterranean Area. Over land, climate model bias is cold during winter and dry-hot during summer. Over the ocean, the bias is weaker, with a constant wet bias throughout the year and a cold bias during winter. The climate model will be used to downscale CMIP5 climate scenarios for the MED-Cordex initiative.

1 Introduction

The Mediterranean Sea is a semi-enclosed basin surrounded by regions characterized by complex orography, which favours the insurgence of strong local winds and triggers interactions and contrasts between ocean, atmosphere and land, driving its own peculiar thermohaline circulation. Both winds and buoyant fluxes are important forcing for the Mediterranean Sea and an effort is required to study the regional climate as a unique atmosphere-ocean coupled system, rather than in its single components.

In this work we present the first results of the climate simulations performed with the Regional Earth System Model (RegESM) [1] in the framework of the Med-CORDEX initiative [2]. Although state of the art climate models, implemented on high performing computing resources, can reach very high spatial resolution, many physical processes still take place on scales smaller than the one explicitly resolved, and physical parameterizations are needed. The choice between different available parameterizations for the same physical processes, as well as an accurate tuning of the parameters in a range of allowed values, are critical in order to model climate of a given region.

2 Setup

In its current configuration, RegESM active components are atmosphere (RegCM 4.5), ocean (MITgcm) and river routing (HD), all of them merged and managed by the driver, the Earth System Modeling Framework (ESMF) which is responsible for the interaction between the components (i.e. boundary data exchange, regridding) and their synchronization.

RegCM4 modelling system is a hydrostatic, compressible, sigma-p vertical coordinate model run on an Arakawa B-grid in which wind and thermodynamical variables are horizontally staggered. The RegCM configuration adopted for this work has 23 vertical levels and the following physical parameterizations: the CCM3 radiative transfer scheme [3]; a modified version of the the Holtslag parameterization of the planetary boundary layer [4]; the NCAR land surface model. For moist

processes, the RegCM4 configuration adopted for this study uses the Grell cumulus convection model [5] with a Fritsch-Chappell scheme for unresolved convection. The resolved scale precipitation is modeled with the SUBEX parameterization [6].

A *hindcast* simulation (aimed to reproduce realistically the recent past climate) has been run with the objective of calibrating the parameterizations of the atmospheric component of the RegESM model. Moreover, it is necessary to evaluate the possible biases of the model, that must be properly taken into account when future scenario simulations are performed. The ERA-interim reanalysis dataset is used as initial and lateral boundary condition for the atmosphere.

The model is run on CRESCO4 in a sequential mode on 256 cpus, which turns out to be the best choice in terms of scalability of the models, over the given domain at the given resolution. The average CPU time for one year of simulation is around 1 day. However, given the relatively low requirements in terms of CPUs, multiple simulation might be performed if necessary.

Three-dimensional 6-hourly output data is stored during the model simulation. Therefore, the amount of storage required for the whole hindcast simulation, covering the years from 1980 to 2013, is of the order of 10 Tb. NetCDF libraries are used by RegESM to manage I/O format.

3 Main results

Building on our past experience on the use of the RegCM, [7] we have tested several aspects of the climate modelling platform.

The Grell parameterization for small-convection has been thoroughly tested with a specific focus on the parameters that control the maximum precipitation efficiency, i.e. the maximum attainable rate of conversion in updrafts. A maximum precipitation efficiency of 0.8 has been chosen to avoid too intense rainfall events associated to atmospheric convection, especially during the summer months.

The SubEx model for cloud formation has also been tested. We have found that, over the area of interest, a correct description of large scale cloud formation processes is obtained by releasing all constraints to the cloud model. In particular, in our configuration the model is able to generate cloud on all but the first – near ground – vertical levels and the maximum allowed fraction cover is 1, i.e. the entire grid-cell is allowed to become cloud covered, which is a reasonable choice for a high-configuration resolution.

Particular attention has been devoted to the tuning of the Biosphere Atmosphere Transfer Scheme (BATS) [8]. By default, land emissivity is computed in the BATS scheme by adopting a formula which relates emissivity to the corresponding estimated values of albedo. For desert and semi-desert regions, land surface emissivity has been set to the values estimated from direct satellite retrievals (column *Exp2* in Table 1) [9], and then slightly corrected to reduce the temperature model bias over the desert area which represent a large fraction of the entire model domain. The values of land surface emissivity adopted for our final configuration are reported in Table 1 under the column *Exp3*. In the BATS scheme, the stomatal resistance of different soil types (crop and evergreen broadleaf) has been also adjusted by following the same rule adopted in previous studies [8].

The performance of the calibrated configuration is summarized in Figure 1. The model has a positive (wet) mean annual bias of rainfall over the ocean and a negative (dry) bias over land. For temperature the model is slightly cold over the entire domain except for a small warm bias in the eastern part of the domain. However, the model systematic bias shows a clear seasonal cycle. Such cycle is more pronounced over land which is generally cold during winter and dry-hot during summer. Over the ocean, the positive bias is mostly persistent during the entire year, while the temperature bias shows a cold phase during summer.

BATS param	Soil type	Exp0	Exp1	Exp2	Exp3
Indemiss(11)	Emissivity - Semidesert	def	0.97	0.85	0.91
Indemiss(8)	Emissivity - Desert	def	0.965	0.76	0.86
Indemiss(19)	Emissivity - Forest/Mosaic field	Def	0.981	0.981	0.985

Table 1. Tuning of the land-surface emissivity.

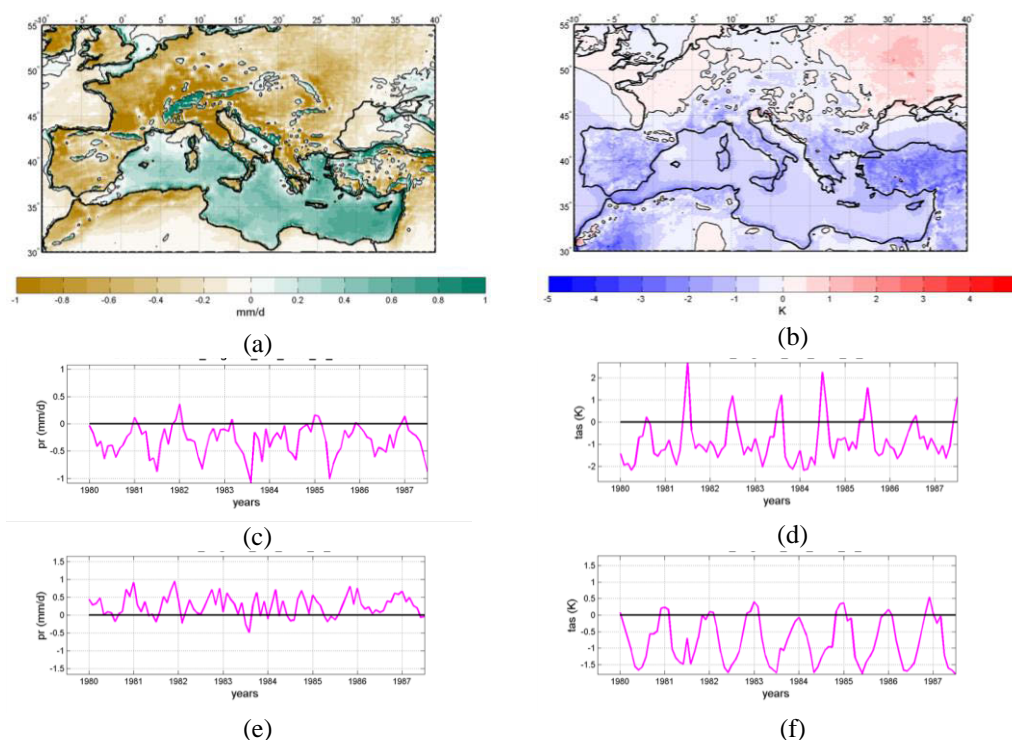


Figure 1. The RegCM4 systematic bias for rainfall (left column) and temperature (right column) in the calibrated configuration. The panels show the mean annual bias (a,b); the seasonal bias over land (c,d) and over sea (e,f).

4 Outlook

The calibration of an high-resolution configuration of RegCM4 for the Mediterranean area will enable ENEA to produce climate scenarios in the framework of the Med-CORDEX initiative [2]. The current plan is to run climate scenarios using at least 3 low resolution global models from the CMIP5 archive to provide lateral boundary conditions to RegCM4 (GFDL-ESM2M, Had-GEM2-ES, CNRM-CM5). For each global model, the three main RCPs scenarios are available and will be considered for the downscaling by giving priority to the scenario RCP45. Depending on available resources a maximum of 9 climate scenarios will be performed. This corresponds to a maximum 1350 years of simulations. Although the corresponding disk usage for the raw model output is huge (approximately 409Tb), a selection of the most required model variables can reduce the long term

archive needs substantially, up to a factor 10. The expected storage requirement will be therefore of about 50Tb for the long-term archive. The total required CPU time amounts to approximately $8 \cdot 10^6$ hour.

References

- [1] Turuncoglu U.U. and Sannino G. Validation of newly designed regional earth system model (RegESM) for Mediterranean Basin. *Clim Dyn* (2017) 48:2919–2947. DOI 10.1007/s00382-016-3241-1
- [2] Ruti P.M. et al., Med-CORDEX Initiative for Mediterranean climate studies. *Bulletin of the American Meteorological Society, American Meteorological Society*, **97** -7, pp.1187-1208 (2016). DOI: 10.1175/BAMS-D-14-00176.1
- [3] Kiehl, J. T., Hack, J. J., Bonan, G. B., Boville, B. A., & Briegleb, B. P. (1996). Description of the NCAR Community Climate Model (CCM3). Technical Note (No. PB--97-131528/XAB; NCAR/TN--420-STR). National Center for Atmospheric Research, Boulder, CO (United States). Climate and Global Dynamics Div..
- [4] Giorgi F., Coppola E., Solmon F., Mariotti L. and others (2012). RegCM4: model description and preliminary tests over multiple CORDEX domains. *Clim Res* 52:7-29. <https://doi.org/10.3354/cr01018>
- [5] Grell, G. A., Dudhia, J., & Stauffer, D. R. (1994). A description of the fifth-generation Penn State/NCAR mesoscale model (MM5).
- [6] Pal, J. S., Eltahir, E. A., & Small, E. E. (2000). Simulation of regional-scale water and energy budgets- Representation of subgrid cloud and precipitation processes within RegCM. *Journal of Geophysical Research*, 105(D24), 29579-29594.
- [7] Artale, V., et al. An atmosphere-ocean regional climate model for the Mediterranean area: Assessment of a present climate simulation. *Clim Dyn*, 35, pp 721-740 (2010). DOI: 10.1007/s00382-009-0691-8
- [8] Dickinson, R. E., P. J. Kennedy, A. Henderson-Sellers, and M. Wilson. Biosphere-atmosphere transfer scheme (bats) for the ncar community climate model, (1986). Tech. Rep. NCARE/TN-275+STR , National Center for Atmospheric Research.
- [9] Jin, Menglin, and Shunlin Liang. "An improved land surface emissivity parameter for land surface models using global remote sensing observations." *Journal of Climate* 19.12 (2006): 2867-2881.

A NEURAL NETWORK FOR MOLECULAR DYNAMICS SIMULATIONS OF HYDROGENATED AMORPHOUS SILICON

Michele Gusso^{1*} and Jörg Behler²

¹*ENEA, C. R. Brindisi, S.S. 7 Appia km 706, 72100 Brindisi, Italy*

²*Theoretische Chemie Institut für Physikalische Chemie, Georg-August-Universität Göttingen, Tammannstr. 6, D-37077 Göttingen, Germany*

ABSTRACT. Machine learning methods can be used to develop force fields for molecular dynamics (MD) simulations. We report some preliminary results for the construction of an artificial neural network (ANN) to calculate energies and atomic forces of hydrogenated amorphous silicon.

1 Introduction

Materials modeling by means of molecular dynamics (MD) is a well assessed approach mainly performed with density functional theory (DFT) or classical analytical interatomic potentials (force fields). The first method is more accurate and able to model very different chemical environments than the second one but computationally much more expensive. In the last years a new approach that takes the benefits of both methods has appeared: the machine learning method. This method consist in developing a flexible and adaptive analytical force field by learning from a rich set of accurate data. In particular in this work we consider a force field obtained by training an artificial neural network (ANN) using a set of ab-initio data. We describe the workflow needed to realize the ANN and report some preliminary results for the construction of an ANN that predicts the energies and the forces of hydrogenated amorphous silicon (a-Si:H).

2 Results

2.1 The method

The method consists in training a feed-forward ANN where the input data are combinations of the atomic coordinates of the atoms surrounding a given central atom (named fingerprints or symmetry functions) and the output of the ANN are the energies of the central atom. The fingerprints (which represent the chemical environment of an atom) must be chosen so as to be invariant under translations, rotations and permutations of the atomic coordinates surrounding the central atoms. Following [1, 2] we used the following fingerprints:

$$G_i^2(\eta, r_s) = \sum_{j(\neq i)} \exp^{-\eta(r_{ij}-r_s)^2} f_c(r_{ij}) \quad (1)$$

*Corresponding author. E-mail: michele.gusso@enea.it.

and

$$G_i^A(\eta, \zeta, \lambda) = 2^{1-\zeta} \sum_{j,k(\neq i)} (1 + \lambda \cos(\theta_{ikj}))^\zeta \exp^{-\eta(r_{ij}^2 + r_{ik}^2 + r_{jk}^2)} f_c(r_{ij}) f_c(r_{ik}) f_c(r_{jk}) \quad (2)$$

where r_{ij} is the distance between atoms i and j , $\theta_{ikj} = \arccos(\mathbf{r}_{ij} \cdot \mathbf{r}_{ik} / r_{ij} r_{ik})$, η , ζ , λ and r_s are real parameters and the damping function is $f_c(r) = 0.5[\cos(\frac{\pi r}{R_c}) + 1]$ for atoms within the cutoff distance R_c and is zero elsewhere. The sum in eqs. (1,2) runs over all neighboring atoms within the cutoff distance R_c . This method is based on the ansatz that the total energy E of a system can be represented by a sum of atomic energy contributions E_i : $E = \sum_i E_i$

2.2 Preparation of input data

The generation of the ANN requires an accurate set of total energies and atomic forces for many atomic configurations. Most of the CRESCO computing time used for this work was to perform these calculations. The starting data set was prepared by performing well converged DFT calculations on about 15200 structures. First we considered the database reported in [3] made of 2698 a-Si:H periodic cells (216 Si atoms and 20 H atoms with lattice parameters of about 17 Å). This database was enlarged by adding randomly distorted structures of the initial data set (about 10000 structures). A further set of 2500 structures were extracted from a MD simulation at very high temperature of a Si crystal. The total energies and atomic forces were calculated with the cp2k code [4] with DFT approximation using the Perdew-Burke-Ernzerhof (PBE) [5] exchange-correlation functional. The Kohn-Sham orbitals were expanded in a triple-zeta-valence plus two polarization (TZV2P) Gaussian-type basis set, and the charge density was expanded in a plane-wave basis set with a cutoff of 400 Ry to efficiently solve the Poisson equation within the QUICKSTEP module. Goedecker-Teter-Hutter pseudopotentials were used and a 2x2x2 Brillouin zone integration was performed. In order to check the accuracy of the forces calculated with this choice of the Gaussian basis we compared the results obtained for some structures with cp2k with those obtained in the same conditions (pseudopotentials, exchange-correlation functional, Brillouin zone integration) but using a well converged plane wave basis using the abinit software [6]. The mean difference on the forces was about $5 \times 10^{-4} \text{ Ha/bohr}$ with a maximum deviation of $2 \times 10^{-3} \text{ hartree/bohr}$. A slight improvements on the value of the forces was obtained using TZV2PX gaussian basis.

2.3 Parameters of the ANN

First of all the parameters of the fingerprints (eqs. 1, 2) must be chosen. In order to set the cutoff radius to properly describe the chemical environment some check of the convergence of the forces increasing the cutoff radius were done. Fig. 1 reports the difference, with respect to the bulk case, of the cartesian components of the forces on the central atom of the a cluster with radius r as a function of the cluster radius. It can be seen that chemical accuracy (i.e. an error of the order of $0.001 \text{ hartree/bohr}$) is achieved with cutoff radii greater than 24 bohr .

Another test in order to size the dependence on the cutoff radius for the calculation of the forces was done by comparing the forces calculated with DFT with a 1x1x1 and 2x2x2 sampling of the Brillouin zone. In fact doubling the Brillouin zone sampling is equivalent to doubling the direct lattice supercell and making again a Γ point calculation. In this way we can measure the effect on the atomic

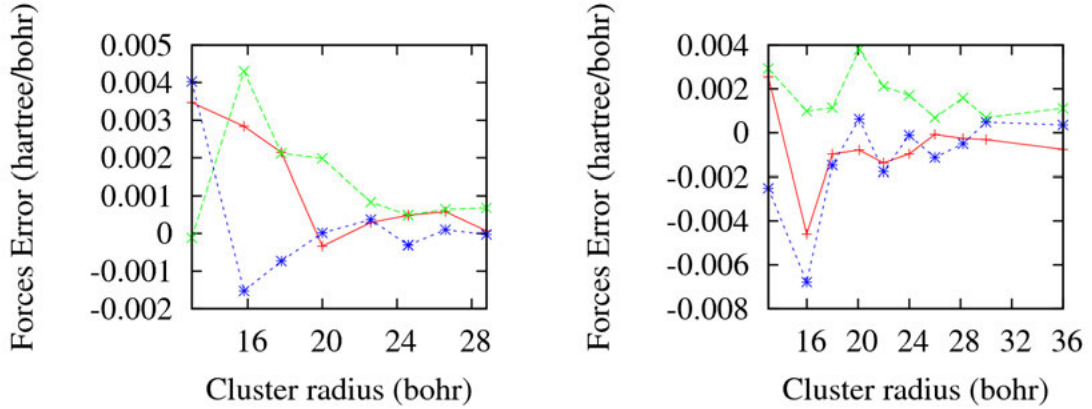


Figure 1: The difference of the three cartesian components of the forces of the central atom of a spherical cluster with radius r with respect to their values in the bulk material. The results for two clusters are shown.

forces when we move further away a perturbation at the boundaries (in this case the perturbation is the constraint imposed by the periodic boundary condition). Comparing the forces between these two calculations for about 80 a-Si:H periodic structures with cell lattice parameters of about $32bohr$ gives a mean difference of $0.001hartree/bohr$ (with a maximum error of $0.007hartree/bohr$) indicating that a cutoff of $32bohr$ is sufficient to have chemical accuracy.

Summarizing these results, and considering that the forces depend on neighboring atoms with a distance up to twice the cutoff radius R_c of the symmetry functions, a cutoff $R_c = 12bohr$ was used. We fixed $r_s = 0$ and the η , ζ and λ values were chosen so as to have quite a complete description of the atomic environment of an atom and discarding symmetry functions that were too correlated between each other. We used 44 symmetry functions for Si atoms and 57 for H atoms.

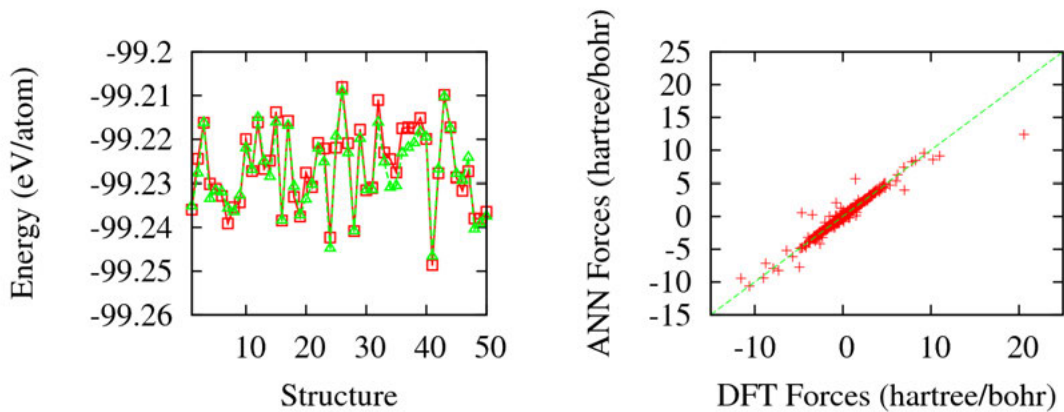


Figure 2: Comparison of DFT total energy per atom and ANN calculated total energy for 50 a-Si:H structures of the testing set and comparison of DFT and ANN forces for the whole database of structures.

network	E(meV/atom)		F(eV/bohr)	
	train	test	train	test
10 10	4.7	5.5	0.28	0.25
15 15	3.9	4.8	0.28	0.31
20 20	3.7	4.4	0.31	0.50
25 25	3.6	4.5	0.29	0.34
30 30	3.2	4.7	0.30	0.28
35 35	3.1	4.1	0.28	0.36
40 40	3.0	4.1	0.29	0.34
45 45	3.1	4.1	0.34	0.29
50 50	2.9	4.3	0.37	0.35
55 55	2.8	3.9	0.34	0.32
60 60	3.2	4.6	0.33	0.29

Table 1: Root mean squared errors for the total energy per atom and the forces for different kind of two hidden layers ANN. The first column reports the number of neurons in the hidden layers.

2.4 Training of the ANN

For the training of the ANN we used the code RUNNER [7]. We tried ANN with one, two and three hidden layers and various neuron activation functions. The initial set of DFT data were divided in a training set (about 90 % of the total data) and a test set the remaining 10 %). The training was performed minimizing the total energies of the structures of the training set using the adaptive global extended Kalman filter and avoiding the overfitting of the training data. Table 2.3 reports the results for a two hidden layer network with hyperbolic tangent as neuron activation function with increasing number of neurons in the two hidden layers. The table reports the root mean squared errors RMSE (calculated with respect to the DFT data) for the total energies and the forces for the training set and the test set.

Fig 2 reports the calculation of the total energy normalized to the number of atoms for 50 a-Si:H structures of the testing set obtained using the network with two hidden layers and 40 neurons in each hidden layer. The same figure shows the comparison of the DFT forces for all the structures in the database with those calculated with the two hidden layer ANN with 40 neuron per hidden layer. It can be seen that there are some structures that are away from the perfect correspondence between DFT and ANN calculated forces (i.e. bisector line). It must be noted that a calculation of the RMSE for the forces for each chemical species shows that the error for Si is $0.26eV/bohr$ while that for H atoms is about three times higher ($0.76eV/bohr$).

To test the behavior of the trained ANN the calculation of energy and forces with a ANN was implemented in the cp2k software. Fig 3 shows the behavior of ten trained ANN (with two hidden layers with 40 neurons) in a NVT molecular dynamics run at T=500K. It can be seen that some of them fail quite early. The configurations for which these ANN failed were included in the original structure database and a new training was performed on the ANNs. Besides during the MD run a check on the calculated atomic environments were performed in order to verify if they were far away from those included in the original database. Also these configurations were added to the database and the ANNs trained again.

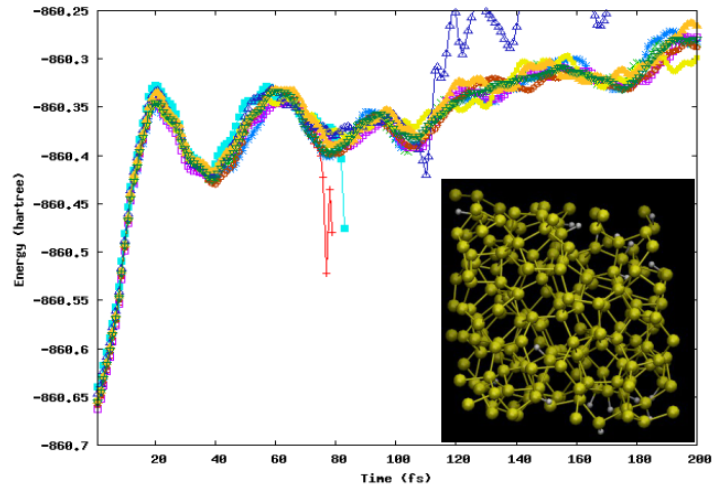


Figure 3: Comparison of calculated total energy of a-Si:H structure for ten ANN in a NVT molecular dynamics simulation at T=500K.

This process was continued recursively.

3 Conclusions

A method to build a feed-forward neural network to be used for MD application with nearly DFT accuracy was briefly presented and some preliminary results were shown. Work is in progress to refine the network by including more DFT data and eventually improve the choice of the fingerprints and the network topology.

References

- [1] J. Behler and M. Parrinello. Generalized neural-network representation of high-dimensional potential-energy surfaces. *Phys Rev Lett*, 98:146401, 2007.
- [2] J. Behler. Atom-centered symmetry functions for constructing high-dimensional neural network potentials. *J Chem Phys*, 134:074106, 2011.
- [3] E. Johlin, L.C. Wagner, T. Buonassisi, and J.C. Grossman. Origins of structural hole traps in hydrogenated amorphous silicon. *Phys Rev B*, 110:146805, 2013.
- [4] <https://www.cp2k.org/>.
- [5] K. Burke, J.P. Perdew, and M. Ernzerhof. Generalized gradient approximation made simple. *Phys. Rev. Lett.*, 77:3865–3868, 1996.
- [6] <https://www.abinit.org/>.
- [7] Jörg Behler, 2017. RUNNER - A program for constructing high dimensional neural network potentials, Universität Göttingen.

INTER-LAYER SYNCHRONIZATION IN NON-IDENTICAL MULTILAYER NETWORKS

I. Sendiña-Nadal^{1,2,*}, I. Leyva^{1,2}, R. Sevilla-Escoboza³, R. Gutiérrez⁴, J.M. Buldú^{1,2}, and S. Boccaletti^{5,6}

¹*Complex Systems Group & GISC, Universidad Rey Juan Carlos, 28933 Móstoles, Madrid, Spain*

²*Center for Biomedical Technology, Universidad Politécnica de Madrid, 28223 Pozuelo de Alarcón, Madrid, Spain*

³*Centro Universitario de los Lagos, Universidad de Guadalajara, Jalisco 47460, Mexico*

⁴*School of Physics and Astronomy, University of Nottingham, Nottingham, NG7 2RD, UK*

⁵*CNR- Institute of Complex Systems, Via Madonna del Piano, 10, 50019 Sesto Fiorentino, Florence, Italy*

⁶*The Italian Embassy in Israel, 25 Hamered st., 68125 Tel Aviv, Israel*

ABSTRACT. This study is the continuation of that produced in the year 2015 using the ENEAGRID/CRESCO infrastructure [1] where inter-layer synchronization in a multiplex network was investigated. Inter-layer synchronization is a dynamical state occurring in multilayer networks composed of identical nodes. The state corresponds to have all layers synchronized, with nodes in each layer which do not necessarily evolve in unison. So far, the study of such a solution has been restricted to the case in which all layers had an identical connectivity structure. When layers are not identical, the inter-layer synchronous state is no longer a stable solution of the system. Nevertheless, when layers differ in just a few links, an approximate treatment is still feasible, and allows one to gather information on whether and how the system may wander around an inter-layer synchronous configuration. We report the details of an approximate analytical treatment for a two-layer multiplex, which results in the introduction of an extra inertial term accounting for structural differences. Numerical validation of the predictions highlights the usefulness of our approach, especially for small or moderate topological differences in the intra-layer coupling.

1 Introduction

Complex networks is one of the most active research topics in today's nonlinear science [5]. As the field is rapidly evolving (mostly due to the huge amount of data collected nowadays), novel features are incorporated to better describe the real world. Among these, the extension of the traditional framework to include the *multilayer* nature of networks has significantly altered the landscape of network science. In a multilayer description, units can be arranged in several layers (each of them accounting for a different kind of relationship or interaction between the nodes), either simultaneously or in an alternating fashion [6, 11, 3].

*Corresponding author. E-mail: irene.sendina@urjc.es.

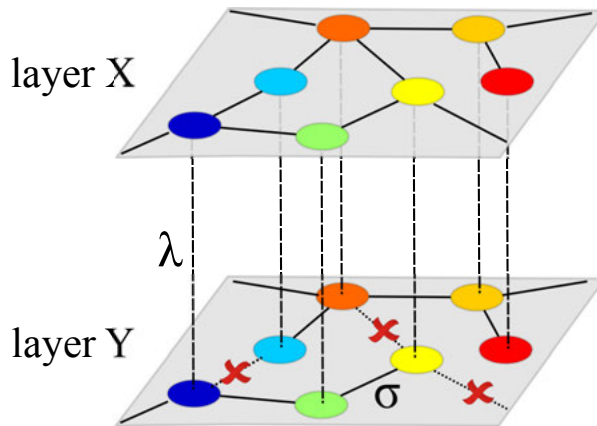


Figure 1: Schematic representation of a multiplex of two layers of identical oscillators. Labels σ and λ denote the intra- and inter-layer coupling strengths, respectively. Each node i (j) in the top (bottom) layer is an m dimensional dynamical system whose state is represented by the vector \mathbf{x}_i (\mathbf{y}_j). The topologies of layers X and Y are encoded in the \mathcal{L}^1 and \mathcal{L}^2 Laplacian matrices, respectively. If we depart from two identical layers, we can write $\mathcal{L}^1 = \mathcal{L}^2 + \Delta\mathcal{L}$ where $\Delta\mathcal{L}$ contains the links that have been deleted in the bottom layer. The different colors of the nodes in each layer indicates different dynamical states. In this case, $\mathbf{x}_i = \mathbf{y}_i, \forall i$, that is, the two layers are synchronized.

On the other hand, synchronization is one of the most relevant dynamical processes encountered in nature, and probably the one that has been most thoroughly studied in the context of complex networks [4, 5]. Only very recently the study of synchronization has been extended to multilayers [3], where the multilayer structure of connections supports a global synchronous state in which all the nodes in all the layers behave coherently. More general forms of synchronization, however, are inherently possible on top of a multilayer structure, as for instance intra-layer synchronization [8] (where nodes evolve synchronously within each layer but layers do not necessarily evolve coherently), inter-layer synchronization [9, 18] (where, instead, layers are synchronized but nodes within each layer are not), and cluster synchronization [10].

Recently, we have provided analytical, numerical and experimental evidence of *inter-layer* synchronization [18], based on a version of the master stability function approach (MSF) for reducing the system dimensionality, and under the assumption that different layers are structurally identical. In this work, we extend the study performed in Ref. [18], where analytical and numerical evidence of inter-layer synchronization under the assumption of identical layers, to the (more realistic) case of layers structurally different. By means of extensive calculations performed in CRESCO during the past year, and as the main result, we provide a comprehensive description of the perturbation effects that the deletion of m links in one of the layers has on the stability of the inter-layer synchronous state, and show a non-trivial relationship connecting the betweenness centrality of the missing links and the intra-layer coupling strength. The results were published in Refs. [13, 17, 18, 12] and presented in several international conferences.

2 Model and methods

2.1 Model

The object of our study is a multiplex of two layers, formed by N identical m dimensional dynamical systems, whose states are represented by the $mN \times 1$ column vectors $\mathbf{X} = [\mathbf{x}_1, \mathbf{x}_2, \dots, \mathbf{x}_N]^T$ and $\mathbf{Y} = [\mathbf{y}_1, \mathbf{y}_2, \dots, \mathbf{y}_N]^T$ with $\mathbf{x}_i, \mathbf{y}_i \in \mathbb{R}^m$ for $i = 1, 2, \dots, N$. Here, we focus on the case in which the topology of the two layers is different, and encoded by the elements of the Laplacian matrices \mathcal{L}^1 and \mathcal{L}^2 respectively, as depicted in Fig. 1. Therefore, the evolution of the system is given by

$$\begin{aligned}\dot{\mathbf{X}} &= \mathbf{F}(\mathbf{X}) - \sigma(\mathcal{L}^1 \otimes \mathbf{G})\mathbf{X} + \lambda(\mathbb{I}_N \otimes \mathbf{H})(\mathbf{Y} - \mathbf{X}), \\ \dot{\mathbf{Y}} &= \mathbf{F}(\mathbf{Y}) - \sigma(\mathcal{L}^2 \otimes \mathbf{G})\mathbf{Y} + \lambda(\mathbb{I}_N \otimes \mathbf{H})(\mathbf{X} - \mathbf{Y})\end{aligned}\quad (1)$$

where the function $\mathbf{F}(\mathbf{X}) = [\mathbf{f}(\mathbf{x}_1), \mathbf{f}(\mathbf{x}_2), \dots, \mathbf{f}(\mathbf{x}_N)]^T$, with $\mathbf{f} : \mathbb{R}^m \rightarrow \mathbb{R}^m$ representing the evolution vectorial function. \mathbf{G}, \mathbf{H} are the $m \times m$ matrices representing the linear intra (\mathbf{G}) and inter-layer (\mathbf{H}) coupling schemes, respectively. The $N \times N$ identity matrix \mathbb{I}_N represents the inter-layer topology for the multiplex network. The parameters σ and λ are the intra- and the inter-layer coupling strengths.

When the layers are identical ($\mathcal{L}^1 = \mathcal{L}^2$), the inter-layer synchronous evolution ($\mathbf{X} = \mathbf{Y}$) is a solution of Eqs. (1), independently of the existence of intra-layer synchronization [18]. When the inner structure of the layers differs ($\mathcal{L}^1 \neq \mathcal{L}^2$), however, $\mathbf{X} = \mathbf{Y}$ is no longer a solution of Eqs. (1) –i.e. the system may satisfy that condition at a given time if e.g. the two layers start from the same initial condition, but the dynamics will move away from the synchronization manifold $\mathbf{X} = \mathbf{Y}$, which is no longer an invariant set of the dynamics. Yet, it can be expected that when the topologies of the two layers are actually *similar* (i.e. when their difference is limited to only a few links), one can proceed with an approximation, which consists in supposing that the dynamics of the system would anyway visit regions of the state space sufficiently close to $\mathbf{X} = \mathbf{Y}$, so that the predictive use of the Master Stability Function (MSF) methodology [15, 5] still makes sense. We here summarize the main steps of the perturbation analysis of Eqs. (1). First, one can always define $\delta\mathbf{X}(t) = \mathbf{Y}(t) - \mathbf{X}(t) = (\delta\mathbf{x}_1, \delta\mathbf{x}_2, \dots, \delta\mathbf{x}_N)^T$ and calculate its law of motion

$$\delta\dot{\mathbf{X}} = \mathbf{F}(\mathbf{Y}) - \mathbf{F}(\mathbf{X}) - \sigma(\mathcal{L}^2 \otimes \mathbf{G})\mathbf{Y} + \sigma(\mathcal{L}^1 \otimes \mathbf{G})\mathbf{X} - 2\lambda(\mathbb{I}_N \otimes \mathbf{H})\delta\mathbf{X}. \quad (2)$$

Notice that the existence of a perfect synchronous inter-layer solution means that $\mathbf{X} = \mathbf{Y} \Rightarrow \dot{\mathbf{X}} = \dot{\mathbf{Y}} \Rightarrow \delta\dot{\mathbf{X}} = \dot{\mathbf{Y}} - \dot{\mathbf{X}} = \mathbf{0}$. Introducing these equivalences into Eq. (2), it leads:

$$\delta\dot{\mathbf{X}} = \mathbf{F}(\mathbf{X}) - \mathbf{F}(\mathbf{X}) - 2\lambda(\mathbb{I}_N \otimes \mathbf{H})\delta\mathbf{X} - \sigma[(\mathcal{L}^2 - \mathcal{L}^1) \otimes \mathbf{G}]\mathbf{X} = -\sigma[(\mathcal{L}^2 - \mathcal{L}^1) \otimes \mathbf{G}]\mathbf{X} = \mathbf{0} \quad (3)$$

which in principle is true if and only if $\sigma = 0$ (isolated nodes) or $\mathcal{L}^1 = \mathcal{L}^2$, that is, the layers are identical. In other words, we can conclude that the solution $\mathbf{X} = \mathbf{Y}$ for all times is not compatible with Eq. (1).

Second, one can define $\Delta\mathcal{L} = \mathcal{L}^1 - \mathcal{L}^2$, as the matrix representing the difference between the two Laplacians. Plugging $\mathcal{L}^1 = \mathcal{L}^2 + \Delta\mathcal{L}$ into Eq. (2), one obtains the following dynamics at the level of individual nodes:

$$\begin{aligned}
\delta\dot{\mathbf{x}}_i &= \mathbf{f}(\mathbf{y}_i) - \mathbf{f}(\mathbf{x}_i) - 2\lambda \mathbf{h}(\delta\mathbf{x}_i) - \sigma \sum_k \mathcal{L}_{ik}^2 \mathbf{g}(\mathbf{y}_k) + \sigma \sum_k (\mathcal{L}_{ik}^2 + \Delta\mathcal{L}_{ik}) \mathbf{g}(\mathbf{x}_k) \\
&= \mathbf{f}(\mathbf{y}_i) - \mathbf{f}(\mathbf{x}_i) - 2\lambda \mathbf{h}(\delta\mathbf{x}_i) - \sigma \sum_k \mathcal{L}_{ik}^2 [\mathbf{g}(\mathbf{y}_k) - \mathbf{g}(\mathbf{x}_k)] + \sigma \sum_k \Delta\mathcal{L}_{ik} \mathbf{g}(\mathbf{x}_k).
\end{aligned} \tag{4}$$

However, let now assume that, in a large enough network the effect of the perturbation $\Delta\mathcal{L}$ is small enough for an inter-layer almost synchronous dynamics $\mathbf{y}_i(t) \approx \mathbf{x}_i(t)$ to emerge. Then, one can take $\delta\mathbf{x}_i$ to be small quantities, and expand to first order around $\mathbf{x}_i(t)$. The equations resulting from the linearization are:

$$\delta\dot{\mathbf{x}}_i = [J\mathbf{f}(\tilde{\mathbf{x}}_i) - 2\lambda J\mathbf{h}(\tilde{\mathbf{x}}_i)] \delta\mathbf{x}_i - \sigma \sum_k \mathcal{L}_{ik}^2 J\mathbf{g}(\tilde{\mathbf{x}}_k) \delta\mathbf{x}_k + \sigma \sum_l \Delta\mathcal{L}_{il} \mathbf{g}(\tilde{\mathbf{x}}_l) \tag{5}$$

where $\tilde{\mathbf{x}}_i$ is the state of node i in an isolated layer evolving according to $\dot{\tilde{\mathbf{x}}}_i = \mathbf{f}(\tilde{\mathbf{x}}_i) - \sigma \sum_k \mathcal{L}_{ik}^1 \mathbf{g}(\tilde{\mathbf{x}}_k)$.

By comparing this result with the identical case [18], it can be seen that the non-identity of the systems is reflected in the last *inertial* term, whose role in pushing the dynamics away from the identical case is expected to become more prominent when the topological differences are large. Additionally, it predicts that the divergence from the inter-layer synchronization will depend on the the intra-layer coupling strength, which is in its own right an interesting result on the rich interplay between intra-layer and inter-layer effects, an aspect of inter-layer synchronization that was thoroughly explored in the identical case in Ref [18]. Following the MSF approach, a negative sign in the maximum conditional Lyapunov exponent (MLE) obtained from Eqs. (5) can be taken as an indication for the presence of inter-layer synchronization [18].

The validity of the approximation is checked by monitoring the value of the inter-layer synchronization error, which is defined as

$$E_{inter} = \lim_{T \rightarrow \infty} \frac{1}{T} \int_0^T \|\delta\mathbf{X}(t)\| dt,$$

where $\delta\mathbf{X}(t) = \mathbf{Y}(t) - \mathbf{X}(t)$ is the vector describing the difference between the layers' dynamics and $\|\cdot\|$ stands for the Euclidean norm. For this purpose, the two layers are initially created as identical, and then structural differences are generated by removing m links in \mathcal{L}^2 . To evaluate the range of impact of the structural differences, we have chosen the m links to be removed following an *edge betweenness* criterion [14]. Accordingly, each simulation is repeated twice, a first time removing the links with the highest edge betweenness (m_+), and a second time removing those that have the lowest edge betweenness (m_-). The procedure never produces a lack of connectedness in the graphs (for the networks and number of removals considered), and in case of degeneracy, a link is chosen at random among those that have the same betweenness. Without lack of generality, we consider two possible kinds of topologies where both layers are either Erdős-Rényi [7] (ER) or scale-free [2] (SF), in both cases with $N = 500$, and average degree $\langle k \rangle = 8$. ER and SF networks are generated by means of the procedures proposed in Refs. [7] and [2], respectively, and therefore the considered SF networks display a degree distribution $p(k) \propto k^{-3}$. Nodes are here Rössler oscillators [16], whose autonomous evolution is given by $\mathbf{f}(\mathbf{x}) = [-y - z, x + 0.2y, 0.2 + z(x - 9.0)]$. The intra- and inter- layer local coupling functions are set to be $\mathbf{g}(\mathbf{x}) = \mathbf{G}\mathbf{x} = (0, 0, z)^T$ and $\mathbf{h}(\mathbf{x}) = \mathbf{H}\mathbf{x} = (0, y, 0)^T$ respectively, so that (according to the standard MSF classification established in Ref. [5]) the intra-layer configuration is within class I (and, therefore, intra-layer synchronization is never possible), whereas the inter-layer configuration corresponds to class II (i.e., synchronization may be stable when the coupling strength

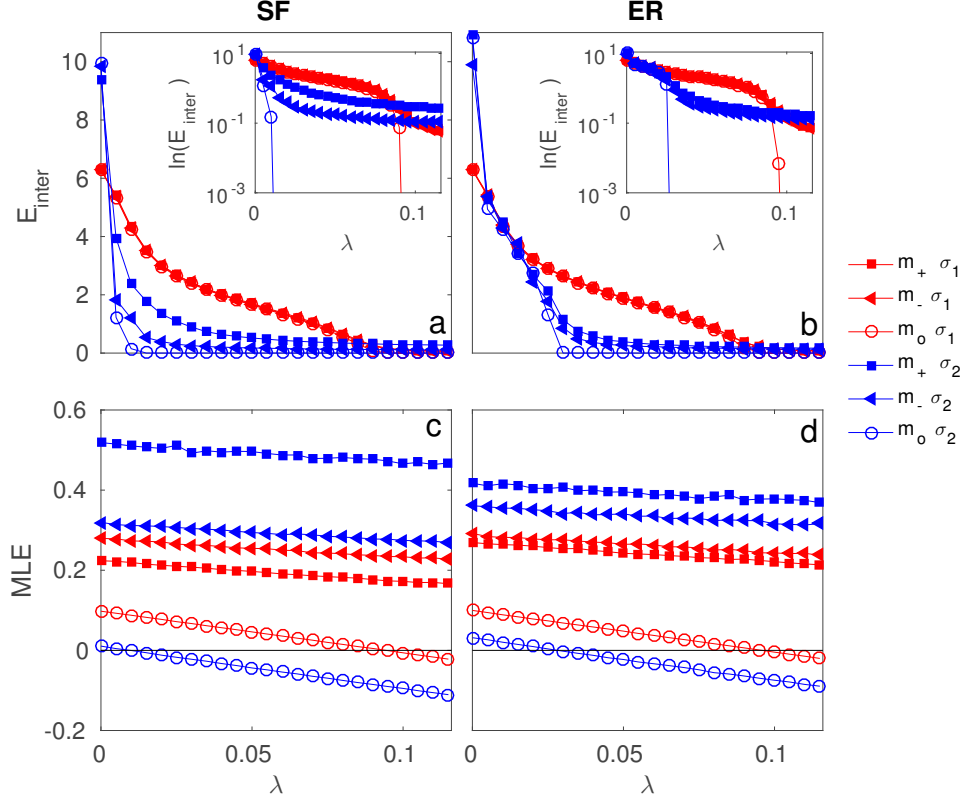


Figure 2: (Color online). Results for inter-layer dynamics as a function of the intra-layer coupling strength λ for class-I layers. E_{inter} (see main text) in multiplexes of SF (a) and ER (b) layers of $N = 500$ Rössler oscillators, for two different values of intra-layer coupling $\sigma_1 = 0.1$ (red symbols) and $\sigma_2 = 1.0$ (blue symbols) when the 50 links with larger (m_+ , \blacksquare) and lower (m_- , \blacktriangle) betweenness are removed from \mathcal{L}^2 , and for identical layers ($m = 0$, \circ). Insets: Detail of the respective panels (a) and (b), in semi-logarithmic scale. (c)-(d) The corresponding MLE for the approximate expression in Eq. (5).

exceeds a certain threshold).

2.2 Numerical methods and use of computational resources

For the numerical integration of the above model and the analysis of the results we used in-house C codes implementing fix-step fourth-order Runge-Kutta integration algorithms, with an optimized time step $dt = 0.01$. The standard GCC compiler was used.

Extensive serial simulations have been performed for large parameters ranges, diverse network topologies and statistical validation of the results. The calculations were performed in Cresco 3 and Cresco 4, using the *h144* queues for full multilayer simulations and *h6* queues for Lyapunov exponent calculations. Homemade MatLab scripts were used for visualizing the results.

3 Numerical results

The first goal was to numerically assess the range of validity of the approximate MSF approach. In Fig. 2 we show the E_{inter} (panels a and b) and MLE (panels c and d) as a function of the inter-layer coupling λ for two different values of intra-layer coupling $\sigma_1 = 0.1$ (red curves) and $\sigma_2 = 1.0$ (blue curves) when the 50 links (i.e. approximately 2.5% of the total number) with the largest (m_+ , squares) and lowest (m_- , triangles) betweenness centrality values are removed from the SF (Fig. 2a,c) and ER (Fig. 2b,d) \mathcal{L}^2 layers. For the sake of comparison, we also report the curves for the case of identical layers (m_0 , circles).

It can be observed that, in spite of the nonidentical layer topologies that make complete synchronization formally impossible, the E_{inter} series presents, in fact, apparently small differences with the identical case for both m_+ and m_- and for the chosen σ values, which can be better appreciated in a logarithmic representation (as shown in the insets of the corresponding figures). Independently of the layer topology, at relatively large σ (σ_2), E_{inter} is seen to follow more closely the trend observed in the identical case when compared with smaller values of σ (σ_1). This form of resilience is in agreement with the fact that the non identity of the layers results in the presence of an inertial term, which depends indeed on the value of σ (see details in the Methods section). The corresponding Maximum Lyapunov Exponent (MLE) is shown in the bottom panels of Fig. 2, confirming the behavior of the inter-layer dynamics depicted in the upper panels. Notice that the effects of removing links with high or low betweenness are more pronounced in multiplexes made of SF layers than in those made of ER ones. Another observation, which will be further highlighted in the following, is that the impact on the inter-layer synchronization of removing high or low betweenness links is reversed depending on the strength of the intra-layer coupling: in both the ER and SF cases, removing m_+ links deteriorates (improves) the synchronization levels with respect to removing m_- links for large (small) σ values.

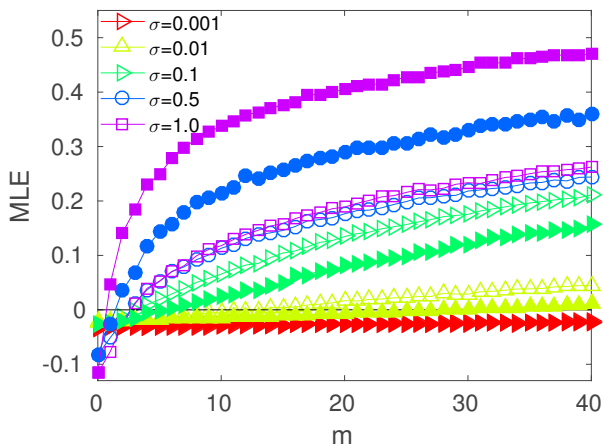


Figure 3: Maximum Lyapunov exponents (MLE) for different intra-coupling strengths σ as a function of the number of links removed m , for the cases in which the removed links have the highest (full markers) or the lowest (void markers) edge betweenness. Layers are SF and of class I with $N = 500$ Rössler oscillators and $\lambda = 0.12$.

An analysis that further elucidates the role of the structural differences is provided in Fig. 3, where the dependence of $MLE(m_+)$ and $MLE(m_-)$ is reported as a function of m , for a fixed value of λ (at which there is inter-layer synchronization for $m = 0$). As predicted by the approximated MSF approach, the dynamics drifts from the identical case at smaller values of m , as σ increases. We here find an unexpected

and interesting feature, already glimpsed before in Fig. 2, that entangles the intra-layer structure with the inter-layer dynamics: for small values of σ , removing the m_- lowest betweenness centrality links results in a stronger perturbation for the inter-layer synchronization than removing the same number m_+ of highest betweenness links. However, for larger values of σ , the effect is reversed.

4 Conclusion

These results allow us to draw a series of important conclusions about the effects of structural layer differences on the capability of multiplex networks to display synchronized layers, with nodes in each layer which do not necessarily evolve in unison. It is important to remark that the study of inter-layer synchronization was restricted so far to the case in which all layers had an identical connectivity structure. When layers are not identical, several conceptual issues arise, the most relevant being that the inter-layer synchronous manifold is no longer invariant under the dynamics, and one has therefore to proceed with approximate treatments.

We have demonstrated that an approximate analytical treatment of a two-layer multiplex results in the introduction of an extra inertial term accounting for structural differences. The predictions have been validated numerically and, most importantly, by means of an experiment with electronic circuits. The conclusion is that, even in this case in which layers are not identical and the exact synchronized solution does not exist, the approximate Master Stability Function is a very good tool to study the inter-layer dynamics of multiplex networks. Using such a framework, indeed, we could predict the effect that missing links in one of the layers has on the inter-layer synchronization, evidencing a non-trivial relationship between the edge centrality of the different links and the balance between intra- and inter-layer couplings. Our results can provide a starting point for the study of inter-layer synchronization in even more general configurations, as unidirected networks [19] or general multilayer networks.

References

- [1] J.A. Almendral, S. Boccaletti, R. Gutiérrez, I. Leyva, J.M. Buldú, A. Navas, and I. Sendiña-Nadal. Synchronization phenomena in complex networks. In *High Performance Computing on CRESCO infrastructure: research activities and results 2015*, page 21. ENEA, 2016.
- [2] Albert-László Barabási and Réka Albert. Emergence of scaling in random networks. *Science*, 286(5439):509–512, 1999.
- [3] S. Boccaletti, G. Bianconi, R. Criado, C.I. del Genio, J. Gómez-Gardeñes, M. Romance, I. Sendiña Nadal, Z. Wang, and M. Zanin. The structure and dynamics of multilayer networks. *Phys. Rep.*, 544(1):1–122, July 2014.
- [4] S Boccaletti, J Kurths, G Osipov, DL Valladares, and CS Zhou. The synchronization of chaotic systems. *Phys. Rep.*, 366(1):1–101, 2002.
- [5] S Boccaletti, V Latora, Y Moreno, M Chavez, and D.-U. Hwang. Complex networks: Structure and dynamics. *Phys. Rep.*, 424(45):175–308, 2006.
- [6] Manlio De Domenico, Albert Solé-Ribalta, Emanuele Cozzo, Mikko Kivelä, Yamir Moreno, Mason A. Porter, Sergio Gómez, and Alex Arenas. Mathematical formulation of multilayer networks. *Phys. Rev. X*, 3:041022, Dec 2013.

- [7] P Erdős and A Rényi. On random graphs I. *Publ. Math. Debrecen*, 6:290–297, 1959.
- [8] L. V. Gambuzza, M. Frasca, and J. Gómez-Gardeñes. Intra-layer synchronization in multiplex networks. *EPL (Europhysics Letters)*, 110(2):20010, 2015.
- [9] R Gutiérrez, I Sendiña-Nadal, M Zanin, D Papo, and S Boccaletti. Targeting the dynamics of complex networks. *Sci. Rep.*, 2:396, 2012.
- [10] Sarika Jalan and Aradhana Singh. Cluster synchronization in multiplex networks. *EPL (Europhysics Letters)*, 113(3):30002, 2016.
- [11] Mikko Kivela, A. Arenas, Marc Barthelemy, James P. Gleeson, Yamir Moreno, and Mason A. Porter. Multilayer networks. *Journal of Complex Networks*, 2(3):203–271, 2014.
- [12] I Leyva, R Sevilla-Escoboza, I Sendiña-Nadal, R Gutiérrez, JM Buldú, and S Boccaletti. Inter-layer synchronization in non-identical multi-layer networks. *Scientific Reports*, 7(45475), 2017.
- [13] A. Navas, J. A. Villacorta-Atienza, I. Leyva, J. A. Almendral, I. Sendiña Nadal, and S. Boccaletti. Effective centrality and explosive synchronization in complex networks. *Phys. Rev. E*, 92:062820, 2015.
- [14] Mark EJ Newman and Michelle Girvan. Finding and evaluating community structure in networks. *Phys. Rev. E*, 69(2):026113, 2004.
- [15] Louis M Pecora and Thomas L Carroll. Master Stability Functions for Synchronized Coupled Systems. *Phys. Rev. Lett.*, 10:2109–2112, 1998.
- [16] O.E. Rössler. An equation for continuous chaos. *Phys. Lett.*, 57(5):397–398, 1976.
- [17] I. Sendiña-Nadal, I. Leyva, A. Navas, J.A. Villacorta-Atienza, J.A. Almendral, Z. Wang, and S. Boccaletti. Effects of degree correlations on the explosive synchronization of scale-free networks. *Physical Review E*, 91(3):032811, 2015.
- [18] R. Sevilla-Escoboza, I. Sendiña Nadal, I. Leyva, R. Gutiérrez, J. M. Buldú, and S. Boccaletti. Inter-layer synchronization in multiplex networks of identical layers. *Chaos: An Interdisciplinary Journal of Nonlinear Science*, 26(6):065304, June 2016.
- [19] Wenwu Yu, Guanrong Chen, Jihu Lu, and Jurgen Kurths. Synchronization via pinning control on general complex networks. *SIAM Journal on Control and Optimization*, 51(2):1395, 2013.

FARO 2.0

A RENEWED GATEWAY TO ENEAGRID RESOURCES

Angelo Mariano^{1*}, Giulio D'Amato², Fiorenzo Ambrosino³, Giuseppe Aprea⁴,
Francesco Buonocore⁴, Massimo Celino⁴, Antonio Colavincenzo³, Marco Fina²,
Agostino Funel³, Simone Giusepponi⁴, Guido Guarnieri³, Filippo Palombi⁵,
Samuele Pierattini⁶, Giovanni Ponti³, Giuseppe Santomauro⁷, Giovanni Bracco⁵
and Silvio Migliori⁸

¹*ENEA, Apulia local office, I-70126 Bari, Italy*

²*Sys-man Progetti & Servizi srl, I-00143 Rome, Italy*

³*ENEA, Portici Research Centre, I-80055 Portici (NA), Italy*

⁴*ENEA, Casaccia Research Centre, I-00123 Rome, Italy*

⁵*ENEA, Frascati Research Centre, I-00144 Rome, Italy*

⁶*ENEA, Tuscany local office, I-50019 Florence, Italy*

⁷*Consortium GARR, I-00196 Rome, Italy*

⁸*ENEA, Headquarters, I-00196 Rome, Italy*

ABSTRACT. Fast Access to Remote Objects 2.0 (FARO 2.0) is a tool for application and desktop virtualization with a strong focus towards user experience (UX), providing trained as well as untrained users a collection of centralized services that can be seamlessly used on their client through a remote desktop protocol. It is a JavaFX application whose graphical user interface (GUI) and whose main logics has been implemented through the well-known Web technologies (HTML5, CSS3, Javascript) for a easier maintainability and customizability, taking full advantage of the WebView component. Its framework has been deployed both as general purpose GUI for remote user access to ENEAGRID resources and as specialized application or workflow oriented GUI. They are applied in a set of applicative domains, ranging from material science to technologies for energy and industry, environmental modeling and nuclear fusion. Some examples and results are also presented

1 The gateway

Developed in the contest of the Italian PON “Smart Cities and Communities” R&C 2007-2013 with the project “EDOC@Work 3.0 - Education and work in the cloud” [3, 7] in collaboration with Sys-man Progetti & Servizi S.r.l. [13], FARO 2.0 [8] is a tool for scientists and students to perform research as

*Corresponding author. E-mail: angelo.mariano@enea.it.

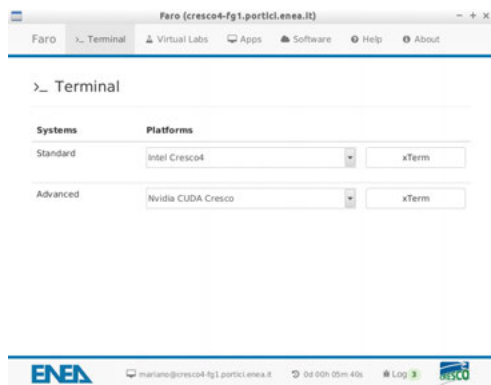


Figure 1: FARO 2.0 xTerm launchers



Figure 2: FARO 2.0 software available

well as train in a real-world HPC environment. FARO 2.0 has been implemented as a drop-in replacement for its predecessor, FARO [12], providing users a software solution with a strong focus towards UX, being a pleasant interface for real-time application and desktop virtualization. The remote desktop protocol used to deliver applications and desktops to end-users is based on NX over an SSH. The compression and transport protocol of NX is used to enhance the native X display protocol performances in such a way that services are usable even with slower links.

The core of FARO 2.0 is its desktop application (a container, in this context) developed in JavaFX, showing a WebView. Instead, its GUI and its main logics have been developed in HTML5, CSS3 and Javascript as a single page application (SPA), replicating the trending paradigm of cross-platform hybrid apps. The container is a lightweight piece of software that implements an ordinary browser, rendering a local web page. However, the container also injects a custom Java class (a bridge) in the Javascript global namespace. Thus, through Javascript calls, the above web page is able to execute any member function that has been made available from the container. In this implementation, the bridge exports methods to launch new processes based on CLI commands and implements the application logic needed to callback registered Javascript member functions in case of a new message in the standard-out or in the standard-error streams; this allows to virtually execute any command on the host backend server that is executing FARO 2.0. Moreover, every command executed is tracked in a user home log that allows administrators to troubleshoot every problem may occur in the execution of remote code. A convenient call from the Javascript runtime environment is, for example, able to let the user remotely open and interact with the command prompt of a standard or an advanced node in a cluster, or launch any kind of scientific software in a dedicated environment (e.g. MATLAB, COMSOL, IDL). More precisely, each launch initiated from FARO 2.0 is redirected through the SSH protocol to the ENEA instance of IBM Load Sharing Facility (LSF), the scheduler that enqueues requests both for interactive and batch jobs[6]. As a matter of fact, any interaction with the ENEAGRID environment can be routed through FARO 2.0. The main interface is shown in Fig.1-2.

FARO 2.0 is easy to maintain and customize, since most of its code reside outside the container package and merely implements a SPA (with bindings to some Java member functions): this allows to reconfigure quite the entire application without the need for a compile process. Moreover, the SPA can run (with a limited functionality) within a web browser; it can thus be previewed in a very agile way. We are even able to provide deeply customized interfaces by creating branches of the SPA, without the need to modify the container. Through the usage of web standards, FARO 2.0 implements a full-featured gateway for application and desktop virtualization in the ENEAGRID distributed computing environment that can also be used as a boilerplate for new applications, such as the “ENEAGRID Virtual Labs”.

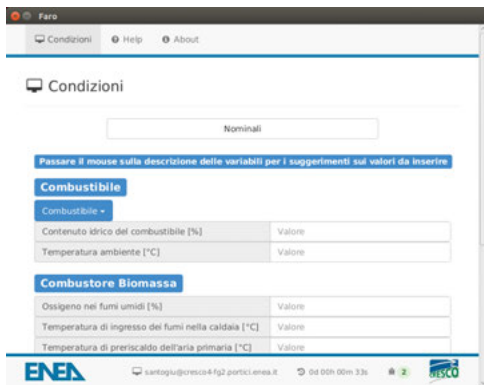


Figure 3: Custom FARO 2.0 for ADP (a)

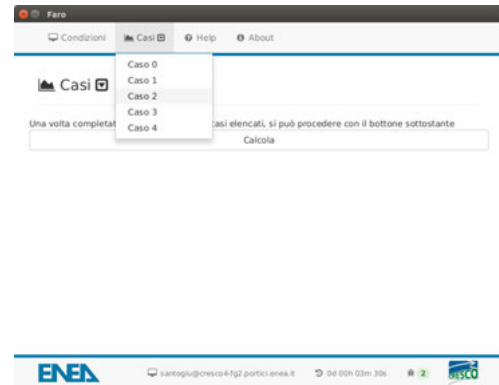


Figure 4: Custom FARO 2.0 for ADP (b)

2 Applications

In the following we will show some interesting applications and customization of FARO 2.0.

The first application is related to the ADP Virtual Lab [1]. The aim is to provide a launcher for a code for the analysis of small-powered wood biomass energy systems (so called COGEGNO). The code has been implemented in Matlab and Scilab environments, and transferred on a web platform, in a “virtual laboratory” powered by the computational systems of ENEAGRID. Among the main components of the model there are the gas recirculation and air staging mobile-grid burner and the thermic gain obtained from the pre-heating of the air in input to the boiler. For the model of the boiler the code uses an helicoidal flow one, with particular attention to the molten salts, for the advantages arising from the possibility offered by these fluids to work in a broader temperature range and at higher temperatures, increasing the gain of the plant. If the power and the electrical efficiency of the cogeneration system are known, the code is able to calculate the performance and the sizes of the main components of the heat generator not only in nominal conditions but also if the operational conditions vary. The code is installed on the AFS filesystem. In particular Scilab code was compiled and only the executable files are stored in AFS. Using the FARO 2.0 interface, users can pass the values of the parameters to the code and choose the operational conditions between dynamically loaded options. These parameters are passed to CLI commands through an easy-to-understand JSON format, that the backend computational core is able to interpret and then execute. A sample illustration of the customized interface is in Fig.3-4.

A second application of FARO 2.0 is developed for the Web Crawling Virtual Lab [16]. The aim of this tool integrated in the related ENEA project is to create a simple interface between the users and the Web crawling environment installed on ENEAGRID. The Web crawling is an activity that automatically and systematically explores the Web, in order to search for contents/documents to download. Starting from the main html page of the interface, an user can create a web crawling session, launch the session and monitor the generated internet traffic. More specifically, this interface is composed of five tabs, in each of them, one can perform some operations. In the first tab, there is a form where one can insert some general informations (such as the title and comments) about the session that wants to create. In the second tab, a user can fill in a module with the configuration options to pass to resource scheduler in order to submit a session job. These options are split between the run configurations and software parameters. As run configuration an user can set the running time of job, the number of nodes to use and the number of agents per node. An agent is a Java process that plays the role of a crawler (i.e. a software that explores and downloads the web pages). As software parameters it is possible to can set

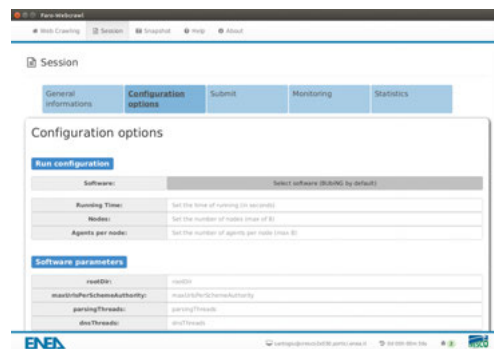


Figure 5: Custom FARE 2.0 for web crawling (a) Figure 6: Custom FARE 2.0 for web crawling (b)

many options for each crawler (e.g., the URLs seed to initially consider, the number of threads and the size of cache memories). If the user does not decide to set these options, automatically the interface creates a session configuration file with default options. In the third tab, an user can submit a batch job for the current session. In the fourth tab, once a web crawling session is submitted, the user can monitoring in real time the downloaded data amount by every agent. Finally, the fifth tab allows to view some statistics at the end of the latest executed session. The tool has been recently equipped with a further feature called “snapshot”, which allows to schedule periodic web crawling sessions. This is particularly useful to create a set of snapshots for some portions of the web, in order to analyze the changes and the evolution over a time period. Periodic scheduled web crawling session parameters can be set in the proper section in the tool interface. Customized interfaces are shown in Fig.5-6

The third application we present is the CMAST Virtual Lab [2]. The aim of this FARE 2.0 interface is to provide a collection of launchers for codes and software tools in the field of materials science that are installed on the AFS file system and executed on the ENEAGRID computational infrastructure. Users can perform a workflow of simulations at either the same scale or different scales in such a way that a multi-scale approach is practicable. Moreover, software for the 2D and 3D visualization of inputs and outputs of the simulations is provided to the user. The characteristic length of the models ranges from nanometers within quantum mechanics approach (where electrons motion is taken into account) to hundred of nanometers for molecular dynamics (MD) description (atoms motion) and to millimeters for process simulations. The simulation and visualization tools are organized in two tabs. The first tab is named “Codes” where buttons to launch the simulation codes are available. As shown in Fig. 7, this tab encloses the launchers for the following software: Matcalc [9] and PWgui [10]. The first one is a scientific software toolbox for computer simulation of the kinetics of microstructural processes and the latter is the open source graphical interface of QUANTUM ESPRESSO [11]. It is an open-source integrated suite of codes for electronic-structure calculations and materials modeling at the nanoscale. It is based on density-functional theory, plane waves, and pseudopotentials. QUANTUM ESPRESSO is compiled on ENEAGRID computational systems exploiting the Message Passing Interface (MPI) parallelization. The codes available in CMAST are not limited to those listed in the Codes tab. Other open source codes, not yet with a stable GUI, are available in the CMAST Virtual Lab and can be launched from terminal, such as CPMD, CP2K (quantum mechanics), GROMACS and LAMMPS (classical mechanics). However, the list of codes available within the CMAST Virtual Lab will be continuously updated. The second tab is “Graphics” that collects the launchers for open source software to be used for the preparation of the input and visualization of the results as 2D plots and 3D models. As shown in Fig.8, this tab encloses the launchers for the following software: Grace is a WYSIWYG 2D plotting tool for the X Window System [5]; XCrySDen is a crystalline and molecular structure

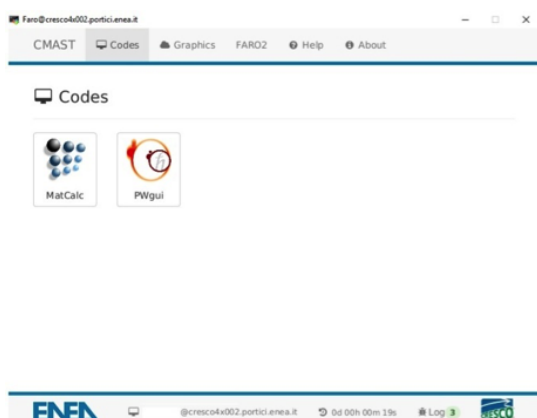


Figure 7: Custom FARO 2.0 for CMAST (a)

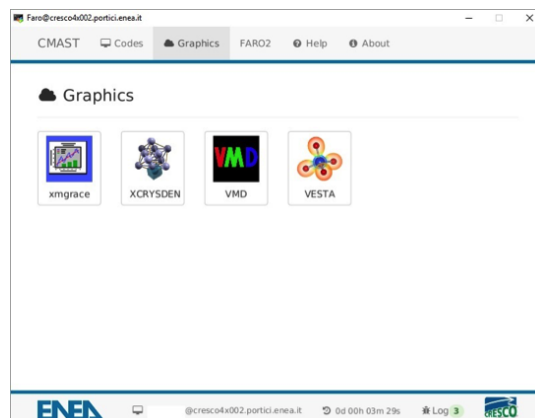


Figure 8: Custom FARO 2.0 for CMAST (b)

visualisation program [17]; VMD is designed for modeling, visualization and analysis of atomic-scale trajectories coming from MD simulations of both materials or biological systems. Moreover, VMD can act as a graphical front end for an external MD code [15]. VESTA is a 3D visualization program for structural models, volumetric data such as electron/nuclear densities, and crystal morphologies [14].

For all the applications, in the submission step, ad hoc shell scripts are used. These scripts read the parameters defined on the mask and usually encoded in a JSON format and launch the codes on execution nodes following the rules defined by the LSF scheduler. The applications provide also an Help page with an useful set of links for users (to submit tickets to ENEAGRID administrators and/or to monitor job execution).

In conclusion, every customized FARO 2.0 application is a workflow-oriented GUI enabling interaction with ENEAGRID computational resources and easily interoperates with every set of scientific tools installed on our grid/cloud environment.

Acknowledgment

The authors would like to thank Alessio Rocchi who was the former developer of FARO application and all the people involved in the management and operation of ENEAGRID/CRESCO infrastructure [4]. We also thank Matteo Caldera who is in charge of the computational core of the ADP Virtual Lab. FARO 2.0 has been developed in the contest of the Italian PON “Smart Cities and Communities” R&C 2007-2013 with the project “EDOC@Work 3.0 - Education and work in the cloud”. Part of this activity has been supported by the ENEA-Forschungszentrum JULICH GmbH contract “Fornitura da parte ENEA di attività di modellistica molecolare”.

References

- [1] ADP Virtual Lab. <http://www.afs.enea.it/project/adp/>.
- [2] CMAST Virtual Lab. <http://www.afs.enea.it/project/cmast/>.
- [3] EDOC@Work 3.0. <https://www.edocwork.it/>.

- [4] ENEAGRID people (2016). <http://www.eneagrid.enea.it/people/2016EneaGridPeople.html>.
- [5] Grace. <http://plasma-gate.weizmann.ac.il/Grace/>.
- [6] IBM LSF. <http://www-03.ibm.com/systems/platformcomputing/products/lsf/>.
- [7] Angelo Mariano et al. CRESCO EDOC (EDUCATION ON CLOUD): cloud computing a servizio della formazione e della didattica per il calcolo scientifico avanzato. In G. Adorni, M. Coccoli, F. Coceva, and I. Torre, editors, *Didamatica 2015 Studio Ergo Lavoro*, pages 409–412. AICA, 2015.
- [8] Angelo Mariano et al. Fast access to remote objects 2.0 a renewed gateway to eneagrid distributed computing resources. In S. Gesing and J. Krüger, editors, *Proc. of IWSG 2016 (8th International Workshop on Science Gateways)*, 8-10 June 2016, Rome, Italy. CEUR-WS.org, 2016.
- [9] MatCalc. <http://matcalc.tuwien.ac.at/>.
- [10] PWGui. <http://www-k3.ijs.si/kokalj/pwgui/>.
- [11] Quantum Espresso. <http://www.quantum-espresso.org/>.
- [12] Alessio Rocchi et al. Faro - the web portal to access eneagrid computational infrastructure. In G. Andronico R. Barbera and G. La Rocca, editors, *Proceedings of the International Workshop on Science Gateways (IWSG2010)*. Consorzio COMETA, 2010.
- [13] Sys-man Progetti & Servizi s.r.l. <http://www.sys-man.it/>.
- [14] Vesta. <http://jp-minerals.org/vesta/en/>.
- [15] VMD. <http://www.ks.uiuc.edu/Research/vmd/>.
- [16] WebCrawl Virtual Lab. <http://www.afs.enea.it/project/webcrawl/>.
- [17] XCrySDen. <http://www.xcrysden.org/>.

CLOUD INFRASTRUCTURE FOR SCALABILITY AND HIGH AVAILABILITY IN BUSINESS ICT APPLICATIONS

Angelo Mariano^{1*}, Francesco Beone² and Alberto Scalise³

¹*ENEA, DTE-ICT-IGEST, Apulian Office, viale Japigia 188, Bari, Italy*

²*ENEA, DTE-ICT-IGEST, Headquarters, Lungotevere Thaon di Revel 76, Rome, Italy*

³*ENEA, DTE-ICT-IGEST, Brindisi Research Center, Cittadella della Ricerca, Brindisi, Italy*

ABSTRACT. In this paper a short description will be given about the cloud infrastructure built in the ENEA Brindisi Research Center, ensuring scalability and high availability for testing purposes in the business ICT sector. Main components will be described and the implementation will be depicted with some examples.

1 Introduction

The ENEA Brindisi Research Center hosts a CRESCO cluster that is devoted to experiment and explore new technologies in the ICT sector. Recently, a cloud infrastructure has been deployed in the context of the Italian PON “Smart Cities and Communities” R&C 2007-2013 with the project “EDOC@Work 3.0 - Education and work in the cloud” [2, 5] for educational purposes. By profiting of these results, we are implementing a new cloud infrastructure devoted to testing and deploying high availability web applications easy to scale horizontally to fulfill requirements in the business ICT sector.

2 Components

In this section we will describe the main components employed in the cloud infrastructure implemented.

2.1 MAAS

Metal-as-a-Service (MAAS) is a provisioning construct created by Canonical and designed to help facilitate and automate the deployment and dynamic provisioning of hyperscale computing environments such as big data workloads and cloud services. MAAS serves as a layer underneath Infrastructure-as-a-Service (IaaS), deploying hardware and services that can dynamically scale up and down. Metal-as-a-Service is summarized by Canonical’s Mark Shuttleworth as a provisioning tool for bringing “cloud semantics to the bare metal world.” The basic idea is that hardware is increasingly a commodity that you buy for what it offers, not what it is. In a cloud environment, you don’t really care too much about the technical details of your CPUs, or bus speeds, or memory channels. You want computational power, and storage, and networking. In other words, MAAS is a way to abstract all the details of the physical computers into what you really care about [6].

*Corresponding author. E-mail: angelo.mariano@enea.it.

2.2 Juju

Juju is an “automatic service orchestration” project launched by Canonical, to deploy, manage and scale software and interconnected services across one or more Ubuntu servers and cloud platforms. It is a service orchestration tool for the cloud and is designed to work with MAAS to help streamline the process of deploying and managing resources and services in hyperscale computing environments. Commonly likened to as “apt-get for the cloud” Juju achieves this goal by using “charms,” which are open source tools that simplify specific deployment and management tasks. They can be written in any executable language and are essentially the building blocks, the containers of all the instructions on how to not only deploy, install, and configure a service but how that service relates to other services in the cloud [3].

2.3 OpenStack

OpenStack is a set of software tools for building and managing cloud computing platforms for public and private clouds. Backed by some of the biggest companies in software development and hosting, as well as thousands of individual community members, OpenStack can be considered the future of cloud computing. It is now managed by the OpenStack Foundation, a non-profit that oversees both development and community-building around the project. It lets users deploy virtual machines and other instances that handle different tasks for managing a cloud environment on the fly. It makes horizontal scaling easy, which means that tasks that benefit from running concurrently can easily serve more or fewer users on the fly by just spinning up more instances. For example, a mobile application that needs to communicate with a remote server might be able to divide the work of communicating with each user across many different instances, all communicating with one another but scaling quickly and easily as the application gains more users. And most importantly, OpenStack is open source software, which means that anyone can access the source code, make any changes or modifications, and freely share these changes back out to the community at large. It is mostly deployed as infrastructure-as-a-service (IaaS), whereby virtual servers and other resources are made available to customers. The software platform consists of interrelated components that control diverse, multi-vendor hardware pools of processing, storage, and networking resources throughout a data center. Users either manage it through a web-based dashboard, through command-line tools, or through RESTful web services [7].

2.4 Ceph

Ceph is an open source software storage platform that implements object storage on a single distributed computer cluster, and provides interfaces for object-, block- and file-level storage. Ceph aims primarily for completely distributed operation without a single point of failure, scalable to the exabyte level, and freely available. It replicates data and makes it fault-tolerant, using commodity hardware and requiring no specific hardware support. As a result of its design, the system is both self-healing and self-managing, aiming to minimize administration time and other costs. It uses an algorithm called CRUSH (Controlled Replication Under Scalable Hashing) to ensure data is evenly distributed across the cluster and that all cluster nodes can retrieve data quickly without any centralized bottlenecks. Ceph object storage is accessible through Amazon Simple Storage Service (S3) and OpenStack Swift Representational State Transfer (REST)-based application programming interfaces (APIs) and includes a native API for integration with software applications. Ceph block storage makes use of a Ceph Block Device, which is a virtual disk that can be attached to bare-metal Linux-based servers or virtual machines. The

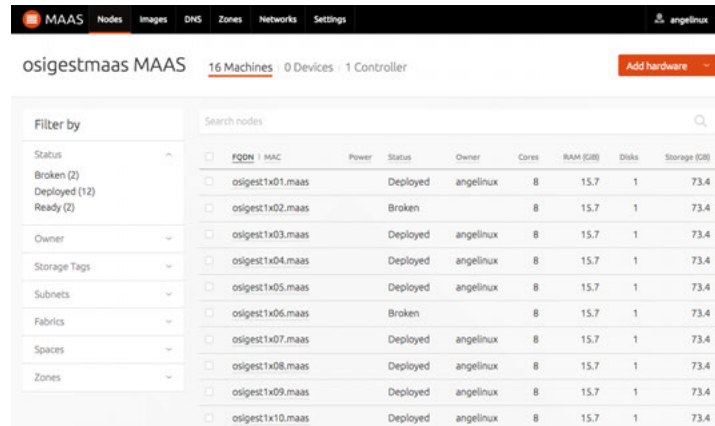


Figure 1: Main MAAS interface

Ceph Reliable Autonomic Distributed Object Store (RADOS) provides block storage capabilities, such as snapshots and replication. The Ceph RADOS Block Device is integrated to work as a back end with OpenStack Block Storage. Ceph file storage makes use of the Portable Operating System Interface (POSIX)-compliant Ceph file system (CephFS) to store data in a Ceph Storage Cluster. CephFS uses the same clustered system as Ceph block storage and Ceph object storage [1].

3 Implementation

This infrastructure allows a development of a cloud service targeted at experimenting new features in Business ICT applications. All the supplies are at the moment in the ENEA Brindisi cluster, but we are planning to create a multisite environment. It has been implemented with the following hardware:

- #1 MAAS Server 2 cpu Dual-core AMD Opteron
- #1 switch Enterasys
- #2 Bladecenter H with 14 blades each ex CRESCO2 HPC hardware
- #1 DotHill iScsi storage 3834

The MAAS server has been connected to the switch with a dedicated VLAN tagged port, in this way it becomes a DHCP server for every blade that is connected to the switch. With this setup there is no need to interfere with the Brindisi local area network, as all the components are inter-connected and rely only on frontier apparatus. In Fig.1 the MAAS interface is shown.

After the MAAS setup, a Juju cluster has been realized in order to install a full OpenStack orchestrated cloud on the blades. In Fig.2 the Juju dashboard shows all the nodes currently used and their function in the orchestration platform of OpenStack. Consider that the Ceph framework is integrated in OpenStack Swift component by using the storage provided by the DotHill 3834.

Through the standard Juju charm for OpenStack with some tweaking and adjustments mainly related to Ceph deployment, we obtained a cloud infrastructure whose example instances are in Fig.3.

In the cloud infrastructure, new virtual machines and services are really easy to set up, see for example Fig.4, that shows a Windows Server set up in minutes.

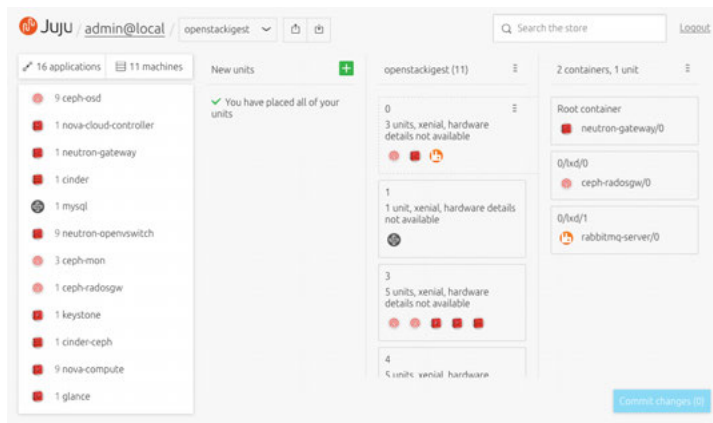


Figure 2: Juju GUI showing how the orchestrated OpenStack solution is implemented

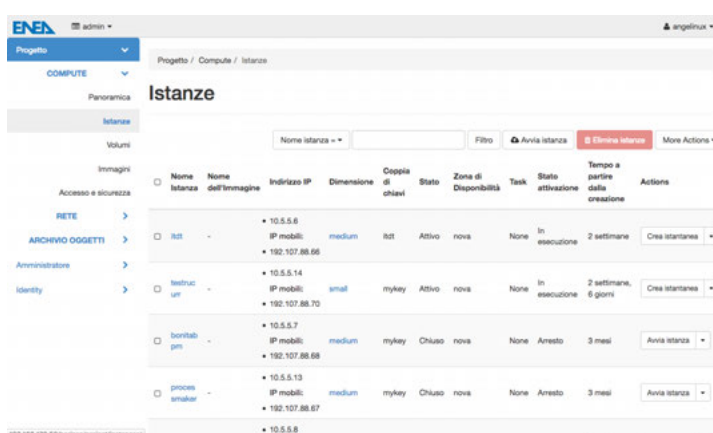


Figure 3: OpenStack instances view for admin project with some web applications for tests

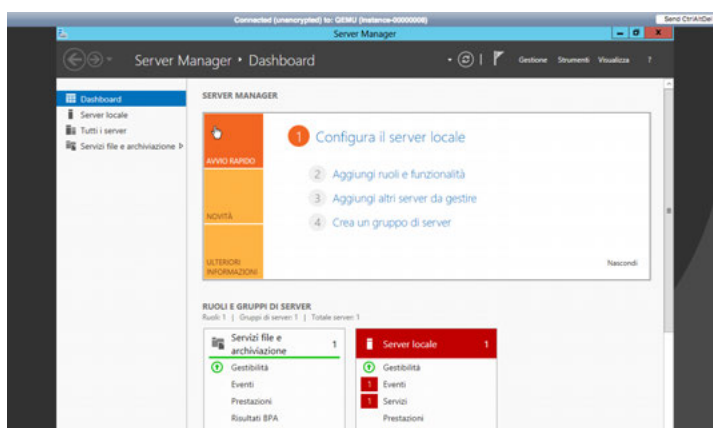


Figure 4: Sample remote desktop viewer for a Windows Server running on OpenStack

On top of our OpenStack infrastructure we are able to deploy a new Juju environment for managing scalable and high available software and service applications in business ICT domain, see for example Fig.5-6.

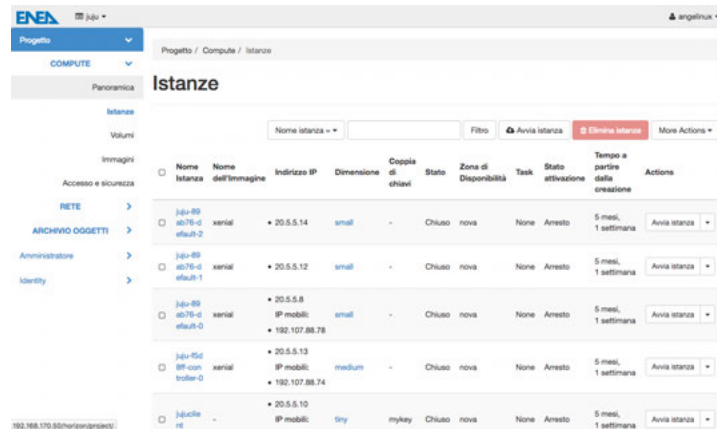


Figure 5: OpenStack instances view showing the project for a virtual Juju environment based on OpenStack

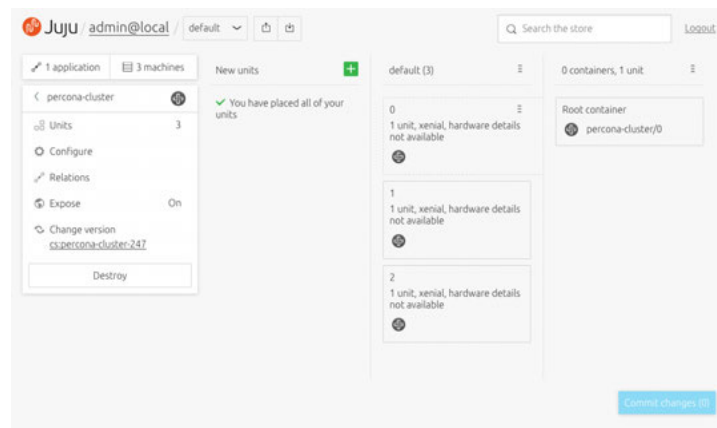


Figure 6: Juju GUI showing a MySQL Percona Cluster running on top of OpenStack

This cloud infrastructure allows implementing high available and scalable applications that can be tested and deployed in highly critical business ICT sector, i.e. by using load balancers and database clusters in multi-tier web-based applications.

4 Future improvements

Many improvements can be applied on this cloud infrastructure, in order to achieve state-of-the-art affordability and availability for business ICT applications. One of them will be the deployment of Kubernetes [4], a powerful system, developed by Google, for managing containerized applications in a clustered environment. It aims to provide better ways of managing related, distributed components across varied infrastructure. In many ways, Kubernetes was designed to address the disconnect between the way that modern, clustered infrastructure is designed, and some of the assumptions that most applications and services have about their environments. Most clustering technologies strive to provide a uniform platform for application deployment. The user should not have to care much about where work is scheduled. The unit of work presented to the user is at the service level and can be accomplished by any of the member nodes. These kind of frameworks can open the door to the advent of so-called

serverless applications and architectures [8]. The term “serverless architectures” refers to applications that significantly depend on third-party services (known as Backend as a Service or “BaaS”) or on custom code that runs in ephemeral containers (Function as a Service or “FaaS”). By using these ideas, and by moving much behavior to the front end, such architectures remove the need for the traditional “always on” server system sitting behind an application. Serverless applications don’t require you to provision, scale, and manage any servers. You can build them for virtually any type of application or backend service, and everything required to run and scale your application with high availability is handled for you. Building serverless applications means that developers can focus on their core product instead of worrying about managing and operating servers or runtimes. This reduced overhead lets developers reclaim time and energy that can be spent on developing great products which scale and that are reliable.

5 Conclusions

By re-using old CRESCO hardware we built in the Brindisi Research Center a cloud-based open source environment to test and deploy web applications. Such a cloud infrastructure guarantees replication, scalability, high availability in a range of deployment that are certainly useful for business ICT applications. Moreover, the great flexibility of the tools chosen and briefly described here, offers undoubtedly advantages with respect to other virtualization technologies in managing complex multi-tier systems.

Acknowledgments

We thank Giovanni Cannataro and Giacinto Caretto (ENEA DTE-ICT-RETE) for their support in the network configuration in the Brindisi Research Center.

References

- [1] Ceph. <http://ceph.com/>.
- [2] EDOC@Work 3.0. <https://www.edocwork.it/>.
- [3] Juju charms. <https://jujucharms.com/>.
- [4] Kubernetes. <https://kubernetes.io/>.
- [5] Angelo Mariano et al. CRESCO EDOC (EDUCATION ON CLOUD): cloud computing a servizio della formazione e della didattica per il calcolo scientifico avanzato. In G. Adorni, M. Coccoli, F. Coceva, and I. Torre, editors, *Didamatica 2015 Studio Ergo Lavoro*, pages 409–412. AICA, 2015.
- [6] Metal-As-A-Service. <https://maas.io/>.
- [7] OpenStack. <https://www.openstack.org/>.
- [8] Serverless architectures. <https://martinfowler.com/articles/serverless.html>.

ANALYSIS OF DIFFRACTION PATTERN FOR CADMIUM SULFIDE NANOCUSTER BY USING DEBYE SCATTERING EQUATION

Emiliano Burrese^{1*}, Massimo Celino², Leander Tapfer³

¹ENEA, SSPT Department, PROMAS Division, MATAS laboratory, C.R. Brindisi

²ENEA, DTE Department, ICT Division, C.R. Casaccia, Rome

³ENEA, SSPT Department, PROMAS Division, C.R. Brindisi

ABSTRACT. For the annual CRESCO computational activities, we report a preliminary approach of the Debye scattering equation (DSE) to investigate the XRD pattern of a small cadmium sulfide cluster. We calculated the diffraction patterns of unrelaxed spherical CdS cluster with increasing size from 40 Å up to 130 Å.

It is remarkable the XRD profile correctly improves with respect the increase of the cluster size. The peak positions are well reproduced in an angular range 20°-90° (2θ). On the contrary, some differences between the peak intensities and the experimental values are detected. The code was successfully tested and used to perform DSE calculation for a small CdS clusters relaxed at 10 K. Some computational data will be compared with experimental pattern got from the literature.

1 Introduction

The need for an accurate analysis of the structural and atomic properties of nanomaterials encouraged us to develop computational tools dedicated to the post-processing of the large amount of data produced by the large scale simulations performed on CRESCO. From the experimental point of view, the X-ray diffraction (XRD) analysis has been widely used to obtain structural information, and in the last decades it was also widely used for nanomaterials. However, in the case of atomic structures with reduced spatial dimensions the ordinary equations for diffraction from crystal materials are no longer valid; hence the reason to build an algorithm based on the Debye approach.

The calculation of the intensity $I(s)$ can be performed considering direct crystalline space. The general Debye formula [1] for the scattering intensity from an object composed of N atoms is:

$$I(\mathbf{s}) = \sum_{j,k=1}^N f_j(\mathbf{s})f_k(\mathbf{s})e^{2\pi i\mathbf{s}\cdot(\mathbf{r}_j-\mathbf{r}_k)} \quad (1)$$

where the sum is performed over the distances between couple of atoms for each value of the scattering vector \mathbf{s} ; f_j are the atomic scattering factors and \mathbf{r}_j are the position of the atoms. This formula is valid for powders, liquids, gas, nanostructures and generally for amorphous materials. When the \mathbf{r}_{jk} vector of the atoms takes all the orientations, the Debye scattering equation becomes:

$$I(s) = \sum_{j,k=1}^N f_j(s)f_k(s) \frac{\sin(sr_{jk})}{sr_{jk}} \quad (2)$$

*Corresponding author: emiliano.burrese@enea.it

The s scattering vector takes the values $s = \frac{4\pi\sin\theta}{\lambda}$, where θ is the Bragg angle and λ the wavelength for incident X-ray.

In order to obtain the intensity for given values of momentum transfer, we need to calculate the atomic form factor. To simplify the calculation, the equation (3) is usually used to obtain the amplitude scattered by the atoms.

$$f(s) = \sum_{i=1}^4 a_i e^{\left(\frac{-b_i s^2}{16\pi^2}\right)} + c \quad (3)$$

This equation provides a rigorous fit of the scattering curve, in our case for cadmium and sulfur as reported in Figure 1. The values of a_i , b_i and c are given in [2]

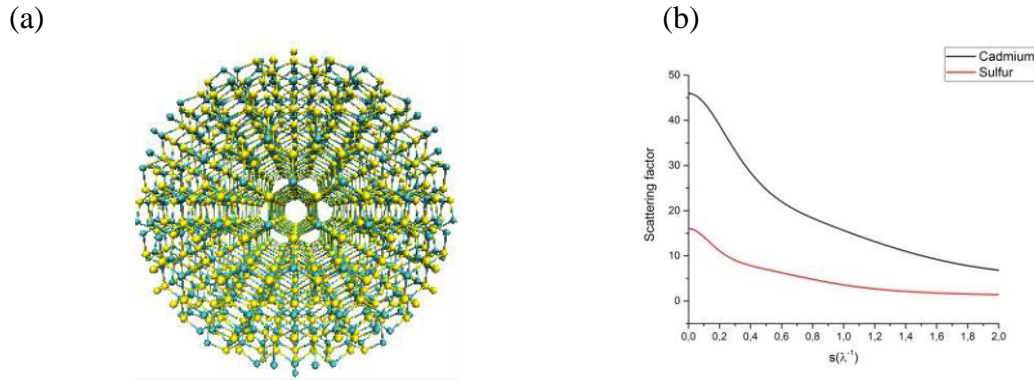


Fig.1: CdS cluster with 4 nm in size (a); the atomic scattering factors (b) for cadmium (black line) and sulfur (red line)

Some unrelaxed CdS clusters with spherical shape and increasing size are built to perform the X-ray diffraction pattern, up to obtain XRD pattern near to the experimental curve. Subsequently, the DSE code has been used to achieve the XRD pattern for CdS clusters with 96 and 324 atoms relaxed with ab-initio molecular dynamics at 10 K.

3 Computational details

In order to calculate the XRD pattern for CdS clusters, a basic DSE algorithm was implemented on CRESCO computational infrastructure. This code was written in Fortran language, it works in serial mode on single processor and it has been added as subroutine to the QDprop program [3]. As reported in Fig 2, the Debye algorithm scaling is N^2 with N the number of atoms, since the size of the clusters are necessarily limited. We calculated XRD pattern for CdS clusters up to 130 Å in diameter and with about 45000 atoms.

The unrelaxed CdS clusters with wurtzite phase and spherical shape were built by starting from the bulk CdS; a cutoff radius from the center of the crystal defines the size of the clusters, as reported in the Table 1.

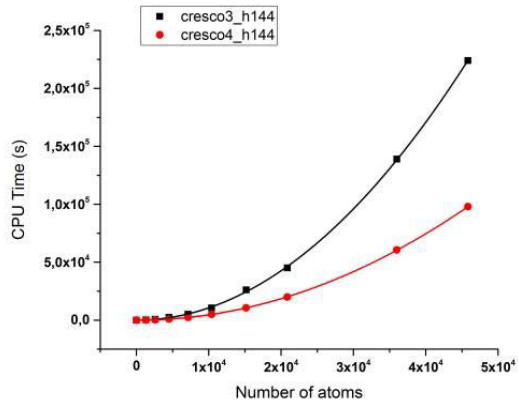


Fig.2: CPU time as a function of the number of cluster atoms.

	CdS40	CdS50	CdS60	CdS70	CdS80	CdS90	CdS100	CdS120	CdS130
Size (Å)	40	50	60	70	80	90	100	120	130
N. atoms	1326	2601	4509	7149	10395	15177	20859	36003	45842

Table 1: Size and number of atoms of the cadmium sulfide clusters investigated in this work.

The DSE algorithm has been implemented following the scheme reported in Figure 3.

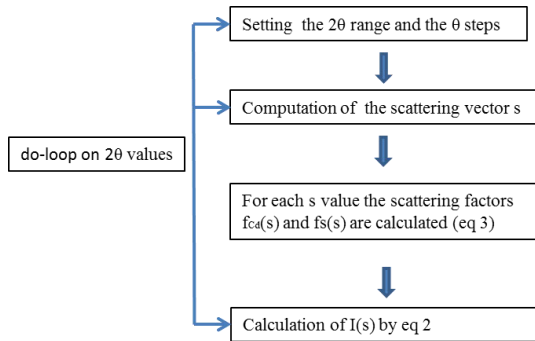


Fig.3: Scheme of the DSE algorithm as implemented on the CRESCO infrastructure.

All the distances between couple of atoms are calculated twice; it is required also the contribution of the single atoms. The step used for θ Bragg angle is 0.02 ranging between 10° - 45° (θ) and wavelength $\lambda = 1.54$ nm which corresponds to the wavelength from a X-ray tube with Cu anode. We analyzed the main peaks in XRD signal by using OriginPro package to obtain information about position and intensity.

The DSE algorithm has been also used to obtain XRD patterns of two CdS cluster relaxed at 10 K with 324 and 96 atoms. In this case, the geometry investigated was computed as the mean of the atomic coordinates over the last 20000 configurations of the trajectory.

For all calculations, the code was executed on CRESCO3 and CRESCO4 platform using the cresco3_h144 and cresco4_h144 queues with single processor.

An improved version of the code has been also implemented to calculate the average scattering intensity $I(s,t)$, in which the intensity is computed for each configuration of the pattern over the length of the trajectory; in this way both static and dynamic displacements were taken into account [4].

3 Results and discussions

The XRD pattern for some the clusters described in Table 1 are reported in Figure 4.

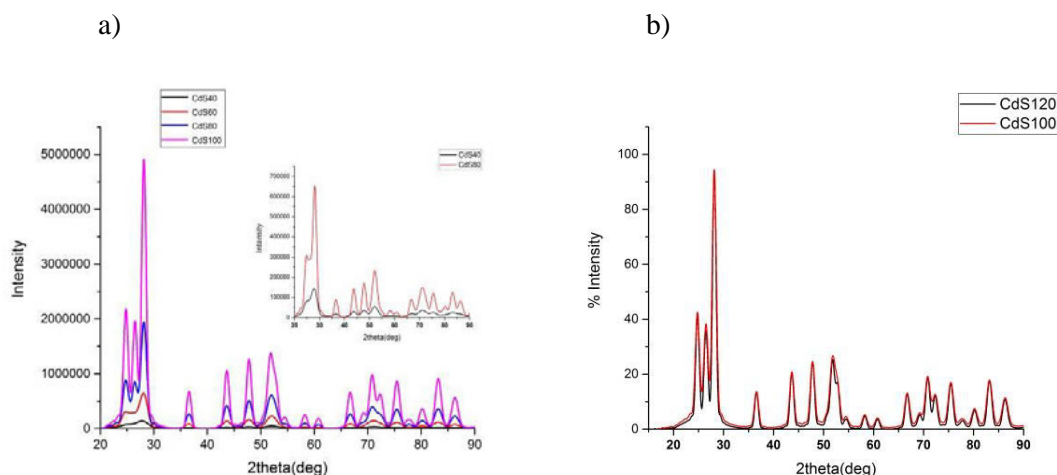


Fig.4: XRD Pattern for CdS40, CdS60, CdS80 and CdS100 (4a), CdS100 and CdS120 in 4b. By increasing the size, for CdS120 it is noticeable that the peaks around 52° are split, approaching slowly towards to the XRD profile reported in ref. pattern ICDD 98-003-1074.

As expected, the increase of the size from CdS40 to CdS100 improves the XRD signal. The crystallographic planes are better defined with increasing cluster size and after CdS60 the XRD pattern is characterized by three peaks around 24° , 26° and 28° (2θ), typical of the hexagonal phase (wurtzite ref. pattern 98-003-1074). For CdS40 and CdS60 the signals up to 30° (2θ) are not well separated. The main three peaks are split for size larger than 60 \AA . In Table 2 we report some computational results regarding the peak values for CdS100 and CdS120 and show a comparison with JCPDS-ICCD card data (experimental data) referred to bulk CdS.

Peak number	$2\theta(\text{deg})$		Intensity (%)		
	Calc.	Exp.	CdS120	CdS100	Exp.
1	24.80	24.75	46	47	59
2	26.48	26.44	41	43	43
3	28.16	28.12	100	100	100
4	36.60	36.53	19	18	47

Table 2: Peak position and peak intensity for CdS100 and CdS120 clusters. Both are compared with experimental bulk data (wurtzite CdS ref. pattern ICDD 98-003-1074).

It is well known that the XRD pattern of nanostructures is not comparable with respect to bulk XRD pattern. These differences increase with decreasing cluster size, i.e. if the periodicity are lost along the three crystallographic directions. So the Debye formula describes correctly the XRD pattern

because the intensity of scattering depends only by distances between couple of atoms and it is not affected explicitly by any kind of crystallographic symmetry. Correctly, we found a good agreement for peak position, because the atoms are localized in the same sites of the wurtzite symmetry both for bulk and nanostructure. On the contrary, the intensity ratio is not completely comparable. The main peaks with 100 % in intensity is higher with respect the peaks at 24° and 26° (2θ). Moreover, up to CdS80 the intensity ratio is not correct because the peaks around 24° and 26° have the similar values. This trend seems to change from CdS100 where the three peaks are well split. The higher value of the peak around 28° probably means that in the $\langle 101 \rangle$ direction there are more crystallographic planes better defined.

It is reasonable that increasing the size of the CdS cluster, the XRD signals approach to the experimental (bulk-like) pattern; obviously the size of these structures are not yet comparable with the dimensions of the bulk structures; indeed the peak intensity appears far from experimental ones. Finally, we report a primarily XRD study for CdS clusters relaxed at 10 K by using ab-initio molecular dynamics. These structures are built with 324 and 96 atoms [3,5], labeled as CdS324 and CdS96, respectively; their XRD pattern is characterized by a strong amorphous-like contribute.

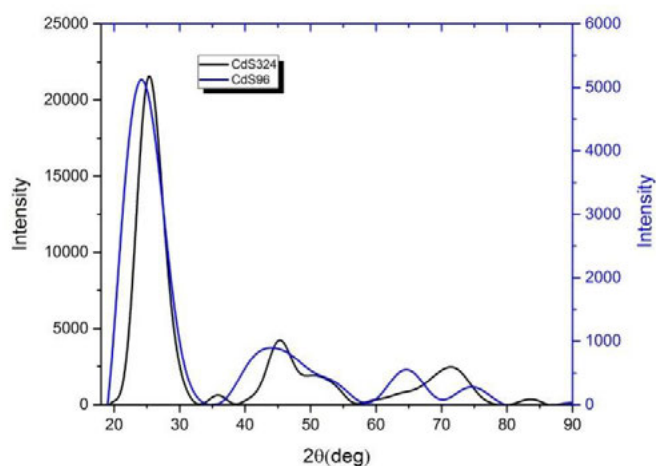


Fig.5:XRD profile for CdS96 (blue line) and CdS324 (black line)

In CdS96 a main peak around 24° (2θ) is recognized, whereas in CdS324 the same peak is shifted towards 25° (2θ). Another signal, broadened between 40° and 60° (2θ) is present both in CdS324 and CdS96. For CdS324 these last signals seem to be split into two secondary peaks, the strongest around 45° (2θ); conversely, this behavior is not observed for CdS96.

By looking experimental results on small CdS nanoparticles [6-7], CdS324 seems to have a satisfactory agreement; in [7] one peak are detected around 25° (2θ) and the broadened band is detected in a similar range, between 40° and 60° (2θ). Once again, the strong difference regards the peak intensities; for experimental XRD pattern the intensity of the first peak at 25° (2θ) is comparable with respect to the other ones, whereas for calculated XRD pattern we detected the same main peak but with too high intensity.

4 Conclusion

We consider this work on DSE algorithm to calculate the XRD profile of CdS clusters very promising. Indeed, it is important to investigate the structures and the time behavior of nanomaterials, in particular from the atomistic point of view. Actually, DSE is the most suitable approach to obtain XRD pattern for nanomaterials.

Moreover, by using the trajectory from ab-initio molecular dynamics, we would apply the DSE to the time-averaged atomic positions in order to get also dynamic atomic displacements. The intensity is calculated on the collection of identical structures over the trajectory which should simulate a perfect experimental powder.

5 References

- [1] A. Guinier, X-ray Diffraction in Crystals, Imperfect Crystals and Amorphous Body. Dover Publications, INC. New York (1994).
- [2] Int. Table for Crystallography. Atomic Scattering Factor for X-Ray, Vol IV, pag 99
- [3] E. Burrelli, M. Celino in “High Performance Computing on CRESCO infrastructure: research activities and results 2015”. Pag. 16 (2016). ISBN: 978-88-8286-342-5
- [4] L. Gelisio and P. Scardi. 100 years of Debye’s scattering equation. *Acta Cryst. A* **72**, pp. 608-620, (2016)
- [5] E. Burrelli, M. Celino. Methodological approach to study energetic and structural properties of nanostructured cadmium sulphide by using ab-initio molecular dynamics simulations. *Solid State Science* **14**, pp. 567-573, (2012).
- [6] N. Herron, Y. Wang and H. Eckert. Synthesis and Characterization of Surface-Capped, Size-Quantized CdS Clusters. Chemical Control of Cluster Size. *J. Am. Chem. Soc.* **112**, pp. 1322-1326, (1990).
- [7] J. Nanda, B.A. Kuruvilla and D.D. Sarma. Photoelectron spectroscopic study of CdS nanocrystallites. *Phys. Rev. B* **59**, pp. 7473-7479, (1999).

THEORY AND MODELING OF ENERGETIC PARTICLE DRIVEN INSTABILITIES

Sergio Briguglio¹, Giuliana Fogaccia^{1*}, Valeria Fusco¹, Gregorio Vlad¹, Xin Wang²
and Tao Wang³

¹ENEA, Dipartimento FSN, C. R. Frascati, via E. Fermi 45, 00044 Frascati (Roma), Italy

²Max-Planck-Institut für Plasmaphysik, Boltzmannstrasse 2, D-85748 Garching, Germany

³Institute for Fusion Theory and Simulation and Department of Physics, Zhejiang University, Hangzhou, People's Republic of China

ABSTRACT. The main activities in 2016, regarding numerical simulation of interaction between Alfvén modes and energetic particles in nuclear fusion devices and using CRESCO HPC facilities, are described.

1 Toward a complete exploitation of HYMAGYC, including the effects of shaped plasma cross section, Finite Larmor Radius and magnetic compression

The benchmark activity [1] between the code HYMAGYC against the code HMGC was pursued in 2016 for a new test case (the so-called ITPA benchmark case) [2]. After the characterization of the MHD spectrum, the results of the energetic particles (EP) drive have been considered, varying first the EP density n_{H0} . In order to ensure numerical stability in HMGC, a value of resistivity corresponding to the inverse Lundquist number $S^{-1}=10^{-6}$ has been assumed for both codes. At low values of n_{H0}/n_{i0} (w.r.t. the reference value $n_{H0}/n_{i0}=7.20655 \times 10^{-3}$, n_{H0} and n_{i0} being, respectively, the on-axis EP and bulk ion density), frequencies and growth-rates are very similar (see Fig.1b and 1a respectively, circles) corresponding to a mode localized in the toroidal gap, i.e., a TAE. For higher values of n_{H0}/n_{i0} , the most unstable mode obtained by HYMAGYC is clearly a mode emerging from the lower Alfvén continuum, i.e., a lower KTAE (see Fig.1b triangle symbols) exhibiting a higher growth rate compared to the most unstable mode observed by HMGC (Fig.1a), which is still a TAE.

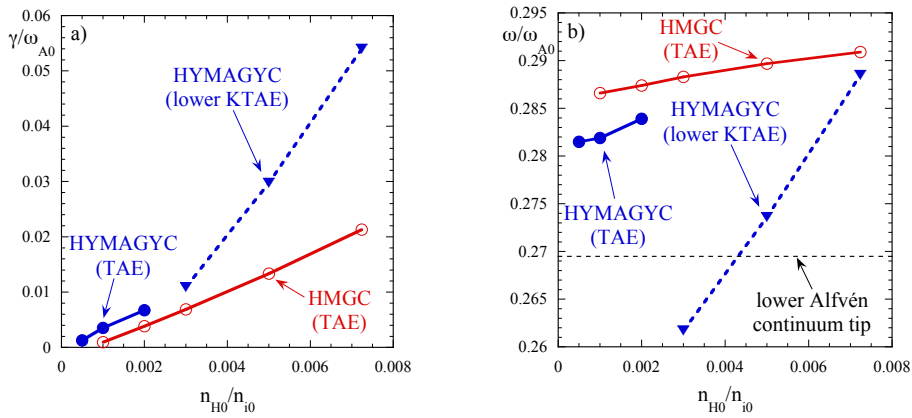


Fig.1: Normalized growth rates (a) and frequencies (b) as a function of n_{H0}/n_{i0} .

In the spirit of the ITPA benchmark, a scan on the EP temperature T_{H0} has been performed at the value $n_{H0}/n_{i0}=2\times 10^{-3}$ (lower than the reference ITPA benchmark case value), in order to compare the two codes in a regime where both observe the same TAE as the most unstable mode. Qualitative agreement is obtained considering the dependence of the growth-rate on T_{H0} , while significant quantitative differences are observed, which reduce when comparing the contribution of the EP drive to the growth rates (see Fig.2). The main discrepancies observed can be traced back to the different response of the MHD solvers, e.g., with respect to the continuum damping and discretization schemes.

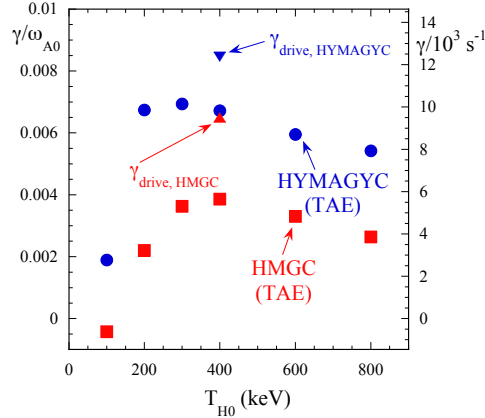


Fig.2: Normalized growth rates (left axis) versus T_{H0} at $n_{H0}/n_{i0}=2\times 10^{-3}$; right axis reports the growth rates in 10^{-3}s^{-1} . Results for HMGC (red square symbols) and HYMAGYC (blue circle symbols) simulations are shown; the triangles at $T_{H0}=400$ keV are the EP γ_{drive} .

The activities related to the code HYMAGYC have continued beyond the previous benchmark. In particular, during 2016, it has been pursued the target of relaxing the limitations considered in the previous benchmarks, namely the assumption of equilibria with small inverse aspect ratio a/R_0 (with a and R_0 the minor and major radius of the torus, respectively), circular plasma cross section, low bulk plasma beta, with negligible Finite Larmor Radius (FLR) and magnetic compression effects. In order to remove one at the time the above mentioned constraints, energetic particle FLR effects and magnetic compression effects have been analyzed with HYMAGYC in equilibria with small inverse aspect ratio, circular plasma cross section and low bulk plasma beta in presence of an energetic particle component. The overall effect is stabilizing, the growthrate reduction being dependent on the considered unstable mode. In order to check the plasma shaping effect and to analyze for a more realistic scenario the previous FLR and magnetic compression effects, a preliminary analysis of an AUG case based on a reference case [3] has been considered, in collaboration with the NLED Enabling Research group, both characterizing the Alfvén continua for different toroidal mode numbers ($n=1,2,3$) and studying the global, ideal MHD TAEs present in such equilibrium using the code MARS (see Fig.3a, 3b). To this purpose, the equilibrium code CHEASE has been used, together with an experimental EQDSK file representing the AUG shot #31213 at $t=0.84\text{s}$, considering a fully shaped plasma surface (note that the proposed reference case [3] considers an equivalent circular shape equilibrium). This AUG case has been used in HYMAGYC to check, at first, the plasma shaping effects and, then, the effects of magnetic compression, in presence of modes driven by an energetic particle component. The effect of considering also FLR effects on the realistic AUG equilibrium is currently under investigation. Moreover, in order to be prepared to analyze more deeply the linear and nonlinear dynamics of global modes driven by energetic particles, phase space diagnostics and test particle Hamiltonian method (TPHM) package [4] have been adapted to the general curvilinear geometry used in HYMAGYC, and successfully tested in HYMAGYC.

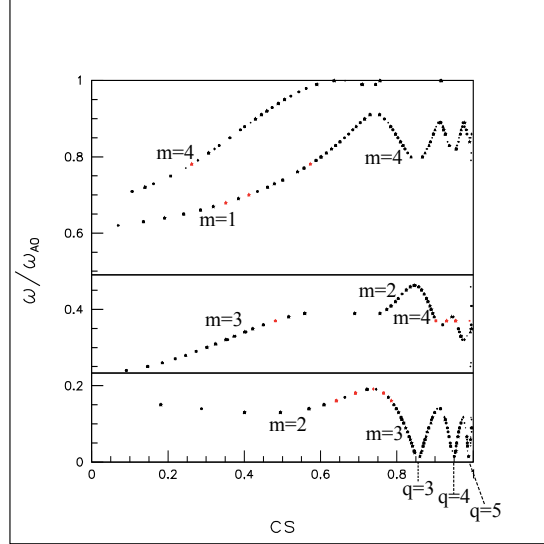


Fig.3a: Ideal MHD continuous spectra for $n=1$ toroidal mode number: frequency ω (normalized to ω_{A0} , the on-axis Alfvén frequency) vs. the square root of the poloidal flux function ψ (normalized to unity at the edge). Local dominant poloidal harmonics and radial location of the rational- q surfaces are also indicated in the figure. The horizontal segments refer to global Alfvén modes (a Toroidal Alfvén Eigenmode (TAE) at $\omega/\omega_{A0} \approx 0.23280$, and an Elliptical Alfvén Eigenmode (EAE) at $\omega/\omega_{A0} \approx 0.495$).

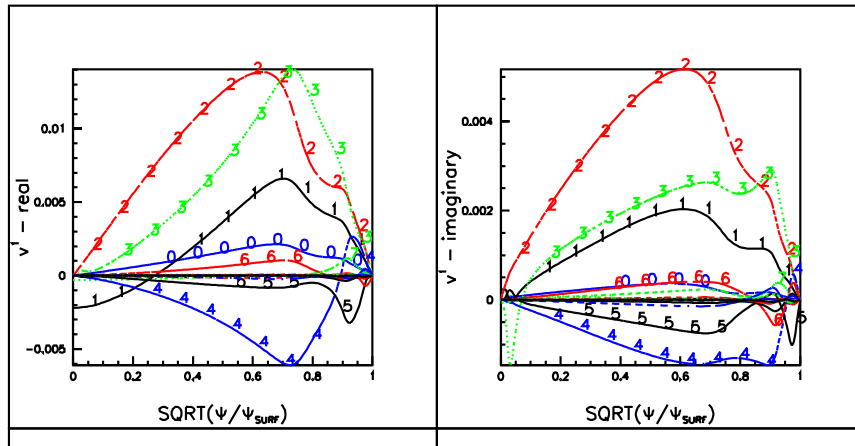


Fig.3b: Toroidal Alfvén Eigenmode (TAE) at $\omega/\omega_{A0} \approx 0.23280$: Real (left) and Imaginary (right) Fourier components (the numbers on the curves indicate the poloidal mode number m) of the contravariant radial perturbed velocity v^1 vs. the radial coordinate (the square root of the poloidal flux function ψ normalized to the edge value).

2 Theory and modeling of electron fishbones

The fishbones modes are internal kink $(m,n)=(1,1)$ instabilities induced by fast particles. They are called ion fishbones when they are induced by ions whilst electron fishbones when they are induced by fast electrons; these last modes were more recently observed. Their linear and nonlinear dynamics have been studied, following a numerical approach, with the HMGC code [5]. Peaked on-axis [6] and

peaked off-axis [7,8] supra-thermal electron density profiles with moderately hollow q-profile have been considered. The linear analysis have clearly demonstrated that the two situations are different in terms of the characteristic resonance frequency of the mode, as well as the fraction of suprathermal particles involved in the destabilization of the mode, confirming theoretical expectations. In fact the mode propagates poloidally parallel to the bulk electron diamagnetic direction for the peaked on-axis profile and parallel to the bulk ion diamagnetic direction for the peaked off-axis profile; particles involved are the trapped particles in the on axis case and barely trapped or circulating particles for the off axis profile [8,9]. It's worth noting that when artificially switching off the contribution of the trapped particles in one case or the barely trapped/circulating particles in the other case, no growing mode appears, thus confirming the energetic particles specific contribution in driving the mode unstable. The study of e-fishbone nonlinear saturation mechanisms has been pursued using the test particle Hamiltonian method (TPHM) package [4] and it has been performed for both the peaked on-axis as well as for the peaked off-axis density profile. The analysis consists in choosing a sample of resonant test particles and observing their behaviour in the Poincare plot: the energetic particles driving the mode, can be represented in a (P_ϕ, Θ) Poincare phase space, where P_ϕ is the toroidal canonical momentum and Θ the wave phase seen by the particle. In Fig.4, e.g., the non-linear dynamics is represented for a peaked off-axis density profile.

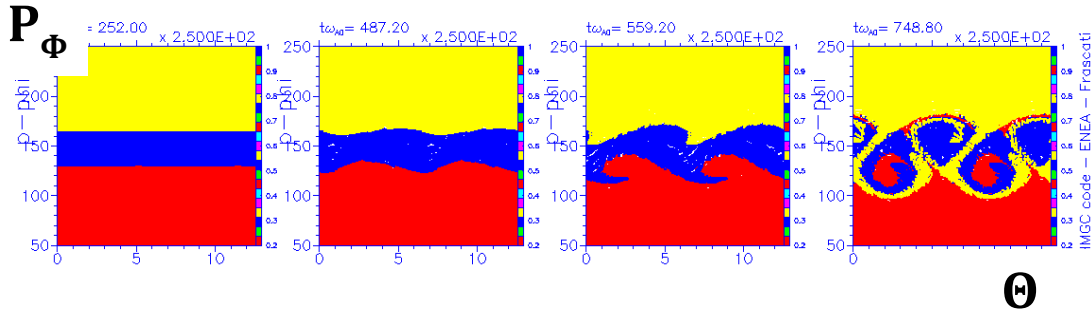


Fig.4: Energetic particles, driving the electron fishbone, are represented with different colors in the (P_ϕ, Θ) Poincare phase space. The colors depend on the position of the particles with respect to the resonance radial position. In this case, there are two resonances. As the saturation condition is reached, particles exchange their position, showing penetrating structures and wave particle trapping.

The two cases, peaked on-axis and peaked off-axis density profile, show different behaviour, even if both reveals the formation of mutually penetrating structures. In fact as the saturation process keeps on, it is readily apparent the formation of mutually penetrating structures that give rise to flattening of the density profile of the energetic particles. Density flattening, reducing the free energy source, contributes to the mode saturation. Moreover, it has been shown that for the peaked on-axis profile, the nonlinear saturation is characterized by a pronounced downward (in absolute value) frequency chirping of the mode, and evident phase locking, causing a large radial transport of energetic particles up to the $q \approx 1$ radius; the peaked off-axis profile one, on the other hand, is characterized nonlinearly by a double resonance structure in the kinetic Poincaré plot, and nonlinear saturation occurs causing energetic particle transport within the two resonance radii. The scaling of the saturation amplitude vs the ratio of the linear growth rate to the frequency of the mode γ_l/ω_0 (Fig.5), for both cases considered, has been shown to compare favorably with theoretical analyses [10]. Both cases evidence an energetic electron density flattening mechanism, which, reducing the free energy source, causes the mode to saturate.

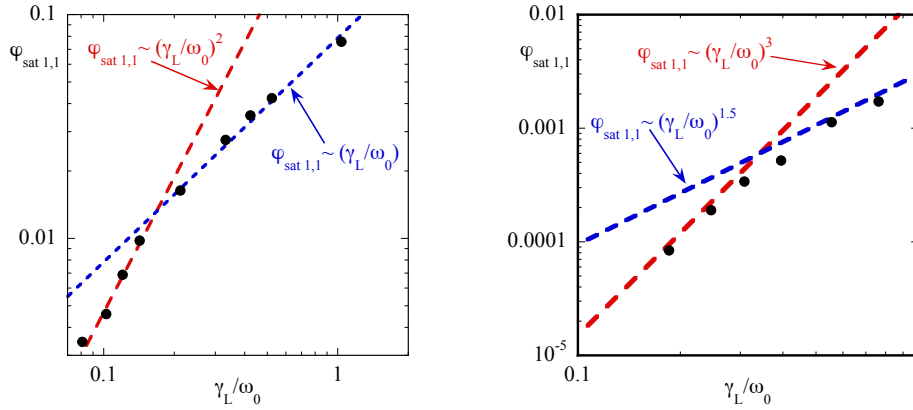


Fig.5: Saturation amplitude of the $m=1, n=1$ Fourier component of the electrostatic potential $\varphi_{sat 1,1}$ versus γ_L/ω_0 for the peaked on axis (left hand side) and peaked off axis (right hand side) energetic electron density profile.

3 Saturation of Alfvén modes in tokamak plasmas investigated by Hamiltonian mapping techniques

A benchmark of XHMGC and LIGKA-HAGIS has been completed for single toroidal mode number by means of Hamiltonian mapping techniques [11]; the transition from a quadratic (resonance detuning) to a linear (radial decoupling) growth-rate scaling for the saturation amplitude has been observed and explained in terms of a simplified pendulum model. It has been shown that the radial width of the single poloidal harmonic sets an upper limit to the radial displacement of circulating fast ions produced by a single toroidal number gap mode in the large n limit, irrespectively of the possible existence of a large global mode structure formed by many harmonics.

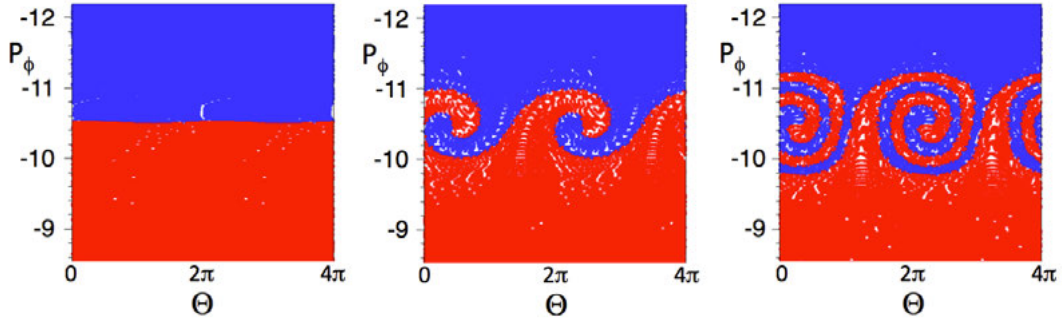


Fig.6: Test-particle markers in the (Θ, P_ϕ) plane at three successive times (corresponding to increasing mode amplitude) during the mode evolution in a LIGKA-HAGIS simulation. Each marker is coloured according to the birth P_ϕ value of the particle (red for $P_\phi < P_{\phi,res}$, blue otherwise; with $P_{\phi,res}$ being the resonance value). The formation of closed-orbit structures, separated from transit orbits, can be seen in the latter two frames, corresponding to the nonlinear phase.

The saturation mechanism of BAEs driven unstable by anisotropic fast-ion populations (co-passing or counter-passing ions) has been investigated, for different single toroidal numbers, by means of XHMGC simulations [12,13]. In the considered case, the radial profile of the resonance frequency for the co-passing fast ions is flatter than that for the counter-passing ones. This results in a much

greater resonance width in the former case, such that, for low toroidal mode numbers, only the radial decoupling regime is observed in the explored growth-rate range. The transition from the resonance detuning regime to the radial decoupling one is appreciated, for co-passing ions, only for the larger toroidal number considered, $n=4$. Modes driven by counter-passing fast ions, instead, exhibit such transition even for the lower n values. Multi- n simulations, retaining only wave-particle nonlinearities, have been performed in order to investigate the synergic effect of different toroidal mode numbers on fast-ion transport. Phase-space diagnostics have been developed in order to check whether particles driving a certain mode in the linear phase are able to drive a different toroidal-number mode after they have been displaced by the nonlinear interaction with the former mode. Chirping frequency EPs have been investigated: it has been shown that, for specific resonant particles, a radial displacement larger than both linear-phase mode and resonance widths is possible, but this does not necessarily imply a large fast-ion density flattening [14,15].

4 Energetic particle dynamics and Alfvénic fluctuation spectra on the Divertor Tokamak Test facility (DTT)

The Divertor Tokamak Test facility (DTT) [16] aims at bridging the gap between ITER and DEMO. Despite its focus is on “power exhaust” and “plasma wall interactions”, the DTT reference scenarios are characterized by substantial integration of core and edge plasma physics. It is, thus, important to understand the energetic particle dynamics and Alfvénic fluctuation spectra on DTT, as these will reflect the similar activities in burning fusion plasmas. Based on similar design proposal, this scenario is studied by HMGC simulations, with the control parameters chosen to match the reference values from previous proposals of ITER and FAST [17]. Fig. 7(a) shows the equilibrium q profile, where inverse aspect ratio ϵ is artificially reduced to 0.18 due to the limitation of the “ $O(\epsilon^3)$ reduced MHD” model in HMGC; Fig. 7(b) shows the EP radial profile; other simulation parameters and profiles are chosen to be as close as possible to the considered reference scenario.

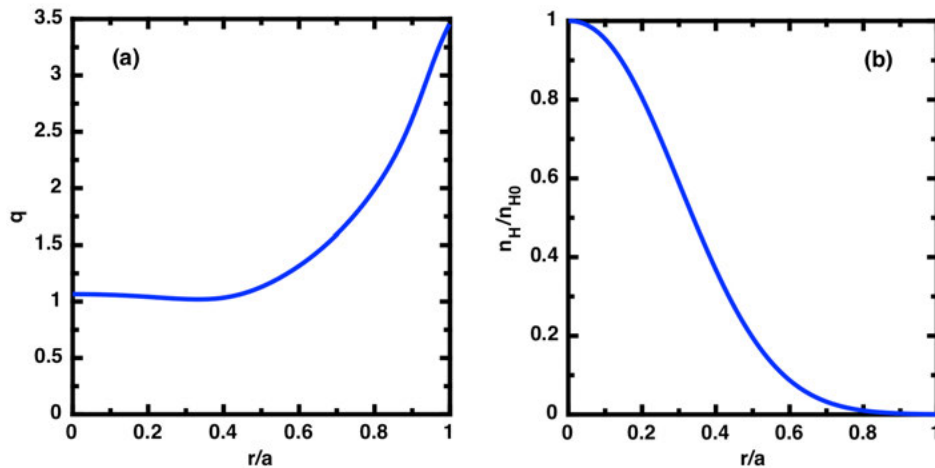


Fig. 7: (a) Equilibrium q profile; (b) Normalized energetic particle radial profile.

Firstly, we focus on an $n = 4$ fluctuation and a reference case with EP on-axis density $n_{H0}/n_{i0} = 3.0 \times 10^{-3}$. The radial mode structures are shown in Fig. 8(a), with real frequency $\omega_r/\omega_{A0} = 0.0858$. This mode shows characters of a reverse shear Alfvén eigenmode (RSAE). In order to further understand the spectrum of this mode, we introduce the simulation output driving rate γ_{drive} , calculated as energy density-weighted integral of wave-particle power density. By definition, damping rate can be calculated as $\gamma_{damp} = \gamma_{drive} - \gamma_{growth}$, where γ_{growth} is the linear mode growth rate. Then, we vary EP density and track the change of these parameters as well as the mode real frequency ω_r . The results are shown in Fig. 8(b)-(d). In addition, we use antenna excitation method to measure the damping

rate and eigenmode real frequency in the MHD limit. In Fig. 8(c) and (d), the results of EP driven cases and antenna excitation cases show good agreement; also, the results suggest that in comparison with the MHD limit, the damping rate and real frequency are greatly changed by increasing EP density, which demonstrates the EP effect here is nonperturbative. Finally, in the reference case, EP induced frequency shift is significantly larger than the distance between the eigenmode frequency and accumulation point of the Alfvén continuous spectrum. This fact shows the reference case is not a “pure” RSAE gap mode, but a fluctuation in the transition to an energetic particle mode (EPM), which further emphasizes the importance of non-perturbative treatment of EPs in the analyzed DTT reference scenario.

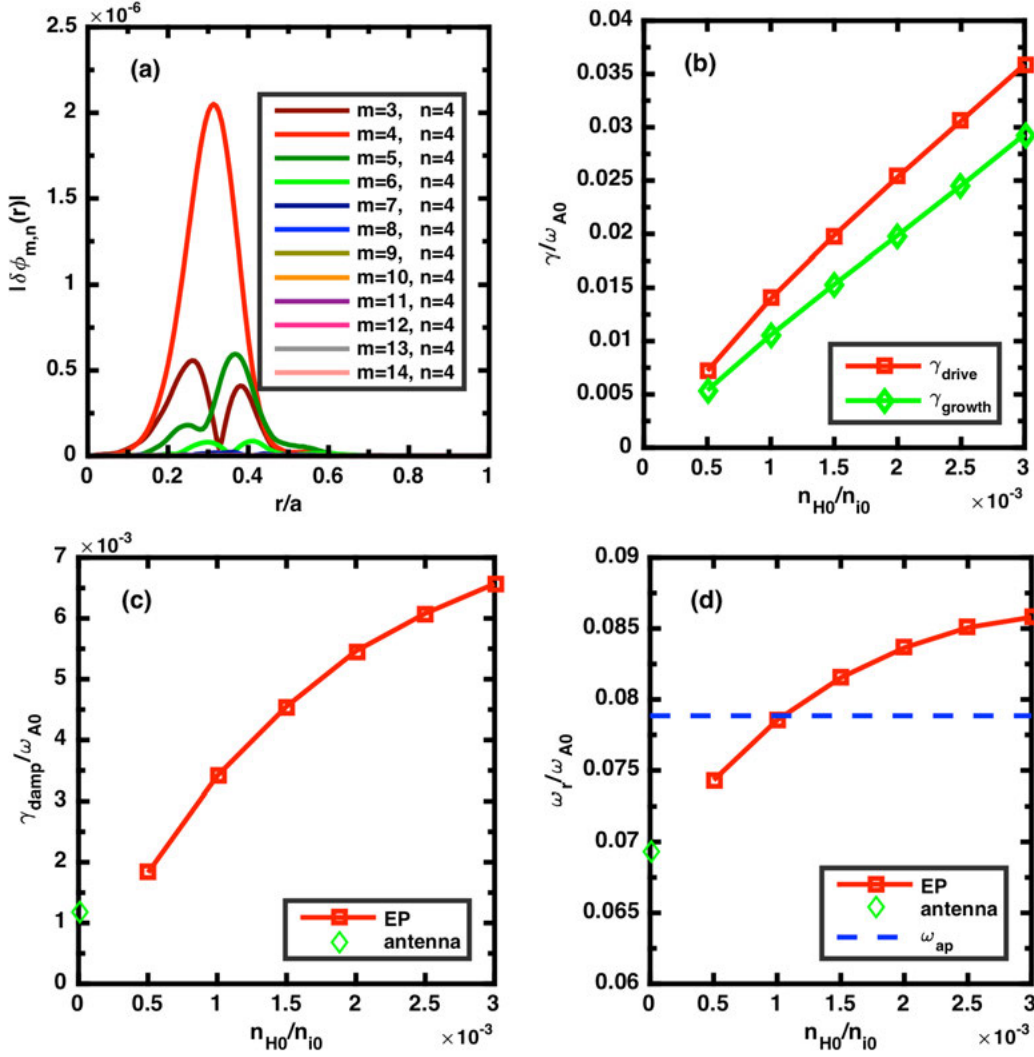


Fig.8: (a) Radial mode structures of reference case with $n_{H0}/n_{i0} = 3.0 \times 10^{-3}$; (b) Driving rate γ_{drive} and linear growth rate γ_{growth} of cases with varying EP density; (c) Damping rate γ_{damp} of cases with varying EP density and antenna excitation; (d) Mode real frequency ω_r of cases with varying EP density and antenna excitation, in addition, RSAE accumulation point ω_{ap} is added as a reference.

References

- [1] S. Briguglio, G. Fogaccia, V. Fusco, M. Martone, G. Vlad, X. Wang, T. Wang. Simulations of linear and nonlinear interactions between Alfvén modes and energetic particles, High Performance Computing on Cresco infrastructure: research activities and results 2015, pages 41–47, (2016)
- [2] G. Fogaccia, G. Vlad, S. Briguglio. Linear benchmarks between the hybrid codes HYMAGYC and HMGC to study energetic particle driven Alfvénic modes Nuclear Fusion 56, 112004 (2016)
- [3] Ph. Lauber et al., NLED- AUG reference case, http://www2.ipp.mpg.de/~pwl/NLED_AUG/data.html
- [4] S. Briguglio, X. Wang, F. Zonca, G. Vlad, G. Fogaccia, C. Di Troia, V. Fusco. Analysis of the nonlinear behavior of shear-Alfvén modes in tokamaks based on Hamiltonian mapping techniques, Physics of Plasmas 21, 112301, (2014)
- [5] G. Vlad, V. Fusco, S. Briguglio, G. Fogaccia, F. Zonca, X. Wang Theory and modeling of electron fishbones. New Journal of Physics, Special Issue on “Fast particle instabilities and transport in fusion, space and astrophysics plasmas”, 18:105004, (2016). doi:10.1088/1367-2630/18/10/105004.
- [6] G. Vlad, S. Briguglio, G. Fogaccia, F. Zonca, V. Fusco, X. Wang. Electron fishbone simulations in tokamak equilibria using XHMGC. Nuclear Fusion, 53:083008, (2013).
- [7] V. Fusco, G. Vlad, S. Briguglio, G. Fogaccia, C. Di Troia, F. Zonca. Analysis of the electron fishbone instability with the XHMGC code, 7th IAEA Technical Meeting on Plasma Instabilities, Frascati, Italy, March 4-6, 2015
- [8] V. Fusco, G. Vlad, S. Briguglio, G. Fogaccia. Electron fishbone dynamics studies in tokamaks using the XHMGC code, 14th IAEA Technical Meeting on Energetic Particles in Magnetic Confinement Systems, paper P28, Vienna 1-4 Sep. 2015.
- [9] G. Vlad, V. Fusco, S. Briguglio, C. Di Troia, G. Fogaccia, F. Zonca, X. Wang. Linear and nonlinear dynamics of electron fishbones. 26th IAEA Fusion Energy Conference (FEC 2016) Kyoto, Japan 17–22 October 2016, paper TH/P4-6.
- [10] L. Chen and F. Zonca. Physics of Alfvén waves and energetic particles in burning plasmas. Review of Modern Physics. 88, 015008 (2016).
- [11] S. Briguglio, M. Schneller, X. Wang, C. Di Troia, T. Hayward, V. Fusco, G. Vlad, G. Fogaccia. Saturation of Alfvén modes in Tokamak plasmas investigated by Hamiltonian mapping techniques. Nuclear Fusion 57 072001 (2017)
- [12] X. Wang, S. Briguglio, Ph. Lauber, V. Fusco, F. Zonca. Structure of wave-particle resonances and Alfvén mode saturation, Physics of Plasmas 23 (1), 012514, 2016
- [13] X. Wang, S. Briguglio. Saturation of single toroidal number Alfvén modes, New Journal of Physics 18 (8), 085009, 2016
- [14] X. Wang, S. Briguglio, M. Schneller, Ph. Lauber, V. Fusco, C. Di Troia et al. On the structure of wave-particle interactions and nonlinear Alfvénic fluctuation dynamics. Poster presented at the 26th IAEA Fusion Energy Conference (FEC 2016) Kyoto, Japan 17–22 October 2016.
- [15] S. Briguglio, M. Schneller, X. Wang. Radial displacement of resonating ions induced by single-n modes: gap modes versus EPs, 17th Meeting of the ITPA Topical Group on Energetic Particles, 24th – 26th October 2016, Kyoto University, Kyoto, Japan
- [16] Divertor Tokamak Test Facility Project Proposal, A. Pizzuto Ed. (ENEA, Frascati), ISBN: 978-88-8286-318-0, 2015
- [17] Pizzuto A. et al., The Fusion Advanced Studies Torus (FAST): a proposal for an ITER satellite facility in support of the development of fusion energy, Nuclear. Fusion 50:095005, 2010.

NEUTRON TRANSPORT ANALYSIS IN DEMO IN-VESSEL COMPONENTS

Rosaria Villari^{*1}, Davide Flammini¹ and Fabio Moro¹

¹*ENEA FSN FUSTEC-TEN, C.R. Frascati, via E. Fermi 45, 00044 Frascati (Rome), Italy¹*

ABSTRACT. Neutronics calculations with MCNP5 Monte Carlo code have been performed in 2016 to support the design of DEMO reactor and in particular of in-vessel components within EUROfusion Power Plant Physics & Technology (PPPT) program. This work summarise results of nuclear analyses for the design and integration of the Pellets Fuelling Lines and Electron Cyclotron launchers.

1 Introduction

In the frame of this activity within the EUROfusion Power Plant Physics and Technology (PPPT) programme, neutronics simulation with MCNP5 [1] Monte Carlo code in parallel mode using MPI on CRESCO cluster have been performed to support design and integration of pellet fuelling lines (PFL) and Electron Cyclotron(EC) launchers in DEMO fusion reactor. Different configurations of the various systems have been integrated in a Helium Cooled Pebble Bed (HCPB) DEMO reactor. The impact on Tritium Breeding Ratio (TBR), neutron flux, nuclear heating and damage on Breeding Blanket (BB), Vacuum Vessel (VV) and Toroidal Field (TF) coil was studied as well nuclear loads on the integrated systems. Strategies to improve in-vessel components design and shielding capability have been suggested to reduce the interface with other systems [2].

2 Integration of Pellet Fuelling Lines

Different options of pellet fuelling lines (PFL) are under study for integration. Neutronics analyses have been performed for three possible configurations of the so-called option “3” of pellet fueling lines that impact the inboard blanket (IB) modules 4 and 5 [3]. The three configurations are listed below and shown in figure 1:

- (3-1) 3° opening cone starting at the BB Back Supporting structure (BSS);
- (3-2) 2° opening cone starting at the BB back supporting structure (BSS);
- (3-3) 2° opening cone starting at the BB back-plate (moved inward of ~ 200 mm with respect to option 1 & 2).

The impact of PLF on TBR is marginal even in worst configuration (for configuration 3-1, -0.0029 with respect to baseline) and the TBR is well above the margin of 1.10.

Behind the large gap between IB4 modules, the maximum heating on the VV is 1.05 W/cm³ for configuration 3-1, doubled relative to baseline and it decreases to 0.74 W/cm³ for case 3-3. The

¹ Corresponding author. E-mail: Rosaria.villari@enea.it.

impact on BB nuclear heating is moderate and the maximum effect in the worst configuration is +40% on total heating on the side left cap (close to the gap) and less than few % on BSS. The maximum nuclear heating in TF coil is above the limit of $5 \times 10^{-5} \text{ W/cm}^3$ for configurations 3-1 ($9.1 \times 10^{-5} \text{ W/cm}^3$) and slightly higher also for configuration 3-2 ($5.7 \times 10^{-5} \text{ W/cm}^3$). Conversely, the peak heating is below the limit for the configuration 3-3.

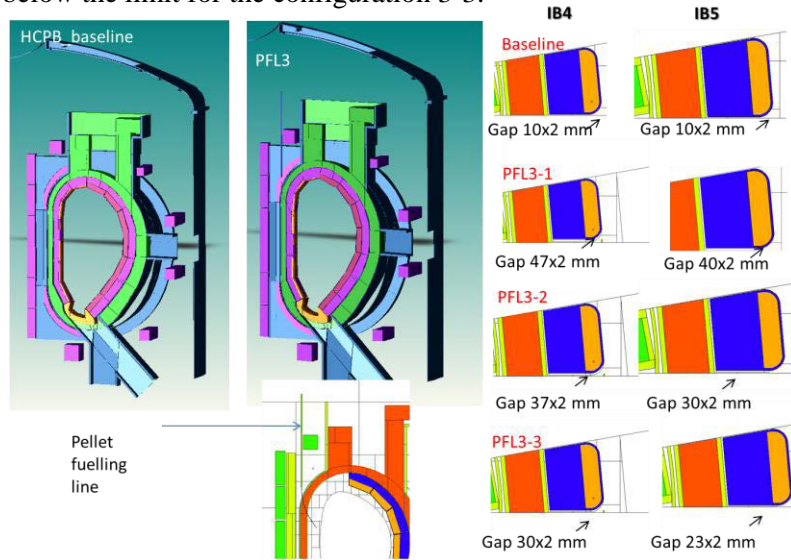


Fig. 1: HCPB MCNP 3-D model of baseline and PFL 3-1 (left), top view of IB4 and IB5 gaps for baseline and for the three configurations.

Great increase of damage in steel is observed behind the gap due to neutron streaming. The cumulated damage on VV is below but very close to the limit of 2.75 dpa over 6 FPY² (max 2.74 dpa over 6 FPY for 3-1 case). For the configurations 3-2 and 3-3 the maximum cumulated damages are 2.25 dpa and 1.9 dpa, respectively (see figure 2).

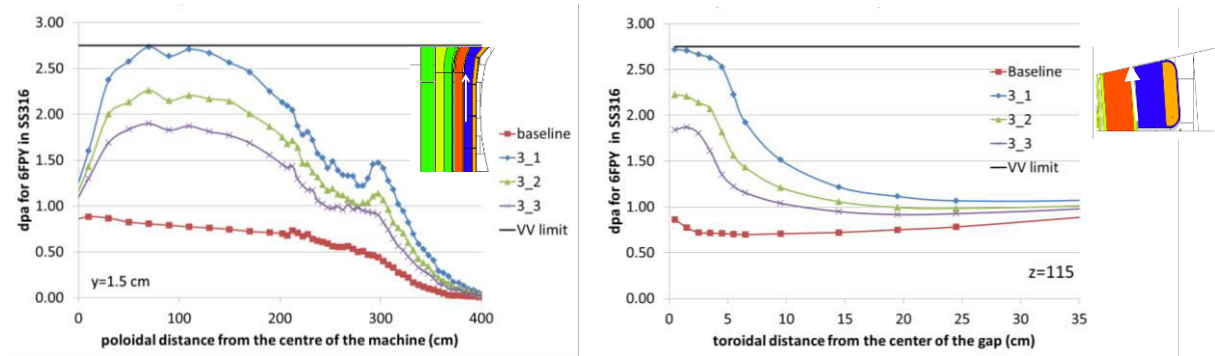


Fig.2: Neutron damage poloidal (left) and toroidal (right) profiles in dpa over 6 FPY in VV inner shell for baseline, PFL 3-1, 3-2 and 3-3 configurations

Regarding the nuclear loads on the pellet fuelling lines the maximum heating and damage in front positions are 9.8 W/cm^3 and 13 dpa/FPY. Behind BSS, the nuclear loads decrease to 0.96 W/cm^3 and

² Full Power Year

0.77 dpa/FPY for configuration 3-1. At this last position the reduction in configuration 3-3 is within 30%.

On the basis of the results of this neutronics analysis, the configuration 3-3 does not pose any neutronics integration issue, even configuration 3-2 might be acceptable providing minimum efforts to improve TF shielding. Indeed the large openings of configuration 1 might be not viable to ensure sufficient protection of VV (the maximum dpa is very close to the design limit) and a great effort is needed to decrease TF loads. The possibility to adopt a trapezoidal gap shape between IB4 and IB5 instead of rectangular might be considered for integration of 3° opening cone pellet fueling line, to help to reduce the zone of VV directly exposed to neutron streaming.

3 Integration of Electron Cyclotron Launchers

Neutronics analyses have been performed to support design and integration of the Electron Cyclotron (EC) launchers in equatorial port. The proposed heating system consists of 5 EC launchers based on 8 Remote Steering Antennas (RSA). Two different configurations have been considered for integration in 2016: two horizontal rows with four RSA each and one vertically stacked array of eight RSA (see figure 3). The present integration strategy consists in removing the equatorial outboard BB modules (Outboard Blanket, OB4), impacted by EC opening, and in replacing them with shielding plug made of steel and water [2][4].

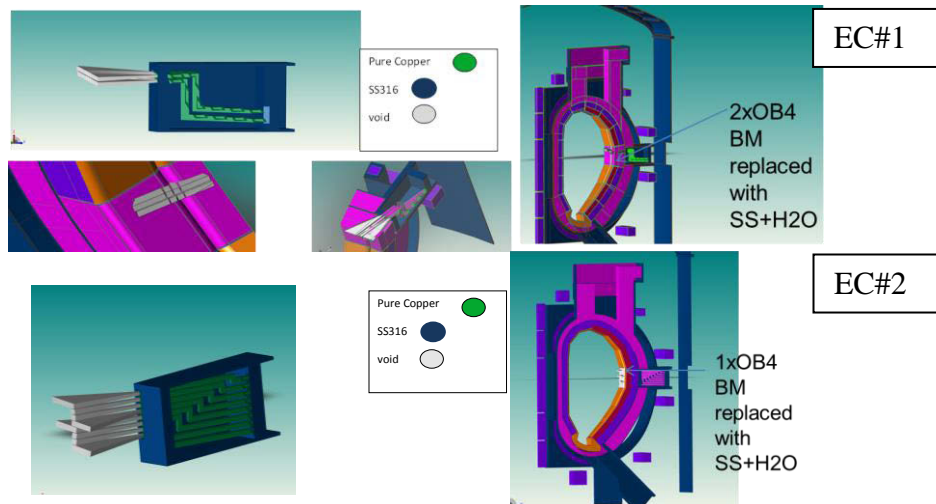


Fig.3: MCNP model of EC configuration #1 (top) and #2 (bottom) and integration in HCPB 10° model

The impact on TBR of 5 EC#1 launchers is high, -0.038 with respect to baseline, due to the complete replacement of 10 OB4 equatorial modules with steel-water plugs. The effect of 5 EC based on conf. #2 is less than EC#1, -0.022 with respect to baseline, due to the complete replacement of 5xOB4 equatorial modules with steel-water plugs. In both cases the total TBR is still above the margin, if the HCPB is considered (the total TBR is 1.175 with EC#1 and 1.192 with EC#2). Total neutron flux, nuclear heating and in particular neutron damage show a remarkable increase in outboard zones with respect to baseline especially for EC#2.

The neutron flux at the level of the rear flange of EC#1 port plug is more than 50 times higher than in baseline model (max $1.2 \times 10^{11} \text{ n} \cdot \text{cm}^{-2} \cdot \text{s}^{-1}$) and more than 3 times higher with EC#2 configuration (max $4 \times 10^{11} \text{ n} \cdot \text{cm}^{-2} \cdot \text{s}^{-1}$). Figure 1.2.4 shows the nuclear heating maps for baseline and the two configurations. The nuclear heating peaks in VV and TF coil are 0.4 W/cm^3 and $8 \times 10^{-4} \text{ W/cm}^3$ (15 times above the limit) for EC#1. With configuration EC#2 the situation get worse and the peaks on VV and TF increase up to 4 W/cm^3 and $2 \times 10^{-3} \text{ W/cm}^3$ (40 times above the limit), respectively.

The impact on neutron damage is greater than the other quantities. Considering configuration EC#1, the dpa peak on VV is 0.15 dpa/FPY (0.9 dpa over DEMO lifetime), still below the VV limit, but with large gradient in the zone close to the port. A 70 cm thick VV-like shield (60% SS+40% H₂O) located behind the front SS shield in EC port can be suitable to reduce the average nuclear loads on VV and rear components and to protect TF coil. At the rear flange the neutron streaming can be reduced to baseline level. Conversely, with EC#2 configuration, the dpa peak on VV is 2.9 dpa/FPY (17.4 dpa over DEMO lifetime) well above the design limit, at the corner in front of the large opening. Increase of dpa level in central outboard OB4 BB and BSS zones close to the opening is also observed. Additional shield in EC#2 plug would help to protect TF, however VV and BB loads need to be mitigated by reducing the opening or including shield in the zone close to EC cone.

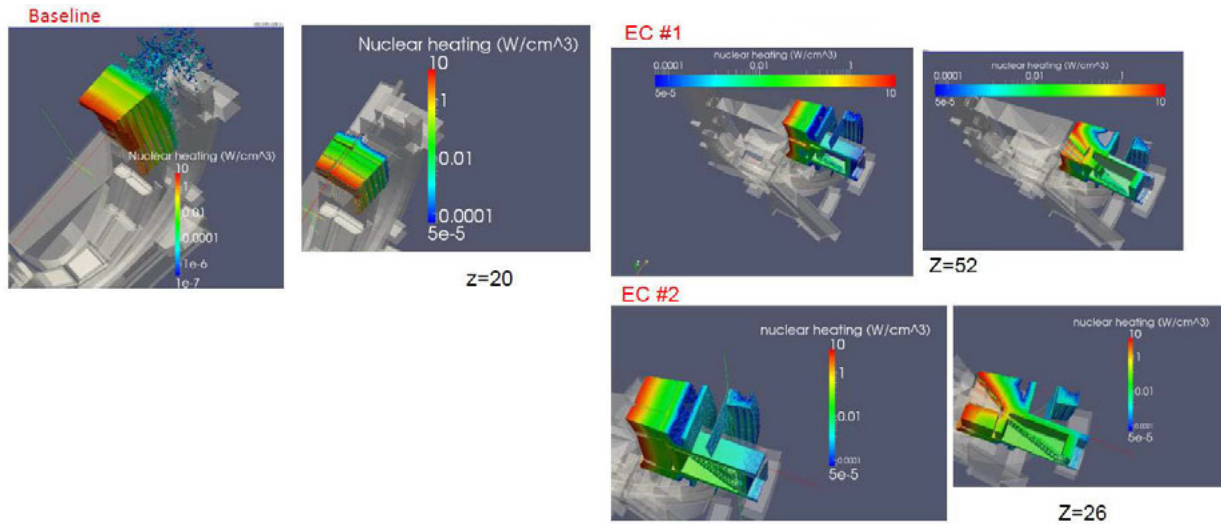


Fig. 4: Nuclear heating maps for Baseline, EC#1 and EC#2 – figures on the right show only NH above TF limit ($5 \times 10^{-5} \text{ W/cm}^3$).

In general, from the neutronics point of view, EC#1 is the preferable option because this configuration presents marginal shielding problems that can be solved with minimum efforts in shield design. Its drawback is the great impact on TBR due to the loss of 10xOB4 breeder modules. This can be mitigated considering an optimized integration in BB system, e.g. by locating the horizontal opening in toroidal gap between OB4 and OB5 and reducing the poloidal sizes of OB4 & OB5 modules impacted by EC.

EC#2 has the only advantage to have a minor impact on TBR. However the large conical opening implies too high neutron streaming and nuclear loads on surrounding components and great design modifications are needed to integrate this option.

References

- [1] X-5 Monte Carlo Team. MCNP - A General Monte Carlo N-Particle Transport Code, Version 5. Los Alamos National Laboratory, Los Alamos, New Mexico, US (2003).
- [2] R. Villari, D. Flammini. Neutron Transport analysis through openings in in-vessel components. Final Report WP PMI-3-3-T008 EUROfusion IDM 2MEP2U (2017)
- [3] F. Cismondi et al. Progress in EU-DEMO In-Vessel Components integration. *Fusion Engineering and Design*, 2017, , ISSN 0920-3796, <https://doi.org/10.1016/j.fusengdes.2017.03.147>
- [4] G. GROSSETTI et al. DEMO Port Plug Design and Integration studies. accepted on *Nuclear Fusion*.

ELECTRONIC EXCITATIONS IN SMALL OLIGOTHIOPHENE MOLECULES

Fabrizio Gala and Giuseppe Zollo *

Dipartimento di Scienze di Base e Applicate per l'Ingegneria, Università di Roma "La Sapienza", Via A. Scarpa 14–16, 00161 Rome Italy

ABSTRACT. First principles calculations based on density functional theory and many body perturbation theory have been employed to study the optical absorption properties of a newly synthesized oligo-thiophene molecule, with a quaterthiophene central unit, that has been designed for solution-processed bulk-heterojunction solar cells. To this aim we have employed the GW approach to obtain quasiparticle energies as a pre-requisite to solve the Bethe-Salpeter equation for the excitonic Hamiltonian. We show that inter-molecular transitions among the π -stacked poly-conjugated molecules explain the experimental absorption peak.

1 Introduction

Organic photovoltaic materials are currently considered for next-generation solar cells due to many appealing properties such as: low fabrication cost, solution processability, transparency and flexibility. Moreover, power conversion efficiencies (PCEs) of polymer based solar cells (PSCs) with bulk-heterojunction (BHJ) architecture have been greatly improved in the recent years [1].

A BHJ material is a solid state mixture of nano-structured donor and acceptor components[2]; light absorption at the donor generates strongly bound Frenkel-type excitons[3] that, at the donor-acceptor interface, are separated and generate the electrical current between the electrodes. While fullerene derivatives are commonly chosen as acceptors, the design and synthesis of efficient donor materials is still needed to improve the organic solar cells performances.

π -conjugated small molecules with with push-pull structure (i.e. with an electron-donating unit (D) central unit and electron-accepting (A) lateral units) are attracting as highly stable, pure and easy energy level design donors in BHJ solar cells with PCEs up to 9~10%[4, 5] but still lower than PSCs. They have been intensively investigated[6, 7] but a full quantitative understanding of the processes involved in the formation of excitons in such molecules (that might be also employed as donors in BHJ solar cells) is still lacking. Theoretical investigations are, thus, mandatory and require an accurate description of electron-hole (eh) interactions that can be achieved by using the GW approximation[8] and the Bethe-Salpeter equation (BSE)[9, 10], in the framework of many-body perturbation theory (MBPT) [11, 12, 13]. In this work we study the absorption peaks of the BT2N (with chemical formula $C_{44}H_{52}N_2O_4S_4$) oligomer-like molecule for organic solar cells [14].

*Corresponding author. E-mail: giuseppe.zollo@uniroma1.it.

2 Theory

The ground state electronic and geometric properties of the investigated systems have been obtained by density functional theory[15, 16] (DFT) with a generalized gradient approximation based on the Perdew-Burke-Ernzerhof formula[17](PBE) functional, and norm-conserving Troullier-Martins scheme[18] pseudopotentials. DFT calculations have been performed using the QUANTUM-ESPRESSO package[19] and the calculation parameters are fully detailed elsewhere [14].

Theoretical band gaps have been obtained with three different levels of accuracy: in the context of ground state DFT either as the difference between the lowest unoccupied molecular orbital (LUMO) and the highest occupied molecular orbital (HOMO) (simply referred as ε_{gap}), or as the difference between the electron affinity and the ionization potential $\varepsilon_{gap}^{\Delta SCF} = E_{N+1} - E_N - (E_N - E_{N-1})$ (the so called Δ -SCF method) [20], and lastly through the GW method that allows the calculation of the quasi-particle (QP) energies in the context of MBPT; the last task has been attained using the YAMBO code[21].

QP energies are computed at first order as:

$$\varepsilon_n^{QP} = \varepsilon_n^{(0)} + Z_n \langle n | [\Sigma(\varepsilon_n^{(0)}) - V_{xc}] | n \rangle \quad (1)$$

where $\varepsilon_n^{(0)}$ and $\langle \mathbf{x} | n \rangle = \phi_n(\mathbf{r})$ are the eigenvalues and eigenfunctions of the DFT hamiltonian respectively, and

$$Z_n = \left(1 - \left. \frac{\partial \Sigma_n}{\partial \omega} \right|_{\omega=\varepsilon_n^{(0)}} \right)^{-1} \quad (2)$$

where $\Sigma_n(\omega) = \langle n | \Sigma(\mathbf{r}_1 \mathbf{r}_2, \omega) | n \rangle$ is the Fourier transform of the dynamical electron self-energy operator. Within the GW approximation[22], $\Sigma(\mathbf{r}_1 \mathbf{r}_2, \omega)$ can be cast in terms of the ground state DFT Green's function $G(\mathbf{r}_1 \mathbf{r}_2, \omega)$ as:

$$\Sigma(\mathbf{r}_1 \mathbf{r}_2, \omega) = i \lim_{\eta \rightarrow 0^+} \int \frac{d\omega'}{2\pi} e^{i\omega'\eta} G(\mathbf{r}_1 \mathbf{r}_2, \omega - \omega') W(\mathbf{r}_1 \mathbf{r}_2, \omega') \quad (3)$$

with

$$W(\mathbf{r}_1 \mathbf{r}_2, \omega) = \int d\mathbf{r}_3 \frac{\epsilon^{-1}(\mathbf{r}_3 \mathbf{r}_2, \omega)}{|\mathbf{r}_1 - \mathbf{r}_3|} \quad (4)$$

the dynamically screened interaction, expressed in terms of the inverse dielectric function ϵ^{-1} of the system and of the bare Coulomb interaction V .

The inverse dielectric matrix is related to the response function $\chi(12) = \delta\rho(1)/\delta V_{ext}(2)$ (where (1) is a short-hand notation for (\mathbf{r}_1, t_1)) via the relation:

$$\epsilon^{-1}(12) = \delta(12) + \int d(3) \frac{\chi(32)}{|\mathbf{r}_1 - \mathbf{r}_3|} \quad (5)$$

In the RPA approximation, χ is related to the non-interacting response function $\chi^{(0)}(12) = G(12)G(21^+)$, through the Dyson-like equation [21]. Another common approximation for the screened interaction is the plasmon pole approximation (PPA)[23, 21], in which the imaginary part of W is assumed to be

peaked at the plasmon frequency; both methods (the GW-RealAxis and the GW-PPA schemes in the following), will be employed here.

A boxlike potential cutoff in the long-range Coulomb potential[21, 11] is used at this stage to simulate truly isolated molecular excited states.

Using the above obtained dynamically screened interaction, the macroscopic complex dielectric function that includes the excitonic effects is obtained by solving BSE in the electron-hole (e-h) space made of e-h pairs $|eh\rangle$ and antipairs $|\overline{he}\rangle$ with the two particle excitonic Hamiltonian[9, 10]:

$$\mathcal{H}^{\text{exc}} = \begin{bmatrix} H^{\text{res}} & H^{\text{coupl}} \\ -(H^{\text{coupl}})^* & -(H^{\text{res}})^* \end{bmatrix} \quad (6)$$

where the resonant term $H^{\text{res}} = (E_e - E_h)\delta_{e,e'}\delta_{h,h'} + \langle eh|K|e'h'\rangle$ is Hermitian, the coupling part $H^{\text{coupl}} = \langle eh|K|\overline{h'e'}\rangle$ is symmetric, and $K = W - 2V$ is the excitonic kernel (the reader is referred to [10] for a detailed explanation of the block terms in \mathcal{H}^{exc}).

The macroscopic dielectric function $\epsilon_M(\omega)$ is calculated from the eigenvalues E_λ and the eigenstates $|\lambda\rangle$ of \mathcal{H}^{exc} as:

$$\epsilon_M(\omega) = 1 - \lim_{\mathbf{q} \rightarrow 0} \lim_{\eta \rightarrow 0^+} \sum_{\lambda\lambda'} \sum_{n_1 n_2} \langle n_1 | e^{-i\mathbf{q}\cdot\mathbf{r}} | n_2 \rangle \frac{A_{n_1 n_2}^\lambda}{\omega - E_\lambda + i\eta} S_{\lambda\lambda'}^{-1} \sum_{n_3 n_4} (f_{n_3} - f_{n_4}) \langle n_4 | e^{i\mathbf{q}\cdot\mathbf{r}'} | n_3 \rangle (A_{n_3 n_4}^{\lambda'})^*$$

with $A_{nn'}^\lambda = \langle nn' | \lambda \rangle$, and $S_{\lambda\lambda'}$ is an overlap matrix of the generally non-orthogonal eigenstates of \mathcal{H}^{exc} .

Lastly we obtain the absorption spectra from the imaginary part of α_\parallel , the polarizability of the system along the leading dimension of BT2N system, calculated through the Clausius-Mossotti relations[13]:

$$\alpha_\parallel = \frac{3\Omega \epsilon_\parallel - 1}{4\pi \epsilon_\parallel + 2} \quad (7)$$

Experimental absorption curves are detailed elsewhere [14]

3 Results

Among the different BT2N isomers reported in Fig.1, DFT indicates as the ground state structure the one shown in Fig.1(a) with an almost planar geometry. The corresponding energy levels and the DFT band gap, have been reported in Table 1, together with experimental values taken from the literature [14].

Table 1: DFT-PBE HOMO-LUMO energies, together with the experimental band gap values [14] for the single BT2N isolated molecule and for two π -stacked BT2N molecules (in parenthesis)

Molecule	ϵ_{HOMO} (eV)		ϵ_{LUMO} (eV)		ϵ_{gap} (eV)	
	DFT-PBE	Exp	DFT-PBE	Exp	DFT-PBE	Exp
BT2N	-4.96 (-4.56)	-4.49	-3.57 (-3.27)	-3.47	1.39 (1.30)	2.02

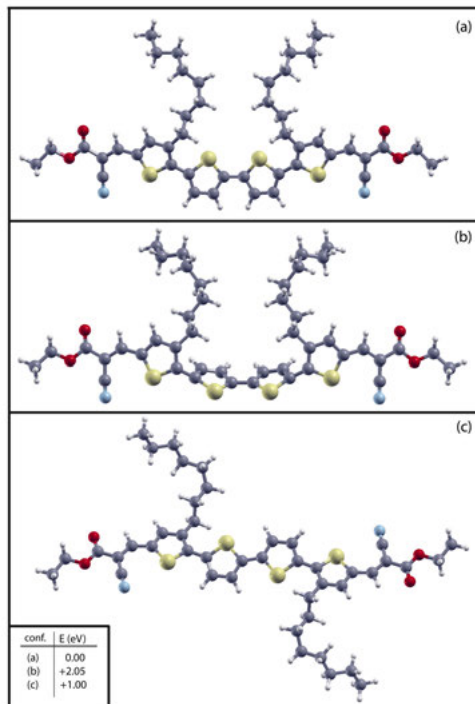


Figure 1: (Color online) Different ground state configurations studied for the single BT2N molecule, together with the relative energies with respect the most stable one.

The BT2N chemical structure suggests a typical acceptor-donor-acceptor (A-D-A) configuration even though it is not marked probably because of the reduced length size of the molecule [14].

As expected, the HOMO-LUMO gap is largely underestimated (being nearly of 1.39 eV) at the DFT-PBE level with respect to the experimental value (see Table 1).

The correct theoretical band gap obtained from Δ -SCF and the quasi-particle band gaps, calculated by GW (with either GW-RealAxis or GW-PPA approximation), are in nice accordance between them (see Table 2) indicating that the computational scheme adopted for GW is correct.

Table 2: Band Gaps (in eV) for the BT2N structures studied obtained with three different computational schemes.

Structure	GW-RealAxis	GW-PPA	Δ -SCF
BT2Nx1	3.84	3.93	3.89
BT2Nx2	3.52	3.60	3.33

The obtained results, however, are much larger than the experimental band gap that is a clear sign of the leading role of excitons in the BT2N molecule that will affect markedly the optical absorbance phenomena too.

The quasi-particle energy levels obtained for both the GW-PPA and the GW-RealAxis are compared to

the DFT-PBE eigenvalues and are shown in Fig.2(c) in the energy range [-1.5 eV, 2.eV] from the HOMO level considered as a reference value at 0 eV. The optical absorption spectrum has been calculated by

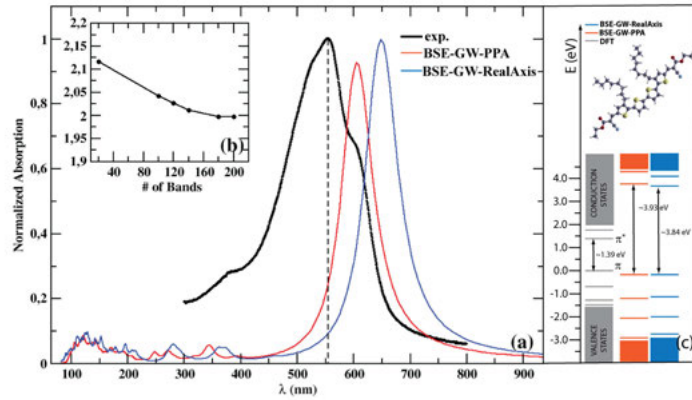


Figure 2: (Color online) Normalized absorption spectra for BT2N molecule, for light polarized parallel to the main axis of the molecule (a). In (b) benchmark of the main peak position as a function of the electron states included in the construction of the excitonic hamiltonian \mathcal{H}^{exc} defined in (6), while in (c) QP corrections to DFT-PBE electron eigenvalues in an energy window ranging from -1.5 eV below to +2.0 eV above the e HOMO level. An artificial Lorentzian broadening of 100 meV has been imposed. The curves are normalized to the maximum of the GW-RealAxis+BSE.

solving the BSE from both GW-PPA and GW-RealAxis energy levels; our results are shown in Fig.2(b) together with the experimental absorption spectrum of a BT2N thin-film [14]. GW+BSE absorption peaks are clearly red-shifted with respect to the experimental ones by nearly $\Delta\lambda \sim 50$ nm /GW-PPA) and $\Delta\lambda \sim 100$ nm (GW-RealAxis). Moreover the GW+BSE spectra do not reproduce the experimental second peak at 600 nm.

A strong exciton, with high excitonic binding energy (1.92 eV and 1.96 eV for GW-PPA+BSE and GW-RealAxis+BSE, respectively) is found being related to the single particle $\pi \rightarrow \pi^*$ transition from the HOMO to the LUMO levels.

In a thin-film solid state phase, molecular packing is expected to play a key role in the optical properties measured and, hence, the adsorption spectrum obtained from two stacked molecules has been calculated[24, 25, 5]. After structural relaxation the electronic structure of the system shows a DFT band gap of 1.3 eV, slightly smaller than the one obtained for the isolated molecule; this fact is due to the splitting into two states of the HOMO π state (one for each molecule) as reported in Fig.4(c). Another remarkable difference with respect to the single isolated BT2N molecule case is that the HOMO and the LUMO do not lie anymore on the same molecule (see Fig.3(b) and (c)) suggesting that the HOMO-LUMO optical transition may be accompanied by an electron charge transfer between the two molecules that might change the transition energy with respect to the isolated molecule.

GW corrections to DFT-PBE energies, with both GW-RealAxis and GW-PPA schemes, result in a gap opening ($\varepsilon_{gap}^{OP} = 3.6$ eV for GW-RealAxis and 3.5 eV for GW-PPA) that is, again, close to the Δ -SCF value of 3.3 eV (see Table 2). The calculated energy gap values again still overestimate markedly the experimental band gap measured by CV thus confirming the leading role of the excitonic phenomena that must be considered in order to explain the experimental results.

The optical absorption spectrum is calculated for the π stacked configuration by solving again the BSE

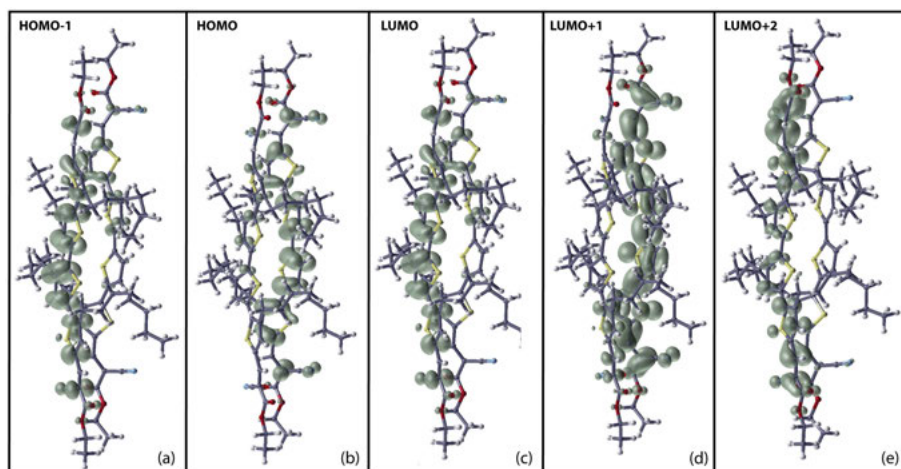


Figure 3: (Color online) Isosurface plots of $||\psi(\mathbf{r})||^2$ for the DFT calculated HOMO-1, HOMO, LUMO, LUMO+1, and LUMO+2 orbitals in (a), (b), (c), (d), and (e) respectively; isosurfaces have been set to $\sim 5\%$ of the corresponding maximum values in order to evidence their symmetry properties.

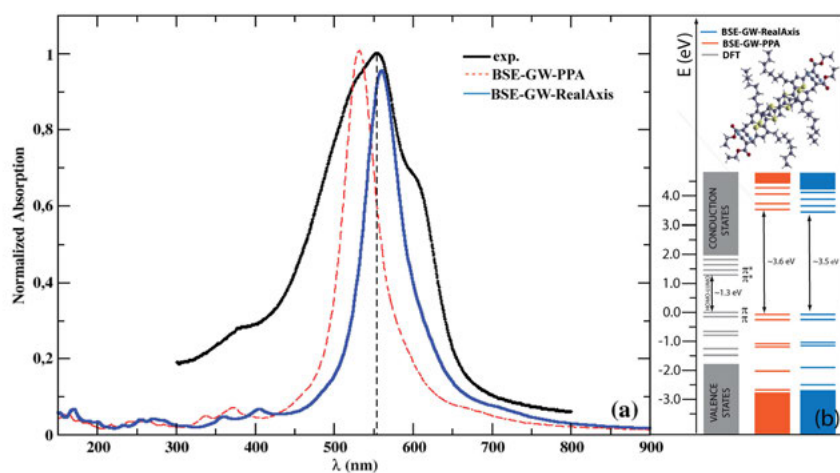


Figure 4: (Color online) Normalized absorption spectra for two π conjugated BT2N molecules, for light polarized parallel to the main axis of the molecule (a), while in (b) QP corrections to DFT-PBE electron eigenvalues in an energy window ranging from -1.5 eV below to +2.0 eV above the e HOMO level. As for the single molecule case absorption curves have been obtained by imposing an artificial Lorentzian broadening of 100 meV and they are normalized to the maximum value of the curve obtained by GW-PPA+BSE.

starting from both GW-PPA and GW-RealAxis energy levels. Our results are shown in Fig.4(a) where it can be seen that, now, the obtained theoretical curves are in close agreement with the experimental absorption spectrum, especially concerning the GW-RealAxis approximation that is the highest level of theory here adopted; indeed the absorption peak predicted in this case is located at 558 nm that is just 4 nm away from the experimental peak position measured at the wavelength of 554 nm.

A better understanding of the excitonic nature of the optical transitions can be obtained by looking at the eigenvalues and eigenvectors of the excitonic Hamiltonian and obtained with a reduced Lorentzian broadening η of Eq.(7) in the GW-RealAxis scheme (see Fig. 5). It appears clearly that the main experimental absorption peak is due to the formation of two nearly degenerate excitons ((b) and (c) peaks in Fig. 5) with binding energies of 1.34 eV and 1.29 eV respectively. A careful inspection of the \mathcal{H}^{exc} eigenstates evidences that the e-h transition corresponding to the (b) peak is the HOMO \rightarrow LUMO+2 transition with the two states located at two different BT2N molecules thus involving a marked charge transfer (CT) between the stacked molecules.

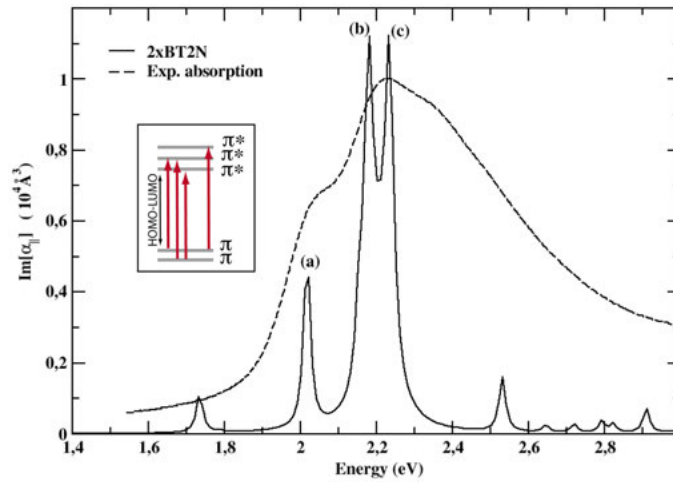


Figure 5: (Color online) $\text{Im}[\alpha_{\parallel}]$ obtained from Eq.(7) with a Lorentzian broadening of 10 meV compared with the normalized absorption spectrum. In the inset the electron-hole transitions that weight more than 10% in the excitonic states (a) (b) and (c) are schematically represented.

The other contribution to the main absorption peak is the e-h eigenstate at (c) that arises from three transitions the HOMO-1 \rightarrow LUMO, the HOMO-1 \rightarrow LUMO+1, and the HOMO \rightarrow LUMO+1, the second one involving the two molecules (see Fig.3).

In Fig.5 a third peak at 2.02 eV is present, that again represents an exciton state with binding energy of 1.50 eV of lower optical strength with respect the (b) and (c) states; this feature is also present in the experimental curve, showing again that a strong hybridization between excitonic states on different molecules is the key for a better understanding of the optical properties of BT2N thin-films and small conjugated molecules in general.

4 Conclusions

In summary we have calculated in the context of the MBPT, using the GW approximation and the BSE for the excitonic Hamiltonian, the absorption spectra of two different systems made either of one

isolated BT2N molecule or two π conjugated BT2N molecules. To this aim, we have tested two different levels of approximations, namely the GW-PPA and the GW-RealAxis. Theory has been compared to the experimental absorption spectrum evidencing, first of all, the excitonic nature of the measured absorption onset and main peak. The experimental peak is completely recovered once the π conjugated geometry of BT2N molecules is considered as a possible organization pattern of oligo-thiophene molecules in the solid state. The analysis of the of the e-h transitions that contribute to the main absorption peak evidences the important role played by the inter-molecular optical transition in explaining the observed absorption behavior. Therefore, the importance of the π conjugation between the molecules is put in evidence in our study showing that the absorption properties of such molecules are tightly related to the way they are arranged in the matrix of organic solar cell device.

Acknowledgements

Computational resources have been provided by CRESCO/ENEAGRID High Performance Computing infrastructure and its staff [26]. CRESCO/ENEAGRID High Performance Computing infrastructure is funded by ENEA, the Italian National Agency for New Technologies, Energy and Sustainable Economic Development and by Italian and European research programmes, see <http://www.cresco.enea.it/english> for information.

References

- [1] L. Dou, J. You, Z. Hong, Z. Xu, G. Li, R.A. Street, and Y. Yang. 25th anniversary article: A decade of organic/polymeric photovoltaic research. *Adv. Mater.*, 25:6642–6671, 2013.
- [2] A.J. Heeger. 25th anniversary article: Bulk heterojunction solar cells: Understanding the mechanism of operation. *Adv. Mater.*, 26:10–28, 2014.
- [3] J.-L.-Brédas, J.E. Norton, J. Cornil, and V. Coropceanu. Molecular understanding of organic solar cells: The challenges. *Acc. Chem. Res.*, 42(11):1691–1699, 2009.
- [4] Q. Zhang, B. Kan, F. Liu, G. Long, X. Wan, X. Chen, Y. Zuo, W. Ni, H. Zhang, M. Li, Z. Hu, F. Huang, Y. Cao, Z. Liang, M. Zhang, T. P. Russel, and Y. Chen. Small-molecule solar cells with efficiency over 9%. *Nature Photonics*, 9:35–41, 2015.
- [5] B. Kan, M. Li, Q. Zhang, F. Liu, X. Wan, Y. Wang, W. Ni, G. Long, X. Yang, H. Feng, Y. Zuo, M. Zhang, F. Huang, Y. Cao, T. P. Russel, and Y. Chen. A series of simple oligomer-like small molecules based on oligothiophenes for solution-processed solar cells with high efficiency. *J. Am. Chem. Soc.*, 137:3886–3893, 2015.
- [6] H. Bai, Y. Wang, P. Cheng, Y. Li, D. Zhu, and X. Zhan. Acceptor-donor-acceptor small molecules based on indacenodithiophene for efficient organic solar cells. *ACS Appl. Mater. Interfaces*, 6(11):8426–8433, 2014.
- [7] Y. Sun and G.C. Welch, W.L. Lin Leong, C.J. Takacs, and G.C. Bazan. Solution-processed small-molecule solar cells with 6.7% efficiency. *Nature Materials*, 11:44–48, 2012.
- [8] L. Hedin. New method for calculating the one-particle green's function with application to the electron-gas problem. *Phys. Rev.*, 139:A796–A823, 1965.

- [9] M. Rohlfing and S. G. Louie. Electron-hole excitations and optical spectra from first principles. *Phys. Rev. B*, 62(8):4927–4943, 2000.
- [10] G. Onida, L. Reining, and A. Rubio. *Rev. Mod. Phys.*, 74:601–659, 2002.
- [11] M. Palumbo, C. Hogan, F. Sottile, P. Bagalá, and A. Rubio. Ab initio electronic and optical spectra of free-bas porphyrins: The role of electronic correlation. *J. Chem. Phys.*, 131:084102, 2009.
- [12] B. Baumeier, D. Andrienko, Y. Ma, and M. Rohlfing. Excited states of dicyanovinyl-substituted oligothiophenes from many-body Green's functions theory. *J. Chem. Theory Comput.*, 8:997–1002, 2012.
- [13] C. Hogan, M. Palumbo, J. Gierschner, and A. Rubio. Correlation effects in the optical spectra of porphyrin oligomer chains: Exciton confinement and length dependence. *J. Chem. Phys.*, 138:024312–1/024312–12, 2013.
- [14] F. Gala, L. Mattiello, F. Brunetti, and G. Zollo. Electronic excitations in solution-processed oligothiophene small-molecules for organic solar cells. *The Journal of Chemical Physics*, 144(8):084310, 2016.
- [15] P. Hohenberg and W. Kohn. Inhomogeneous electron gas. *Phys. Rev.*, 136:B864–B871, Nov 1964.
- [16] W. Kohn and L. J. Sham. Self-consistent equations including exchange and correlation effects. *Phys. Rev.*, 140:A1133–A1138, Nov 1965.
- [17] J.P. Perdew, K. Burke, and M. Ernzerhof. Generalized gradient approximation made simple. *Phys. Rev. Lett.*, 77(4):3865–3868, 1996.
- [18] N. Troullier and J.L. Martins. Efficient pseudopotentials for plane-wave calculations. *Phys. Rev. B*, 43(14):1993–06, 1991.
- [19] P. Giannozzi, S. Baroni, N. Bonini, M. Calandra, R. Car, C. Cavazzoni, D. Ceresoli, G. L. Chiarotti, M. Cococcioni, I. Dabo, A. Dal Corso, S. de Gironcoli, S. Fabris, G. Fratesi, R. Gebauer, U. Gerstmann, C. Gougoussis, A. Kokalj, M. Lazzeri, L. Martin-Samos, N. Marzari, F. Mauri, R. Mazzarello, S. Paolini, A. Pasquarello, L. Paulatto, C. Sbraccia, S. Scandolo, G. Sclauzero, A. P. Seitsonen, A. Smogunov, P. Umari, and R. M. Wentzcovitch. Quantum espresso: a modular and open-source software project for quantum simulations of materials. *J. Phys.: Condens. Matter*, 21(19):395502–1–19, 2009.
- [20] R. M. Martin. *Electronic Structure: Basic Theory and Practical Methods*. Cambridge University Press, 2008.
- [21] A. Marini, C. Hogan, M. Grüning, and D. Varsano. *Comput. Phys. Comm.*, 180:1392–1403, 2009.
- [22] L. Hedin and S. Lundqvist. *Solid State Physics: Advances in Research and Application*. Academic Press: New York, San Francisco, London, 1969.
- [23] F. Aryasetiawan and O. Gunnarsson. The gw method. *Rep. Prog. Phys.*, 61:237–312, 1998.
- [24] K. Gierschner, M. Ehni, H.-J. Egelhaaf, B. M. Medina, D. Belhonne, H. Benmansour, and G. C. Bazan. Solid-state optical properties of linear polyconjugated molecules: π -stack contra herringbone. *J. Chem. Phys.*, 123:144914–1–144914–9, 2005.

- [25] R. Fitnzer, E. Reinold, A. Mishra, E. Mena-Osteritz, H. Ziehlke, C. K'orner, K. Leo, M. Riedde, M. Weil, O. Tsaryova, A. Weiss, C. Urich, and M. Pfeiffer abd P. B'auerle. Dicyanovil-substituted oligothiopenes: Structurer-property relationship and application in vacuum processed small-molecule organic solar cells. *Adv. Func. Mater.*, 21:897–910, 2011.
- [26] G. Ponti, F. Palombi, D. Abate, F. Ambrosino, G. Aprea, T. Bastianelli, F. Beone, R. Bertini, G. Bracco, M. Caporicci, B. Calosso, M. Chinnici, A. Colavincenzo, A. Cucurullo, P. dAngelo, M. De Rosa, P. De Michele, A. Funel, G. Furini, D. Giammattei, S. Giusepponi, R. Guadagni, G. Guarnieri, A. Italiano, S. Magagnino, A. Mariano, G. Mencuccini, C. Mercuri, S. Migliori, P. Ornelli, S. Pecoraro, A. Perozziello, S. Pierattini, S. Podda, F. Poggi, A. Quintiliani, A. Rocchi, C. Scio, F. Simoni, and A. Vita. The role of medium size facilities in the hpc ecosystem: the case of the new cresco4 cluster integrated in the eneagrid infrastructure. *IEEE HPCS*, 6903807:1030–1033, 2014.

MONTE CARLO SIMULATIONS SUPPORTING SAFETY STUDIES OF PWR'S AND IRRADIATION TESTS IN TAPIRO RESEARCH REACTOR

Patrizio Console Camprini^{1*} and Kenneth W. Burn¹

¹ *ENEA, Fusion and Technology for Nuclear Safety and Security Department, 40129, Bologna, Italy*

Abstract. In the framework of the Development of Expertise in Nuclear Safety, studies are carried out within the Project B.3.1 funded by the Italian Ministry of Economic Development – Annual Plan 2015. Evaluations concerned mainly the following topics: Nuclear Safety analyses for Gen-II and Gen-III PWR's, preliminary studies supporting some irradiation campaigns in TAPIRO research reactor. PWR reactor evaluations have been carried out working on the MCNP6.1 code source to define a custom fixed neutron source, in order to reproduce a pin-by-pin description of the fundamental mode of the core neutron flux. Moreover, the TAPIRO research reactor – located in ENEA Casaccia research center – was proposed as a facility for integral irradiation experiments of minor actinides, in the framework of an OECD-NEA working group on nuclear waste management. Thus, simulations are conducted preparing these tests, mainly concerning fission and absorption reaction rates in actinide samples placed in the experimental channels of the core and the reflector.

1 Fission Source Definition for Gen-II and Gen-III PWR'S

Monte Carlo simulations for nuclear reactor cores are performed with the MCNP6.1 [1] code in order to obtain either integral or differential responses regarding the system. Safety studies usually require the evaluation of detailed scores relating to flux or fluence at specific positions. Considerable efforts are made in implementing variance reduction techniques, since only a relatively few channels in phase space need to be sampled, as far as the simulation objectives are concerned.

In this context, the requested results are flux or general response functions at particular positions outside the vessel and far from the core. These locations mainly concern activation calculations and doses to electronic equipment, which is involved in on-line diagnostics and control, both for normal operation and during accidents. The vessel dose due both to neutron and gamma radiation is a relevant parameter as well.

Moreover, the volumes and surfaces at which these responses are applied are relatively small, compared to the system dimensions. Thus, this kind of Monte Carlo analysis has to be carried out employing so-called deep penetration problem techniques and a consistent application of variance reduction methods is necessary.

Within the present work, firstly a fixed neutron source is defined inside the core and obtained by sampling the fundamental mode - treating a previous eigenvalue problem and scoring neutron production on a particular axial binning and on a pin-by-pin pattern. Ex-core responses are then studied with the flux distributed according to the fundamental mode in a fixed source problem, aiming at all the specific tallies requested by the needs of safety analysis. This approach utilises a

fixed pin-by-pin volumetric source in which the energy and direction distributions are set according to neutron generation from fission [2].

In order to support this analysis of Gen-II and the Gen-III PWR's, the calculation method and the cross-sections utilised within this study have been verified on an experimental benchmark provided in the framework of OECD-NEA reactor shielding benchmark group SINBAD. The selected case is the PCA-Replica experiment (NEA-1517/93), performed at Winfrith at the NESTOR research reactor (see Fig.1). Here, a highly enriched fissile plate - outside the reactor core - is the neutron source that irradiates a multilayer neutronic system composed as follows: a water slab simulating the inner vessel coolant, a thermal shield specimen made of stainless steel, a second water layer, a mild steel vessel slab and then a void chamber.

Dosimeters are placed along the central axis of the system at different distances from the fission plate through the material layers. They provided measurements of both flux and neutron spectrum at several positions: 10 locations for various neutron dosimetric responses and 2 locations for the spectrum (Fig. 2).

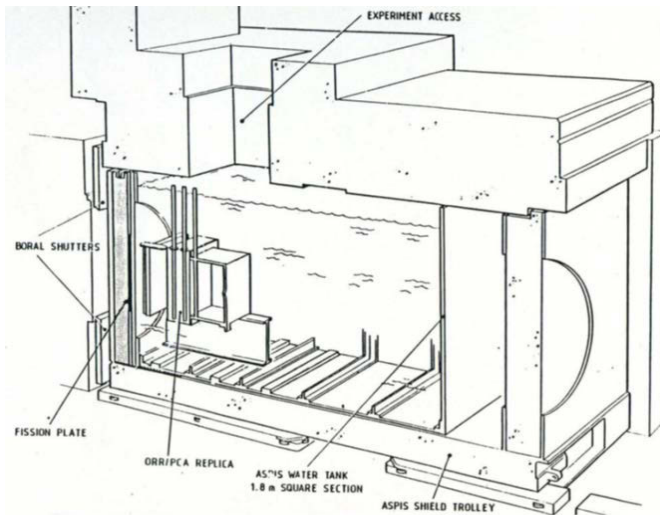


Fig.1: PCA-Replica irradiation facility.

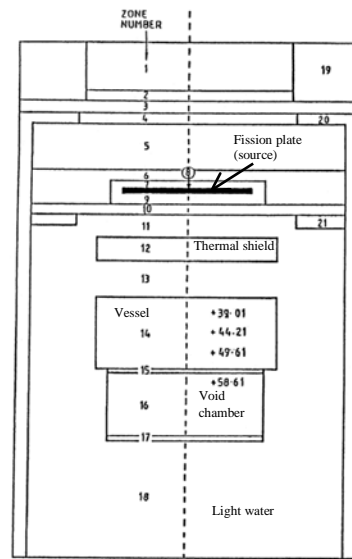


Fig.2: PCA-Replica calculation scheme.

The geometry and material definition have been modelled as well as all the problem responses to be compared with the experimental data through dosimeter readings. The following nuclear data sets have been tested for particle transport: ENDF/B-VI.6, ENDF/B-VII.1, JEFF-3.1, JEFF-3.1.2, JEFF-3.2 and JENDL-4.0. In addition, some dosimetry files data have been employed: 531DOS, 532DOS, LLLDOS, IRDF2002 and IRDFv1.05.

The DSA variance reduction method has then been utilised in support of the MCNP6.1 code to provide detector responses, at the various distances from the fission source. The obtained results are consistent with the experimental data and the performed calculation has been considered a methodological validation of the simulation data and procedure [3].

Concerning the Gen-II and Gen-III reactor cores, the preparation of the source and its relative implementation is performed by an in-house patch of the MCNP source code as well as some modifications to message passing routines for the particle sampling and the broadcasting to all the calculation nodes. The fixed source simulation is launched instead of the eigenvalue problem, thus further fission reactions are suppressed and considered as absorption events.

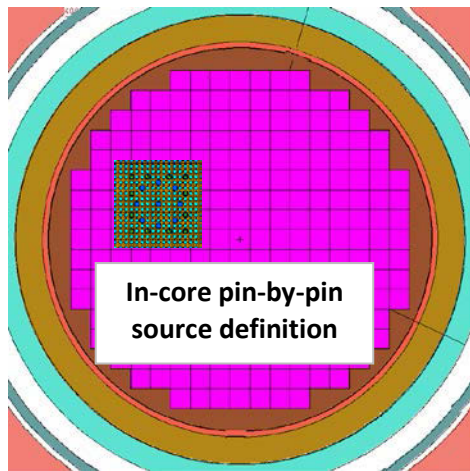


Fig.3: PWR reactor core cross-section.
(fuel assembly – FA – cross-section is highlighted)

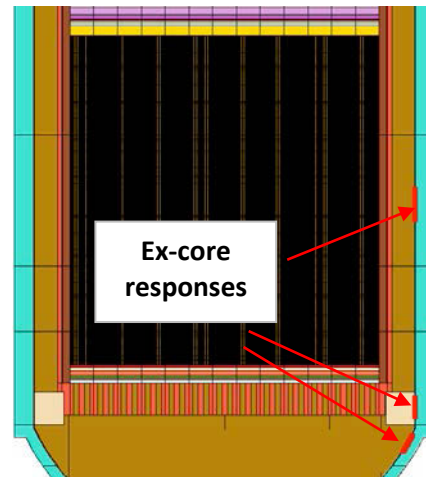


Fig.4: PWR reactor vessel, vertical section.

The maximization of the figure of merit for a single or for multiple responses produces the variance reduction parameters: they can be expressed in weight window form to easily utilise the MCNP calculational facility [4].

The framework of the work is the Project B.3.1 funded by the Italian Ministry of Economic Development – Annual Plan 2015 – about the Development of Expertise in Nuclear Safety. In particular Subproject A2 [5].

2 Evaluations of TAPIRO Reactor Irradiation Campaign

Within the NEA Expert Group dealing with Integral Experiments for Minor Actinides Management (EGIEMAM), the TAPIRO research reactor has been proposed as a relevant facility for integral experiments with a fast fission spectrum (Fig. 5). In fact, the feasibility of the fuel cycle of future Gen-IV nuclear reactors is strongly dependent on their capability of managing and burning a significant amount of minor actinides currently produced by light water reactors (PWR and LWR), avoiding long-term storage issues. In order to evaluate this aspect, a collaboration between ENEA and the French Atomic Energy Commission (CEA) has been established and some irradiation campaigns have been prepared with the aim of irradiating samples of minor actinides inside the TAPIRO research reactor at the Casaccia, ENEA Research Center.

The Monte Carlo MCNP6.1 code has been used to represent 3D geometry and the continuous-energy reaction cross-sections. The nuclear data library utilized is JEFF3-1 provided by the NEA Data Bank and processed at a temperature of 300 K. The normalization of the model is made at the flux peak according to standard reference [6]. The considered operative thermal power was 5 kW and the corresponding peak of the total neutron flux (at the core centre) was $3.00 \cdot 10^{12}$ n/cm²/s.

The simulation considered the following irradiation channels: the diametrical channels (1 and 2), the tangential channel and the radial channel 1 (see Fig.6).

The DSA variance reduction methodology has been utilised in this context mainly to enhance the precision of the results, particularly in irradiation positions far from the reactor core [7].

The framework of the work is the Project B.3.1 funded by the Italian Ministry of Economic Development – Annual Plan 2015 – concerning the Development of Expertise in Nuclear Safety, and in particular Subproject A1 [8].

The samples provided by CEA are planned to be irradiated inside the TAPIRO experimental channels during the AOSTA campaign, aiming at performing both fission and capture cross-section measurements for the following interesting actinide nuclides, prepared in a ceramic matrix (Tab. 1):

Table 1: Fissile and fissionable nuclides in AOSTA irradiation campaign at TAPIRO reactor.

^{235}U	^{239}Pu	^{241}Am	^{243}Cm
^{238}U	^{240}Pu	^{243}Am	^{244}Cm
^{237}Np	^{242}Pu		^{245}Cm

The modifications and the patches applied to MCNP6.1 code source are written in Fortran90 – according to the language in which MCNP is developed – and compiled within CRESCO environment through gnu gcc suite for standalone applications and through the intel-12 compiler for building the MCNP binary. MPI distribution is openmpi according to flavour 1.5.4 (intel-12).



Fig.5: The TAPIRO facility hall.

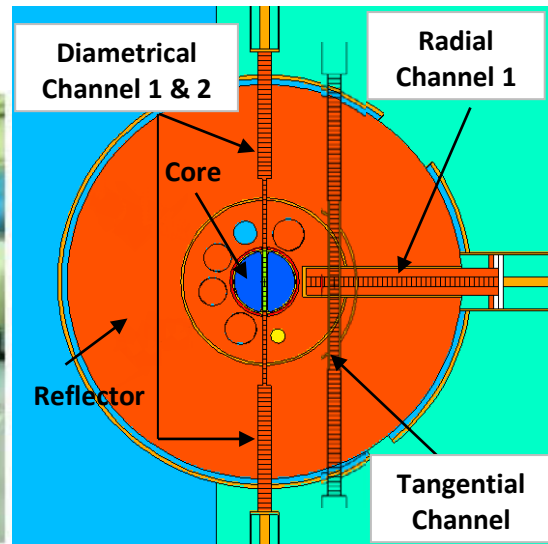


Fig.6: The TAPIRO MCNP model, half-core plane and channels subdivided in cells for responses (in reality tangential channel is positioned at different depth)

Acknowledgement

The work on Gen-II and III PWR's was carried out in close collaboration with l'Institut de Radioprotection et de Sûreté Nucléaire (IRSN). In particular, IRSN supplied the MCNP geometric models and the responses of interest: for this the authors would like to thank Mariya Brovchenko and Isabelle Duhamel.

All the information to perform the simulations supporting irradiation in TAPIRO reactor have been provided by Valentina Fabrizio and the ENEA colleagues of the research reactor laboratory team (FSN-FISS-RNR), under the guidance of Mario Carta.

References

- [1] J.T. Goorley et al., “Initial MCNP6 Release Overview - MCNP6 version 1.0”, LA-UR-13-22934 (2013).
- [2] M. Brovchenko et al. “Neutron-gamma flux and dose calculations in a Pressurized Water Reactor (PWR)”, *International Conference on Radiation Shielding (ICRS13)*, Paris, 3-6 Oct 2016
- [3] P. Console Camprini and K.W. Burn, “Calculation of the NEA-SINBAD Experimental Benchmark: PCA-Replica”, ENEA Report SICNUC-P000-014
- [4] K.W. Burn, “Optimizing Monte Carlo to Multiple Responses: The Direct Statistical Approach, 10 Years On”, *Nuclear Technology*, 175:1, 138-145, (2011)
- [5] K.W. Burn and P. Console Camprini, “Development and Application of Monte Carlo Neutronics Methodologies for Safety Studies of Current Operating Reactors”, ENEA Report ADPFISS-LP1-079
- [6] M. Carta et al. "TRIGA RC-1 and TAPIRO, ENEA Research Reactors", ENEA, Italian National Agency for New Technologies, Energy and Sustainable Economic Development C.R Casaccia, Vienna, June 10-12, 2013.
- [7] K.W. Burn and P. Console Camprini, “Radiation transport out from the reactor core: to decouple or not to decouple”, *International Conference on Radiation Shielding (ICRS13)*, Paris, 3-6 Oct 2016
- [8] M. Carta et al. “TAPIRO: feasibility study of minor actinides irradiation campaign”, ENEA Report ADPFISS-LP2-083-rev01 509(A), Ottawa (2013).

NUCLEAR RESPONSES IN THE ITER IVVS PORT CELL

Davide Flammini^{*1}, Fabio Moro¹ and Rosaria Villari¹

¹ENEA, Fusion Department, ENEA C. R. Frascati, via E. Fermi 45, 00044 Frascati (Roma), Italy

ABSTRACT. The ITER In-Vessel Viewing System (IVVS) consists of six identical units located at the B1 level of the Tokamak complex, at lower ports 3, 5, 9, 11, 15 and 17. It can be used for visual inspection of the plasma chamber in between plasma pulses. The IVVS extends from the VV up to the port cell (PC): in this work relevant nuclear quantities in the PCs hosting the IVVS have been calculated by means of the MCNP Monte Carlo code in a full 3-D geometry, including the IVVS and its shielding blocks. A comprehensive MCNP model of the PC has been developed including a detailed description of the Bioshield plug, pipes, penetrations, cask rails and PC door. The radiation field in the PC includes the radiation from the plasma (at about ≈ 10 m from it) and the radiation from the activated water flowing in the PC pipes. Large computational effort was needed to achieve statistical significant results and different techniques have been used to transport particles from the plasma up to the PC. Relevant nuclear quantities in PC have been calculated: neutron and gamma fluxes, absorbed dose on sensitive components over the ITER lifetime and the shutdown dose rate distribution at 1 day after shutdown.

1 Introduction

The ITER in-vessel viewing system (IVVS) is an ITER diagnostic for visual examinations of plasma-facing components. It is located at the outboard lower level of the vacuum vessel (VV). When not in use, it is housed inside a dedicated port extending from the VV outer wall to the port cell (PC). The final design of the IVVS must fulfil specific operational requirements: in particular, the occupational exposure imposes that the shutdown dose rate (SDDR) in the PC, where in-situ maintenance activities are foreseen, does not exceed 10 $\mu\text{Sv/h}$ 24 hours after shutdown. Also electronic component will be located in the PC, so an evaluation of the radiation field inside the PC is needed. The aim of this work is to perform nuclear analyses in the PC hosting the IVVS system. Calculations include both the neutron streaming through the Bioshield plug and the neutron and photon emission from activated water source flowing in the Primary Heat Transfer System (PHTS) pipes in the PC and in its vicinity. A comprehensive and detailed MCNP model of the PC has been developed including detailed description of the Bioshield plug, pipes, penetrations, cask rails and PC door. Neutron and photon fluxes, absorbed dose integrated over the ITER lifetime on sensitive electronic components and SDDR at 1 day after shutdown have been evaluated. The CAD model used to build the MCNP model is reported in Fig. 1

2 Procedures and code

The nuclear analyses have been carried out with MCNP5 [1] and MCNP6 [2], using the FENDL 2.1 nuclear data library [3]. The preparation of the neutronic CAD model has been accomplished using the SpaceClaim Engineering 2015+ software [4]. The conversion from CAD to MCNP geometry has been performed using MCAM 5.2 [5]. MCNP simulations have been performed using the multiprocessors MPI capability on the CRESCO4 cluster.

* Corresponding author. E-mail: davide.flammini@enea.it.

Due to the large number of radiation sources, the complexity of the model and the statistical uncertainty required, the whole set of calculations includes 13 runs with typical computing time of 2×10^7 s for 3×10^9 source particles per run on 256 processors. This computational time does not include all the calculations performed for preliminary calculations, verification of the models and setting up of simulations parameters. An estimation of the total amount of computational time used is about a factor 3 larger.. The outputs of the calculations can be estimated to be about 10 Gb of data that have then been analysed to produce the desired results. In the following the main results of this study will be presented.

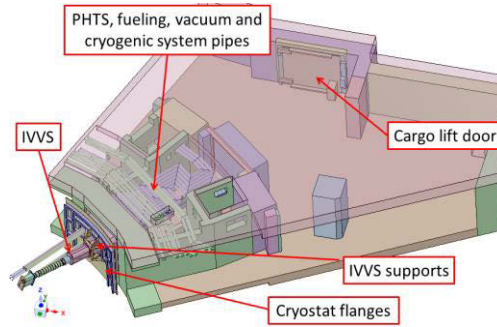


Fig.1: Simplified CAD model of the PC and the IVVS.

The PC at the B1 level of the tokamak building is located outside the bioshield, so very far from the plasma (≈ 10 m far from the first wall). At this large distance from the plasma, radiation transport calculations and, in particular, SDDR assessment require large computational efforts. In order to provide statistically reliable results in PC and gallery, the neutron emission from plasma has been transported up to the bioshield and then by means of a secondary source, transported into the PC. In order to have a careful evaluation of the SDDR, a strategy has been adopted which combines the use of R2Smesh [6] and Advanced D1S [7] methods and four distinct secondary sources located at the bioshield plug. The shutdown dose rate has been calculated considering the SA2 irradiation scenario [8].

3 Results

During ITER operations there will be two contributions to the neutron flux: the neutron radiation from the plasma and neutrons emitted by the ^{17}N decay from activated water. In Fig. 2 the neutron flux maps inside the PC due to irradiation from the plasma and due to ^{17}N decay are shown, in a vertical section passing through the IVVS.

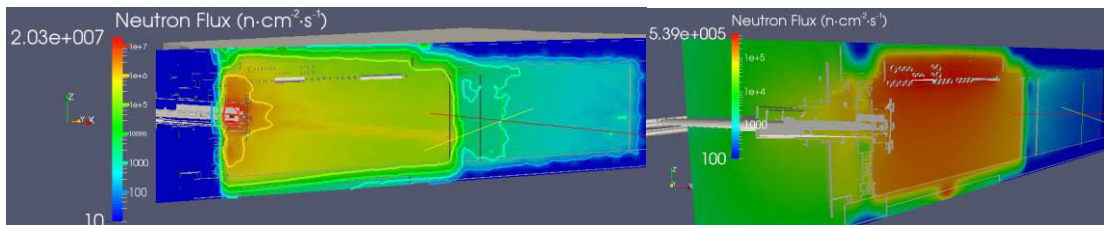


Fig.2: Neutron flux distribution in the PC due to the neutron radiation from the plasma (left) and emission from ^{17}N decay (right)

A hot zone has been found at the closure plate of the IVVS where the flux is maximum, and is approximately $10^7 \text{ n}\cdot\text{cm}^{-2}\cdot\text{s}^{-1}$, due to streaming through the IVVS penetration, for plasma neutrons. The relative statistical error is below 10% inside the PC. ^{17}N decay neutrons are emitted from the PHTS divertor pipes, located just below the ceiling and from the Lower Pipe Chase (LPC) located below the floor. The maximum neutron flux is approximately $10^6 \text{ n}\cdot\text{cm}^{-2}\cdot\text{s}^{-1}$, about an order of magnitude lower than the peak value of neutron flux from plasma. The photon flux during operation is dominated by the contribution of the ^{16}N decay photon emission inside the PC. The ^{16}N decay has a photon source strength which is more than 3 orders of magnitude larger than that of the ^{17}N neutron emission. As a result, the maximum photon flux observed in the PC is of the order of $10^9 \gamma\cdot\text{cm}^{-2}\cdot\text{s}^{-1}$, as shown in Fig. 3. Instead, the photon flux due to the interaction of plasma neutrons with PC is approximately 4 orders of magnitude smaller than photons flux from ^{16}N . The photon flux is found to be still high in the gallery, close to the ceiling, due to the penetration through the lintel of the PC door. The lintel has been modelled leaving the holes for cables empty: this produces a high penetration of radiation from the PC to the gallery. The effect is clearly visible in the radiation maps, also because the pipes are at the same height of the lintel. Values of the photon flux in the gallery are about $10^7 \gamma\cdot\text{cm}^{-2}\cdot\text{s}^{-1}$ at the pipes level and $\sim 10^5 \gamma\cdot\text{cm}^{-2}\cdot\text{s}^{-1}$ at the floor level.

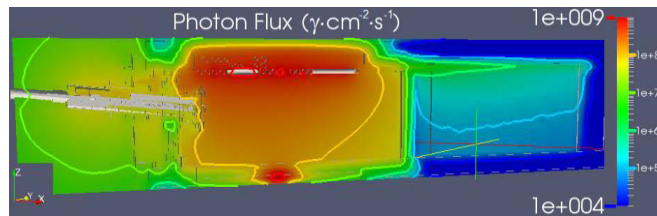


Fig.3: Photon flux distribution inside the PC due to the emission of ^{16}N decay photons

Due to the higher photon flux produced by the ^{16}N decay, also the nuclear loads in the PC area during plasma operations are dominated by activated water. The absorbed doses in silicon inside the PC, integrated over the ITER lifetime, are larger than 10 kGy, and up to 500 kGy close to the pipes, while the contribution due to the plasma neutron source (including secondary gammas) is about 3 orders of magnitudes lower. The map of the absorbed dose in Silicon is shown in Fig. 4.

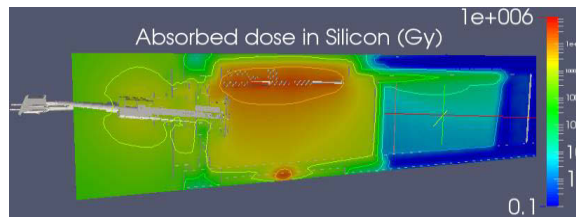


Fig.4: Absorbed dose distribution in Silicon, map with contour plot (vertical cut).

The SDDR in PC has been calculated at 1 day after shutdown with the combined approach of Advanced D1S and gamma transport with secondary source at the bioshield plug in a separate PC model and it is shown in Fig 5. The relative error inside the PC area is below 1%, while in the gallery it is $\approx 20\%$. The maximum dose rate at 1 day after shutdown is $51.6 \mu\text{Sv/h}$, inside the IVVS. The limit of $10 \mu\text{Sv/h}$ is exceeded only inside the IVVS and in two small hotspot at the bioshield plug just above the IVVS. The hotspots arise from the two dogleg penetrations of the bioshield plug that produce streaming of decay photons emitted by activated components inside the bioshield. As these two hotspots are the only locations in available space of the PC in which the limit of SDDR is exceeded, a possible mitigation strategy is to reduce the width of the doglegs as much as possible (for

example by using plugs to be inserted in the doglegs). Nuclear analyses presented here were performed for the IVVS PC to assess the radiation environment and relevant responses in the port cell and gallery during operations and at the shutdown. Different source of radiation have been considered to obtain a full description of the radiation field in the PC and in the gallery. As a result, the neutron flux is dominated by the plasma neutrons, while the photon flux and the absorbed dose in Silicon are dominated by the gamma emission from ^{16}N in activated water. The SDDR at 1 day after shutdown is below the limit except in two hotspots. More details of this study can be found in [9].

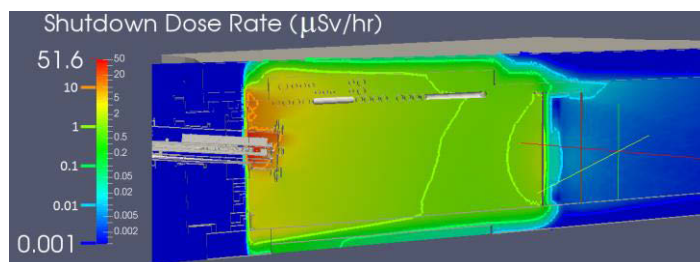


Fig.5: Shutdown dose rate distribution at 1 day after shutdown, map with contour plot (vertical cut).

Acknowledgements

This work was funded by F4E under contract F4E-OMF-466-T06. The views and opinions expressed herein do not necessarily reflect those of F4E or the ITER Organization. F4E is not liable for any use that may be made of the information contained herein.

References

- [1] X-5 Monte Carlo Team: MCNP - A General Monte Carlo N-ParticleTransportCode, Version 5, Los Alamos National Laboratory, Los Alamos, New Mexico, USA, April 2003.
- [2] J.T. Goorley, et al., Initial MCNP6 Release Overview–MCNP6 Version 1.0, 2013,LA-UR-13-22934.
- [3] FENDL-2.1 Fusion Evaluated Nuclear Data Library (Dec. 2004) <https://www-nds.iaea.org/fendl21/>
- [4] www.spaceclaim.com
- [5] Y. Wu, et al., “CAD-based Monte Carlo program for integrated simulation of nuclear system SuperMC”, Annals of Nuclear Energy, Volume 82, August 2015, Pages 161-168
- [6] P. Pereslavytsev, U. Fischer, et al., “Novel approach for efficient mesh based Monte Carlo shutdown dose rate calculations,” Fusion Engineering and Design, 88 (2013), pp. 2719–2722
- [7] R. Villari, U. Fischer, F. Moro, P. Pereslavytsev, L. Petrizzi, S. Podda, A. Serikov, “Shutdown dose rate assessment with the Advanced D1S method: Development, applications and validation”, Fusion Engineering and Design, Volume 89, Issues 9–10, October 2014, Pages 2083-2087
- [8] ITER_D_2V3V8G v 1.1, ‘Recommended Plasma Scenarios for Activation Calculations’, M.J. Loughlin, October 2009
- [9] D. Flammini, U. Fischer, F. Moro, R. Pampin, A. Puiu, Y. Qiu, R. Reichle, A. Travleev, R. Villari, “Nuclear responses in the ITER IVVS port cell”, Fusion Engineering and Design, Article in Press (2016), ISSN 0920-3796, <http://dx.doi.org/10.1016/j.fusengdes.2017.02.033>.

EDGE MODELLING WITH SOLEDGED2-EIRENE CODE IN RFX-MOD AND TCV FUSION DEVICES

P. Innocente

*Consorzio RFX (CNR, ENEA, INFN, Università di Padova, Acciaierie Venete SpA), Corso Stati Uniti 4 - 35127
Padova, Italy*

ABSTRACT. The knowledge of edge plasma transport parameters and plasma edge phenomena is a key element in the design the divertor and the first wall for a magnetically confined fusion experiment. In this report will be presented the modelling performed in two fusion experiments: the RFX-mod (Reversed Field eXperiment) reversed field pinch experiment and the small size TCV (Tokamak à Configuration Variable) tokamak. In RFX-mod heat flux deposition profiles on the wall have been evaluated from infrared temperature measurements of insertable graphite limiters. In TCV device experiments have been performed in Snowflake and Single Null divertor magnetic configurations to evaluate the relative advantage in terms of divertor heat load and detachment threshold. Modelling of edge radial profiles and divertor parameters and heat fluxes has been done using the SOLEDGE2D-EIRENE edge code. In RFX-mod edge modelling has shown that measured decay lengths are compatible with energy diffusion coefficients in Scrape Off Layer (SOL) smaller than those commonly evaluated at plasma edge; the cause of the reduced diffusion in the SOL will be discussed in the paper. In TCV only preliminary results of the single null configuration have been obtained showing that transport parameters have to be increased with the density.

1 Introduction

The study of transport phenomena and the evaluation of transport parameters at the plasma Edge/SOL is a key element for the improvement of plasma performance the reduction of heat low at the target divertor and the optimization of the first wall (FW) response to the plasma wall interaction (PWI). In the Reversed Field Pinch (RFP) devices these phenomena have not been investigated thoroughly partially because the presence of strong deformation of the last close flux surface (LCFS) and edge $m=0$ magnetic islands makes measurements and fluid description of the transport rather difficult and also because the lack of transport codes able to deal with a full interacting first wall instead than a limiter as it was typical in limiter tokamak devices. In the RFX-mod device ($R/a=2/0.46$ m, $I_t \leq 2$ MA) [1,2] by better control of LCFS deformation by feedback control of edge radial fields [2,3] small deformation have been obtained making more suitable a fluid description of the edge plasma. Here we present the first attempt to study the transport in the plasma Edge/SOL of the RFX-mod device analysing the power load on an insertable graphite limiter and modelling it with a 2D edge fluid code. To extract quantitative information on plasma transport from the computed heat flux we have used the recently developed SOLEDGE2D-EIRENE edge fluid code [4]. In TCV ($R/a=0.88/0.3$ m, $I_t \leq 1$ MA) a study of the exhaust properties of Snowflake (SF) divertor geometries in L-mode core plasmas at low/high density and with impurity seeding has been performed. The final aim of the study was the comparison between the SF and the standard Single Null (SN) configuration of heat and particle loads onto the divertor targets. This comparison is motivated by the fact that intolerable heat and particle loads onto the divertor targets limit the development of the tokamak concept towards the reactor scale. This motivated the proposal of advanced divertor configurations, such as the snowflake (SF) divertor [5].

The SF configuration is characterized by a second-order null in the poloidal magnetic field (B_p), where both B_p itself and its spatial derivatives vanish ($B_p = 0, \nabla B_p = 0$). This splits the separatrix near the null into six segments: two enclose the confined plasma and four lead to the machine wall (the divertor legs). Here we present the initial modelling activity devoted to evaluate the optimal transport parameter in the reference SN discharges.

2 The SOLEDGE2D-EIRENE code

To get some insight into the plasma transport properties of the edge and of the RFX-mod and TCV SOL the code SOLEDGE2D-EIRENE has been used [4]. It is a 2D transport code with a multi-species plasma solver coupled to EIRENE for neutrals; it solves the continuity equations for densities, parallel velocities, temperatures and electric potential. One of the main advantages of SOLEDGE2D code is the ability to simulate the plasma up to the first wall (FW) [4]. In other codes, e.g., UEDGE [6] and EDGE2D [7] the computational domain usually does not extend up to the FW or, like for the SOLPS code, custom solutions are adopted to deal with the FW [8,9]. Instead in SOLEDGE2D the FW is managed by the penalization method [10,11], which extends the solution of fluid equations inside the wall and controls the sharp gradients which form at the wall interface by the penalization parameter. The method enables the modelling of very complex FW geometry by simply adjusting the penalization mask that splits the solid and plasma regions. This is a major requirement in the RFX-mod case considering the absence of a limiter able to keep plasma far from the FW and the shaped surface of the FW tiles. In the SF case the SOLEDGE code takes advantage of a very general internal description of magnetic topology and of a generalized grid generator which (again differently from others codes like EDGE2D and SOLPS) which makes possible grid generation for any of the present magnetic configurations.

2 Edge modelling in RFX-mod

To evaluate transport parameters (D and χ) in RFX-mod edge and SOL plasma regions, they have been optimized to match measured density, temperature, particles influxes and heat flux decay length on the limiter with those computed by the simulations. As regards temperature and density, the comparison is limited to nearly-edge plasma region because in RFX-mod SOL profile measurements are not routinely available at high plasma current. Electron temperature was measured with a multipoint Thomson scattering (TS) system. Electron density was computed by Abel inverting the integral of the line density measured with a 8 chord mid-infrared CO_2 interferometer.

In setting up SOLEDGE2D-EIRENE simulation many simplifying assumptions have been done: the localized limiter and the magnetic equilibrium have been considered toroidally symmetric, using the magnetic equilibrium measured at the toroidal position of the limiter; the ohmic input power has been attributed 50-70% to electrons and 50-30% to deuterium ions, in RFP devices this is a strong assumption because there are many uncertainties about the mechanism of ion heating through collisions with electrons or anomalous heating (see ref. [12] and there in); thermal conductivity has been assumed equal between electrons and ions ($\chi_e = \chi_i$) which is also a strong assumption considering the uncertainties in the nature of the transport at the edge/SOL.

Several set of transport parameters (D and χ) have been tested. The simplest schematization assumed the same value of D and χ in the plasma edge and SOL (flat profile across the last closed flux surface) and for discharges at 700 kA a good matching of temperature, density and influxes was obtained with $D=3-6 \text{ m}^2/\text{s}$ and $\chi=20-60 \text{ m}^2/\text{s}$.

These values are in good agreement with previous evaluations of D and χ_e at plasma edge performed with the ASTRA code from profiles measurements in RFX-mod [13,14], but they did not provide the

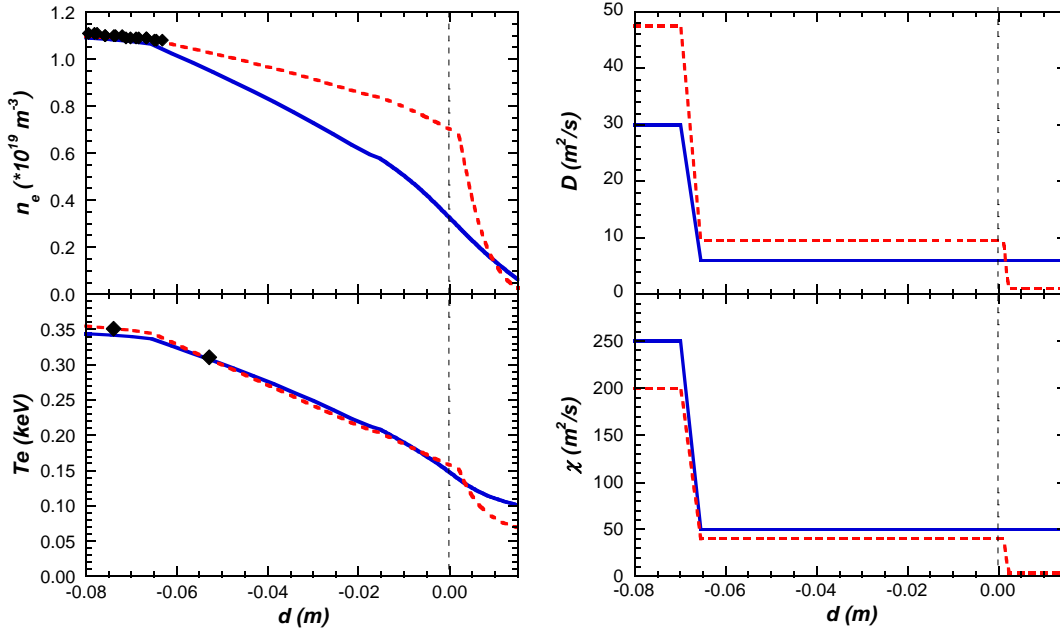


Figure 1. Edge/SOL density (n_e) and temperature (T_e) at the equatorial plane computed with SOLEDGE2D-EIRENE for a low density 700 kA pulse and two transport profiles (D , χ). Diamonds show experimental values measured with interferometer and Thomson scattering, the vertical dash line represents the position of LCFS.

heat flux profiles measured on the limiter. Instead, in order to match also the heat flux profiles, it is necessary to assume D and χ reduced by a factor of about ten in the SOL with respect to plasma edge.

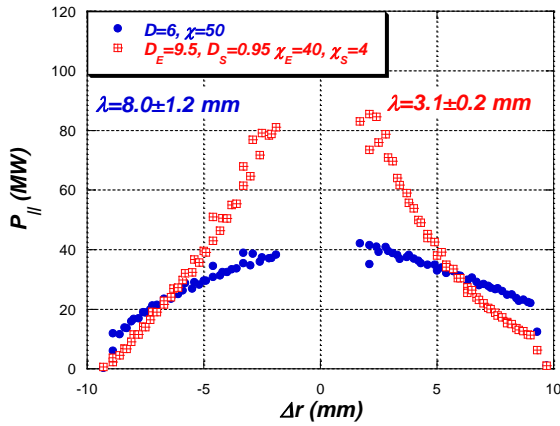


Figure 2. Plot of the parallel heat flux profiles computed at the limiter with constant transport parameters (blue closed circles) and lowered SOL transport parameters (red open squares).

Figure 1 shows the results of two SOLEDGE2D-EIRENE simulations of a low density 700 kA discharge with the two transport coefficient profiles: constant in the edge/SOL regions (blue) and with ten times reduction of D and χ in the SOL (red). In both simulations 60% of the 12 MW input power was assigned to electron (40% to ions) and transport parameters were changed to match the measured density, temperature and average particle influx. For the same simulations, figure 2 shows (with the same colour code) the parallel heat flux profiles on the limiter and the computed decay lengths. In fig. 2 it is clearly seen that the high transport values in the SOL produce a large spread of the heat flux which is not in agreement with experimental evaluation of the decay length, instead the ten times reduced transport values are able to reproduce the measurements.

A possible explanation of the lower values of the transport parameters in the SOL is based on the RFX-mod experimental observation that the edge transport is mainly due to poloidal blobs (or long filaments) of increased pressures moving radially [15]: in our case the presence of the limiter reduces blobs transport cutting their length and radial size.

3 Preliminary modelling of a SN discharge in TCV

For the TCV analysis before analysing SF discharges a reference SN discharges at the same plasma density and current (250 kA) has been analysed to evaluate with the SOLEDGE2D-EIRENE code the best transport parameters able to match the midplane density and temperature profiles measured with Thomson scattering and the divertor target parameters (n , T , J_{sat} and q_w) measured with Langmuir probes.

As for the RFX-mod case in setting up SOLEDGE2D-EIRENE simulation some simplifying assumptions have been done: the 330 kW ohmic input power has been attributed 50/50% to electrons and ions; transport parameters have assumed constant at the edge/near-SOL/far-SOL while thermal conductivity has been assumed equal between electrons and ions ($\chi_e = \chi_i = \chi$). With these assumption at low density it has been possible to match measured density and temperature at midplane with $D = \chi = 0.95 \text{ m}^2/\text{s}$ (see fig. 3) a relatively good agreement has been obtained also for heat flux and saturation current measured at divertor targets with Langmuir probes (not shown). Increasing density higher values of D and χ are necessary to match plasma parameters at midplane.

References

- [1] P. Sonato et al., Fus. Eng. Design **161** (2003) 66.
- [2] P. Martini et al. Nucl. Fusion **53** (2015) 104018.
- [3] M.E. Puiatti et al. Nucl. Fusion **55** (2015) 104012
- [4] H. Bufferand et al., J. Nucl. Mater. **438** (2013) S445
- [5] D.D. Ryutov et al. Phys. Plasmas **15** (2008) 092501
- [6] M.E. Rensink, et al., J. Nucl. Mater. **266–269** (1999) 1180
- [7] R. Simonini, et al., Contrib. Plasma Phys. **34** (1994) 368
- [8] F. Subba, et al, Comp. Phys. Comm. **179** (2008) 194
- [9] M. Baelmans, et al., Nucl. Fusion **51** (2011) 083023
- [10] L. Isoardi, et al., J. Comp. Phys. **229** (2010) 2220
- [11] A. Paredes, et al., J. Nucl. Mater. **438** (2013) S625
- [12] L. Garzotti, B. Pégourié, R. Bartiromo, P. Innocente, and S. Martini, Phys. Rev. Lett. **84** (2000) 5532
- [13] R. Lorenzini et al., Nucl. Fusion **52** (2012) 062004
- [14] F. Auriemma et al., Nucl. Fusion **55** (2015) 043010
- [15] P. Scarin, M. Agostini, R. Cavazzana, F. Sattin, G. Serianni, M. Spolaore and N. Vianello, J. Nucl. Mater. **390–391** (2009) 444

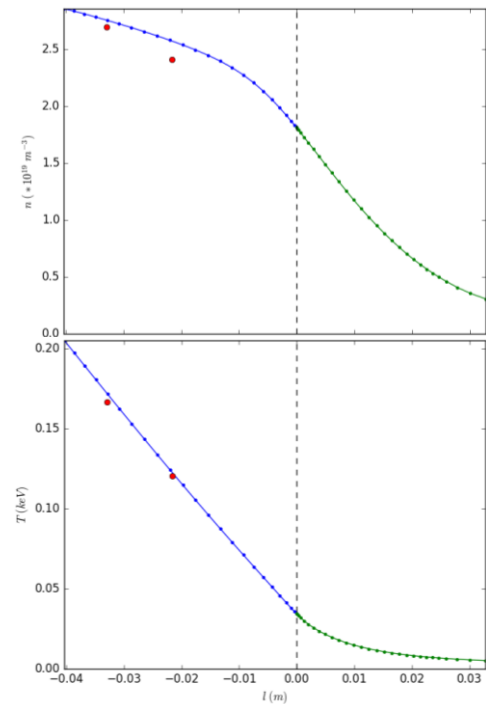


Figure 3. Comparison between experimental measurements (red dots) and n_e and T_e computed profiles at plasma midplane.

AB-INITIO STUDY OF THE *c-Si/a-Si:H* INTERFACE FOR PV TECHNOLOGY

Simone Giusepponi^{1*}, Massimo Celino¹, Michele Gusso²,
Urs Aeberhard³ and Philippe Czaja³

¹ ENEA, C. R. Casaccia, via Anguillarese 301, 00123 Rome, Italy

² ENEA, C. R. Brindisi, S.S. 7 Appia km 706, 72100 Brindisi, Italy

³ IEK-5 Photovoltaik, Forschungszentrum Jülich, D-52425 Jülich, Germany

ABSTRACT. In order to improve the optoelectronic properties of Silicon heterojunction solar cells, an atomistic model of the crystalline-amorphous (*c-Si/a-Si:H*) interface is developed. A preliminary analysis of the local microscopic structure at the interface is reported in order to characterize the atomic-scale features that influence the macroscopic optical properties

1 Introduction

To characterize the microscopic features of the crystalline-amorphous *c-Si/a-Si:H* interface in Silicon heterojunction solar cell, a reliable physical model of the interface between crystalline Silicon (*c-Si*) and hydrogenated amorphous Silicon (*a-Si:H*) is developed. To this aim, the models of crystalline Silicon and hydrogenated amorphous Silicon, already presented in the previous CRESCO report are used [1]. The *ab-initio* PWscf (Plane-Wave Self-Consistent Field) code of the Quantum ESPRESSO suite is used [2, 3] to perform total energy calculations and Born-Oppenheimer Molecular Dynamics (BOMD) simulations. PWscf performs many different kinds of self-consistent calculations of electronic structure properties within Density-Functional Theory (DFT) [4, 5], using a Plane-Wave (PW) basis set and Pseudo-Potentials (PP). All the calculations are performed in the supercell approximation with periodic boundary conditions (PBC) meant to mimic infinitely extended systems. We use the Si and H ultrasoft pseudopotentials with Perdew-Burke-Ernzerhof (PBE) [6] approximant GGA exchange-correlation potential, available in the Quantum ESPRESSO library [3]. In view of very demanding simulations, we use results from the benchmark of Quantum ESPRESSO on the ENEA infrastructure [7], to make best use of HPC resources and save computational times.

2 The *c-Si/a-Si:H* interface

As shown in Fig.1a), the interface is built by putting nearby two free surfaces obtained by cutting both the crystalline silicon and the hydrogenated amorphous silicon. The relaxed $p(2 \times 1)$ symmetric reconstruction of the Si(001) surface constitutes the *c-Si* side of the interface. It is formed by 192 Si atoms: 12 layers of silicon each of them with 16 atoms. The *a-Si:H* side of the system is generated

*Corresponding author. E-mail: simone.giusepponi@enea.it.

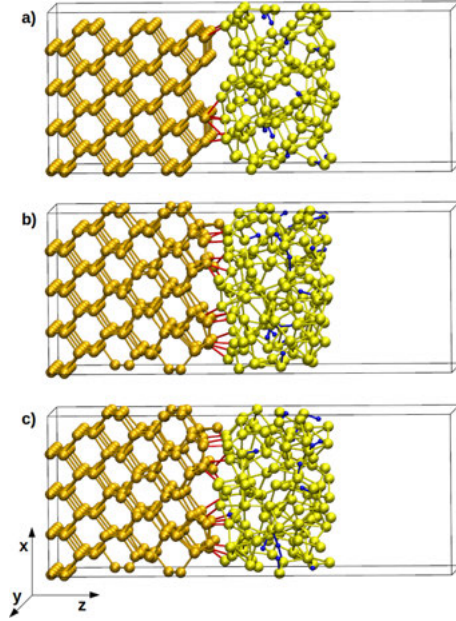


Figure 1: Snapshots of the c-Si/a-Si:H interface in the simulation box. Hydrogen atoms and bonds with Silicon atoms are in blue, Silicon atoms and their bonds are in dark yellow in the c-Si side and are in light yellow in the a-Si:H side. Bonds between c-Si and a-Si are in red. a) initial configuration, b) configuration at 25 ps and c) configuration at 35 ps.

replicating and cutting the a-Si:H system [1] to have a surface equal to the c-Si side and a thickness of about 12 Å. It is composed of 128 Si atoms and 16 H atoms. A void region of 10 Å in z-direction is adequate to suppress the interaction between the external surfaces (this distance was checked by convergence tests with respect to the void region size), then periodic boundary conditions are applied to the supercell. The total length of the system is $L_z = 38.66$ Å (the z-direction is perpendicular to the interface), while in the x and y direction the system has $L_x = L_y = 15.46$ Å. In view of long time simulations, the Brillouin zone integration is sampled at Gamma point in order to save computational time. At first, total energy calculations of the interface at different distances between c-Si and a-Si:H slabs, are performed to find the interface configuration corresponding to the lowest total energy. The configurations are built moving rigidly by hand the a-Si:H part and keeping fixed the c-Si one. Then, the found configuration is used as starting point for the MD simulation.

3 Molecular dynamics simulations

The interface shown in Fig.1a), is used as starting configuration for BOMD simulations on the electronic ground state at constant volume and constant temperature (NVT), with timestep $t_s = 20$ Rydberg atomic units. The ionic temperature is fixed at $T = 300$ K and it is controlled by using an Andersen thermostat [8]. The first four layers of c-Si atoms on the left are kept fixed to impose a bulk like behavior to the crystalline silicon part of the system. The MD simulation is performed for more than 35 ps, the first 25 ps of the simulation are used to thermalize the system and reach a stable configuration, then, the last 10 ps of the simulation (from 25 ps to 35 ps) are used to analyze and characterize the system. In panels b) and c) of Fig.1, the snapshots of the c-Si/a-Si:H interface at 25 ps and 35 ps respectively, are shown.

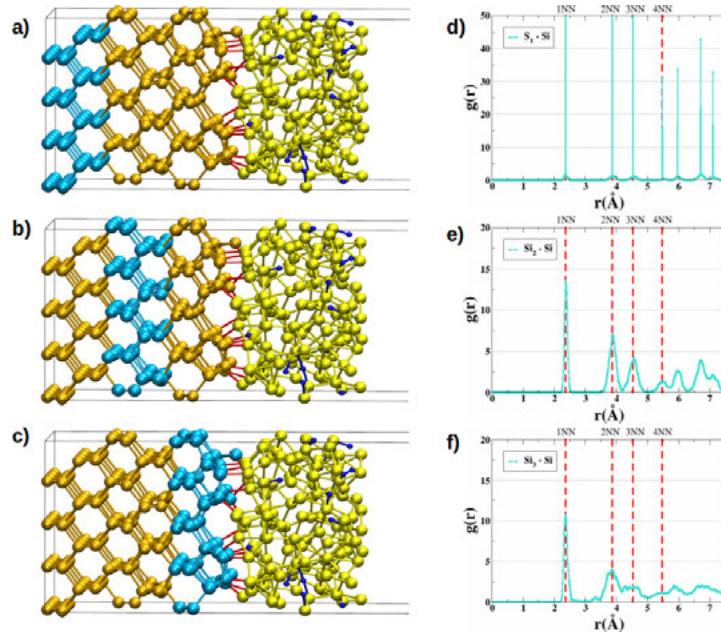


Figure 2: Selected groups of Si atoms (in pale blue) S_1 , S_2 and S_3 (panels a, b and c, respectively) and the corresponding radial pair correlation functions $g(r)$ (panels d, e and f, respectively) computed considering the Si group and the Si atoms. Both Si and $g(r)$ are depicted in pale blue. Red dashed lines indicate the NNs distances of the crystalline phase.

To characterize the interface we consider six distinct groups of Si atoms at different distances from the interface, denominated S_i , with i ranging from 1 to 6. Three sets of atoms: S_1 , S_2 and S_3 in the c-Si side (see atoms in pale blue in Fig.2 panels a, b and c), and three sets of atoms: S_4 , S_5 and S_6 in the a-Si side (see atoms in pale blue in Fig.3 panels a, b and c). For each group of atoms the radial pair correlation function $g(r)$ is calculated and averaged in the last 10 ps of simulation, taking one configuration of the system every ten timesteps.

In panels d), e) and f) of Fig.2 and Fig.3, the pale blue curves are the six $g(r)$ computed between atoms of the Si group and the neighbor silicon atoms, whereas the green curves are the $g(r)$ computed considering the Si group (only for $i = 4, 5, 6$) and the hydrogen atoms. Moreover, the $g(r)$ calculated from a-Si:H is reported for comparison in the graphs of Fig.3. From graph in panel d) of Fig.2, the $g(r)$ of S_1 has the expected bulk-like behavior with well-defined peaks corresponding to the NNs (Nearest Neighbors) Si atoms of the crystalline phase. The peaks are at 2.37 Å (1NN), 3.87 Å (2NN), 4.54 Å (3NN) and 5.47 Å (4NN), respectively. For the second group, S_2 , in the middle of the c-Si side, the influence of the amorphous silicon shows up, in fact the $g(r)$ has less sharpened peaks corresponding to the NNs that become broader and loose the shape of the crystalline phase with increasing distance r . The presence of the amorphous Silicon is more evident for the c-Si atoms near the interface (group S_3), as a consequence, $g(r)$ has both the crystalline and amorphous trends. The crystalline shape with well-defined peak corresponding to the 1NN is still present at small distances but is lost increasing r where the $g(r)$ has a more evident amorphous character. Graphs in Fig.3, show Si-Si radial pair correlation functions (pale blue curves) that have trends very similar to that of a-Si:H (red curve), with a peak corresponding to the 1NN Si atoms. Furthermore, the Si-H $g(r)$ (green curves) point out the Si - H bonds at about 1.5 Å.

In conclusion, in this report an interface model for c-Si/a-Si:H is presented and its main structural

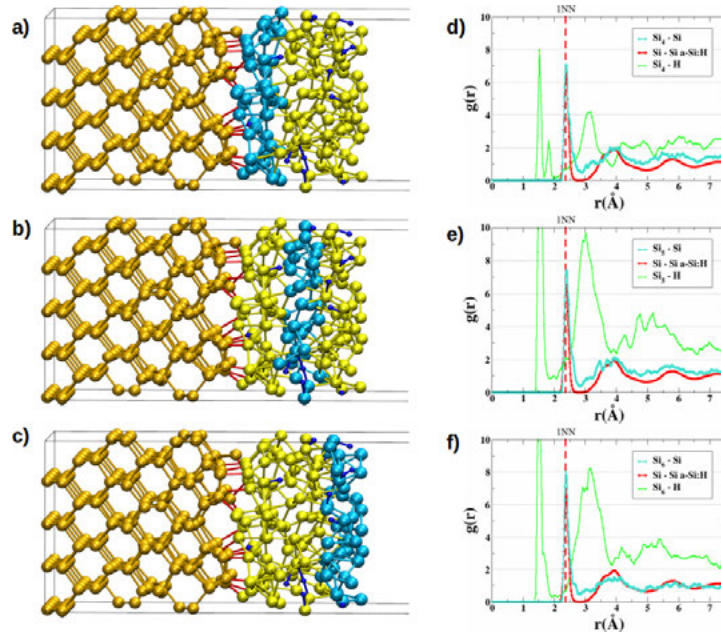


Figure 3: Selected groups of Si atoms (in pale blue) S_4 , S_5 and S_6 (panels a, b and c, respectively) and the corresponding radial pair correlation functions $g(r)$ (panels d, e and f, respectively) computed considering the Si group and the Si atoms (curves in pale blue), and considering the Si group and the H atoms (curves in green). In addition, the $g(r)$ calculated from a-Si:H (curve in red) is reported for comparison. Red dashed line indicates the 1NN distance of the crystalline phase.

features described. Silicon atoms were characterized on the base of their distance from the interface, analyzing the radial pair correlation functions $g(r)$. However, further analysis is underway, to characterize the atoms examining their coordination. This structural characterization is finalized to a deeper understanding of the atomic-scale configurations, an information not easily accessible to experiments and to assess the reliability of the numerical model that will be used to compute optical properties.

References

- [1] S.Giusepponi *et al.* In *High Performance Computing on CRESCO infrastructure: research activities and results 2015*, pages 88–92. ENEA, 2016.
- [2] P. Giannozzi *et al.* *J. Phys.: Condens. Matter.*, 21:395502, 2009.
- [3] www.quantum-espresso.org.
- [4] P. Hohenberg and W. Kohn. *Phys. Rev.*, 136:B864, 1964.
- [5] W. Kohn and L.J. Sham. *Phys. Rev.*, 140:A1133, 1965.
- [6] K. Burke J.P. Perdew and M. Ernzerhof. *Phys. Rev. Lett.*, 77:3865, 1996.
- [7] S.Giusepponi *et al.* In *High Performance Computing on CRESCO infrastructure: research activities and results 2015*, pages 93–98. ENEA, 2016.
- [8] H.C. Andersen. *J. Chem. Phys.*, 72:2384, 1980.

MOLECULAR DYNAMICS OF GeO_2 : CAR-PARRINELLO SIMULATIONS IN THE RANGE 10-4000 K

G. Mancini^{1*}, M. Celino², A. Di Cicco¹

¹*Università di Camerino Via Madonna delle Carceri 62032, Camerino (MC), Italy*

²*ENEA, Ente per le Nuove Tecnologie, l'Energia e lo Sviluppo Economico Sostenibile
C. R. Casaccia, Via Anguillarese 301, 00123 Roma, Italy*

ABSTRACT. First-principles molecular dynamics simulations have been carried out for a relatively large system consisting of 240 GeO_2 atoms at 4000 K. We have finally covered the range 3000-4000 K, completing a long simulations process aimed to obtain a high temperature GeO_2 system entirely by ab-initio simulations in the whole range 10-4000 K.

1 Introduction

In this paper we present the results and details of our ab-initio Car-Parrinello (CPMD) simulations [1,2] of a system formed by 240 atoms, 160 oxygen and 80 germanium – a relatively large system for first principles simulations - at 4000 K.

We consider these results the last step of a series of first-principles simulations carried out to prepare a numerical sample of liquid GeO_2 at high temperature to start production runs, from which distinct amorphous GeO_2 configurations at room temperature can be obtained and studied.

First principles simulations take their very start from a suitable initial configuration, virtually at 0 K, to be taken up to a target temperature through a series of intermediate, equilibrated states. The generation of the initial configurations of GeO_2 to get stable simulations can result into a long, delicate process; in fact, simulations often diverge after a few steps. This fact and the short timescales provided by first-principles simulations are the reasons for which first-principles simulations are often started on initial high temperatures configurations obtained by classical molecular dynamics methods. We here stress the fact that we have covered the entire temperature interval 10-4000 K using ab-initio methods.

It is experimentally known that the activation energy of the structural relaxation time for GeO_2 is about 3.4 eV; at a temperature of 3000 K this time is longer than 100 ps. Due to the intrinsic limitations arising from the shorter typical timescales of ab-initio simulations – namely CPMD in our case - a temperature of 3000 K has to be considered as the lowest one to carry out production CPMD simulations, provided smaller systems and shorter times than classical molecular dynamics are considered [3].

We have reported the results of our 24 ps-long CPMD simulations at 3000 K in [4]. In that paper a comparison of the results obtained from different simulation parameter considerably affecting the computing times has been presented, showing no significative differences. As a matter of facts, our preferred approach was in favour of the fastest runs; nevertheless we flanked them by longer and potentially more accurate simulations so as to ascertain that the results only depended on the sole configuration of our system.

*Corresponding author. E-mail: giorgio.mancini@unicam.it

To reach the final 4000 K temperature, characterised by a faster dynamic during production runs, we only continued with the most demanding approach in terms of computational times - the one using a plane wave cut-off of 90 Ry - for easier, more homogeneous results comparison.

2 Computational details

We started from a well equilibrated GeO_2 system at 3000 K consisting of 240 atoms in a cubic simulation box of edge 15.602 Å, corresponding to a density $\rho = 3.66 \text{ gr/cm}^3$ [4]. The software we used is CPMD (Car-Parrinello Molecular Dynamics [1,2]).

The self consistent evolution of the electronic structure during the motion is described within the density functional theory. A generalized gradient approximation (BLYP-GGA) has been adopted for the exchange and correlation parts of the total energy [5,6]. For the core-valence interactions, norm conserving pseudo-potentials with the BLYP exchange–correlation functional using the Troullier–Martins parametrization [7] has been chosen.

Car-Parrinello molecular dynamics simulations have been carried out on the system heated up and equilibrated from 3000 to 4000 K by steps of 200 K.

For faster equipartitioning, a “massive” thermostating has been used for the ions (a Nosé-Hoover chain thermostat placed on each ionic degree of freedom [2,8,9]). A second Nosé-Hoover chain thermostat has been set on the electronic degrees of freedom to prevent electrons from provoking improper ions damping or departures from the Born-Oppenheimer surface. Thermostats have been systematically employed throughout all simulations; characteristic frequencies of 1000 cm^{-1} for ions and 10000 cm^{-1} for electrons have been used. The default value of 400 a.u. has been used for the fictitious electronic mass. A plane wave cut-off of 90 Ry and a time step of 3 a.u. have been used during all simulations.

3 Computational resources

The calculations were performed using the facilities and services available at the ENEA GRID infrastructure (Italy). Molecular Dynamics simulations have been carried out using CPMD v3.15.3 running on CRESCO4 cluster. 800 GB of disk storage has been granted on the PFS/gporq1_256k file system.

4 Results and conclusions

As expected, in its final state at 4000 K the system shows broader distributions than at 3000 K, still retaining the same central values. Figs. 1-3 clearly show this behaviour.

From our simulations we have for the positions of the first $g_{\alpha\beta}(r)$ peaks (fig.1): 3.12 Å for Ge-Ge, 1.69 Å for Ge-O and 2.75 Å for O-O distances, respectively. They are in perfect agreement with the values from other mixed classical/ab-initio simulations, e.g. [10], and in good agreement with classical MD and experimental results [10,11,12], the slight variations are commonly attributed to the different system preparation procedures (we are considering the possibility of repeating the whole set of simulations on a different initial GeO_2 configuration than presented here, so as to verify this point).

Similar considerations apply for the average coordination numbers (fig.2): our simulations give $Z_{\text{GeGe}}=4.1$, $Z_{\text{GeO}}=4.0$ and $Z_{\text{OO}}=6.8$ (all values are taken at the intersection points of the 4000 K and 3000 K curves: it seems particularly reasonable for Z_{OO} , since the associate distribution curves show no clearly defined plateau). Finally fig.3 gives the initial and final structure factors: it's easily seen how they too are in good agreement with the ones reported in literature.

We can thus conclude we actually have obtained a reliable, relatively large liquid GeO_2 system at high temperature entirely in the frame of first-principles molecular dynamics. The system will be used for production runs to obtain amorphous GeO_2 systems to be studied at room temperature.

The resources available at HPC CRESCO systems make CPMD simulations using Goedecker pseudo-potentials [13] – commonly considered out of reach a target when dealing with a significant number of atoms - a feasible goal. Such pseudo-potentials are analytical - that ensures their separability - and have no “ghost states”, but they generally need higher plane wave cut-offs (100-200 Ry) than the corresponding Troullier-Martins ones.

We have started new simulations - on the same initial GeO_2 configuration we have presented in this paper - using Goedecker pseudo-potentials with 100 and 200 Ry cut-offs, so as to evaluate the differences, if any, due to distinct potentials. The results will be a subject of future communications as soon as they are obtained.

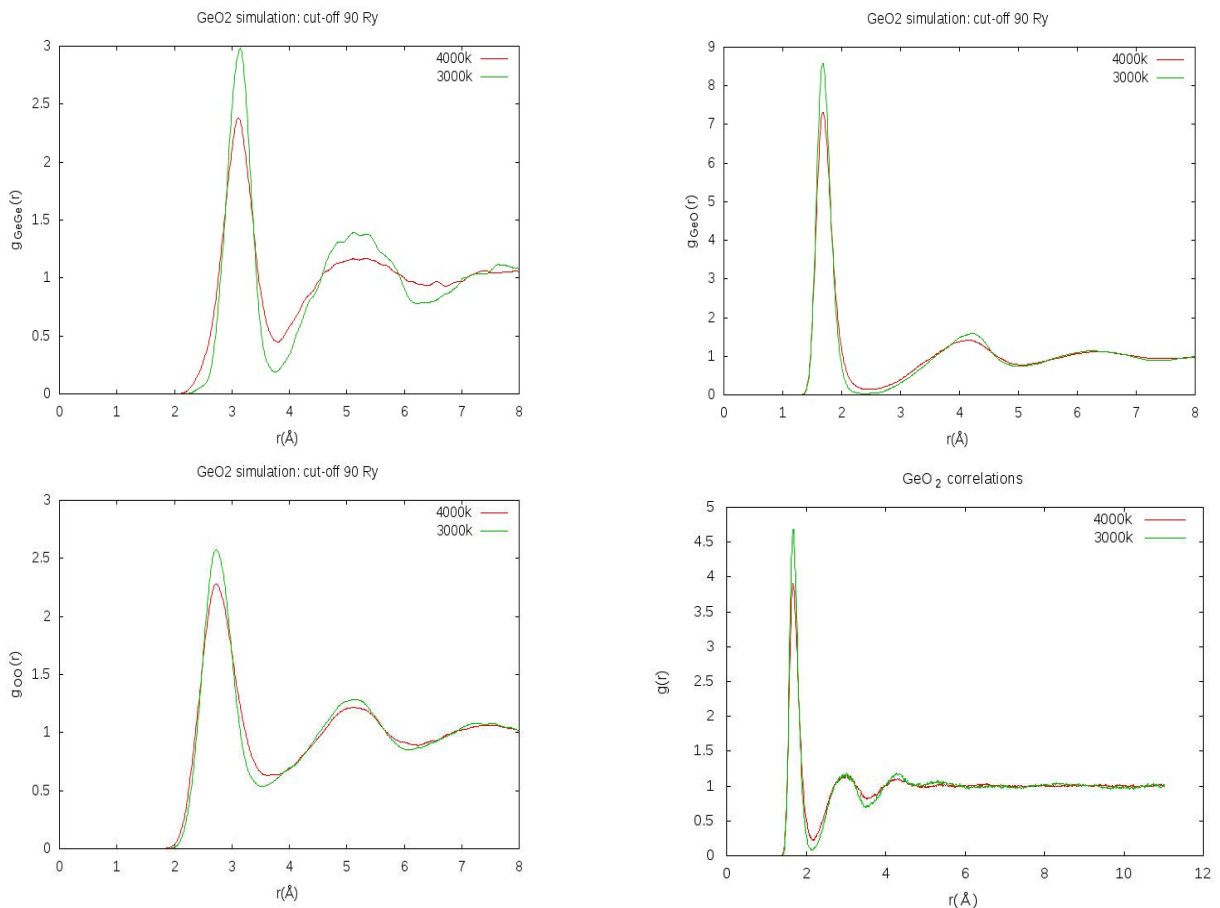


Fig.1: Radial distribution functions from the simulated GeO_2 system at 3000K and 4000K.

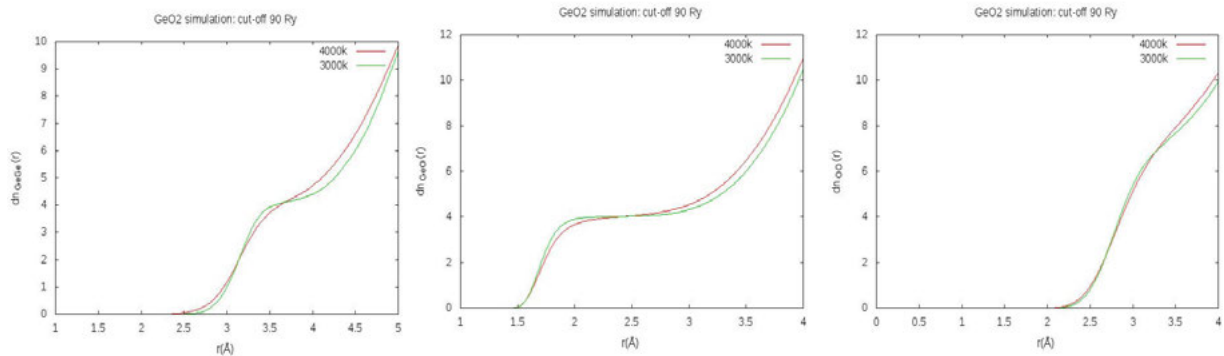


Fig. 2: $Z_{\alpha\beta}(r)$ distribution from the simulated GeO_2 system at 3000K and 4000K.

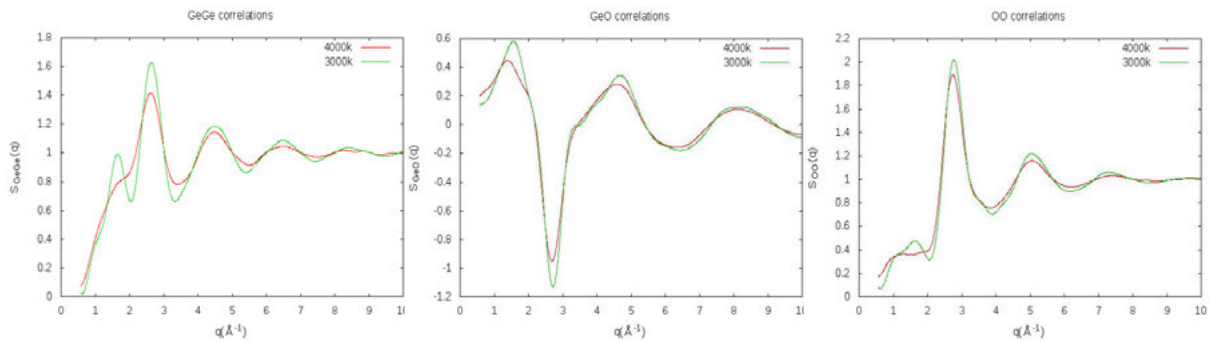


Fig.3: $S_{\alpha\beta}(q)$ structure factors from the simulated GeO_2 system at 3000K and 4000K.

References

- [1] CPMD v3.13.2 copyright ibm corp 1990-2008, copyright mpi für festkörperforschung stuttgart 1997-2001.
- [2] The CPMD Consortium. The CPMD Consortium. "Car-Parrinello Molecular Dynamics: An ab initio Electronic Structure and Molecular Dynamics Program". Manual for CPMD version 3.15.1.
- [3] M. Hawlitzky, J. Horbach, K. Binder. "Simulations of Glassforming Network Fluids: Classical Molecular Dynamics versus Car-Parrinello Molecular Dynamics". *Physics Procedia* **6** (2010) pp. 7–11
- [4] G. Mancini, M. Celino and A. Di Cicco "Ab Initio Carr-Parrinello Simulations of High Temperature GeO_2 : a comparison of the effects of plane waves cut-off and time step choice". Published in the book "*High Performance Computing on CRESCO infrastructure: research activities and results 2015*", (2016) pp. 6-9. ISBN: 978-88-8286-342-5.
- [5] A.D. Becke "Density-functional exchange-energy approximation with correct asymptotic behavior". *Phys. Rev. A* **38** (1988) pp. 3098
- [6] C. Lee, W. Yang and R.G. Parr "Development of the Colle-Salvetti correlation-energy formula into a functional of the electron density". *Phys. Rev. B* **37** (1988) pp. 785-789.
- [7] N- Troullier and J.L. Martins "Efficient pseudopotentials for plane-wave calculations". *Phys. Rev. B* **43** (1991) pp.1993-2006

- [8] S. Nosé “A molecular-dynamics method for simulations in the canonical ensemble”. *Mol. Phys.* **52** (1984) pp. 255-268.
- [9] S. Nosé “A unified formulation of the constant temperature molecular dynamics methods”. *J. Chem. Phys.* **81** (1984) pp. 511-519.
- [10] T. Tamura, G-H Lu, R. Yamamoto, M. Kohyama “First-principles study of neutral oxygen vacancies in amorphous silica and germania”. *Phys. Rev. B* **69**, (2004) pp.195204 (9pp)
- [11] P.S. Salmon “The structure of tetrahedral network glass forming systems at intermediate and extended length scales” . *J. Phys.: Condens. Matter* **19** (2007) pp. 455208 (16pp)
- [12] M. Hawlitzky, J. Horbach, S. Ispas, M. Krack and K. Binder “Comparative classical and ab initio molecular dynamics study of molten and glassy germanium dioxide”. *J. Phys. Condens. Matter* **20** (2008) 285106 (15pp)
- [13] S. Goedecker, M. Teter, J. Hutter “*Separable dual-space Gaussian pseudopotentials*” *Phys. Rev. B* **54** (1996) , pp. 1703-1710.

DEVELOPMENT OF THE NEW CIRCULATION FORECAST MODEL FOR THE MEDITERRANEAN SEA

G. Sannino^{*1}, A. Carillo¹, A. Bargagli¹ and E. Lombardi¹

¹*ENEA SSPT-MET-CLIM Via Anguillarese 301, 00123 Rome, Italy*

ABSTRACT. A new 3D circulation oceanic model covering the Mediterranean and the Black Sea has been developed and tested using CRESCO4 cluster. The model has an irregular horizontal grid reaching the resolution of some hundreds of meters in the main straits and includes explicitly the effect of tides. After a test period the model is now running in an operational mode.

1 Introduction

In the last years, the EU growing interest in the Blue Energy sector has determined also in Italy an increase in the research in this field. A promising source of energy from the sea, in the Mediterranean basin, is represented by the tidal energy; to evaluate the potential of this resource the detailed characterization of the circulation in the basin is essential. Forecast of the circulation in the basin are then necessary in view of the installation of energy converters.

The Mediterranean is connected with the Atlantic Ocean through the strait of Gibraltar that is characterized by a complex bathymetry with a succession of sills and contractions. The interaction of tides inflowing from the Atlantic Ocean with this bathymetry determines the characteristics of the exchange between the two basins. In a similar way the exchange with the Black Sea is controlled by the Turkish Strait System, composed by the Bosphorus and Dardanelles Straits and the Marmara Sea.

The simulation of the ocean circulation for the entire system composed by the Mediterranean and Black Sea requires very high horizontal and vertical resolution in the straits, as demonstrated by different models, recently implemented at ENEA for the Mediterranean and its straits [1,2].

The new model implemented is based on a horizontal non-uniform grid with an overall regular resolution locally enhanced in the Straits in order to satisfy the minimum requirements dictated by findings of the previous experiments. The setup of the new model required a series of experiments that have been realized on CRESCO4 cluster. The actual version has been implemented for the use in operational mode and produces forecast of the main hydrological parameters for the next days.

2 Model description

The model used for the simulation is the 3D ocean circulation model MITgcm (Massachusetts Institute General Circulation Model) developed by Marshall et al. [3], that represents the state of the art of the ocean numerical models. The model has been used in its hydrostatic, implicit free-surface, partial step topography formulation. MITgcm is written in pure Fortran77 and can be easily compiled on a huge number of different clusters. It is parallelized via MPI through a horizontal domain decomposition technique.

The model domain extends from the Gulf of Cadiz and includes both the Mediterranean and the Black Sea. The horizontal grid is kept constant at the resolution of $1/48^\circ$ in the central part of the domain and increases both in the strait of Gibraltar and in the Turkish Strait System, reaching a resolution of the order of the hundreds of meters, to describe accurately the exchange of water with the Atlantic Ocean and with the Black Sea. An example of the model bathymetry is shown in Figure 1 for the Turkish Strait System. The total grid points are 2500×752 . The model is discretized vertically using 100 unevenly distributed Z-levels; with a minimum thickness of 2 m in the upper layer.

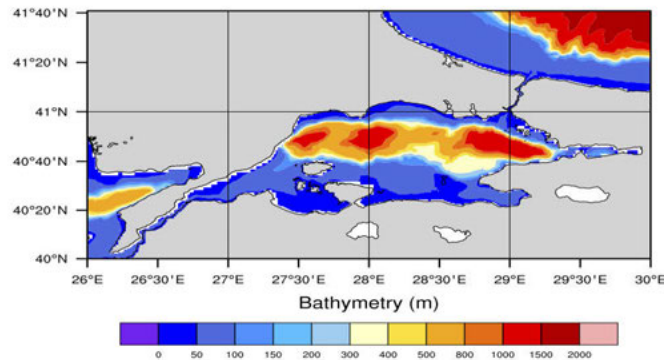


Fig. 1: Bathymetry of the model in the Turkish Strait System.

The fundamental characteristic of the model is the direct simulation of tides, both the internal component and the advected tides incoming through the Strait of Gibraltar. The first 4 tidal components, with period of about 24 (O1 and K1) and 12 hours (M2 and S2) have been included. The setup of the tidal forcing was obtained through a series of experiments aimed to verify the correctness of phase and amplitude of the different components simulated against experimental data, inside the domain. The incoming tidal component has been applied at the western Atlantic boundary using tidal components derived from the OTIS global inverse tide model.

At present the model is running operatively on 800 CPUs of CRESCO4. The simulations start daily and produce forecast for the next 4.5 days of the principal thermodynamic variables. The model is re-initialized weekly using 3D salinity and temperature fields from a coarser resolution Mediterranean forecast system (MFS). MFS provides also lateral boundary conditions in the Atlantic sea. The model is forced at the surface by winds and other atmospheric data derived from the meteorological regional model SKIRON developed by the Atmospheric Modelling and Weather Forecasting Group of the University of Athens.

3 Results

The validation of the modelled tides has been checked in a simulation in which only the tidal components were prescribed. The harmonic analysis of the sea surface height has been verified against the values of the OTIS model. M2 is the predominant component in the Mediterranean. In Figs. 2 and 3 are shown amplitude and phase derived from MITgcm and from the global inverse

model. All the principal characteristics are well reproduced, with maximum amplitudes in the Mediterranean, near the strait of Gibraltar, in the northern Adriatic and in the Gulf of Gabes. Also the positions of the amphidromic points, represented in the map of phase, are in good agreement with the OTIS model.

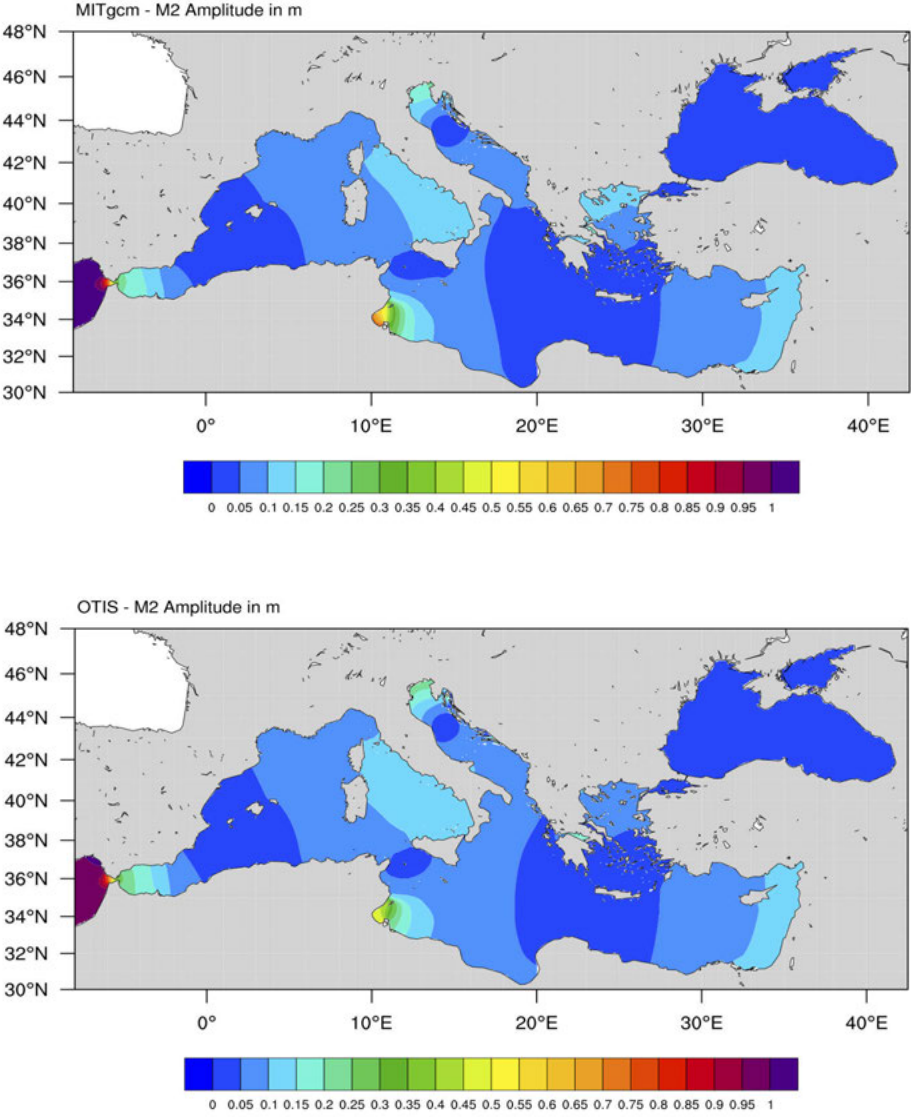


Fig. 2: Amplitude (in m) of M2 tidal component derived from the model (upper panel) and from OTIS data (lower panel).

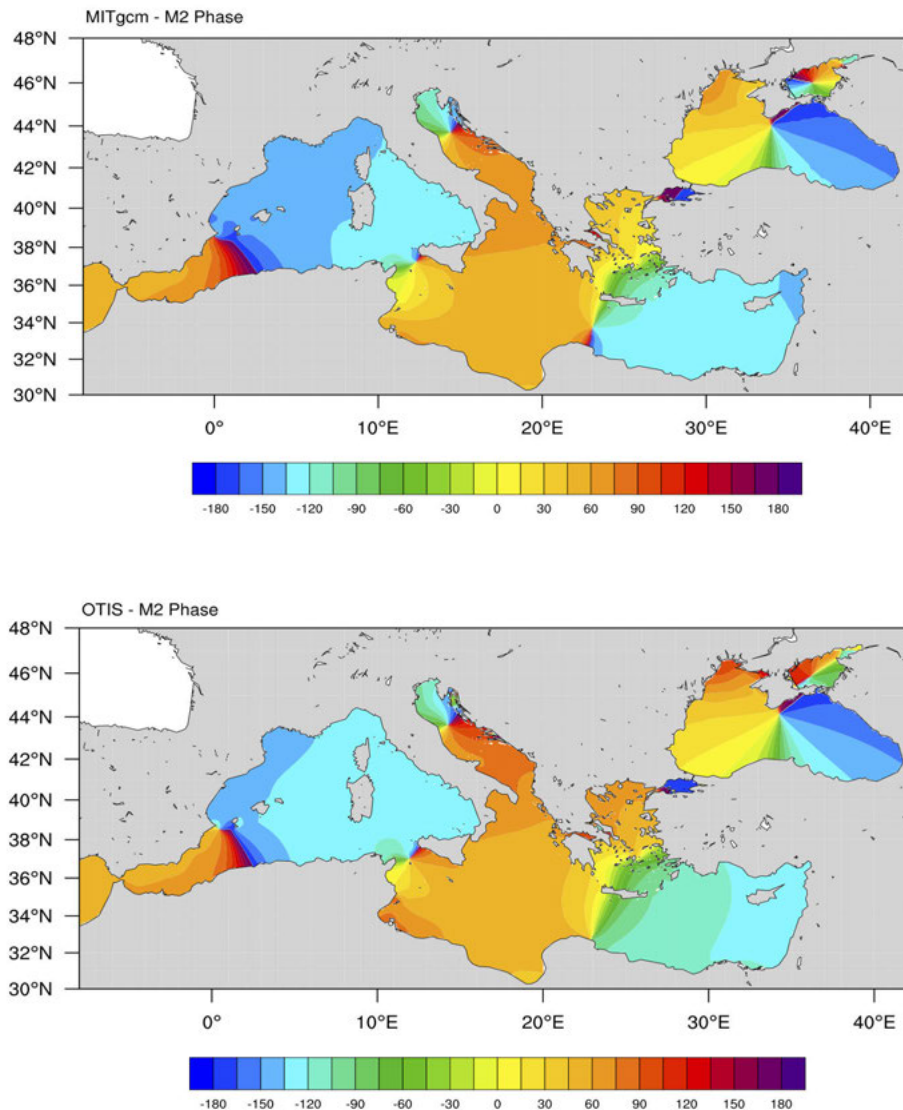


Fig. 3: Phase in degrees of the M2 tidal component derived from the model (upper panel) and from OTIS data (lower panel).

References

- [1] G. Sannino, A. Carillo, G. Pisacane, C. Naranjo. On the relevance of tidal forcing in modelling the Mediterranean thermohaline circulation *Progress in Oceanography*, **134**, pp. 304-329. (2015) DOI: 10.1016/j.pocan.2015.03.00
- [2] G. Sannino, M. Herrmann, A. Carillo, V. Rupolo, V. Ruggiero, V. Artale, P. Heimbach. An eddy-permitting model of the Mediterranean Sea with a two-way grid refinement at the Strait of Gibraltar (2009) *Ocean Modelling*, **30** (1), pp. 56-72. DOI: 10.1016/j.ocemod.2009.06.002
- [3] J. Marshall, A. Adcroft, C. Hill, L. Perelman, C. Heisey A finite-volume, incompressible Navier Stokes model for studies of the ocean on parallel computers. *J. Geophys. Res.* **102** -C3 (1997) pp. 5753–5766.

COMPUTATIONAL DESIGN AND VALIDATION OF A RECONFIGURABLE THREE-DIMENSIONAL DNA NANOSTRUCTURE

Federico Iacovelli¹ and Mattia Falconi¹

¹*Università degli Studi di Roma “Tor Vergata”, Dipartimento di Biologia, Via della Ricerca Scientifica 1, 00133, Roma, Italia*

e-mail: falconi@uniroma2.it, federico.iacovelli@uniroma2.it

ABSTRACT. In the last twenty years, DNA has been extensively used as an efficient building block for the creation of predesigned, self-assembling 2D or 3D nanostructures. Molecular dynamics (MD) is now becoming essential for this kind of biological research, with promising opportunities and challenges. In recent years, MD atomistic simulations have been successfully used by our group to characterize the structure and dynamics of different nanostructures, spanning by simple DNA polygons to complex dynamical structures able to trap and release a cargo. In this paper, we used this computational approach to design and simulate, through the CRESCO HPC systems, the behavior of a novel octahedral DNA nanocage, able to change its conformation from a closed to open state, upon binding of four complementary DNA sequences (fuel oligonucleotides) by using a strand-displacement mechanism. Experimental assembly of the structure confirmed the results obtained by the simulations, assessing the validity of simulative approach in the prediction of DNA nanostructures stability and behavior.

1. Introduction

DNA nanotechnology has provided novel outstanding chemical approaches for designing and engineering smart nanomaterials and nanodevices.[1–4] Current methodologies and synthetic strategies, such as DNA tiles, origami or supramolecular assembly, allowed the production of complex nanostructures of different shapes and dimensions.[5–8] The unparalleled versatility of these approaches allow precise positioning of molecule-responsive switching elements in specific locations of DNA nanostructures, leading to the construction of more complex functional nanodevices.[9,10] DNA motifs that rely on non-canonical DNA interactions, such as G-quadruplex, triplex, i-motif, hairpin and aptamers, can be used to design such nanodevices, due to their dynamic-responsive behaviour towards chemical and environmental stimuli.[11,12] These responsive units often respond to specific chemical inputs through a binding-induced conformational change mechanism that leads to a measurable output or function. The synergy between experiments and molecular dynamics (MD) simulations may provide significant information for the rational design of functional nanodevices and in recent years MD atomistic simulations have been successfully used to characterize structure and dynamics of DNA nano-structures.[10,13] Exploration of the properties of a truncated octahedral DNA nano-cage family has permitted us to show unusual curvature and stacking imposed by the nano-structure that have never been observed in the simulation of short DNA strands.[14] Recently we couple experimental and simulative techniques to deeply characterize the structural/dynamical behaviour of a pH-triggered switching mechanism based on the formation of a parallel DNA triple helix.[15] These results validate the pH-controlled behaviour of the designed structure, show that simulative approaches can be successfully coupled with experimental data to

characterize responsive DNA-based nanodevices, and indicate that the use of DNA nano-cage designed for controlled encapsulation, release and cell target-delivery of biomolecules represents an ambitious target in nano-biomedicine. In this paper we describe the results achieved using the HPC CRESCO facilities to design and characterize a reconfigurable 3D DNA nanostructure. This nanostructure, based on a previously published octahedral geometry hosting DNA hairpins,[10] is able to change its conformation from a closed to open state upon binding of four complementary DNA sequences (fuel oligonucleotides) by using a strand-displacement mechanism. Experimentally, incubation of the nanocages with the fuel oligonucleotides leads to a deformation and opening of the structure induced by the hairpins displacement. The presence of a tail at the end of the fuel, complementary to the antifuel, acts as a primer for a second strand displacement mechanism, where addition of antifuel oligonucleotides reverts the nanocage conformation to the closed state (Fig. 1).

2. Materials and Methods

Model building of the DNA cages. The octahedral portion of the DNA nanocage was built using our Polygen software,[16] using oligonucleotides sequences previously designed to experimentally assemble truncated octahedral geometries.[10] The cage states modelling was executed using the SYBYL 6.0 program (TRIPOS, <http://www.tripos.com>), manually adding to the octahedral structure four DNA hairpins, modelling the closed (Fig 1A) and open (Fig 1B) states. The steric clashes introduced by the modelling procedure have been removed through the SYBYL anneal module and then a first minimization of the entire structures has been performed using the SYBYL maximin2 module. The system topologies and the coordinates, used as input for the NAMD 2.12 MD package,[17] have been obtained through the AmberTools14 tLeap module,[18] parameterizing the structures through the AMBER parmbsc1 force field.[19] The structures have been immersed in a cubic box filled with TIP3P water molecules, imposing a minimum distance between the solute and the box of 14 Å, whereas the charges have been neutralized adding, in electrostatically favorable positions, magnesium counter-ions to the solvated systems.

Equilibration and MD protocol. The nanocages were subjected to two minimization runs. In the first one restraints of 5.0 kcal/mol-Å² have been imposed on all the cages atoms to relax the water molecules and the ions, in the second one the cages have been minimized without any restraint to relax the entire system. A thermalization procedure, using the NVT ensemble has been carried out on the minimized structure gradually heating the systems from 0 K to 300 K, increasing temperature of 10 K every 30 ps. The optimized systems have been then simulated using periodic boundary conditions for 200 ns, with a 2.0 fs time-step, using the isobaric-isothermal ensemble (NPT). The electrostatic interactions have been calculated every 4.0 fs, using a cut-off of 10 Å for the evaluation of short-range non-bonded interactions and the PME method for the long-range electrostatic interactions. The SHAKE and the SETTLE algorithms have been used to constrain the nucleic acids and the water molecules, respectively. Temperature has been fixed at 300 K using Langevin dynamics, while pressure has been held constant at 1 atm through the Langevin piston method. The atomic positions have been saved every 1000 steps (2.0 ps) for the analyses. The simulations have been performed using 16 nodes, for a total of 256 CPUs, on the CRESCO 4 partition of the ENEA HPC cluster.

Experimental assembly of the designed cage. The experimental assembly of the structures has been performed as previously reported.[20]

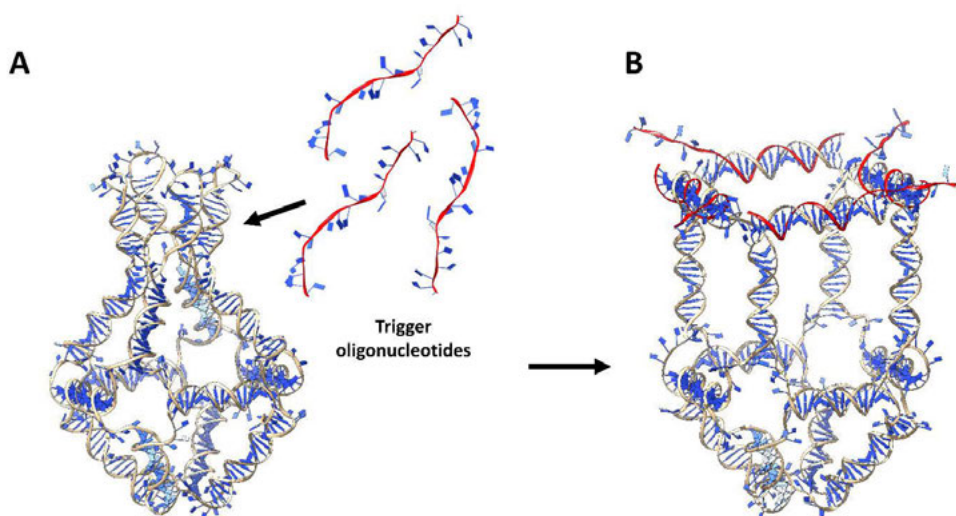


Fig. 1. Three-dimensional representations of the closed (A) and open (B) states of the designed octahedral DNA nanostructure. The binding of the fuel oligonucleotides (trigger) to the hairpins in closed state induces the cage remodeling into the open configuration.

3. Results

Simulative characterization of the DNA nanostructure

Figure 2 shows the total RMSD calculated as a function of time over all the atoms of the closed (black line) and open (red line) nanocage states, using as reference the final coordinates obtained from the equilibration procedure. The closed and open cage RMSD values increase slightly differently in the first 140 ns, reaching the stability only in the last 40 ns. The large increase in the RMSD values is mostly due to the oscillation of the DNA hairpins over the octahedral geometry in the case of the closed state, while in the open it is mainly due to a shrink of the bottom region of the scaffold, which balances the structural deformations induced by the binding of the four hairpins with the fuel oligonucleotides. In line with previous simulations of similar DNA nanostructure, the octahedral scaffold is well conserved along the entire trajectories.[14,21]

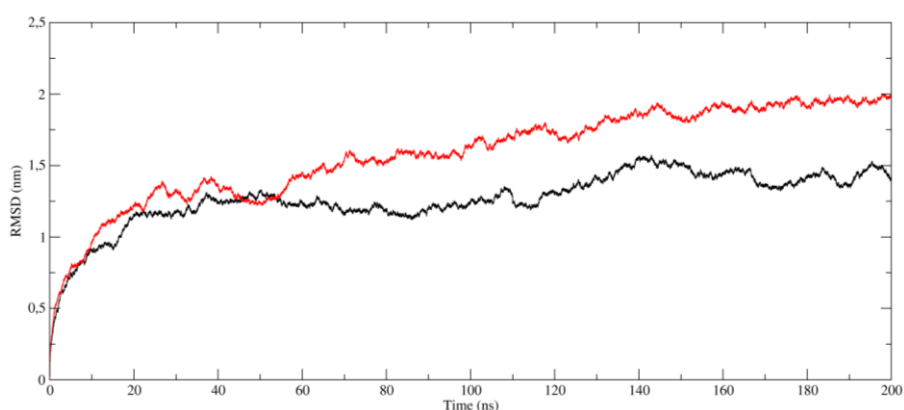


Fig. 2. RMSD calculated as a function of time over all the atoms of the closed (black line) and open (red line) nanocage states.

The radius of gyration (RG) of the open state (Fig. 3, red line) is constantly larger than that of the closed state (Fig. 3, black line), the average RG values being approximately 7.2 and 6.2 nm for the open and closed states simulation, respectively, indicating that the difference between the two structural states could be easily detected through a simple gel electrophoresis experiment. These analyses indicate that both states are stable and suggest the possibility to control the open and close states of the structure. To further validate this hypothesis, time dependent evolution of hydrogen bonds has been evaluated for the four hairpins in the case of the closed state and for the tails of fuel oligonucleotides in the case of the open state.

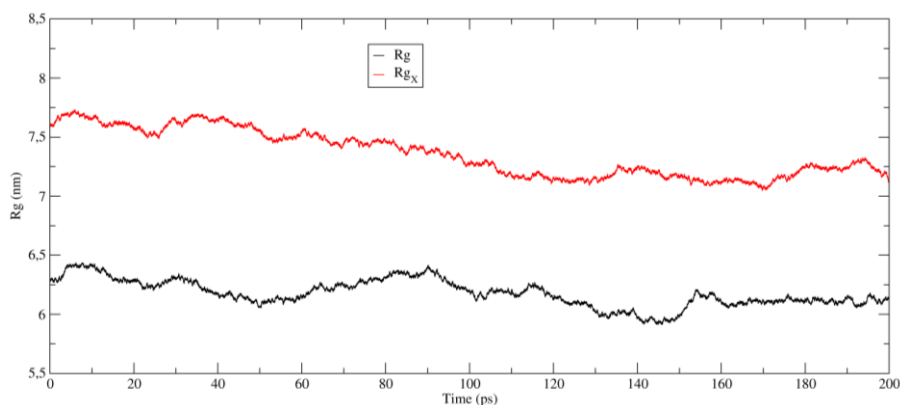


Fig. 3. Radius of gyration calculated as a function of time over all the atoms of the closed (black line) and open (red line) nanocage states.

In detail, in Fig. 4 is reported the evolution of the hydrogen bonds (HBs) evaluated for the four DNA hairpins hosted in the octahedral geometry. The average HBs number oscillates around 15-17, out of 28 possible, indicating that the hairpins are not fully stable and are prone to interact with the designed fuel oligonucleotide. Fig. 5 shows the results of the same analysis performed to evaluate the number of HBs interactions between the terminal parts of the fuel oligonucleotides with the cage scaffold. As can be observed, only 2 out of 10 possible hydrogen bonds can be detected for the four tails, indicating that they are not firmly interacting with the cage scaffold and are free to interact with the antifuel oligonucleotides. These computational results confirm that the designed structure can efficiently works as a reconfigurable structure and can be assembled for this purpose.

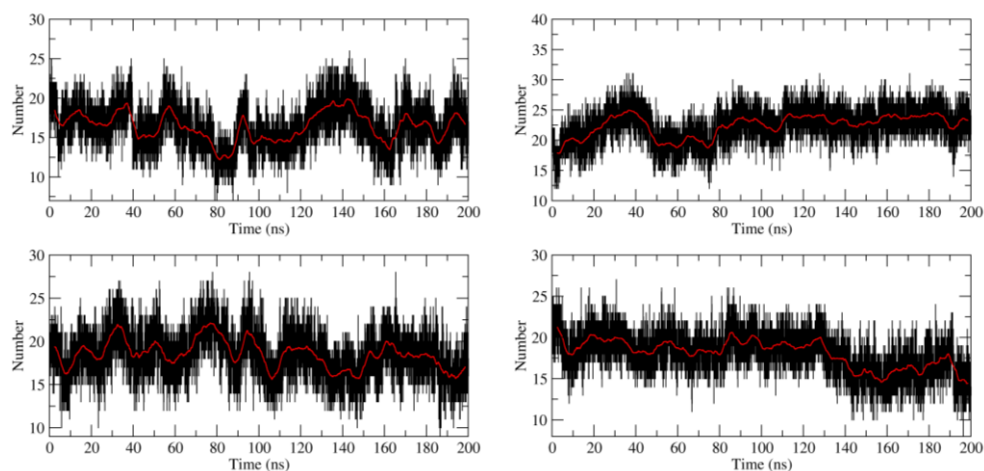


Fig. 4. Number of hydrogen bonds calculated as a function of time for the four DNA hairpins hosted on the cage. The red line shows the same values averaged every 500 frames.

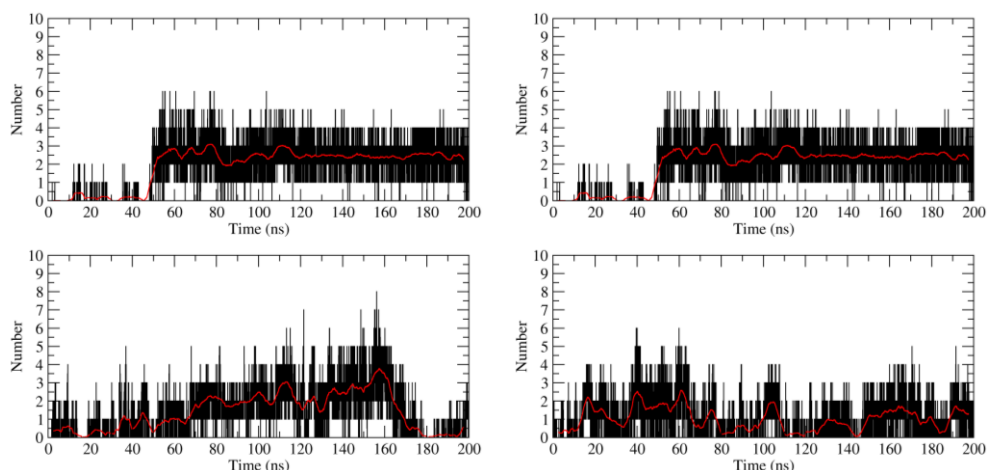


Fig 5. Number of hydrogen bonds calculated as a function of time between the tails of the fuel oligonucleotides and the cage's scaffold. The red line shows the same values averaged every 500 frames.

Experimental assembly and analysis of the cage structural reconfiguration To verify the ability of the nanocages to bind the fuel oligonucleotides, three different samples have been prepared: a) nanocages, b) nanocages plus fuel oligonucleotides and c) sample treated with the fuel followed by the addition of the antifuel oligonucleotides. A change in conformation can be monitored on a native polyacrylamide gel. As noticed from the gel, the band of the untreated cage (Fig. 6, lane 1) is shifted upon the addition of the fuel (Fig. 6, lane 2) and it reverts to the same height upon addition of the antifuel (Fig. 6, lane 3), validating the prediction obtained through the MD simulations analyses indicating the correctness of the design.

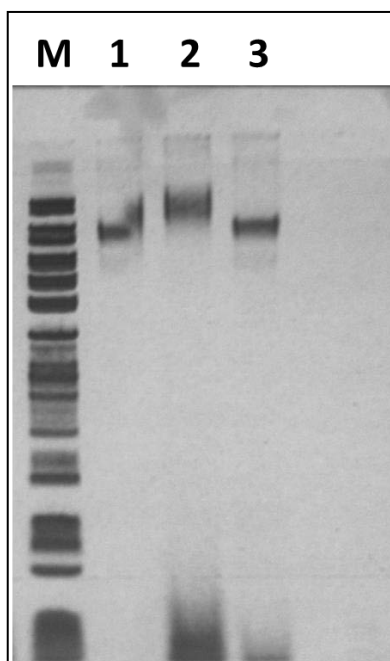


Fig. 6. Gel electrophoretic results of the structural reconfiguration experiment, where the fuel oligonucleotide was added to the closed cage (lane 1) to induce the opening of the structure (lane 2). When the antifuel oligonucleotides are added to the sample treated with the fuel, the closed state is reformed (lane 3). Lane M contains DNA markers.

4. Conclusions

Concluding, with the help of the HPC resource available on ENEAGRID platform, we were able to perform the design and molecular dynamics simulation of a novel DNA nanostructure that is able to change its 3D conformation upon binding of small DNA oligonucleotides. Given the huge size of the simulated systems (over a million atoms) this result would have been unfeasible without the use of the computational capabilities of CRESCO 4 HPC cluster. The ability of this new structure could be implemented, upon proper nucleotide sequence modifications, in novel reconfigurable nanodevices designed for biomedical purposes to entrap and release small molecules as well as to detect or sequester circulating miRNAs.

5. References

- [1] Kuzyk A, Schreiber R, Fan Z, Pardatscher G, Roller E-M, Högele A, et al. DNA-based self-assembly of chiral plasmonic nanostructures with tailored optical response. *Nature* 2012;483:311–4. doi:10.1038/nature10889.
- [2] Veneziano R, Ratanalert S, Zhang K, Zhang F, Yan H, Chiu W, et al. Designer nanoscale DNA assemblies programmed from the top down. *Science* 2016;352:1534. doi:10.1126/science.aaf4388.
- [3] Liu W, Halverson J, Tian Y, Tkachenko A V., Gang O. Self-organized architectures from assorted DNA-framed nanoparticles. *Nat Chem* 2016;1–7. doi:10.1038/nchem.2540.
- [4] Ke Y, Meyer T, Shih WM, Bellot G. Regulation at a distance of biomolecular interactions using a DNA origami nanoactuator. *Nat Commun* 2016;7:10935. doi:10.1038/ncomms10935.
- [5] Rothemund PWK. Folding DNA to create nanoscale shapes and patterns. *Nature* 2006;440:297–302. doi:10.1038/nature04586.
- [6] Douglas SM, Marblestone AH, Teerapittayanon S, Vazquez A, Church GM, Shih WM. Rapid prototyping of 3D DNA-origami shapes with caDNAno. *Nucleic Acids Res* 2009;37:5001–6. doi:10.1093/nar/gkp436.
- [7] Wei B, Dai M, Yin P. Complex shapes self-assembled from single-stranded DNA tiles. *Nature* 2012;485:623–6. doi:10.1038/nature11075.
- [8] McLaughlin CK, Hamblin GD, Aldaye F a, Yang H, Sleiman HF. A facile, modular and high yield method to assemble three-dimensional DNA structures. *Chem Commun (Camb)* 2011;47:8925–7. doi:10.1039/c1cc11726b.
- [9] Andersen ES, Dong M, Nielsen MM, Jahn K, Subramani R, Mamdouh W, et al. Self-assembly of a nanoscale DNA box with a controllable lid. *Nature* 2009;459:73–6. doi:10.1038/nature07971.
- [10] Juul S, Iacovelli F, Falconi M, Kragh SL, Christensen B, Frøhlich R, et al. Temperature-Controlled Encapsulation and Release of an Active Enzyme in the Cavity of a Self-Assembled DNA Nanocage. *ACS Nano* 2013;7:9724–34. doi:10.1021/nn4030543.
- [11] Yatsunyk LA, Mendoza O, Mergny JL. “Nano-oddities”: Unusual nucleic acid assemblies for DNA-based nanostructures and nanodevices. *Acc Chem Res* 2014;47:1836–44. doi:10.1021/ar500063x.
- [12] Wang F, Liu X, Willner I. DNA switches: From principles to applications. *Angew Chemie - Int Ed* 2015;54:1098–129. doi:10.1002/anie.201404652.
- [13] Franch O, Iacovelli F, Falconi M, Juul S, Ottaviani A, Benvenuti C, et al. DNA hairpins promote temperature controlled cargo encapsulation in a truncated octahedral nanocage structure family. *Nanoscale* 2016. doi:10.1039/c6nr01806h.
- [14] Iacovelli F, Falconi M, Knudsen BR, Desideri A. Comparative simulative analysis of single and double stranded truncated octahedral DNA nanocages. *RSC Adv* 2016;6:35160–6. doi:10.1039/C5RA27591A.

- [15] Iacovelli F, Idili A, Benincasa A, Mariottini D, Ottaviani A, Falconi M, et al. Simulative and Experimental Characterization of a pH-Dependent Clamp-like DNA Triple-Helix Nanoswitch. *J Am Chem Soc* 2017;139:5321–9. doi:10.1021/jacs.6b11470.
- [16] Alves C, Iacovelli F, Falconi M, Cardamone F, Morozzo Della Rocca B, De Oliveira CLP, et al. A Simple and Fast Semiautomatic Procedure for the Atomistic Modeling of Complex DNA Polyhedra. *J Chem Inf Model* 2016;56:941–9. doi:10.1021/acs.jcim.5b00586.
- [17] Phillips JC, Braun R, Wang W, Gumbart J, Tajkhorshid E, Villa E, et al. Scalable molecular dynamics with NAMD. *J Comput Chem* 2005;26:1781–802. doi:10.1002/jcc.20289.
- [18] Salomon-Ferrer R, Case DA, Walker RC. An overview of the Amber biomolecular simulation package. *Wiley Interdiscip Rev Comput Mol Sci* 2013;3:198–210. doi:10.1002/wcms.1121.
- [19] Ivani I, Dans PD, Noy A, Pérez A, Faustino I, Hospital A, et al. Parmbsc1: a refined force field for DNA simulations. *Nat Methods* 2015;13:55–8. doi:10.1038/nmeth.3658.
- [20] Vindigni G, Raniolo S, Ottaviani A, Falconi M, Franch O, Knudsen BR, et al. Receptor-Mediated Entry of Pristine Octahedral DNA Nanocages in Mammalian Cells. *ACS Nano* 2016;10:5971–9. doi:10.1021/acsnano.6b01402.
- [21] Iacovelli F, Alves C, Falconi M, Oteri F, de Oliveira CLP, Desideri A. Influence of the single-strand linker composition on the structural/dynamical properties of a truncated octahedral DNA nano-cage family. *Biopolymers* 2014;101:992–9. doi:10.1002/bip.22475.

CALCULATION OF CORRECTION FACTORS FOR SOLID-STATE DETECTORS IN RADIOTHERAPY PHOTON BEAMS

Maria Pimpinella* and Luca Silvi

ENEA-FSN-INMRI, National Institute of Ionizing Radiation Metrology, C. R. Casaccia, Via Anguillarese 301, 00123 Rome, Italy

ABSTRACT. Correction factors accounting for effects due to the non-water equivalence of detector materials and the detector size are calculated by Monte Carlo simulations as a function of field size in 6 MV beams for a silicon diode and a diamond detector. Simulations are performed on CRESCO4 cluster using the EGSnrc Monte Carlo system. Results show that to perform accurate dosimetry in small radiotherapy photon beams the silicon diode requires correction even larger than 5% while corrections are always within 1.5% for the diamond detector.

1 Introduction

Use of small photon beams in modern radiotherapy techniques such as Intensity Modulated Radiation Therapy (IMRT), Volumetric Modulated Arc Therapy (VMAT) and Stereotactic Radiotherapy (SRT) allows to generate dose distributions with high degree of conformity to the target volume and sparing of healthy tissue. On the other hand the accuracy of a radiotherapy treatment delivery depends on dosimetric data on which the treatment planning system is based. Then, when using advanced radiotherapy modalities accurate absorbed dose measurements in small fields are required to ensure that the correct amount of radiation is delivered to the patient. Dosimetry in small fields differs significantly from measurement in broad beams because the absence of lateral charge particle equilibrium and the not sufficiently large region with uniform particle fluence make the well-established dosimetric methods based on ionization chamber measurements [1] not applicable. Solid-state detectors are characterized by small size and therefore are more suitable than ionization chambers for measurements in small beams, however correction factors accounting for the non-water equivalence of the detector materials and the finite size of the active volume need to be evaluated to perform accurate absorbed dose to water (D_w) measurements. According to [2] reference dosimetry by a solid-state detector requires the detector calibration in terms of D_w in broad beam (10 cm x 10 cm field size) against a reference ionization chamber and the determination of specific correction factors accounting for the dependence on beam size of the detector response.

In this work the overall field size correction factor is expressed as a product of two factors k_m and k_{vol} . k_m accounts for differences in atomic properties and mass density between water and all the detector materials and k_{vol} accounts for effects due to the detector size (*volume averaging effect*). The factors k_m and k_{vol} are determined by Monte Carlo calculation for two commercial solid-state detectors in 6 MV clinical beams.

2 Methods

Assuming that the detector signal is proportional to the absorbed dose in the detector sensitive medium, (i.e. the ratio between the energy deposited by radiation in the active material and its mass) k_m and k_{vol} can be calculated by Monte Carlo simulation as:

$$k_m = \frac{D_{w,det}}{D_{m,det}} \quad (1)$$

$$k_{vol} = \frac{D_{w,point}}{D_{w,det}} \quad (2)$$

where $D_{m,det}$ and $D_{w,det}$ are the average absorbed doses scored in the detector active volume by simulating the irradiation in water of the actual detector (shape and materials according to the manufacturer's drawings) and of an ideal detector with the same shape entirely made of water.

$D_{w,point}$ in (2) is the absorbed dose to water scored in a small cubic voxel centred at the measurement point in homogeneous water. The voxel size is chosen small enough to make the beam non-uniformity across the voxel negligible thus the point value of absorbed dose is well approximated by the average value scored in the voxel.

In this work k_m and k_{vol} have been determined for a silicon diode, type PTW 60017 (Si), and a diamond detector, type PTW 60019 (mD) in 6 MV photon beams with field size from 5 mm to 100 mm. The detector characteristics pertaining to the Monte Carlo simulations are reported in Table 1.

The tools BEAMnrc [3] and *egs_chamber* [4] available in the EGSnrc Monte Carlo system [5] have been used. Firstly phase-space files (PSFs) describing the actual photon beams produced by a clinical accelerator were obtained using the BEAMnrc code. Then each PSF was used as input radiation source into *egs_chamber* for simulating the detectors irradiation in a water tank 30x30x30 cm³ at 5 cm depth and scoring the absorbed doses to be used for determining k_m and k_{vol} according to equations (1) and (2).

Cross section data for the radiation transport in all the detector materials were generated by the PEGS4 code included in the EGSnrc package. Three independent simulations were run for each field size and detector. The number of simulated histories varied according to the simulation geometry (beam size and type of detector) so as to obtain a statistical uncertainty of the absorbed dose results of less than 0.3%.

EGSnrc is installed on the cluster CRESCO4 in shared mode. Calculations were performed in parallel using a number of cores ranging from 12 to 100. Total CPU time was in the range from 20 to 70 hours for the beam simulations (longer time for the smallest field sizes) and in the range from 100 to 400 hours for the absorbed dose calculations (longer time for the largest field sizes).

Table 1: Silicon diode (Si) and diamond detector (mD) characteristics.

Detector type	Active volume thickness (μm)	Active volume diameter (mm)	Active material density (g cm ⁻³)	Active material Z	Extra cameral materials
Si	30	1	2.3	14	8
mD	1	2.2	3.5	6	8

3 Results and discussion

Figure 1 shows the k_m factor calculated by Monte Carlo for the Si and mD detectors as a function of field size from 10 cm to 0.5 cm in 6 MV photon beams. Variations in the k_m value relative to the value in the reference field (10 cm) are significant for the mD detector only at the smallest field sizes

(i.e. below 2 cm) while variations are always significant for the Si detector. Moreover it should be noted that the maximum k_m variation is below 3% for the mD and up to 7 % for the Si. The stronger non-water equivalence effects found out for the Si detector can be ascribed to the higher Z value (16) compared to the effective Z value of water (6.4) even if effects due to extra cameral materials cannot be excluded. Diamond has atomic number (6) very close to water and its non-water equivalence is mainly due to the high mass density relative to water. However, it is well known that the mass density affects the detector response only in absence of lateral charge particle equilibrium (i.e. below 1.5 cm in 6 MV beams) [6], and this is consistent with the k_m variation shown in Figure 1.

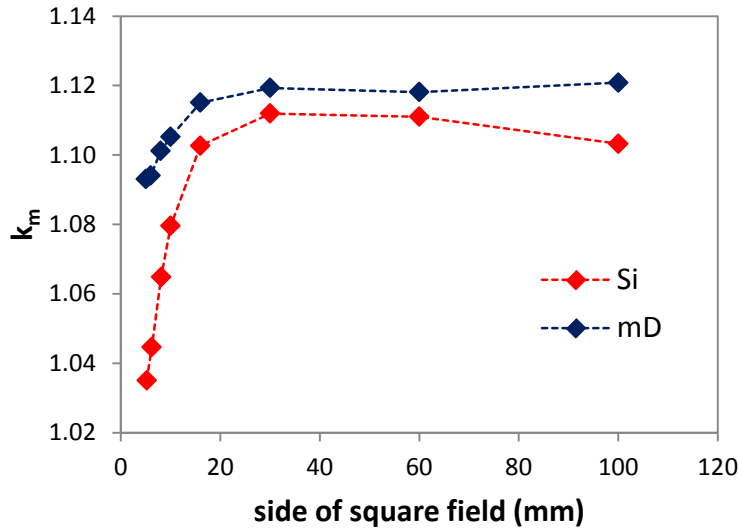


Fig.1: Correction factors accounting for the non-water equivalence effects of Si and mD detectors in 6 MV photon beams.

Concerning the k_{vol} factor, deviations from unity are no larger than 0.4% for the Si while up to 3% for the mD. Despite the active volume is smaller for the mD than for the Si, a larger k_{vol} correction is obtained for the mD. Indeed the volume averaging effect is mainly related to the beam non-uniformity over the detector section perpendicular to the beam direction. Then the larger diameter of the mD causes a stronger volume averaging effect. However, it is worth noting that the mD volume effect becomes significant only in field sizes smaller than 8 mm.

Figure 2 shows the overall field size correction factor for the Si and mD detectors. For the Si a slight increase in the correction is observed from 10 cm to 3 cm field size, then the correction quickly decrease with field size below 3 cm. Due to the weak volume effect the overall Si correction is very close to the k_m factor, indicating a detector overresponse response larger than 5% in very small field sizes compared to the reference field. For the mD detector the overall correction does not changes more than 1.5% over all the range of field sizes studied. The behaviour of the overall mD correction factor observed in Figure 2 originates from a trade-off between non-water equivalence and volume averaging effects. Indeed when the field size decrease below 1 cm the non-water equivalence causes a detector over response and the volume averaging a detector under response, then the two effects partially compensate each other reducing the dependence of detector response on field size. An experimental validation of the overall correction factors presented in this report can be found in [7].

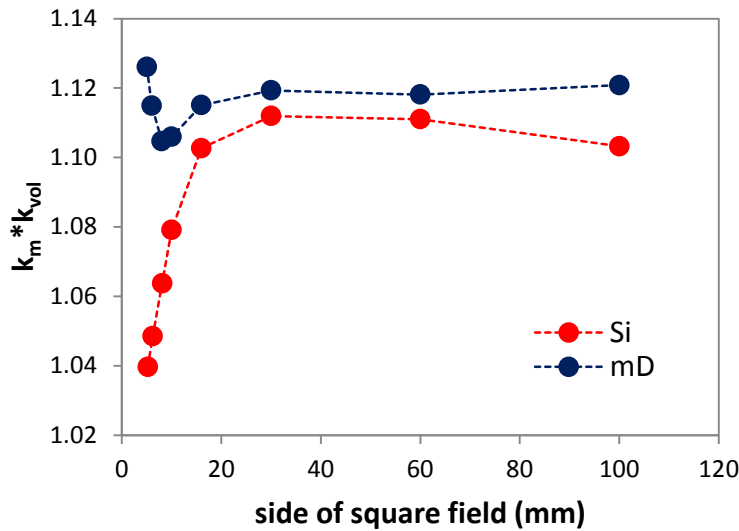


Fig.2: Overall field size correction factors for Si and mD detectors in 6 MV photon beams.

Acknowledgment

The authors would like to thank PTW-Freiburg, Germany, for providing detailed drawings of the two solid-state detectors.

References

- [1] P. Andreo, D.T. Burns, K. Hohlfeld, M. Huq, T. Kanai, R.F. Laitano, V. Smyth and S. Vynckier. Absorbed dose determination in external beam cancer therapy; An International Code of Practice for Dosimetry Based on Standards of Absorbed Dose to Water. IAEA-TRS 398, Vienna (2000).
- [2] R. Alfonso, P. Andreo, R. Capote, M. Saiful Huq, W. Kilby, P. Kjäll P et al. A new formalism for reference dosimetry of small and nonstandard fields. *Med. Phys.* **35**, pp. 5179–5186, (2008).
- [3] D.W.O. Rogers, B. Walters and I. Kawrakow. BEAMNRC Users Manual, NRC Report PIRS 509 (A) Rev. L, Ottawa (2013).
- [4] J. Wulff, K. Zink and I. Kawrakow. Efficiency improvements for ion chamber calculations in high energy photon beams. *Med. Phys.* **35**, pp.1328-1336, (2008).
- [5] I. Kawrakow, E. Mainegra-Hing, D.W.O. Rogers, F. Tessier and B.R.B.Walter. The EGSnrc Code System: Monte Carlo simulation of electron and photon transport NRC Report PIRS 701, Ottawa (2013).
- [6] A.J. Scott, S. Kumar, A.E. Nahum and J.D. Fenwick. Characterizing the influence of detector density on dosimeter response in non-equilibrium small photon fields. *Phys. Med. Biol.* **57**, pp. 4461-4476, (2012).
- [7] V. De Coste, P. Francescon, Marco Marinelli, L. Masi, L. Paganini, M. Pimpinella, G. Prestopino, S. Russo, A. Stravato, C. Verona and G. Verona-Rinati. Is the PTW 60019 microDiamond a suitable candidate for small field reference dosimetry?. *Phys. Med. Biol.* **62**, pp. 7036-7055, (2017).

HYDROGEN INTERACTION WITH TiO₂ SURFACE

Radojka Vujasin^{*}, Bojana Paskaš Mamula,
Jasmina Grbović Novaković, Nikola Novaković

Vinča Institute of Nuclear Sciences, University of Belgrade, P.O. Box 522, 11001 Belgrade, Serbia

ABSTRACT. The hydrogen interaction with the rutile TiO₂ (110) surface has been investigated. Numerical model was set up to perform first principle calculations based on density functional theory, using CPMD code. Molecular dynamic simulations were performed to investigate the impact of hydrogen surface coverage on the properties and behavior of the system.

1 Introduction

Titanium dioxide attracts a lot of interest because of its low price, non-toxicity and safe usage. TiO₂ is material used in wide variety of industries, such as in environmental applications and electronic devices. Due to its electronic and optical properties, TiO₂ is known as a good catalyst. It was shown that addition of metal oxides can improve sorption properties of magnesium hydride, one of the most promising materials for hydrogen storage [1, 2]. Development of appropriate hydrogen storage materials is important for safe and sustainable implementation of hydrogen economy.

Studies on hydrogen behaviour and motion through oxide surface have been done to understand the mechanism of the reaction [3]. Yin et al. [4] have investigated hydrogen coverage on TiO₂ (110) surface under different experimental conditions of exposure to atomic hydrogen. They obtained that maximum H monolayer coverage on TiO₂ (110) surface is only 70% at room temperature, regardless of applied partial pressure of hydrogen. The same group confirmed that during heating of the hydrogenated sample, H atoms migrate into TiO₂ bulk. Kowalski et al. obtained the same results [5]. This is unusual behaviour, since desorption of H₂ (or H₂O) molecules into the gas phase is common characteristic of hydroxylated oxide surface.

Filippone et al. carried out research which showed that hydrogen behaves as a deep donor in rutile phase and forms an OH⁺ complex by interaction of H atom with oxygen vacancy, where H formed bond with a prevailing ionic character [6]. They have showed that electronic localization effects treatment have major influence on nature of bonding and charge distribution due to hydrogen incorporation. Also, Ti⁺³ species are formed as a result of localization of H and OH⁺ electronic levels on some Ti neighbours.

Theoretical investigations of rutile TiO₂ with one H and two H atoms adsorbed on the (110) surface were performed with the intention to examine its influence on hydrogen surface coverage on the properties of the system at different temperature.

^{*} Corresponding author. E-mail: radojka.vujasin@gmail.com

2 Details of calculations and results

Numerical study is performed by CPMD (Car–Parrinello Molecular Dynamics) code [7, 8] which uses a plane wave/pseudopotential implementation of Density Functional Theory (DFT) [9, 10]. We use the CPMD compiled with Intel Fortran Compiler, MKL (Math Kernel Library), ACML (AMD Core Math Library) and MPI (Message Passing Interface) parallelization on the high performance ENEA CRESCO computing facilities [11].

Our system is TiO_2 slab supercell with 21 atomic layers with total of 84 atoms of TiO_2 and 1 or 2 H atoms. The surface of the supercells was separated from its periodic image in direction perpendicular to the (110) surface by 15 Å of vacuum. The cell parameters were $a= 5.9779$ Å, $b= 6.6124$ Å, $c= 37.0424$ Å. Three bottom layers were fixed to simulate the bulk. Troullier–Martins normconserving pseudopotentials with GGA-PBE exchange–correlation potential were used for all atoms [12, 13]. The electronic wave functions are expanded in plane-wave basis set with a kinetic energy cut-off equal to 70 Ry.

Two systems were investigated. The first one with one H atom (marked with TiO_2 -1H system), in the first atomic layer, has 50% of surface coverage. The second system (labelled with TiO_2 -2H system) has two H atoms and 100% of surface coverage. One H atom is positioned near O atom in the first atomic layer, and the other is positioned near O atom in the second atomic layer. H atoms are initially positioned at distances corresponding to short O–H bond (approximately 1 Å) in all cases (see Fig. 1).

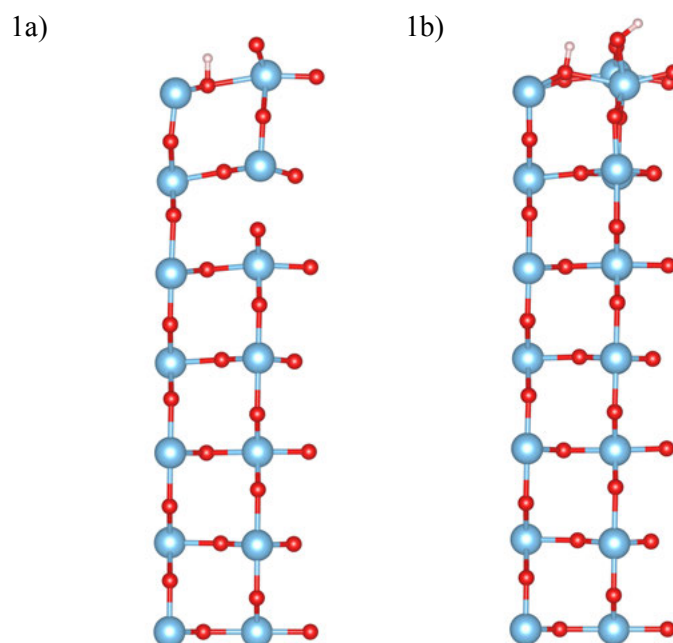


Fig. 1. Slab supercell of TiO_2 surface with H atoms on the surface after geometry optimization. a) TiO_2 -1H system, b) TiO_2 -2H system (Ti atoms – blue, O atoms – red, H atoms - white spheres).

Total energy calculation followed by geometry optimisation was performed for both systems. Structural analysis after geometry optimisation was analysed. In the Fig. 1a) and 1b) are shown supercells of systems after geometry optimization. Ionic relaxations show that there are no

differences in systems comparing to O-H distances, in both cases are 0.98 Å. The addition of the second H atom only slightly disordered the atoms in the first layer of the supercell.

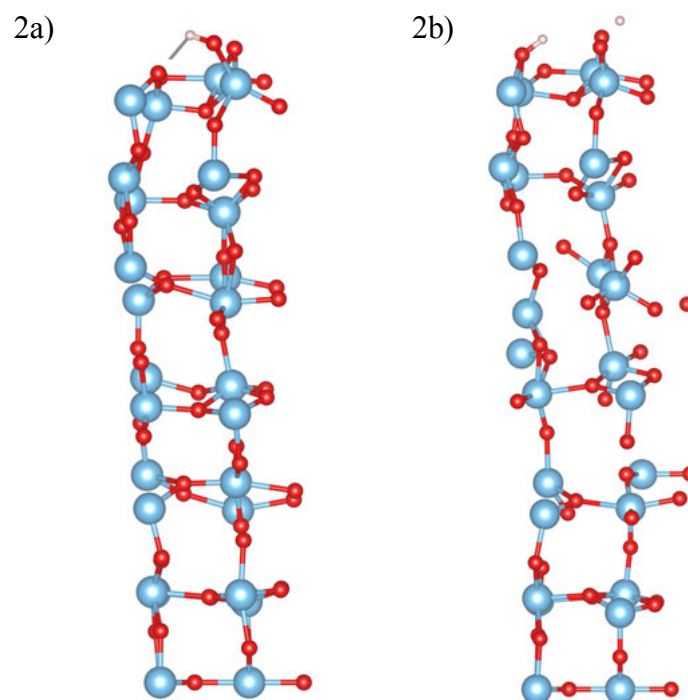


Fig. 2. Snapshot of the systems after 3 ps MD simulations at 450 K. a) $\text{TiO}_2\text{-1H}$ system, b) $\text{TiO}_2\text{-2H}$ system (Ti atoms – blue, O atoms – red, H atoms - white spheres).

MD simulations at constant temperature and constant volume were performed after geometry optimisation of the systems. Temperatures used in simulations were in range 200-500 K in steps of 50 K. MD simulations were performed for about 3 ps with timestep of 4 a.u. at each temperature and hydrogen atoms behavior were characterized. Snapshot of the systems after MD simulations at 450 K are shown in Fig. 2. Displacements of atoms in supercell structure are noticeable in both systems. H atoms are still on the surface near O atoms at the distance of about 1 Å.

To conclude, we performed geometry optimization and MD simulations of rutile TiO_2 (110) surface with adsorbed H atoms to investigate possibility for hydrogen uptake by titanium dioxide during the heating of the system. Heating the systems up to 500 K causes a disorder in both systems without changes H surface coverage.

Acknowledgements

We acknowledge ENEA-HPC team for supporting our computational activities on the ENEAGRID infrastructure. This work was supported by the Ministry of Education, Science and Technological Development of the Republic of Serbia under the Grant III 45012.

References

- [1] L. Schlapbach, A. Züttel. Hydrogen-storage materials for mobile applications. *Nature* **414**, pp 353-358, (2001).
- [2] M. Polanski, J. Bystrzycki. Comparative studies of the influence of different nano-sized metal oxides on the hydrogen sorption properties of magnesium hydride. *Journal of Alloys and Compounds* **486**, 697-701, (2009).
- [3] J. Leconte, A. Markovits, M.K. Skalli, C. Minot, A. Belmajdoub. Periodic ab initio study of the hydrogenated rutile TiO₂ (110) surface. *Surface Science* **497**, pp. 194-204, (2002).
- [4] X.L.Yin, M. Calatayud, H. Qiu, Y. Wang, A. Birkner, C. Minot, Ch. Woll. Diffusion versus desorption: Complex behavior of H atoms on an oxide surface. *Chem.Phys.Chem.* **9**, pp. 253-256, (2008).
- [5] P.M. Kowalski, B. Meyer, D. Marx. *Physical Review B* **79**, pp. 115410, (2009).
- [6] F. Filippone, G. Mattioli, P. Alippi, A. Bonapasta. Properties of hydrogen and hydrogen–vacancy complexes in the rutile phase of titanium dioxide. *Physical Review B* **80**, pp 245203, (2009).
- [7] R. Car, M. Parrinello. Unified Approach for Molecular Dynamics and Density-Functional Theory. *Physical Review Letters* **55**, pp. 2471-2474 (1985).
- [8] CPMD V3.17.1 Copyright IBM Corp 1990-2011, Copyright MPI fuer Festkoerperforschung Stuttgart 1997-2001.
- [9] P. Hohenberg, W. Kohn. Inhomogeneous electron gas. *Physical Review* **136**, pp. B864-B871 , (1964).
- [10] W. Kohn, L. Sham. Self-Consistent Equations Including Exchange and Correlation Effects. *Physical Review* **140**, pp. A1133-A1138, (1965).
- [11] www.cresco.enea.it.
- [12] J.P. Perdew, K. Burke, M. Erzerhof. Generalized Gradient Approximation Made Simple. *Physical Review Letters* **77**, pp. 3865-3868, (1996).
- [13] N. Troullier, J.L. Martins. Efficient pseudopotentials for plane-wave calculations *Physical Review B* **43**, pp. 1993-2006, (1991).

AN ALTERNATIVE USE OF PROMPT-SELF POWERED NEUTRON DETECTORS: SPECTRAL-DECONVOLUTION FOR MONITORING HIGH-INTENSITY NEUTRON FLUXES

Luigi Lepore^{1*}, Romolo Remetti¹, and Antonino Pietropaolo²

¹*SAPIENZA, University of Rome, SBAI Department, Via Antonio Scarpa, 14 - 00161 Rome – Italy*

²*ENEA FSN, Frascati Research Center, via Enrico Fermi, 45 - 00044 Frascati (Rome) - Italy*

ABSTRACT. Self-Powered Neutron Detectors (SPNDs) are currently used in reactors' environment to sense the magnitude of neutron-fluxes, usually for spatial-distribution mapping of the fuel region as to optimize burn-up strategies.

During the development of tailored instrumentation for Lead-cooled Fast Reactors, the possibility to perform online spectral deconvolution of fast neutron-fluxes was recognized.

Seven geometrically similar SPNDs with different neutron-sensitive materials, have been characterized by the Monte Carlo transport code MCNPX. Thanks to a database of spectral sensitivities vs. neutrons' energy, a mathematical deconvolution process from 7 electric current values virtually measured by SPNDs was started, retrieving spectral information, in terms of 7 energy windows, of the neutron-flux the detectors are subjected by.

This paper describes the procedure that led to those results, prefiguring future development to improve proposed method.

1 Introduction

Efforts to make nuclear energy safer and more sustainable were conceived and put in place from 2000 on. The Generation IV International Forum [1] is proposing different concepts for nuclear reactors, especially regarding radioactive waste production and management. In such a context, Fast Reactors (FRs), and Lead Fast Reactor particularly, could mitigate the radio-toxicity of long-lived wastes vs. time thanks to Minor Actinides transmutation and destruction [2], as a perspective for a closed nuclear-fuel cycle [3] [4]. Recently, R&D in material science made the lead-coolant attractive once again for critical (power reactor) and sub-critical applications (ADS, Accelerator Driven System), thanks to the development of special protective layers for steels [5]. Moreover, the chemical stability of this coolant when in contact with water and air if compared to sodium (the concurrent coolant in SFRs) makes lead-applications particularly interesting.

Inside the European Framework, ongoing LFR projects are MYRRHA [6] and ALFRED [7], the first being a sub-critical demonstrator for ADS-type plant, the second being a medium-power demonstrator reactor for electricity production.

Unlike SFRs, Lead Fast Reactors are quite new as neutron-multiplication systems, then LFRs-cores need to be carefully monitored continuously vs. time, at positions close to the fuel region, where the neutron-flux may cause a harsh environment to detector's lifetime. Such a need asks for some solution to be found. Previous work presented in [8], [9], and [10], showed that current devices for fast neutron-flux monitoring in high-temperature environments can be adopted in LFR plants. However, there is evidence that such devices are not completely suitable, due to the maximum burn-up the detectors can tolerate, and gamma-field interferences with neutron signals. Fission chambers

(FCs) have been already tested in the past at SFRs environments [11], as to evaluate responses and performances when monitoring fast neutron fluxes. Even being suitable for such application in terms of detector's sensitivity, they are not foreseen to be used to monitor a fast neutron-flux at power-level continuously, due to the excessive burn-up. FCs appear to be the unique detectors to be applied in reactor start-up, when neutron flux is poor and high sensitivity on counters is needed. At power level, with neutron fluxes at 10^{14} - 10^{15} $\text{n}\cdot\text{cm}^{-2}\cdot\text{s}^{-1}$, prompt-Self Powered Neutron Detectors seem to be the best solution to get a monitoring device capable in lasting several months. However, prompt-SPNDs behaviour as reactor-control instrumentation should be deepened and demonstrated experimentally.

SPNDs, especially in their prompt version, do not have a consolidated irradiation experience, such as fission chambers. In the past, experiences with delayed-SPNDs in thermal, epithermal and fast neutron fluxes were carried out, [12], [13], and [14]), while prompt-SPNDs seem to have been tested in thermal or epithermal conditions only, [15], [16], and [17]). While neutron energies are in the MeV order of magnitude, cross-sections are so small that only high-intensity neutron fluxes ($>10^{12}$ $\text{n}\cdot\text{cm}^{-2}\cdot\text{s}^{-1}$) could generate a measurable electric current signal in prompt-SPNDs. On considering that high-intensity fast-neutron flux facilities turn out to be quite recent, prompt-SPNDs do not have a solid and confirmed irradiation experience as control instrumentation.

Thus, prompt-SPND technology should be deepened to demonstrate capability for safe-and-prompt monitoring of fast neutron fluxes, as envisaged in LFR Demonstrator ALFRED [10]. As a first step for studying SPND performances simulations by the Monte Carlo transport-code MCNPX ver. 2.7.0 (Monte Carlo N-Particles X-version) [18] were carried out, as to reproduce SPNDs characteristics in a virtual world first. A 'mathematical-simulated' model has been proposed and tested in [19], and [20], as to reproduce in simulation SPNDs' responses and performances compatible with real experiments. With such a model, Monte Carlo calculations have been used as a screening tool to initiate a preliminary study on tailored SPNDs, while investigating new materials, geometries, and to conceive new detector prototypes.

In this framework, a new possibility for SPND-use emerged. In studying new materials for activating prompt-SPNDs, 7 nuclides were found worth to be deepened in burn-up studies, and response characterization. In particular, spectral sensitivities, i.e. current response per unit of neutron flux vs. neutron energies, have been considered. During this study, a hypothesis for a new method for realizing online neutron-flux fast-spectrum measurement was conceived, and its proposal is described in this paper.

By means of MCNPX: i) 7 different SPNDs were placed together as an assembly of detectors at a known irradiation position, with the hypothesis that due to detectors' dimensions, each instrument was subjected to the same neutron flux; ii) 7 responses were generated and measured during the exposure to neutron-flux; iii) a mathematical deconvolution process was started, and the neutron-flux spectrum was got in terms of 7 energy-windows, by means of an appropriate algorithm.

This paper shows the basis of such a new use of SPNDs. Simulation applications, involving fast reactors, are used as test-cases.

2 Methodology

SPNDs detectors' output is the record of electric current as a function of time. When such a signal is taken as is, each detector suffers all the limitations mentioned in [19], [21]. about the dependencies of the SPND's current value vs. neutron-flux magnitude and its spectral component contemporary.

With the availability of spectral information vs. time, the flux-weighted neutron cross-section of the sensitive material inside the detector can be correctly evaluated. Then, it would allow to calculate the neutron-flux magnitude from the SPND current measurements, even in those cases that foresee neutron spectrum varying with time.

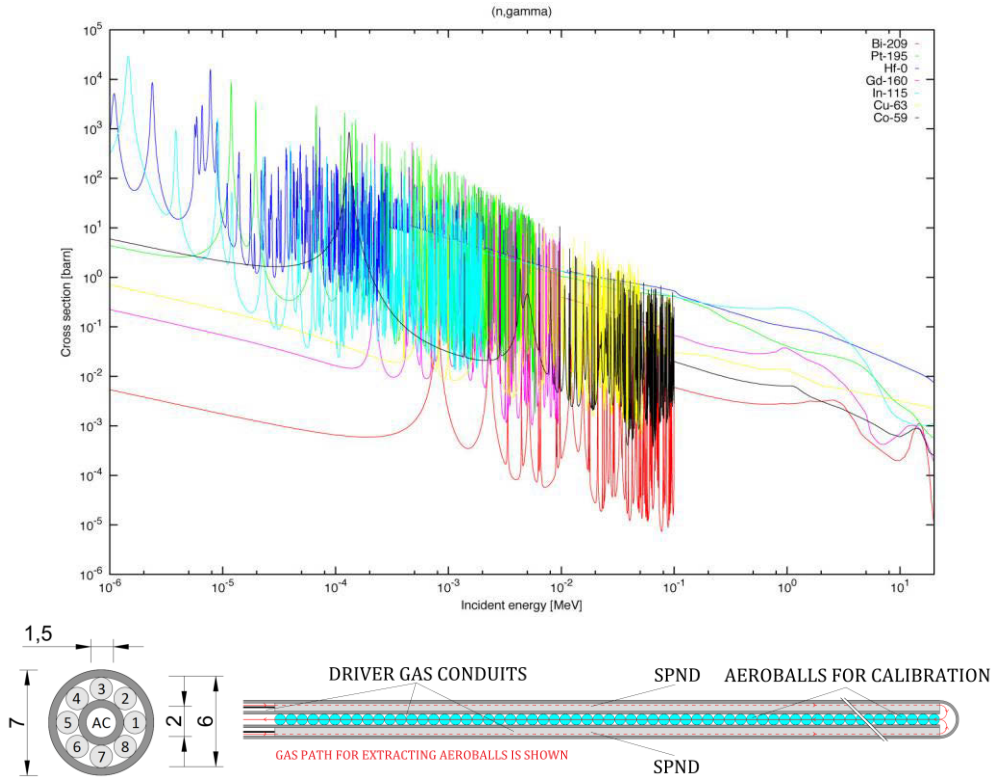


Fig. 1 Up: (n,γ) neutron cross section vs. energy for all isotopes involved. Down: arrangement of the 7 SPNDs inside the spectrometer assembly.

A fixed position \vec{r} inside the reactor is considered, then all dependencies vs. positioning will be neglected to simplify the notation: $\varphi(E) = |p| \cdot \psi(E)$, where φ is the neutron flux decomposed in its components p , magnitude, and ψ , the energy spectrum of neutrons.

On considering a single SPND powered with a material m the reaction rate R into the sensitive volume of the instrument is given by $R = N \cdot V \cdot |p| \cdot \int_0^{\infty} \psi(E) \cdot \sigma_c dE$, where subscript c is referred to neutron-radiative-capture reaction by material m , N is the atomic density of the isotope, V is the volume of the sensitive material inside the detector.

Considering that the SPND operates in current mode, its measured current response I_{TOT} , is the sum of: i) prompt neutron-contribution, ii) prompt gamma-current from the reactor gamma-ray field, iii) delayed contribution due to the detector's materials activation, iv) neutrons and gamma-rays variations associated to reactor's dynamic, v) noise signals, e.g. generated into the detector cable. The amount of such contributions depends firstly on the SPNDs emitter materials. This is due to macroscopic cross-section values, and decay characteristics of the nuclide chosen for sensing neutrons. Some parts of these contributions can be a priori evaluated by simulations. Other ones require experimental measurements. A combination of simulated calculations and real measurements could return the portion of interest $I_{(n,\gamma)}$ of the total current I_{TOT} .

Condensing all parameters, such portion of the measured current can be arranged as $I_{(n,\gamma)} = \int_0^{\infty} S(E) \cdot \varphi(E) dE$ where $S(E)$ is the

spectral sensitivity of material m contained within the SPND. $S(E)$ is the characteristic curve of the SPND; it can be calculated via Monte Carlo simulation of the detector, and stored in a database.

When considering the last equation for $i=1\dots M$ materials in M different SPNDs exposed to the same

neutron-flux, the system of equations $I_{(n,\gamma)}(i) = \int_0^{\infty} S(i,E) \cdot \varphi(E) dE$ becomes a Fredholm equation

of the first kind. The i th domain is discrete, while the E -domain is continuous. $I_{(n,\gamma)}(i)$ electric

currents are measured, and $S(i,E)$ are taken from a database. $\varphi(E)$ can be calculated only if the

energy domain E is discretized, e.g. in K energy-windows. Moreover, integral functions can be

decomposed as sums of j components, with $j=1\dots K$. For the i th detector, $I_{(n,\gamma)}(i) = \sum_{j=1}^K S_{W_j}(i) \cdot \varphi_{W_j}$

is obtained.

S_{W_j} and φ_{W_j} are the spectral sensitivity and the neutron-flux in the W_j energy-window, respectively.

The linear equation system when M detectors are considered, $[\varphi_w] = [S_w]^{-1} \times [I_{(n,\gamma)}]$ only

when $K \equiv M$, then the number of energy-windows to be considered corresponds to the number of detectors involved.

It is clear that the solution $[\varphi_w]$ relies on the particular selection of W_j energy-windows width.

Mathematically, many solutions may exist for different sets of the W_j windows selected: as a consequence, a smart algorithm to reject unacceptable solutions is needed to help in finding the more likelihood values. Details can be found in [21].

By a practical point of view, 7 different materials (^{59}Co , ^{63}Cu , ^{115}In , Hf , ^{160}Gd , ^{195}Pt , ^{209}Bi) for activating prompt-SPNDs are being considered: with reference to the notation used before,

$K \equiv M = 7$, seven energy windows are considered. The main criterion to the choice for selecting materials has been identified in sensitive differences in neutron-capture cross-sections in the energy range of interest for neutrons.

Regarding the matrix where sensitive isotopes are contained in, ^{59}Co , ^{63}Cu , ^{160}Gd , and ^{209}Bi are intended as pure isotopes in metal form; ^{115}In is contained as pure isotope in a In_2O_3 matrix; Hf is contained at its natural abundance in a HfO_2 matrix; ^{195}Pt is intended at its natural abundance in a Pt metal form.

A virtual device made as an assembly of 7 different SPNDs geometrically similar, has been developed in MCNPX, and "irradiated" in known conditions. Virtual electric current values from each SPND were recorded. The resolution algorithm described in [21] has been implemented in a Matlab code script. It takes as input spectral sensitivities $S(E)$ discretized in 49 channels for all 7 materials, and 7 online current values. All suitable solutions are plotted for a visual evaluation by the user, while the other ones are being rejected as outliers.

3 Results and Discussion

The case studies analyzed include an irradiation position into the ENEA TAPIRO Fast Reactor [22] MCNPX model, and 3 irradiation positions (here not discussed for sake of brevity; results can be found in [21]) in the LFR Demonstrator ALFRED MCNPX model [10]. The agreement between calculated data and target values shows to be promising, encouraging for further developments the technique.

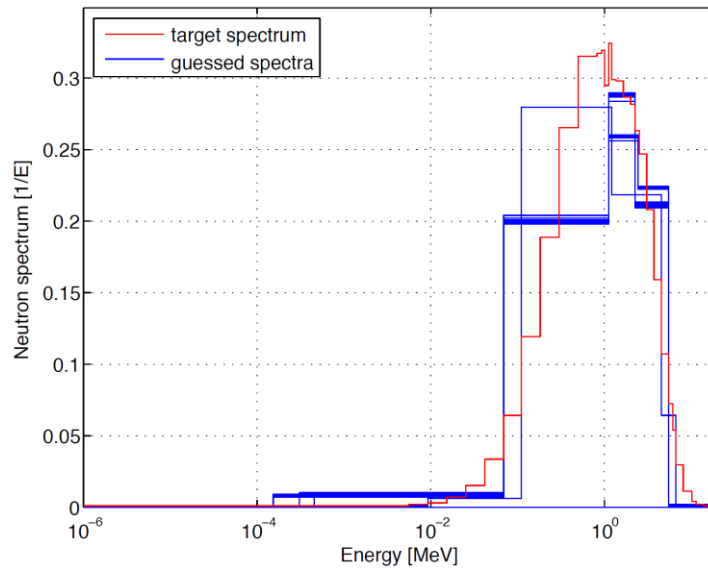


Fig. 2 Results from the *unfolding* algorithm initialized from currents virtually measured in the ENEA TAPIRO Fast Reactor MCNPX model. As clearly stated in the text, multiple solutions are got as guessed spectra. As can be seen, calculated values (in blue) are gathering around the target values (in red).

The test case in TAPIRO is regarding the maximum neutron flux available, i.e. in the diametral channel at maximum power. The availability of the TAPIRO reactor MCNPX model at ENEA Casaccia Centre Research Reactor Laboratory, allowed to test the SPNDs-assembly discussed before. It should be noted that the local neutron flux, being in the order of $10^{12} \text{ n}\cdot\text{cm}^{-2}\cdot\text{s}^{-1}$, can be considered as a low-intensity magnitude if compared with Fast Reactors of commercial size or high-intensity neutron irradiation facilities. However, TAPIRO's availability could provide an experimental evidence for the method here proposed.

Simulations required a high number of histories inside the MCNPX code for obtaining uncertainties $<0.1\%$. Different simulations have been run to evaluate the neutron and gamma responses from the SPNDs into the assembly-device, at the reactor irradiation conditions. The current contributions from neutron and gamma excitations showed in [21] are reporting a significant influence of the gamma-induced disturbance to the measured current: both neutron and gamma contributions appear at the same order of magnitude. Gamma currents could be characterized experimentally or by simulation, or a combination of both techniques, as usually done in LWRs. Once the neutron-induced currents are extrapolated from real measurements via mathematical considerations, the unfolding algorithm proposed can be implemented.

The application of the methodology reported before provides the calculation results in the figure. As stated in the text, multiple solutions from the unfolding algorithm are obtained as guessed spectra. As can be seen, calculated values (in blue) are gathering around the target values (in red). It should be noted that 11 of 13 solutions obtained from the unfolding algorithm are quite similar: the thickening in the figure is due to the overlapping of such similar solutions. Being the target spectrum reported in 49 energy channels, and guessed spectra in 7 energy groups only, coarse differences are clearly expected. However, it can be concluded that the algorithm and the device proposed seems to well identify the qualitative trend of the target neutron spectrum.

4 Conclusions and future developments

This paper proposes an innovative use for prompt-SPND detectors, as instrumentation targeted for real-time monitoring of fast neutron-fluxes in terms of spectral fluence rate. Their inherently scarce sensitivities make such detectors suitable for sensing high-intensity neutron-flux only. That is why their application had not been truly experimented in the past.

Recent developments in Fast Reactors targeted for commercial use, and high-intensity neutron-flux facilities for material irradiation and testing, and radioisotopes production could provide a sufficient condition for that instrumentation to work. Prompt-SPNDs, when confirmed in their safe, fast, and reliable response vs. a fast neutron-flux field, can be implemented as control instrumentation.

In such a paper, a SPND model has been implemented in MCNPX code and seven sensitive materials suitable to get a prompt-signal from neutron irradiation (^{59}Co , ^{63}Cu , ^{115}In , Hf , ^{160}Gd , ^{195}Pt , ^{209}Bi) have been tested in terms of response, burn-up calculations, and neutron spectral sensitivity. With the spectral sensitivity database completed for all materials identified, a new hypothesis for SPND-use emerged. i.e. a deconvolution process started from the electric current signals recorded by 7 geometrically similar SPNDs that differ in sensitive materials, as to get a spectral characterization of the neutron flux impinging on detectors. The mathematical approach to neutron spectrum calculation presented here, provides a solution in terms of 7 energy-windows. As expected, multiple solutions - residing all around the range of the true solution- may be accepted by a physical point of view, due to some energy-condensation of the neutron energy domain that may differ slightly. The algorithm here realized and tested represents a first tentative to face the issue.

The main limitation on the spectrometer capabilities of the device proposed is found to be into the little number of materials irradiated inside the assembly-device: increasing the number of detectors in the assembly may lead to a refinement of the results, increasing resolution of the calculated spectra. Moreover, new materials with different spectral capabilities may be included in future works, as to improve performances. Regarding the application in LFRs, the SPNDs low burn-up, the lead-coolant shielding effect, and the neutron spectral-sensing capabilities, suggest that LFRs could successfully exploit SPNDs as reactor control-instrumentation. However, improvements in R&D still need to be carried out. In such a framework, the ENEA TAPIRO Fast Reactor may play a significant role in first experimental verifications of the hypothesis proposed.

Acknowledgements

The authors would like to express special thanks to Dr. Mario Carta, head of ENEA Casaccia Research Centre Nuclear Reactors Laboratory (FSN-FISS-RNR), and Dr. Lina Quintieri of the National Institute of Ionizing Radiation Metrology (INMRI) for their precious advice and infinite disposability in dialogue.

Thanks go to Mr. Orlando Fiorani and Dr. Alfonso Santagata for providing detailed information and MCNP input regarding TAPIRO Fast Reactor.

A special thanks goes to all ENEA-UTICT technicians, in particular to Eng. Guido Guarnieri, for their perseverance, disposability, and competency in solving all issues about HPC. The computing resources and the related technical support used for this work have been provided by CRESCO/ENEAGRID High Performance Computing infrastructure and the staff [23]. CRESCO/ENEAGRID High Performance Computing infrastructure is funded by ENEA, the Italian National Agency for New Technologies, Energy and Sustainable Economic Development, and by Italian and European Research Programmes; see <http://www.cresco.enea.it/english> for more information.

References

- [1] Generation IV International Forum, "A Technology Roadmap for Generation IV Nuclear Energy Systems," , 2002.
- [2] M. Salvatores and G. Palmiotti, "Radioactive waste partitioning and transmutation within advanced fuel cycles: achievements and challenges," *Progress in Particle and Nuclear Physics*, vol. Volume 66, Issue 1, pp. Pages 144-166, 2011.
- [3] Carlo Artioli, Giacomo Grasso, and Carlo Petrovich, "A new paradigm for core design aimed at the sustainability of nuclear energy: The solution of the extended equilibrium state," *Annals of Nuclear Energy*, vol. 37, no. 7, pp. 915-922, 2010.
- [4] Przemysław Stanisław, Mikołaj Oettingen, and Jerzy Cetnar, "Monte Carlo modeling of Lead-Cooled Fast Reactor in adiabatic equilibrium state," *Nuclear Engineering and Design*, vol. 301, pp. 341-352, 2016.
- [5] D.V. Andreeva and E.V. Skorb, "13 - Multi-layer smart coatings for corrosion protection of aluminium alloys and steel," in *Handbook of Smart Coatings for Materials Protection.:* Makhlouf, Abdel Salam Hamdy, 2014, pp. 307-327.
- [6] SCK-CEN. (2016) Myrrha: an Accelerator Driven System (ADS). [Online]. <http://myrrha.sckcen.be/en/MYRRHA/ADS>
- [7] Alessandro Alemberti. (2013, March) The Lead Fast reactor: Demonstrator ALFRED and ELFR Design. [Online]. <https://www.iaea.org/nuclearenergy/nuclearpower/Downloadable/Meetings/2013/2013-03-04-03-07-CF-NPTD/T2.1/T2.1.alemberti.pdf>
- [8] Luigi Lepore, Romolo Remetti, and Mauro Cappelli, "Fast Neutron-Flux Monitoring Instrumentation for Lead Fast Reactors: A Preliminary Study on Fission Chamber Performances," in *22nd International Conference on Nuclear Engineering (ICONE22)*, vol. Volume 6, Prague, 2014, p. 9.
- [9] Luigi Lepore, Romolo Remetti, and Mauro Cappelli, "Evaluation of the Current Fast Neutron Flux Monitoring Instrumentation applied to LFR Demonstrator ALFRED: capabilities and limitations," in *Proceedings of 23rd International Conference On Nuclear Engineering*, vol. Volume 6: Nuclear Education, Public Acceptance and Related Issues; Instrumentation and Controls (I&C); Fusion Engineering; Beyond Design Basis Events, Makuhari Messe, Chiba, Japan, 2015.
- [10] Luigi Lepore, Romolo Remetti, and Mauro Cappelli, "On capabilities and limitations of current fast neutron-flux monitoring instrumentation for the DEMO LFR ALFRED," *Journal of Nuclear Engineering and Radiation Science*, no. NERS-15-1205, 2016.
- [11] J. P. Trapp, S. Haan, L. Martin, J. L. Perrin, and M. Tixier, "High temperature fission chambers: state-of-the-art," in *In-core instrumentation and reactor core assessment. Proceedings of a Specialist meeting, Mito-shi (Japan), 1997*, pp. 191-202. [Online]. <https://www.oecd-nea.org/science/rsd/ic96/4-3.pdf>
- [12] M. Angelone et al., "Development of self-powered neutron detectors for neutron flux monitoring in HCLL and HCPB ITER-TBM," *Fusion Engineering and Design*, vol. 89, pp. 2194–2198, 2014.
- [13] G. Bignani, J.C. Guyard, C. Blandin, and H. Petitcolas, "Direct Experimental Tests and Comparison between Sub-miniature Fission Chambers and SPND for Fixed In-core Instrumentation of LWR," in *In-core instrumentation and core assessment, Mito-shi, Japan, 14-17 October, 1996*.
- [14] S.V. Guru and D.K. Wehe, "INSTANTANEOUS FLUX MEASUREMENTS USING THE BACKGROUND SIGNAL OF THE RHODIUM SELF-POWERED NEUTRON DETECTOR," *Annals of Nuclear Energy*, vol. 19, no. 4, pp. 203-215, 1992.

- [15] C. Blandin and S. Breaud, "Selective and prompt self-powered neutron detectors for characterization of mixed radiation fields in reactors," in *Reactor Dosimetry: Radiation Metrology and Assessment*, Philadelphia, Jan 2001.
- [16] W.H. Todt, "Characteristics of Self-powered Neutron Detectors Used in Power Reactors," in *In-core instrumentation and core assessment*, Mito-shi, Japan, , 14-17 October, 1996.
- [17] T. Seidenkranz, K. Bohme, U. Kagemann, R. Maletti, and H. Stein. EXPERIENCES WITH PROMPT SELF-POWERED DETECTORS IN NUCLEAR REACTORS OP WWER TYPE. [Online].
http://www.iaea.org/inis/collection/NCLCollectionStore/_Public/18/009/18009870.pdf
- [18] Briesmeister, J. F., "MCNP – A general purpose Monte Carlo code for neutron and photon transport," Los Alamos National Laboratory, NM (USA), Technical Report LA-7396-M-Rev.2 ON: DE87000708, September 1996. [Online].
<http://www.osti.gov/scitech/biblio/5191995Fay0sj6yM9i2t-Nxtt6GxSK7AVgQ&b>
- [19] Luigi Lepore and Romolo Remetti, "Application of Prompt Self Powered Neutron Detectors to the LFR Demonstrator ALFRED: a critical evaluation," *Journal of Nuclear Engineering and Radiation Science*, vol. Accepted for publication. Available at \url
- [20] Luigi Lepore, "Ottimizzazione della strumentazione di monitoraggio neutronico del nocciolo di un reattore LFR," Sapienza - University of Rome, Tesi di Dottorato <http://dx.doi.org/10.13140/RG.2.2.29359.12960>, 2016.
- [21] Luigi Lepore, Romolo Remetti, and Antonino Pietropaolo, "A proposal for an alternative use of prompt-Self Powered Neutron Detectors: Online spectral-deconvolution for monitoring high-intensity neutron flux in LFRs," *Nuclear Engineering and Design*, vol. 322, pp. 536-546, 2017.
- [22] Rocco Bove. Nuclear Research Reactor: TAPIRO. [Online].
http://www.enea.it/it/Ricerca_sviluppo/documenti/nucleare/TAPIROBove.pdf
- [23] Giovanni Ponti, "The role of medium size facilities in the HPC ecosystem: the case of the new CRESCO4 cluster integrated in the ENEAGRID infrastructure," in *2014 International Conference on High Performance Computing and Simulation*, pp. 1030-1033.

Neutronic analyses in support of the WCLL DEMO design development

Fabio Moro¹, Davide Flammini¹ and Rosaria Villari¹

¹ENEA, Fusion Department, ENEA C. R. Frascati, via E. Fermi 45, 00044 Frascati (Roma), Italy

ABSTRACT. In the frame of the EUROfusion Consortium program, the Water Cooled Lithium Lead (WCLL) option has been chosen as a candidate for the breeding blanket (BB) of the European fusion power demonstration plant (DEMO) conceptual design. Neutronic analyses play a fundamental role in the development of the WCLL blanket, providing guidelines for its design based on the evaluation of the nuclear performances.

A detailed three-dimensional MCNP model of the latest WCLL layout has been generated and integrated in a DEMO MCNP generic model suitably designed for neutronic analyses. Three-dimensional neutron and gamma transport simulations have been performed using the MCNP5v1.6 Monte Carlo code and JEFF 3.2 nuclear data libraries, in order to assess the WCLL-DEMO tritium self-sufficiency and the shielding capabilities of the breeding blanket/manifold system to protect the vacuum vessel and toroidal field coils. Furthermore, radial profiles of the neutron flux, nuclear heating, neutron damage and he-production have been assessed in the Inboard and Outboard equatorial planes.

The outcome of the present study highlights the potential and suitability of the WCLL breeding blanket for the application to DEMO, both in terms of tritium production and shielding performances.

1 Introduction

The neutronic calculations on the WCLL breeding blanket aim at the evaluation of the nuclear performances of the present design of the blanket concept, providing feedback for its future development.

The main objective of the present studies is the verification the WCLL DEMO tritium self-sufficiency, the shielding capabilities of the BB/manifold system. Moreover, the radial profiles of the nuclear loads (neutron flux, nuclear heating, neutron damage and he-production) have been assessed at equatorial level, providing indication about their behaviour on the first wall (FW), BB, supporting structures and manifolds.

Neutronics studies carried-out in 2015 were based on the DEMO1 2015 configuration, integrating a WCLL breeding blanket represented by homogenized compounds with volume percentage of each material extracted by the engineering CAD files. The results showed that the tritium breeding capability was sufficient to achieve the required Tritium Breeding Ratio (TBR) ≥ 1.1 to ensure self-sufficiency and the shielding performances were sufficient to protect the super-conducting toroidal field coils (TFC), mainly because of the heavy BSS/manifold configuration.

The present studies have been performed using an upgraded MCNP WCLL DEMO model, introducing a detailed description of the breeding blanket in the Inboard and Outboard equatorial modules: analyses have been carried out in order to support the WCLL blanket improvement and to verify its suitability in terms of neutronics requirements. Moreover, a new layout of the WCLL DEMO, based on a single module approach, is presently under development: the nuclear analyses of this novel design are currently ongoing, however a first assessment of the TBR is provided.

2 Procedures, codes and 3D modelling

The three-dimensional coupled neutron and gamma transport simulations have been performed according to specifications [1] by means of the MCNP5v1.6 Monte Carlo code [2] and JEFF 3.2 nuclear data libraries [3]. The development of a detailed MCNP model of the WCLL Outboard #4 blanket module (OB#4, Fig. 1) has been performed though the pre-processing and simplification of

* Corresponding author. E-mail: davide.flammini@enea.it.

the original CAD file by means of the 3D modeling software Ansys SpaceClaim 2015 [4] in order to generate a model suitable for neutronic analyses. A single breeding unit (BU: the components included between two neighbouring stiffening plates, red area in fig. 2), containing 21 cooling water pipes embedded in the LiPb breeder, has been isolated and singularly converted into the equivalent MCNP geometry through the CAD-to-MCNP interface MCAM (SuperMC_MCAM5.2 [5]).

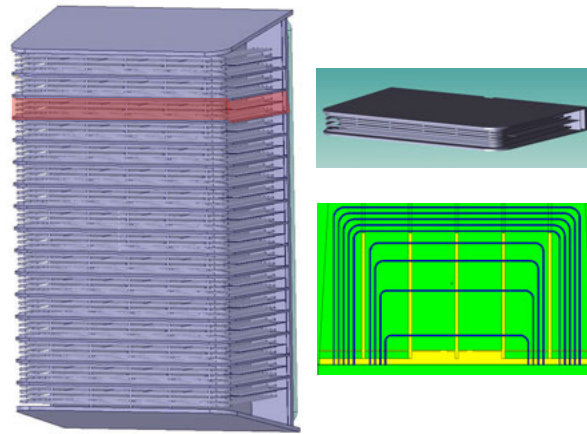


Fig. 1. WCLL blanket module: overview of the BB inner structure (left panel) detail of a BU (top right) and a section of the equivalent MCNP model along the cooling pipes axis

Successively, the single breeding unit has been recursively integrated filling the DEMO MCNP generic model Inboard and Outboard (full and halved) blanket modules #4. As far as the Inboard module (IB#4) integration is concerned, the development of detailed Inboard configuration was based on adaptation of Outboard layout by keeping the distance between the FW and the outermost cooling channel (Fig. 2).

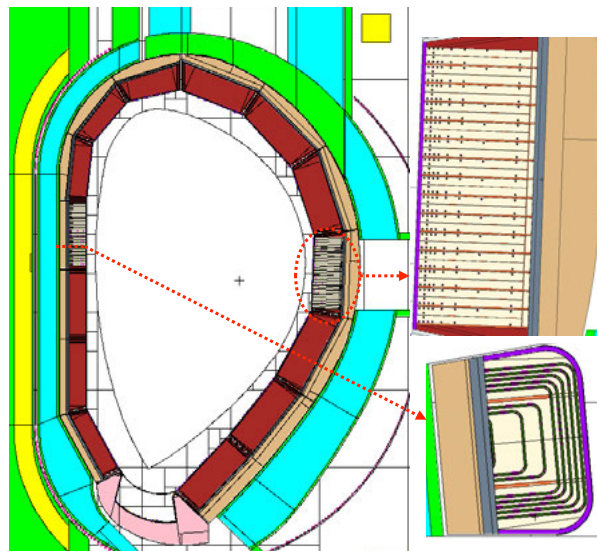


Fig. 2. MMS WCLL DEMO MCNP model integrating the detailed blanket in the IB#4 and OB#4

The complexity of the model and the necessity of statistically reliable results (statistical error below 10% in the outer area of the tokamak) required the use of the MCNP MPI multiprocessor version installed on the CRESCO cluster available in ENEA [6].

Each MCNP run generates $1e10$ particles (neutrons, photons or both depending on the nuclear responses evaluated), using 800 processors for a total computing time of about $2.2e5$ seconds. The typical dimension of a single output file is approximately 300 Mbyte, thus the overall study required the analysis of some Gbyte data.

3 Results

The model so far described has been used to evaluate the performances of the WCLL DEMO in terms of shielding capability to protect the Toroidal Field Coils and tritium self-sufficiency. Moreover, the neutron flux, nuclear heating, damage and He-production radial profiles have been assessed on the equatorial mid plane, thus taking into account the detailed description of the breeding blanket structure. Results have been normalized to 2037 MW fusion power (neutron yield: 7.232×10^{20} n/s), according to the plasma parameters specified in Table 1. Standard cell-based (F4/F6 tallies) and mesh tallies (FMESH tally) with proper multiplier have been used to calculate the nuclear quantities of interest for the WCLL design development, performances assessment and verification of design requirements.

N° of Toroidal Field Coils	18
Major radius (m)	9.072
Minor radius (m)	2.927
Aspect ratio	3.1
Plasma elongation	1.59
Plasma triangularity	0.33
Fusion power	2037
Average neutron wall loading	1.05
Net electric power	500

Table 2: main parameters of the DEMO baseline configuration.

The tritium breeding ratio (TBR) has been calculated using track-length estimator (F4 tally) with proper tally multipliers (FM card) that take into account the cross sections of the reactions producing tritium on Li-6 and Li-7. The global TBR evaluated on a full homogeneous model is 1.14, so the results confirm that the present WCLL design fully achieve the design target. The effect of heterogeneity has been quantified through the comparison between the TBR produced in the heterogeneous blanket modules (OB#4 and IB#4) and the corresponding values obtained using the homogenized material. The assessed correction factors showed that the detailed and more realistic description of the breeding blanket could provide a further increase in the total TBR of about 3% [7]: this evaluation has to be confirmed through the calculation performed on a full heterogeneous WCLL DEMO. Moreover, a dedicated study to evaluate the impact of the variation of the Outboard breeding zone radial thickness on the global TBR has been performed: results [10] show that most of the Tritium (about 82%) is generated in the 30 cm of BU closer to the plasma and that the TBR saturates at a BU radial size of about 1 m [8].

The shielding performances of the WCLL BB have been assessed through the estimation of the neutron flux, nuclear heating, dpa and He-production in steel components have been calculated along the inboard and outboard mid-plane. The nuclear quantities are averaged on a poloidal extension of 50 cm (from $z=10$ to $z=60$ mm), thus considering the detailed breeding blanket description. The FMESH tally feature of MCNP has been applied to evaluate the nuclear responses. The total and fast ($E > 100$ keV) neutron fluxes radial profiles (Fig. 3) at the Inboard FW are 5×10^{14} n/cm²/s and 3.4×10^{14} n/cm²/s respectively; the blanket/manifold system provides an attenuation of more than two orders of magnitudes to the VV inner shell and the neutron flux further decreases of several orders of magnitude across the VV, being 4.8×10^8 n/cm²/s (total), and 2.9×10^8 n/cm²/s (fast) on the TFC, well below the 10^9 n/cm²/s design limit.

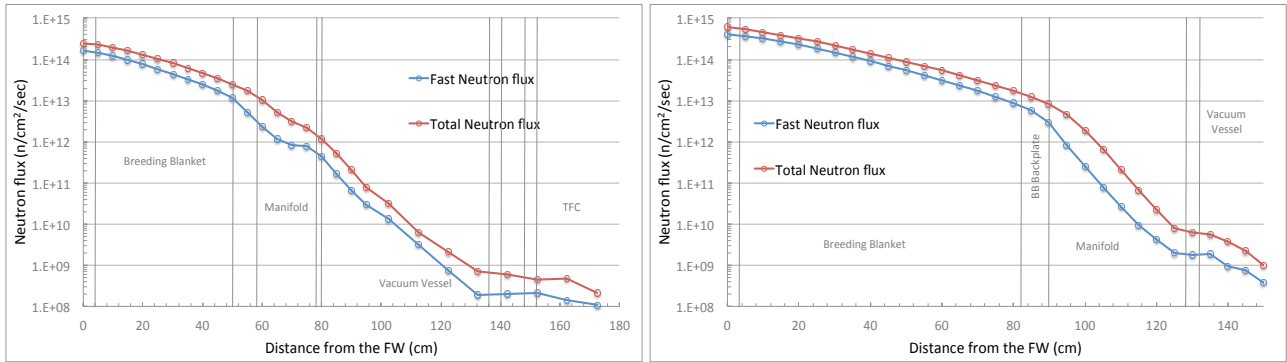


Fig. 3. Inboard (left) and Outboard (right) radial profile of the total and fast neutron flux.

The radial profiles of the nuclear heating evaluated on steel components are plotted in fig. 4: the maximum values at the FW Eurofer are $\sim 7.5 \text{ W/cm}^3$ for the Inboard and $\sim 9.2 \text{ W/cm}^3$ for the Outboard. At the VV inner shell the heat load decreases to 0.1 W/cm^3 in the Inboard and to $2 \times 10^{-3} \text{ W/cm}^3$ in the outboard. In the TFC winding pack the heat load density is $1.4 \times 10^{-5} \text{ W/cm}^3$, thus satisfying the design limit of 50 W/m^3 .

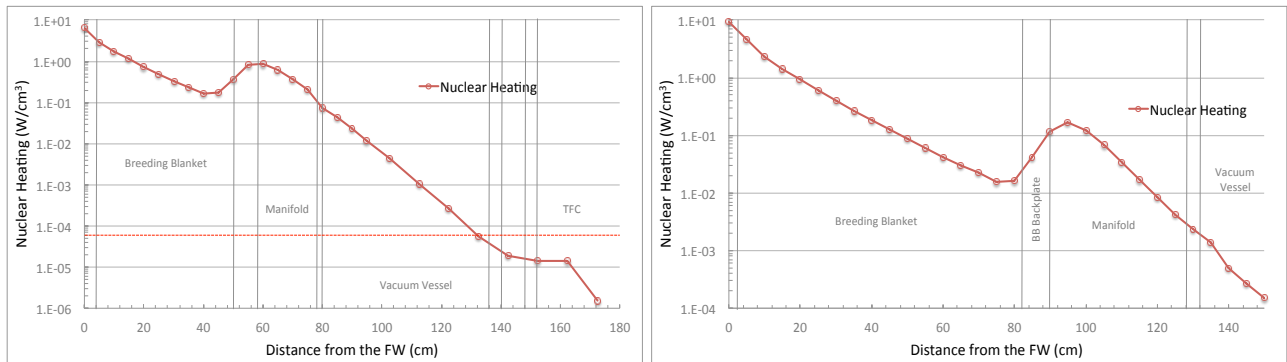


Fig. 4. Inboard (left) and Outboard (right) nuclear heating radial profiles in steel (the red dotted line indicates the design limit for the TFC).

The estimation of the damage in Eurofer and SS-316 per full-power-year (FPY) showed that the present configuration ensures a sufficient protection over the whole DEMO lifetime (VV steel: $\sim 6.2 \times 10^{-3} \text{ dpa/FPY}$ and $3.3 \times 10^{-5} \text{ dpa/FPY}$ for Inboard and Outboard respectively, design limit: 2.75 dpa/FPY). As far as the He-production in steel is concerned the estimation performed on the Inboard area highlights a reduction of about 2 orders of magnitude from the FW (100 appm/FPY) to the VV (1 appm/FPY); in the Outboard, the He-production drops of more than 4 orders of magnitude from the FW to the VV. Behind the Vacuum Vessel the He-production drops to values below 10^{-4} appm/FPY .

The WCLL design team has recently developed an updated concept of the WCLL BB based on a SMS approach [9]; the MCNP model of the SMS WCLL DEMO has been generated (fig. 5) and the nuclear analyses in support of its design are presently ongoing. A first assessment of the global TBR has been carried out and the results highlight that the tritium self-sufficiency is guaranteed also in this configuration [10]. An enhancement of the shielding performances for the SMS WCLL BB has to be expected because the removal of the poloidal gaps reduces drastically the direct neutron streaming from the plasma to the outer structures of the machine (VV, TFC).

This work has been carried out within the framework of the EUROfusion Consortium and has received funding from the Euratom research and training programme 2014-2018 under grant agreement No 633053. The views and opinions expressed herein do not necessarily reflect those of the European Commission.

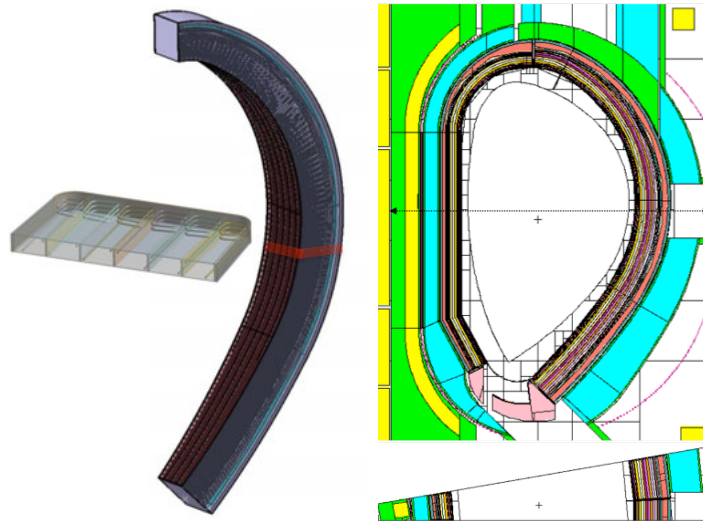


Fig. 5. WCLL SMS: overview of the Outboard module and detail of a single BU (left) and SMS WCLL DEMO MCNP model (right)

References

- [1] U. Fischer et al., Neutronic analyses and tools development efforts in the European DEMO programme, Fusion Engineering and Design Vol. 89, Issue 9-10 (2014) 1880-1884.
- [2] X-5 Monte Carlo Team: MCNP - A General Monte Carlo N-ParticleTransportCode, Version 5, Los Alamos National Laboratory, Los Alamos, New Mexico, USA, April 2003.
- [3] JEFF3.2 nuclear data library, http://www.oecd-nea.org/dbforms/data/eva/evatapes/jeff_32/.
- [4] www.spaceclaim.com
- [5] Y. Wu, et al., “CAD-based Monte Carlo program for integrated simulation of nuclear system SuperMC”, Annals of Nuclear Energy, Volume 82, August 2015, Pages 161-168
- [6] <http://www.cresco.enea.it/>
- [7] A. Tassone et al., Recent progress in the WCLL breeding blanket design for the DEMO fusion reactor, IEEE Transactions on Plasma Science (2017), in press.
- [8] C. Bachmann et al, Overview over DEMO design integration challenges and their impact on component design concepts, ISFNT – 13, Kyoto, September 2017
- [9] E. Martelli et al, Advancements in DEMO WCLL breeding blanket design and integration, Int. J. Energy Res. (2017), in press, doi: 10.1002/er.3750.
- [10] F. Moro et al., Neutronic analyses in support of the WCLL DEMO design development, ISFNT – 13, Kyoto, September 2017

REPORT ON CFD SIMULATIONS OF LOVA (LOSS OF VACUUM ACCIDENT) WITH ANSYS CFX 17.0 EUROFUSION ENGINEERING GRANT SAFETY ANALYSIS

Fabio Tieri,

C.R.E.A.T.E Consortium Via Claudio 21, 80125 Napoli, Italy

ABSTRACT. This report included in the Agreement Work Program (AWP) 2015 deals with the safety aspects of DEMO as reported in [1]. In particular this report summarized the results obtained during the first year, focusing the attention on the CFD simulations performed to validate the resuspension model inside a LP code called “ASTEC” used for the safety analysis in the nuclear field. To validate the model have been considered the experimental data taken from the past experiments at the STARDUST facility placed at the University of “Tor Vergata”.

1 Scope of the work

The scope of the STARDUST experiments is to build a base of knowledge about the dust behavior in a fusion plant, in which slightly vacuum conditions and relatively high temperatures are present, in particular when a loss of vacuum accident occurs. The facility is a stainless steel cylindrical tank having the features described in [2]. The tank is wrapped around by means of electrical resistances to heat up the walls and then by insulating materials. The connection to the compressed air passes through an electrical valve and a flow meter, able to control the air inlet at the required rate. The dusts have been placed in a tray suitable to be weighted. To have a quantitative estimate of this amount the dust is weighted before and after the experiment. A quartz glass window is hollowed in the front lid of the VV tank to permit the visualization of the dust tray inside. The facility is currently placed at the Industrial Engineering building at the “Tor Vergata” University in Rome.

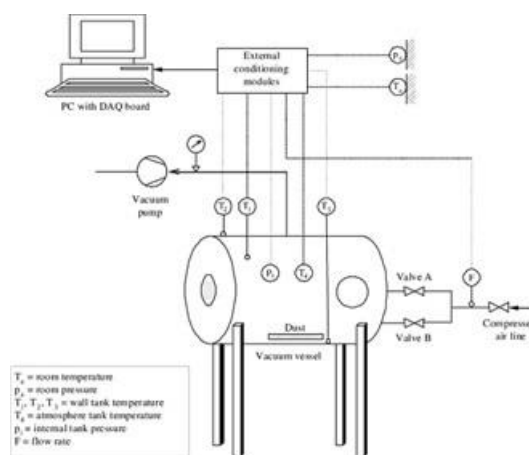


Figure 1: Stardust facility

2 ANSYS CFX simulations

The ANSYS CFX 17.0 tool has been used in order to evaluate properly the thermal hydraulic parameters during the transient, in fact as pointed out in [2] the evaluation of the velocity for this type of phenomenon it is difficult task for a LP code (such as ASTEC). Even more so with the peculiar conditions of a LOVA.

ANSYS calculated all the local thermal-hydraulic parameters such as pressure, temperature, velocity and friction velocity on the tray's wall. All these variables affect the ASTEC calculations.

The geometry considered in ANSYS is shown in Figure 1. Only the fluid domain has been taken in account because the walls' temperature are constant, then their temperature was imposed as a boundary condition . The inlet pipe in ingress is 0.15 meter long.

The initial conditions adopted are 100 Pa for pressure and 368.15 K for tank atmosphere temperature and 381.15 K for walls temperature, these last ones kept constant for all the experimental duration. The inlet mass flow rate is taken from the experimental data.

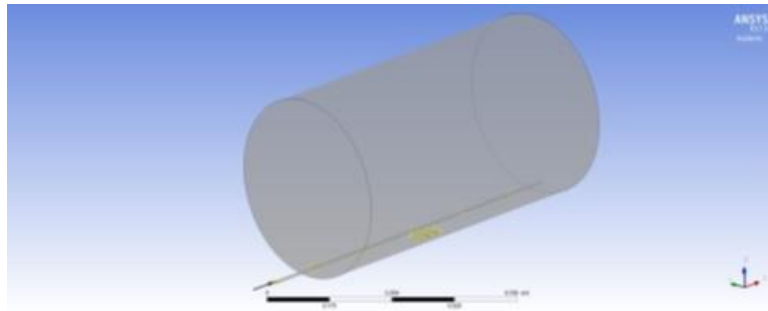


Figure 2: ANSYS CFX model for case B at 300 Pa/s

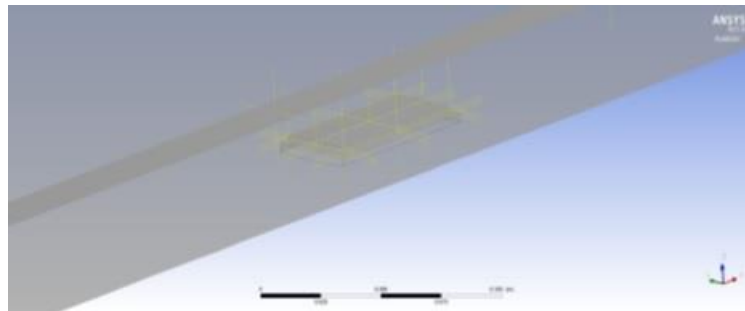


Figure 3: ANSYS CFX model for case B at 300 Pa/s: particular of the tray's domain

The mass flow rate in ingress is a time dependent function that has been extrapolated from the experimental data. The function was interpolated by means of Matlab.

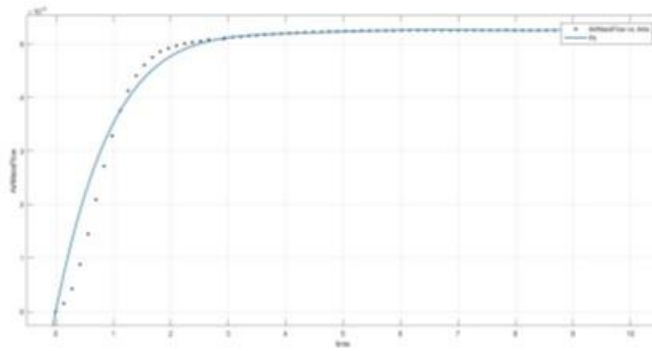


Figure 4: Mass flow rate function trend vs experimental data for cases at 300 Pa/s

Figure 5 show the results for the first 20 seconds of simulation.

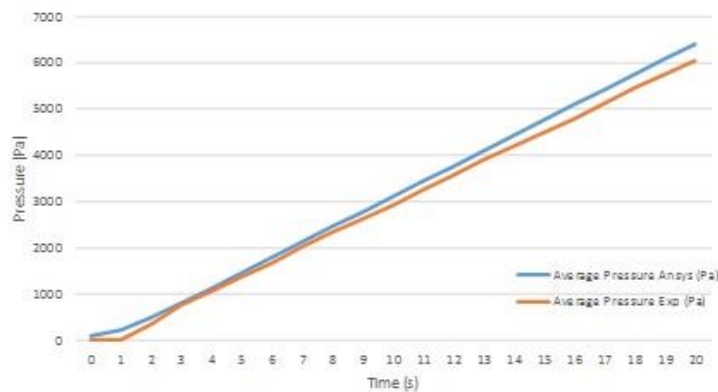


Figure 5: ANSYS vs experimental data comparison of the STARDUST internal pressure for case B at 300 Pa/s

Other important parameters calculated with ANSYS are the local density, kinematic viscosity, velocity inside the dust volume (where is placed the tray) and the friction velocity correlated with the bottom wall on which the dust were deposited.

The thermal-hydraulic parameters calculated inside the tray domain have been used in ASTEC (as input parameters) to compute the local velocity. The results obtained comparing the two codes are in good agreement:

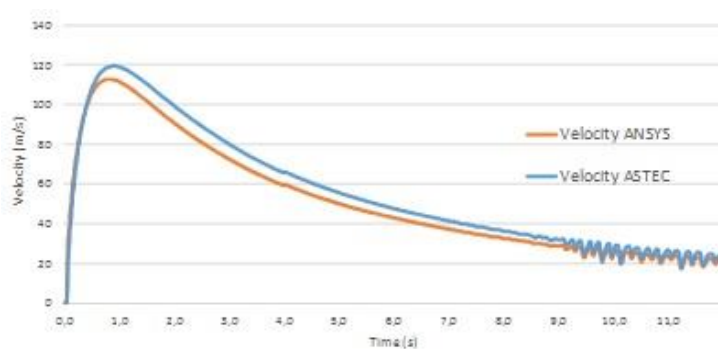


Figure 6: ASTEC and ANSYS average velocities in the tray volume for 300 Pa/s (case B)

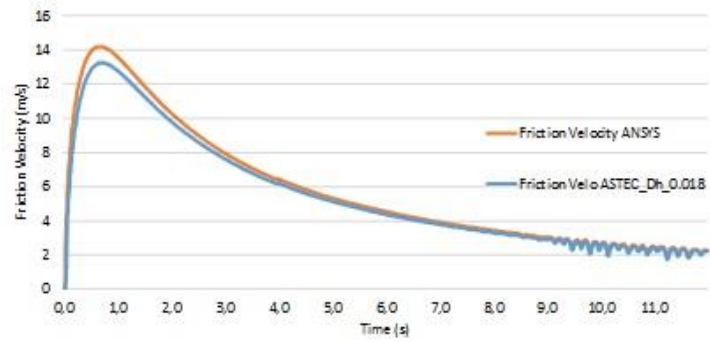


Figure 7: Friction Velocity-ANSYS vs ASTEC on the try's wall for 300 Pa/s (case B)

References

- [1] AWP15-EEG-ENEA-Tieri, 2015
- [2] M. T. Porfiri, N. Forgione, F. Frediani, S. Libera, S. Paci, A. Rufoloni, L. Verdini, , EFDA Task TW3-TSS-SEA5.1 Milestone 2, (2003).

QUANTITATIVE IN SITU GAMMA SPECTROMETRY IN CONTAMINATED SOIL

Massimo Altavilla¹

¹*National Center for Nuclear Safety and Radiation Protection, The Italian National Institute for Environmental Protection and Research, ISPRA, Via Vitaliano Brancati 48, 00144, Rome, Italy¹*

ABSTRACT. The aim of the work is to improve potentialities of in situ gamma spectrometry when measuring soil massic activities for assessing radioactive contamination. Monte Carlo calibration of detector was required to determine absolute detection efficiencies of gamma rays emitted from soil. The soil volume actually seen by detector, for each energy involved, was determined by the ray-tracing technique. Results of in field tests have been compared to laboratory gamma spectrometry, obtaining satisfactory results. The novelties of this work are both to have carried out Monte Carlo calibration of collimated broad energy germanium detectors, and to have developed a soil volume calculation method which is not restricted to ¹³⁷Cs only. Such a method is capable to account for also low energies gamma rays.

1 Introduction

In situ gamma spectrometry may represent a powerful mean to determine massic activity within a certain Field Of View (FOV) defined by a collimator, but to obtain affordable results the FOV shall be well defined. Up to now, usual definition of FOV was obtained making recourse to the traditional deterministic distinction between intrinsic and geometrical detection efficiency, [1], [2]. This is the usual simplification of a problem that, rigorously, should be interpreted by the radiation transport formalism. In other words, deterministic methods for area calculation are poorly applicable, because the area is function of detected gamma-rays energy.

2 Description of the Monte Carlo procedure

Monte Carlo simulation of gamma-ray radiation detectors is a powerful tool for determining detection efficiency in many measurement configurations, even if, as focused by many authors, it requires a thorough knowledge of structural characteristics of the detectors. For germanium detectors the determination of geometrical parameters can be enough complicated. For instance, Vargas et al. [3], dealing with a coaxial n-type HPGe detector, describe seven main parameters: diameter and height of the crystal, diameter and height of the internal core, thickness of the beryllium window, distance between the crystal top and the Be window, and the thickness of the dead layer of Ge. For the present work a broad energy germanium detector has been utilized, and for this kind of detectors simulation is even more complicated, due to the presence of two dead layers: the top dead layer and the lateral one. More details of the detector simulation procedure are given by the Authors in [4] and

¹ Corresponding author. E-mail: massimo.altavilla@isprambiente.it.

[5]. Monte Carlo simulations carried out for this work have been mainly based on MCNPX version 2.7.0 code, [6]. The code's geometrical input reproduced, as accurately as possible, detector, collimator, measurement set-up, and soil composition. In order to account for possible scattering and absorption effects, also the air surrounding the detector-collimator assembly, and the supporting metal cart were considered.

The portion of ground soil viewed by the collimated detector was calculated by the ray-tracing stochastic technique [7], based on DXTRAN MESH TALLY (TYPE 4) [6]. This tally is an analytical tool useful in determining the behavior of detectors and how they may be effectively placed in the problem. To understand the meaning of the tracks in the DXTRAN MESH TALLY, it is important to understand the operation of the DXTRAN sphere. Use of DXTRAN sphere is a variance reduction method. It is like a point detector in which virtual particles are sent to the detector surface from interactions elsewhere in the problem. Once they reach the surface, the particles are made real, and transport continues as normal from there. The “rays” of the mesh tally are the tracks of these virtual particles. For applying DXTRAN MESH TALLY, the source and type of radiation particles were specified, by MCNPX's SDEF command, considering a source term described by a semi-infinity distribution into the soil (taking into account radionuclides' gamma ray energies attenuation in the ground soil).

Having implemented radionuclides' massic activity depth profile, derived from laboratory gamma spectrometry of collected vertical soil samples, and from site history, absolute detection efficiency of the radionuclides involved was calculated. MCNPX simulations' output was given in terms of the Pulse Height Tally F8 [6], i.e. the tally reproducing the energy distribution released within the detector, thus allowing calculation of the absolute detection efficiency for the radionuclides' energies involved.

The number of histories was set so that the fractional standard deviation, i.e. the relative error R, was less than 0.05. Being MCNPX' statistical error indicative of the precision of the estimated quantities, the accuracy of the results depended on the models used for the simulation, uncertainties in the cross sections, adequacy of the input data as being representative of the experimental set-up, etc.

3 Conclusion

The aim of the present work was to improve potentialities of environmental in situ gamma spectrometry for allowing accurate determination of soil massic activity. This was obtained by solving the radiation transport problem of the correct calculation of the contaminated area/volume seen by detector at a certain gamma-ray energy. MCNPX version 2.7.0 was utilized. The code's geometrical input reproduced, as accurately as possible, detector, collimator, measurement set-up, and soil composition. The portion of ground soil viewed by the collimated detector was calculated by the ray-tracing stochastic technique, based on MCNPX's DXTRAN variance reduction method.

The first step of this work has been focusing on low gamma emission energy radionuclides such as ^{241}Am . Cresco is particularly important for the developing of this work especially in the case in which point source of ^{241}Am is considered into 15 cm of soil depth which results in absolute efficiencies in the range of $\sim 10^{-12}$ with a total nps simulation of $\sim 8 \times 10^{13}$.

References

- [1] ISO 18589-7-2013 (E) – “Measurement of radioactivity in the environment – Soil – Part 7: In situ measurement of gamma-emitting radionuclides”, First edition 2013-10-01”.
- [2] Knoll G. F, (2000) Radiation Detection and Measurement, third ed., John Wiley & Sons, New York.

- [3] Vargas M. J, Timon A. F, Diaz N. C, Sanchez D. P, (2002) Influence of the geometrical characteristics of an HpGe detector on its efficiency, *Journal of Radioanalytical and Nuclear Chemistry* 253: 439-443.
- [4] Altavilla M, Remetti R, (2013) Development of a stochastic detection efficiency calibration procedure for studying collimation effects on a broad energy germanium detector, *Nucl. Instr. and Meth. in Phys. Res. A* 712: 157-161.
- [5] Altavilla M, Remetti R, (2014) The active area shadow-shielding effect on detection efficiency of collimated broad energy germanium detectors, *Nucl. Instr. and Meth. in Phys. Res. A* 739: 10-20.
- [6] Pelowitz D. B (ed.), (2011) MCNPX528 TM User's Manual Version 2.7.0, LA-CP-11-00438, Los Alamos.
- [7] Glassner A (ed.), (1989) *An introduction to ray tracing*, Elsevier.

INFLUENCE OF MASS MEDIA IN THE NAMING GAME

Filippo Palombi^{1*}, Stefano Ferriani² and Simona Toti³

¹*ENEA — Italian National Agency for New Technologies, Energy and Sustainable Economic Development*
Via Enrico Fermi 45, 00044 Frascati Italy

²*ENEA — Italian National Agency for New Technologies, Energy and Sustainable Economic Development*
Via Martiri di Monte Sole, 4, 40129 Bologna Italy

³*ISTAT — Italian National Institute of Statistics*
Via Cesare Balbo 16, 00184 Rome Italy

ABSTRACT. We study the phase structure of the Naming Game in presence of periodic external fields representing mass media. The Naming Game is a multi-agent model originally developed to study the spontaneous emergence of a globally shared language. We find that *i*) a single periodic external field is able to reverse the majority opinion of a whole population of agents, provided the frequency and the effectiveness of its messages lie above well-defined thresholds; *ii*) in presence of two competing periodic external fields the system relaxes to periodic equilibrium states in which the average opinion densities of the agents are reversed with respect to natural expectations. These states are observed when the frequencies of the field messages are different but close to each other and also when the frequencies are equal and the relative time shift of the messages does not exceed half a period. We interpret them as a result of the interplay between the external fields and the internal dynamics of the model.

1 Introduction

The Naming Game (NG) is a simple and popular multi-agent model, expressly conceived to study the spontaneous emergence of globally shared languages. Inspired by the pioneering work of refs. [1, 2], it was first proposed in ref. [3]. Its goal is to let a population of agents name an initially unnamed object. Each agent taking part in the game is endowed with a notebook, in which he/she writes names. Agents lie on the nodes of a complex network, with edges representing acquaintances. The game consists in repeated elementary interactions, each involving a pair of agents who play respectively as speaker and listener. In each interaction the speaker is chosen randomly among the agents, while the listener is chosen randomly among the speaker's neighbors. The binary version of the model, introduced in ref. [4], assumes only two competing names, conventionally denoted by letters A and B. In this case the basic interaction rule is described by Table 1 (left). It has been shown that the whole population eventually adopts one of the competing names while dropping all others. Consensus on the chosen name is reached in a finite time, depending on the size and the topological structure of the agent network. More precisely, the time to consensus always diverges as the size of the network increases, whereas the pace of divergence depends on the specific topology of it.

A massive body of literature has been developed over the past years, dealing with various aspects of the

*Corresponding author. E-mail: filippo.palombi@enea.it.

before interaction	after interaction
$S \rightarrow L$	$S - L$
$A \xrightarrow{A} A$	$A - A$
$A \xrightarrow{A} B$	$A - AB$
$A \xrightarrow{A} AB$	$A - A$
$B \xrightarrow{B} A$	$B - AB$
$B \xrightarrow{B} B$	$B - B$
$B \xrightarrow{B} AB$	$B - B$
$AB \xrightarrow{A} A$	$A - A$
$AB \xrightarrow{A} B$	$AB - AB$
$AB \xrightarrow{A} AB$	$A - A$
$AB \xrightarrow{B} A$	$AB - AB$
$AB \xrightarrow{B} B$	$B - B$
$AB \xrightarrow{B} AB$	$B - B$

before interaction	after interaction
$M \rightarrow L$	$M - L$
$A \xrightarrow{A} A$	$A - A$ with prob. 1
$A \xrightarrow{A} B$	$A - AB$ with prob. α_B
$A \xrightarrow{A} AB$	$A - A$ with prob. α_{AB}

Table 1: (left) table of interactions of the binary NG (S =speaker, L =listener); (right) table of media-listener interactions (M =media, L =listener).

NG. We refer the reader to ref. [5] for a recent review. An important topic that has not been considered so far is the behavior of the model under the action of periodic external fields, interpreted as mass media enacting a campaign. These are intuitively expected to influence the reaching of consensus to some extent. However no rigorous investigation of their effects on a large scale has been conducted yet. This kind of study belongs to the general field of non-equilibrium statistical mechanics.

2 The NG in presence of one single periodic external field

We consider N agents, lying on the nodes of a complete graph (with edges representing acquaintances) and playing the binary NG. Each agent is assumed to be initially in state B . We represent media as an additional fictitious agent M connected to the whole population, taking part in the game and invariably carrying opinion A . When interacting with an agent, media always play the role of speaker. A media-agent interaction results in a change of the agent's state: agents in state B switch to state AB with probability α_B ; agents in state AB switch to state A with probability α_{AB} ; agents carrying opinion A retain it after the interaction. These rules are summarized in Table 1 (right) for the reader's convenience. We refer to α_B and α_{AB} as effectiveness parameters of the media campaign. As mentioned in sect. 1, we assume that media act like an impulsive periodic perturbation of the internal dynamics of the system, reaching instantaneously all agents. We let $T = \tau N$ be the period of the campaign. If we define a sweep as a number N of microscopic interactions (each agent plays as speaker once in a sweep on average) and take it as a macroscopic time unit, then $\tau \geq 1$ represents the macroscopic period. In this model the media action is parametrized by the 3-tuple $(\alpha_B, \alpha_{AB}, \nu)$, where $\nu = 1/\tau$ is the macroscopic frequency. We also assume that media send the first message at time $t = 0$. Accordingly, all subsequent messages are sent at macroscopic times $t_k = k\tau$ for $k = 1, 2, 3, \dots$. Although the model is well-defined for $\tau < 1$ too, we consider only macroscopic periods in the sequel. Mean field equations (MFEs) of the model read

$$\begin{cases} \frac{dn_A}{dt} = [1 - n_A - 2n_B + n_B^2] + \alpha_{AB} (1 - n_A - n_B) \delta(t \bmod \tau) , \\ \frac{dn_B}{dt} = [1 - n_B - 2n_A + n_A^2] - \alpha_B n_B \delta(t \bmod \tau) , \end{cases} \quad (1)$$

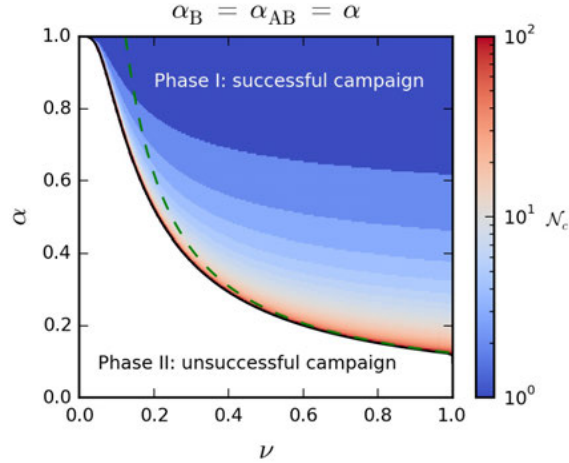


Figure 1: Density plot of \mathcal{N}_c in the mean field approximation from numerical integration of MFEs; the green dashed line represents an approximate analytic solution to eqs. (1).

with n_X denoting the fraction (or density) of agents with opinion $X = A$ or B . Terms in square brackets represent contributions to the evolution of the densities induced by agent-agent interactions belonging to the binary NG, while terms with Dirac-delta functions describe the effects of the periodic external field on the opinion densities.

Eqs. (1) can be integrated numerically with initial conditions

$$n_A(0) = 0, \quad n_B(0) = 1. \quad (2)$$

Depending on the values of the effectiveness parameters and the frequency of the external field, two distinct asymptotic solutions are observed: either the system goes to consensus on opinion A or it relaxes to a periodic equilibrium, with the opinion densities oscillating around average values

$$\bar{n}_X = \lim_{t \rightarrow \infty} \frac{1}{\tau} \int_t^{t+\tau} n_X(\sigma) d\sigma, \quad X = A, B. \quad (3)$$

Change from one solution to the other is not smooth. It occurs abruptly for critical values of the model parameters. To show this, we define \mathcal{N}_c as the number of periods needed to the external field in order to bring the system to consensus on opinion A. In Fig. 1 we show a density plot of \mathcal{N}_c as a function of ν and $\alpha_B = \alpha_{AB} \equiv \alpha$. We observe that \mathcal{N}_c keeps finite and small in the upper part of the plot, while it surges in proximity of the black curve separating the upper and lower part of the plot. This curve represents a critical line separating the two phases of the model. Below it we have $\mathcal{N}_c = +\infty$. In this region, the system never goes to consensus on opinion A. The black curve is well approximated by the hyperbole

$$\alpha_c(\nu) = \frac{1}{23} (9 \cdot 2^{2/3} + 6 \cdot 2^{1/3} - 19) \frac{1}{\nu} = \frac{0.123745 \dots}{\nu}, \quad (4)$$

provided $\nu \geq 0.5$. This is represented by a green dashed curve in Fig. 1.

3 The NG in presence of two competing periodic external fields

We then study the system under the influence of two competing external fields. As previously, we consider N agents interacting according to the dynamics of the binary NG, but now we assume that

before interaction	after interaction	before interaction	after interaction
$M_A \rightarrow L$	$M_A - L$	$M_B \rightarrow L$	$M_B - L$
$A \xrightarrow{A} A$	$A - A$ with prob. 1	$B \xrightarrow{B} B$	$B - B$ with prob. 1
$A \xrightarrow{A} B$	$A - AB$ with prob. β_B	$B \xrightarrow{B} A$	$B - AB$ with prob. γ_A
$A \xrightarrow{A} AB$	$A - A$ with prob. β_{AB}	$B \xrightarrow{B} AB$	$B - B$ with prob. γ_{AB}

Table 2: table of media-listener interactions (M_A = media broadcasting opinion A, M_B = media broadcasting opinion B, L = listener).

half of the agents are initially in state A and the rest are in state B. We represent media as two additional fictitious agents M_A and M_B , both connected to the whole population and advertising opinions A and B respectively. When interacting with the agents, media always play the role of speaker. The basic rules for the media-agent interactions are reported in Table 2. We assume that M_A (M_B) broadcasts a message every $T_A = \tau_A N$ ($T_B = \tau_B N$) agent-agent interactions, with $\tau_A \geq 1$ ($\tau_B \geq 1$). We also assume that M_A broadcasts the first message at time $t = 0$, while M_B does it at macroscopic time $t = t_{\text{del}}$ with $0 \leq t_{\text{del}} \leq \tau_B$. The media action is now parametrized by the 7-tuple $(\beta_B, \beta_{AB}, \gamma_A, \gamma_{AB}, \nu_A, \nu_B, \phi)$ with $\nu_A = 1/\tau_A$, $\nu_B = 1/\tau_B$ and $\phi = t_{\text{del}}/\tau_B$. Owing to the high dimensionality of the parameter space, studying the model is more complicated than we did in sect. 2. First of all, whatever choice of parameters we make the system never relaxes to a steady state. Even if consensus is reached on either opinion A or B at some point in time, the subsequent action of the other media always reintroduces disagreement among the population. In full generality, MFEs read

$$\begin{cases} \frac{dn_A}{dt} = (1 - n_A - 2n_B + n_B^2) + \beta_{AB}(1 - n_A - n_B) \delta(t \bmod \tau_A) - \gamma_A n_A \delta[(t - t_{\text{del}}) \bmod \tau_B], \\ \frac{dn_B}{dt} = (1 - n_B - 2n_A + n_A^2) + \gamma_{AB}(1 - n_A - n_B) \delta[(t - t_{\text{del}}) \bmod \tau_B] - \beta_B n_B \delta(t \bmod \tau_A), \end{cases} \quad (5)$$

and the initial conditions we impose on them are

$$n_A(0) = n_B(0) = 1/2. \quad (6)$$

We consider three different cases:

- i) competing external fields with different frequencies: we assume $\beta_B = \beta_{AB} = \gamma_A = \gamma_{AB} = \alpha$ and $t_{\text{del}} = 0$ but $\tau_A \neq \tau_B$. For each $\alpha = \alpha^*$, the system lives on a plane (ν_A, ν_B) parallel to the plane $(\hat{\nu}_A, \hat{\nu}_B)$ generated by the coordinate axes $\hat{\nu}_A$ and $\hat{\nu}_B$;
- ii) competing external fields with different effectiveness: we assume $\tau_A = \tau_B = \tau = 1/\nu$ and $t_{\text{del}} = 0$ but $\beta_B = \beta_{AB} = \beta$ and $\gamma_A = \gamma_{AB} = \gamma$ with $\beta \neq \gamma$. For each $\nu = \nu^*$, the system lives on a plane (β, γ) which is neither parallel to the plane $(\hat{\beta}_B, \hat{\gamma}_A)$ generated by the coordinate axes $\hat{\beta}_B$ and $\hat{\gamma}_A$ (this would correspond to having $\beta_{AB} = \text{const.}$ and $\gamma_{AB} = \text{const.}$) nor parallel to the plane $(\hat{\beta}_{AB}, \hat{\gamma}_{AB})$ generated by the coordinate axes $\hat{\beta}_{AB}$ and $\hat{\gamma}_{AB}$ (this would correspond to having $\beta_B = \text{const.}$ and $\gamma_A = \text{const.}$);
- iii) competing external fields with relative time shift: we assume $\tau_A = \tau_B = \tau = 1/\nu$ and $\beta_B = \beta_{AB} = \gamma_A = \gamma_{AB} = \alpha$ but $\phi = t_{\text{del}}/\tau \neq 0$. For each $\nu = \nu^*$, the system lives on a plane (α, ϕ) that is not parallel to any coordinate plane, just like we have in case ii).

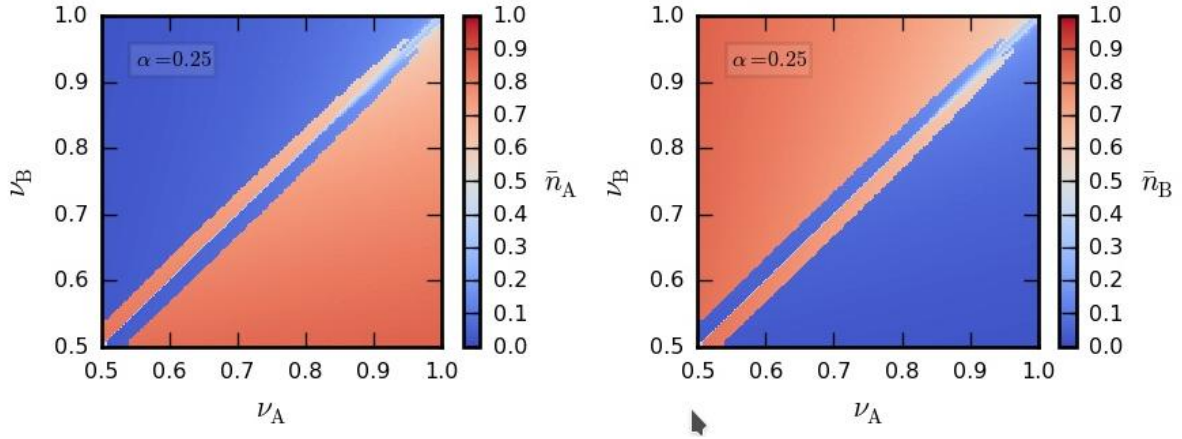


Figure 2: Average densities \bar{n}_A and \bar{n}_B at periodic equilibrium for $\tau_A \neq \tau_B$ from numerical integration of MFEs.

3.1 An example: case *i*)

In this contribution we consider only case *i*) and refer the reader to our paper [6] for a systematic description of all cases. For $\tau_A > \tau_B$ it is natural to expect that $\bar{n}_A < \bar{n}_B$ and the other way round. In other words, if M_A broadcasts with lower frequency than M_B , it should also be less effective. Moreover, the larger the ratio τ_A/τ_B , the larger the expected ratio \bar{n}_B/\bar{n}_A . This is what we meant by *natural expectation* in the abstract. It turns out, however, that things are not always as simple as naturally expected. In Fig. 2 we report density plots of \bar{n}_A and \bar{n}_B corresponding to $\alpha = 0.25$, obtained from numerical integration of eqs. (5) with initial conditions eq. (6). Due to limitations in our computational budget, we could only perform simulations for $0.5 \leq \nu_A, \nu_B \leq 1.0$. We notice the presence of two stripes, parallel and close to the symmetry diagonal, where the average opinion densities are unexpectedly swapped. It can be shown that the starting point of the stripes shifts progressively to lower frequencies along the main diagonal as α increases. Over the rest of the plot \bar{n}_A and \bar{n}_B are qualitatively as common sense suggests. The coordinates $\nu_A = \nu_B = \nu_{\text{cusp}}$ of the starting point of the stripes can be analytically estimated with decent approximation. We find

$$\nu_{\text{cusp}} = \frac{1}{1 + 2\sqrt{2}} \frac{1}{\alpha}. \quad (7)$$

In order to explain the origin of the observed stripes, we must consider that after each field sends a message, the system has a certain time to react to it before the other field sends a subsequent message. This time can be considered as period during which the former field influences the population in its favor. It is reasonable to expect that the winning field is also the one that has more time to influence the agents. This depends on the frequencies ν_A and ν_B . In the setup of case *i*) the agent dynamics is symmetric under the exchange $n_A \leftrightarrow n_B$ for $0 \leq t < \min\{\tau_A, \tau_B\}$, while the symmetry gets definitely broken for $t \geq \min\{\tau_A, \tau_B\}$. For $\tau_A < \tau_B$ we can regard M_B as broadcasting with the same frequency as M_A but with positive time delay $t_{\text{del},\ell} = \ell(\tau_B - \tau_A)$, increasing at each subsequent period, i.e. for $\ell = 1, 2, \dots$. Therefore, for $t \geq \tau_A$, M_A (M_B) can be regarded as a *first (second) mover*. This jargon belongs naturally to business strategy. It is meant to describe industrial competitions where the order of actions is a relevant discriminating factor, determining which player taking part in the competition is bound to win it. If $\tau_B - \tau_A \ll \tau_A/2$, the increase rate of $t_{\text{del},\ell}$ is very slow. In this case M_B behaves like a fast follower over many periods. It has more time than M_A to influence the agents. As a consequence, the system relaxes to a periodic equilibrium in which M_B prevails over M_A (second-mover advantage),

while the imbalance of the opinion densities becomes eventually too large to be reversed after a number ℓ of periods such that $t_{\text{del},\ell} \simeq \tau_A/2$. By contrast, if $\tau_B - \tau_A \lesssim \tau_A/2$, the increase rate of $t_{\text{del},\ell}$ is faster. In this case, a small number ℓ of periods is sufficient to have $t_{\text{del},\ell} \simeq \tau_A/2$. If this occurs before the system has relaxed to its ultimate equilibrium, then M_A has sufficient time to let the internal dynamics of the agents work in its favor and M_B has no chance to overtake M_A (first-mover advantage).

4 Conclusions

We have investigated the influence of periodic external fields, representing mass media, on the dynamics of agents playing the binary Naming Game (NG). Our major motivation for studying this is understanding to what extent consensus can be exogenously directed in the framework of an empirically grounded opinion model. In this regard we recall that theoretical predictions derived from the NG have been shown to reproduce correctly experimental results in Web-based live games with controlled design. In our study, we have found that *a*) a single external field is able to convert an entire population of agents within a finite time provided it acts with sufficiently high frequency and effectiveness and *b*) two competing external fields, contending for supremacy, lead the population to a complex periodic equilibrium.

It is important to remark that the application domain of the NG goes beyond the mere understanding of how language conventions arise. If we interpret letters A and B as opposite arguments rather than as names, one argument being *in favor of* and one *against* a given choice, we can regard an agent in state A or B as one who has made the choice (A and B are certainty states) and an agent in state AB as one who has not made it yet and holds both arguments for further consideration (AB is an uncertainty state). There are plenty of real-life situations where such dichotomous dynamics occur in first approximation. Just as a reference example the reader may consider the longstanding debate concerning the legitimacy of the European institutions. Since several years EU political elites are addressing the problem of how improving the level of acceptance of the European governance among citizens. The issue of the EU legitimacy as well as the potential impact of the media coverage in such a process have been the subject of scholarly research. Our work represents hopefully a useful theoretical abstraction for such concrete problems.

References

- [1] L. Steels. A self-organizing spatial vocabulary. *Artif. Life*, 2(3):319–332, 1995.
- [2] L. Steels. Self-organizing vocabularies. In C. G. Langton and K. Shimohara, editors, *Artif. Life V*, pages 179–184. Nara, Japan, 1996.
- [3] A. Baronchelli, M. Felici, E. Caglioti, V. Loreto, and L. Steels. Sharp transition towards shared vocabularies in multi-agent systems. *J. Stat. Mech. Theor. Exp.*, P06014, 2006.
- [4] A. Baronchelli, L. Dall’Asta, A. Barrat, and V. Loreto. Nonequilibrium phase transition in negotiation dynamics. *Phys. Rev. E*, 76:051102, 2007.
- [5] A. Baronchelli. A gentle introduction to the minimal Naming Game. *Belgian J. Ling.*, 30:171–192.
- [6] F. Palombi, S. Ferriani, and S. Toti. The influence of periodic external fields in multi-agent models with language dynamics. *arXiv:1706.07092*, 52 pages.

FORCES EXERTED BY A SOLITARY WAVE ON HORIZONTAL CYLINDER

Luana Gurnari¹ and Pasquale Filianoti¹

¹Università “Mediterranea” degli studi di Reggio Calabria, Dipartimento DICEAM, Loc. Feo di Vito, 89122 Reggio Calabria, Italia. E-mail: filianoti@unirc.it, luana.gurnari@unirc.it

ABSTRACT. Several authors have studied the solitary wave load on a submerged horizontal cylinder. In the present work, a CFD analysis of the horizontal force exerted by a solitary wave on a horizontal cylinder is presented. The evaluation of the horizontal force is based on the speed drop factor Fr , that is the ratio (greater than one) between the time needed by the wave pressure to cross the solid body and the travel time across a transparent cylinder. The Fr is calculated numerically through an experiment in a numerical wave flume, using the Computational Fluid Dynamics (CFD) technique. The numerical simulation was carried out through CRESCO platform, using the cresco5 cluster. In this work, we used the cresco5_16h24 code with a number of cores set at 48 (16x3). Several simulations with different amplitudes of solitary waves were made.

1 Analytical method to estimate the wave loads

The analytical solution proposed hereafter is derived by the original approach proposed by [1] for a rectangular submerged barrier. The methodology is based on the speed drop of a periodic wave passing over a submerged obstacle.

Referring to Figure 1, the time lag $\Delta t'$ spent by the pressure fluctuation to cover the distance from point ①' to point ②', both lying on the surface of a solid obstacle, is greater than the time Δt spent to cover the same distance between the points ① and ②, in the absence of the obstacle. Let us indicate by $Fr (> 1)$ the ratio $\Delta t'/\Delta t$ which corresponds to the reduction factor in the propagation speed of the solitary wave passing over the cylinder. The existence of Fr let us to explain why the horizontal force on the solid body is different from the Froude-Krylov force (i.e. the force on a transparent body), even if the amplitudes of pressure fluctuations are unchanged on points ①' and ①, and on ②' and ②. The same phenomenon occurs in the interaction between surface waves and cylinders of arbitrary position, provided that they can be considered as “large bodies” ([2]), in order that wave loads are practically inertial. The speed $\underline{C}_{\Delta p}$ of pressure head waves propagating across the cylinder is the ratio between distance AA' (see Fig. 2) and the time spent by the wave crest to cover it, averaged for $-\pi/2 < \beta < \pi/2$. The $\underline{C}_{\Delta p}$ in the undisturbed field can be calculated in the same way. The ratio $\underline{C}_{\Delta p}/\underline{C}_{\Delta p}$ furnishes the speed drop factor Fr .

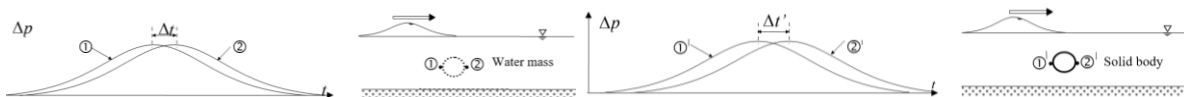


Fig.1. Definition sketch for the speed drop factor Fr . on the left: pressure time series at points ① and ② on the equivalent water mass. On the right: pressure time series at points ①' and ②' on the solid body represented by the cylinder.

The horizontal component of the unitary force acting on the water cylinder during the passage of the solitary wave can be calculated as:

$$F_h(t) = F_{h_A}(t) - F_{h_B}(t), \quad (1)$$

where F_{h_A} and F_{h_B} are the horizontal forces acting on semi-cylinder A and B (see Fig.2), respectively:

$$F_{h_A}(t) = \int_{-\pi/2}^{\pi/2} \Delta p(-\varepsilon/2, t) r \cos \beta d\beta, \quad F_{h_B}(t) = \int_{-\pi/2}^{\pi/2} \Delta p(\varepsilon/2, t) r \cos \beta d\beta. \quad (2)$$

where Δp is the wave pressure on the semi-cylinder, β is the angle defined in Fig. 2, and ε is the phase angle:

$$\varepsilon = D|\cos \beta| \quad \text{for the water cylinder; } \varepsilon = \mathcal{F}_r D|\cos \beta| \quad \text{for the solid cylinder.} \quad (3)$$

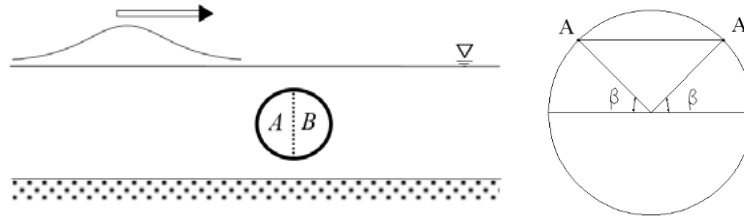


Fig.2: A is the frontal semi-cylinder, that is the side facing the incoming direction of the solitary wave. B is the opposite semi-cylinder. On the right, the definition of angle β for the calculation of forces.

Considering the weighted average value of $\cos \beta$ in the phase angle ε , equal to $\frac{\pi}{4}$ and substituting in the equations of ε , permits us to integrate Eqs. (2), obtaining

$$F_{h_A}(t) = \rho g A D \left\{ 1 - \tanh^2 \left[-k \mathcal{F}_r \frac{\pi}{8} D - k c t \right] \right\}, \quad F_{h_B}(t) = \rho g A D \left\{ 1 - \tanh^2 \left[k \mathcal{F}_r \frac{\pi}{8} D - k c t \right] \right\}. \quad (4)$$

2 the CFD Model

The computational domain is a wave-flume having a piston-type wavemaker placed on the left extremity. At 12 m far from the wavemaker and 0.2 m below the water level, it was placed an horizontal cylinder (0.127 m diameter). The sketch of the wave-flume is shown in Fig. 3.

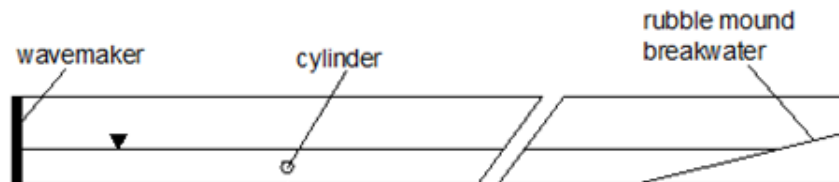


Fig.3: The computational domain of the wave flume. The wavemaker is on the left side.

At the opposite side of the wavemaker a rubble mound breakwater was placed. The distance between the wavemaker and the breakwater is about 41 m; the slope of this breakwater is 1:5 and the flume water depth is 0.4 m. The computational domain was discretised by ANSYS Meshing application using triangular element in which the maximum size of the elements is 5 cm. In the domain near the cylinder a refinement of the element size was done, reducing the elements size until 2 mm. In order to match the behaviour of a physical wave tank, we have to set the boundary conditions of the numerical wave tank. Smooth no-slip wall boundary conditions have been assigned to all solid walls and to the cylinder surface, whilst the upper domain boundary is defined as a pressure outlet with zero-gauge pressure. The wave-flume has a piston-type wavemaker placed on the left extremity of the computational domain. Starting from rest condition, the wave generation process has been simulated assigning a velocity to the left vertical wall of the wave flume, by means of a User Defined Function (UDF). The numerical approach is based on a two-dimensional CFD simulation using the Euler-Euler approach, implemented in the commercial code Ansys Fluent 14.5, Academic Version. We used the volume of fluid (VOF) model to represent the air-water interface, where the two fluids (phases) are not interpenetrating between each other. The multi-phase flow CFD simulation, in which both air and water flows have been assumed unsteady, was solved by the Navier-Stokes equations. To solve the RANS equations there are several turbulence models. In the present case, we used the $k-\omega$ turbulence model.

3 The wave generation by a piston-type wavemaker

The law of the paddle motion to generate solitary waves in a wave flume was carried out by several approaches.

The differences among these formulations are just on how to describe the displacement of the paddle of the wavemaker. To generate solitary waves, [3] used Boussinesq's first-order solution for the solitary wave profile and the wave paddle trajectory can be described with an implicit law

$$\xi(t) = \frac{A}{kd} \tanh[k(ct - \xi)], \quad (5)$$

where $\xi(t)$ is the wave paddle position along the y-axis, and k is the wave number. As described by [4], the total duration of the wave paddle motion is infinity in theory. As [5] suggested, the wave profile is completely generated after 99.9% of the total stroke length.

The explicit solution for the displacement of the wavemaker based on Rayleigh's formulation is

$$\xi(t) = \frac{A}{kd} \frac{d \tanh(k(ct))}{d + A \{1 - \tanh^2[k(ct)]\}}, \quad (6)$$

where k has a different expression than in Boussinesq theory:

$$k = \sqrt{\frac{3A}{4d^2(A+d)}} \quad (7)$$

3 Results of the numerical simulation

Solitary waves with several amplitudes were generated. We measured the pressure fluctuation $\Delta p(t)$, both along the solid cylinder surface and along the surface of a water cylinder having the same diameter and draft of the solid one. The pressure $\Delta p(t)$, was recorded in twenty-four points of the

external contour of the cylinder, at 15° intervals. In order that the water cylinder was undisturbed by the presence of the solid one, we choose the position of the center of the water equivalent cylinder 7m far from the wavemaker and 5 m before the solid cylinder. Both horizontal and vertical forces on the cylinder have been carried out by integrating $\Delta p(t)$, over the cylinder contour (indeed, we considered the force acting on a strip of cylinder of unit length). Also, the speed drop factor F_r , is calculated. To this aim, we calculated the phase shift between forces $F_{h_A}(t)$ and $F_{h_B}(t)$ acting on half cylinder, respectively. Values of F_r for solitary wave with different values of A/d , are shown in Tab. 1. The time histories of the horizontal and vertical force produced by a solitary wave with amplitude $A=0.0390\text{m}$, on the equivalent water cylinder and on the solid cylinder, are shown in Figure 4. Horizontal force on the transparent cylinder is clearly inertial and it is a confirmation of the effectiveness of the numerical simulation. In the same Figure, the vertical force was represented too. The maximum vertical force F_{v_max} , is an order of magnitude smaller than the maximum horizontal force F_{h_max} , and it occurs few instants before the occurrence of the maximum horizontal force. Moreover, the vertical force is null when F_{h_max} occurs, vice versa the horizontal one is null when the minimum vertical force occurs. This is because, in the inertial regime, the horizontal force is synchronous with the horizontal acceleration, while the vertical force is synchronous with vertical acceleration. As a further confirmation of the effectiveness of the numerical model, we show also the horizontal force calculated with the theoretical model (Eqs. 1, 4), considering as an input $F_r = 1.0$. The agreement between numerical and theoretical values is very good.

Tab. 1- Summary of results of the CDF simulation.

A	A/d	F_r	A	A/d	F_r
0.015	0.0375	1.64	0.1	0.25	1.55
0.032	0.0792	1.80	0.12	0.3	1.93
0.0390	0.0975	1.93	0.16	0.4	1.94
0.0508	0.1270	1.71	0.2	0.5	1.73
0.0624	0.156	2.02	0.3	0.75	1.94
0.0782	0.1955	1.57			

The horizontal force on the solid cylinder is no more antisymmetric in respect to the zero. The amplitude of the negative peak is much smaller (absolutely) than the positive peak amplitude.

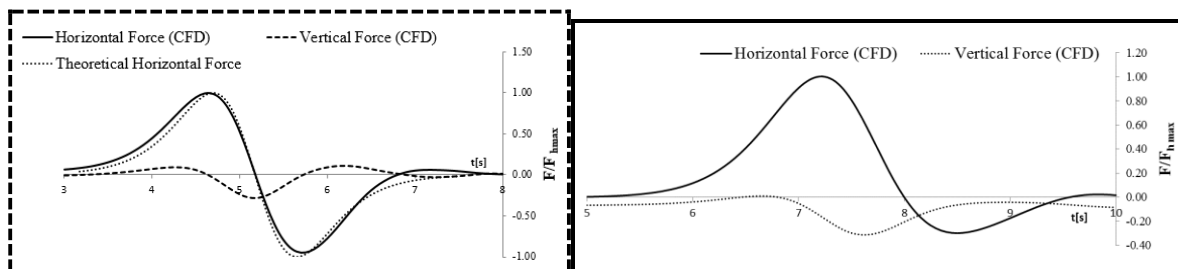


Fig.4: Horizontal and vertical forces on the water equivalent cylinder (dashed panel) and on the solid cylinder (continuous panel) exerted by a solitary wave with amplitude $A=0.0390\text{m}$.

The Fig. 5 shows the amplitude of the maximum horizontal force F_{h_max} as a function of A/d . The dotted line represents the values obtained through the CFD model. The continuous line has also obtained analytically, but starting from the values of F_r , obtained by means of the CFD. The

theoretical curve underestimates the F_{h_max} , calculated by integrating the numerical pressure fluctuations $\Delta p(t)$ recorded on the cylinder contour

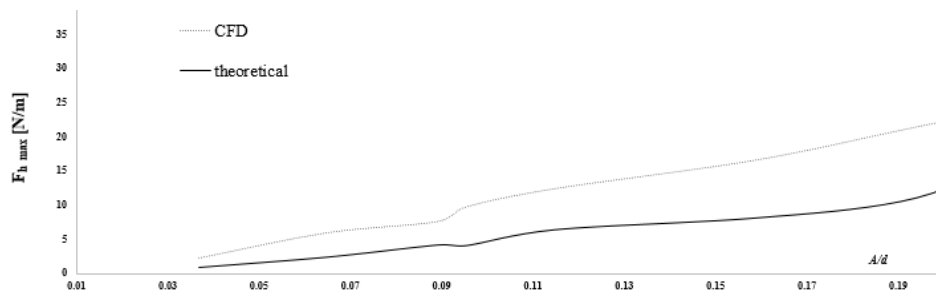


Fig.5: F_h max vs. relative amplitude A/d , of the solitary wave.

2 Conclusions

The loads exerted by a solitary wave on a submerged horizontal cylinder have been dealt with in this paper. The methodology followed is the numerical experiment. A circular cylinder of 0.127 m of diameter was put in a flume 41 m long and 0.4 m depth, raised 0.135 m from the bottom. Various solitary waves having different amplitudes have been generated by a piston type wavemaker. Forces were measured and compared with the theoretical model. Comparisons revealed that the analytical model tends to underestimate the horizontal force on the cylinder. The underestimation is 50% in average up to $A/d=0.20$. For larger A/d , the relative difference become narrower, with an average underestimation equal to 17% for the analytical solution in the range $0.125 < A/d < 0.4$.

References

- [1] Filianoti P. and Piscopo R., 2008. "On the tsunami wave-submerged breakwater interaction". Proceedings of MERCEA, Seismic Engineering International Conference commemorating the 1908 Messina and Reggio Calabria Earthquake.
- [2] BOCCOTTI 2000. *Caisson breakwaters embodying an OWC with a small opening - Part II: A small-scale field experiment*, Ocean Engineering 34 (5-6), 820-841.
- [3] Goring, D. G., (1979). "Tsunami: The propagation of long waves onto a shelf," Report KH-R-12-38, W. M. Keck Laboratory of Hydraulics and Water Resources, California- Institute of Technology, Pasadena, California.
- [4] HUGHES, S.A., 1993, "Physical Models and Laboratory Techniques in Coastal Engineering", Advanced Series on Ocean Engineering, Vol. 7. World Scientific, London, 568 pp.
- [5] Goring, D.G. and Raichlen, F., 1980, "The generation of long waves in the laboratory", Proc. 17th International Conference of Coastal Engineering, Sydney- Vol 1, pp 289-314.

HIGH PRESSURE PREMIXED CH₄/H₂ – Air FLAMES

D. Cecere^{1*}, E. Giacomazzi¹, N. Arcidiacono¹ and F.R. Picchia¹

¹*Process and Energy Systems Engineering Laboratory, ENEA, Rome, Italy*

ABSTRACT. A numerical study on lean turbulent premixed methane/hydrogen-air slot flames at high pressures is conducted through two-dimensional Direct Numerical Simulation (DNS). A single equivalence ratio flame at $\Phi = 0.7$ and 50% of hydrogen content is explored for three different pressures (0.1, 1, 4 MPa respectively). Due to the decreased kinematic viscosity with increasing pressure, the turbulent Reynolds numbers increase with an associated decrease of the smallest turbulence scales that wrinkle the flame front.

A general description of the three flames is provided, evidencing their macroscopic differences in terms of turbulent displacement speed, flame surface areas and mean flame brush thickness. Furthermore, topological features of the flames are explored by analyzing the probability density functions of several quantities: curvature, curvature shape factor, alignment between vorticity and principal strain rate vectors with flame surface normal, displacement speed and its components. Finally the differential diffusivity effect on the local equivalence ratio in the three flame is investigated showing a strong effect of the turbulent flame thickness of the high pressure flames on light species differential diffusivity.

1 Description of Numerical Simulations

The present work deals with the Direct Numerical Simulation of a slot burner CH₄/H₂/Air premixed flame at pressures ranging from atmospheric to 40 MPa and described in terms of flames front curvatures, flame surface density, displacement speeds. First the slot burner test case conditions are reported, and the numerical results concerning the pressure effects on instantaneous and average flame properties are shown.

The test case consists in an unconfined premixed slot-burner Bunsen flame at three different pressures (1, 10, 40 bar). The shape of the device is similar to that experimentally analyzed in [1] but with smaller dimensions and higher bulk velocities to artificially decrease the convective DNS times. A central slot-jet of premixed reactants is surrounded on both longer sides by two coflowing jets. The central slot-duct is 1.2 mm wide (h) and 4 mm long; its two walls have a thickness $h_w = 0.18$ mm and are assumed adiabatic in the simulation (more details in [7]).

The central jet is a lean (equivalence ratio $\Phi = [(X_{H_2} + X_{CH_4})/X_{O_2}]/[(X_{H_2} + X_{CH_4})/X_{O_2}]_{stoich} = 0.7$) mixture of methane, hydrogen and air with fuel molar fractional distribution of 50% H₂ and 50% CH₄ for the three flames. Mixture temperature is 588 K, the surrounding jets have the composition and temperature of the combustion products of the laminar freely propagating flame associated to the central jet mixture. The unstrained laminar flames properties at these conditions computed using OpenSmoke [2] are summarized in Table 1. In this table, T_u is the unburnt gas temperature, T_b the burnt gas temperature, S_L represents the unstrained laminar flame speed, $\delta_L = (T_b - T_u)/|\partial T/\partial x|_{max}$ is the flame

*Corresponding author. E-mail: donato.cecere@enea.it.

Case	P [bar]	n_{H_2}	T_u [K]	T_b [K]	S_L [cm s ⁻¹]	δ_L [cm]	ρ_u [kg m ⁻³]
A	1.0	0.5	588	2076	120.06	0.0331	0.547
B	10.0	0.5	588	2095	49.55	0.0060	5.474
C	40.0	0.5	588	2099	21.35	0.0030	21.898

Table 1: CH₄/H₂ – Air laminar flames characteristics (A-B-C) based on the 23-species chemical mechanism adopted in the present DNS [4]. The number of Hydrogen moles n_{H_2} is defined as $n_{\text{H}_2} = x_{\text{H}_2}/(x_{\text{H}_2} + x_{\text{CH}_4})$.

Jets	$U_{0,in}$ [m/s]	T_{in} [K]	u'_{in} [m/s]	$\delta_{z,in}^{corr}$ [mm]	L_{Duct} [mm]	h [mm]
Central	100	588	10	0.4	4	1.2
Surrounding	25	2076-2095-2099	0.01	0.1	0.5	7

Table 2: Boundary conditions imposed at the inlet of the three channels. In particular, $u'_z = u'_x = u'_y$ and $\delta_{z,in}^{corr}$, $\delta_{x,in}^{corr} = \delta_{y,in}^{corr} = \delta_{z,in}^{corr}/2$ are used as input to the Klein procedure to produce synthetic turbulence at the inlet of the three channels. Units: [m/s] for velocity, [K] for temperature, [mm] for turbulent correlation length scale, duct length, L_{Duct} , and its width, h .

Jet exit velocity peak, U_0 [m s ⁻¹]	110
Jet exit velocity fluctuation, u' [m s ⁻¹]	10
Jet exit turbulent length scale, L_t [mm]	1.05
Jet Reynolds number, $Re_{jet} = U_0 h/\nu$	2447 – 24470 – 97880
Turbulent Reynolds number, $Re_t = u' L_t/\nu$	194 – 1940 – 7760
Kolmogorov length scale, η_K [μm]	17.42 – 3.5 – 1.6
Turbulent/chemical speed ratio, u'/S_L	8.33 – 20.18 – 46.83
Turbulent/chemical length scale ratio, L_t/δ_L	3.02 – 16.6 – 33.3
Damköhler number, $S_L L_t/u' \delta_L$	0.380 – 0.867 – 0.747
Karlovitz number, $(\delta_L/\eta_K)^2$	361 – 293 – 351

Table 3: Actual turbulent combustion parameters characterizing the simulated CH₄/H₂ – Air lean premixed flames. The turbulent velocity fluctuation and the integral length scale were evaluated at the center exit of the central slot-duct. The laminar flame speed and the flame front thickness including the Soret effect were assumed as combustion parameters. The dynamic viscosity used in the calculation of the central jet Reynolds number is that of the inlet CH₄ – H₂/Air A mixture, $\mu = 2.95 \cdot 10^{-5}$ kg m⁻¹s⁻¹.

front thermal thickness based on the maximum temperature gradient, and ρ_u is the unburnt density.

The central jet has a bulk velocity of 100 m/s (imposed as a mean plug-flow at the inlet of the central duct). Homogeneous isotropic turbulence is artificially generated at the inlet of the central duct by forcing a turbulent spatial correlation scale in the streamwise direction $\delta_{z,in}^{corr} = 0.4$ mm and a streamwise velocity fluctuation $u'_z = 10$ m/s used as inputs to the Klein’s procedure [3] (see Table 2). The surrounding flows have a velocity of 25 m/s (imposed as a mean plug-flow) and no turbulence is forced. Other parameters characterizing the present lean premixed turbulent flames are reported in Table 3. These constant parameters locate the present flames nominally in the Thin Reaction Zone of the combustion diagram.

The computational domain is composed of four structured blocks, three for the inlet channels and one

for the main zone. The domain size of this zone in the streamwise (z), crosswise (y) and spanwise (x) directions is $L_x \times L_y \times L_z = 24h \times 15h \times 2.5h$; it is discretized through $2800 \times 2200 \times 1$ computational nodes, and its smallest grid size is $1.0 \mu\text{m}$. The grid is refined in the y and z direction near the inlet duct walls and coarsened (up to $\Delta y \sim 500 \mu\text{m}$) only in the y direction far from the central jet at the surrounding ($y > 0.015 \text{ m}$) where non reflecting boundary conditions are applied and fluctuations are small.

The DNS was run at $1.0 - 10.0 - 40.0 \text{ bar}$ pressures using a 22 species and 124 elementary reactions kinetic mechanism [4]. Improved staggered non-reflecting inflow and outflow boundary conditions (NSCBC) were adopted at the edges of the computational domain in the y and z directions [5, 6].

The simulations were performed using the in-house ‘‘HeaRT’’ code which solves the fully compressible reactive Navier-Stokes equations in their conservative formulation. Details about the numerics and models of molecular transport can be found in Cecere et al. [7, 8]. The simulations were performed on the linux cluster CRESCO (Computational Center for Complex Systems) at ENEA requiring 1.5 million CPU-hours running on 3500 processors. The solution was advanced at a constant time step of 1.5 ns ; after the flame reached stationary statistics, the data were collected through $4 \tau_U$, $\tau_U = 0.218 \text{ ms}$ being the flow through time based on the jet exit duct centerline velocity and the total streamwise domain length.

1.1 General description of the turbulent flames

In the three flames, as soon as the fresh mixture injected from the central slot mixes with the coflowing hot products, ignites thus resulting in two continuous flame sheets anchored at each edge of the slot and connected at the flame tip.

At the exit of the central slot, the Favre averaged axial velocity \widetilde{U}_z reaches a maximum value of 110 m s^{-1} , greater than its inlet value. In fact, the formation of the channel boundary layer produces a flow section restriction, resulting in a velocity acceleration effect. Downstream, a crosswise component is generated resulting in the entrainment of the coflowing hot products towards the central jet core.

Figure 1 shows instantaneous temperature snapshots of the flames at the three different pressures. The more pressure increases, the shorter the flame is. The position of the flame is a consequence of the equilibrium between the burning velocity and the mean flow velocity of the fresh gases. Since the mean flow velocity of the fresh gases remains constant for the three numerical conditions, a decrease of the flame height corresponds to an increase of the turbulent burning velocity.

Figure 2 shows the location of the three investigated flames in the turbulent combustion diagram u'/S_L vs l/δ_L . The correlation length $l_0 = \int_{-\infty}^{+\infty} R(r) dr / R(0)$ (with $R(r) = \sum_i R_{ii}(r)$, $R_{ii}(r) < u'_i(x)u'_i(x+r) >$), is calculated on the isosurface $c = 0.1$ with the velocity fluctuation u' . The flame thickness is calculated measuring the curvilinear length starting from each point of the $c = 0.1$ isosurface and tangent to the progress variable gradient ∇c up to $c = 0.99$. The laminar flame speed is obtained using the laminar flame speed correlations proposed by Bougrine et al. [9],

$$S_L(\alpha, \phi, Y_{res}^u, p) = U_1^0 \cdot (\alpha, \phi) \cdot \left(\frac{T^u}{T^0}\right)^{\alpha_T} \cdot \left(\frac{p}{p^0}\right)^{\alpha_p} \cdot (1 - \alpha_{res} \cdot f(Y_{res}^u)), \quad (1)$$

where α is the hydrogen rate in fuel, ϕ the equivalence ratio, Y_{res}^u the diluent mass fraction, p the pressure, U_1^0 , α_T , α_p , α_{res} and f are functions defined and calibrated in [9], $p^0 = 10^5 \text{ Pa}$ and $T^0 =$

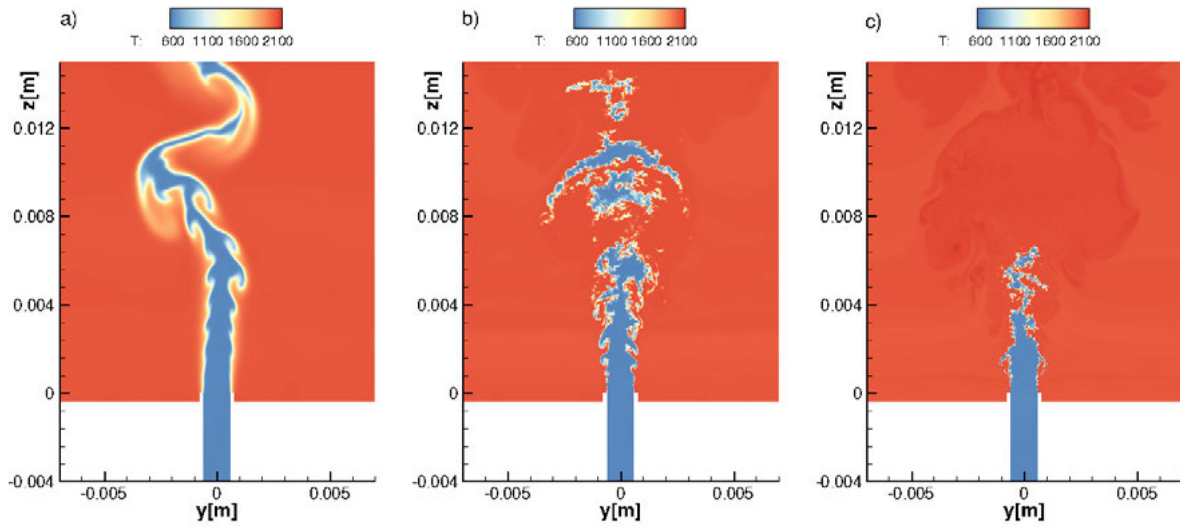


Figure 1: Comparison of instantaneous temperature profile of the three flames: a) 1 bar; b) 10 bar; c) 40 bar.

300 K are the reference pressure and temperature respectively. This correlation is valid in a domain of high proportions of hydrogen in the CH_4 , high residual burned gas mass ratios as well as high pressures and temperatures. If we describe turbulent premixed flames as an ensemble of flame elements, it resembles steadily propagating strained or curved laminar flames. When Karlovitz (Ka) number (defined with the diffusive flame front thickness) is between 1 and 100 small eddies can penetrate the diffusion preheating zone of the flame thus increasing the mixing process, but not the thinner reaction layer that remains close to a wrinkled laminar reaction zone. The present flames belong to this regime, identified as "Thin Reaction Zone (TRZ)" regime. As the pressure increases, the flame points shift towards the upper right zone of the diagram, still remaining within the TRZ regime. This is due mainly due to the decreasing of flame front thickness and the flame speed as the pressure increases. Anyway, as shown in Fig. 2, some points are in the region at $Ka_r > 1$, indicating that the smallest eddies of size η can enter into the inner layer thickness δ (typically one tenth of the preheat zone thickness which is of the same order of magnitude as the flame thickness δ_L).

The instantaneous structure of the three flames is shown in Fig. 1a-b-c by means of the instantaneous flame temperature. It is seen that the two flames at high pressure show a fine, convoluted flame front structure with convex and concave cusps superimposed on large scale flame branches, typical of turbulent premixed flames at high pressure [10]. The enhanced small scale wrinkling of the high pressure flames is due to the increase of u'/S_L values and the decrease of Kolmogorov scales. The increase of pressure has the effect of reducing the total flame length at constant reactants bulk velocity, indicating therefore an increased mixture reactivity, despite the fact that laminar propagation velocity decreases strongly with increasing pressure (see Table 1).

Figure 3 shows the three flame mean lengths at different pressures. The corresponding iso- $c = 0.5$ lines have a length of 2.06×10^{-2} m, 1.49×10^{-2} m, 1.12×10^{-2} m respectively.

At the exit of the slot, the mean turbulent flame brush decreases as the pressure increases, showing that the 40 bar flame is able to resist at higher strain rate ($\delta_T = 1.2 \times 10^{-4}$ m, 2.76×10^{-5} m, 1.05×10^{-5} m for the 1, 10, 40 bar respectively). At the flame tip, the flame brush thickens but the high pressure flame has always the thinnest δ_T ($\delta_T = 1.5 \times 10^{-3}$ m, 1.3×10^{-3} m, 7.5×10^{-4} m for the 1, 10, 40

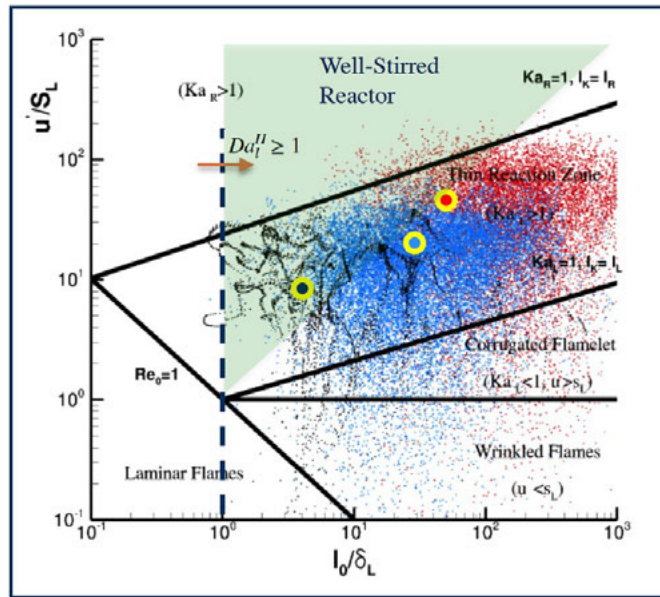


Figure 2: Turbulent combustion regimes of the investigated flames. (Black points) 1 bar; (Blue points) 10 bar; (Red points) 40 bar. The three coloured points represent the nominal operational regimes based on constant values of turbulence (u' , l_0) and flame (S_L , δ_L) characteristics.

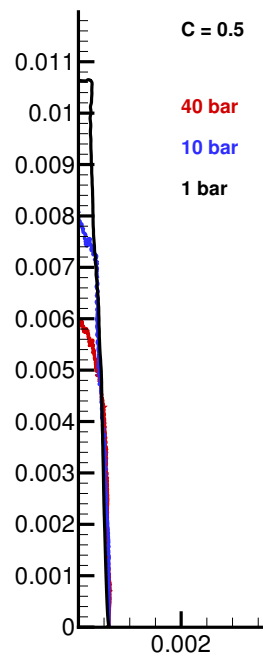


Figure 3: Mean progress variable iso-lines at $c = 0.5$ of the three flames.

bar respectively).

The increased reactivity of flames by increasing pressure is also measured through the global turbulent flame speed [1], i.e.,

$$\bar{S}_T = \dot{m}_u / (\rho_u \mathcal{A}_{\bar{c}=0.5}). \quad (2)$$

ρ_u being the unburnt density mixture, \dot{m}_u the inlet reactant mass flow rate and $\mathcal{A}_{\bar{c}=0.5}$ the area of the average iso-surface $\bar{c} = 0.5$. This analysis provides $\bar{S}_T = 5.69 \text{ ms}^{-1}$, $\bar{S}_T = 8.03 \text{ ms}^{-1}$ and $\bar{S}_T = 10.62 \text{ ms}^{-1}$ for the flames at 1 bar, 10 bar, 40 bar, respectively.

2 Conclusions

Two-dimensional DNS of three turbulent premixed slot $\text{CH}_4/\text{H}_2 - \text{Air}$ flames at different pressures have been carried out using detailed kinetics. A general description of the flames was provided, evidencing their macroscopic differences by means of turbulent consumption speed and flame surface density. Furthermore, topological features of the flames were also explored: flame height, statistics of curvatures and displacement speeds. A progress variable, c , has been defined as sum of four species mass fractions: $\text{CO}_2 + \text{CO} + \text{H}_2\text{O} + \text{H}_2$. Each individual species has its own mass diffusion coefficient (modeled according to the Hirschfelder and Curtiss law). The flames at high pressure show a fine, convoluted flame front structure and an enhanced small scale wrinkling. The increase of pressure has also the effect of reducing the total flame length (from $\sim 0.011 \text{ m}$ to $\sim 0.006 \text{ m}$) at constant reactants bulk velocity, indicating therefore increased mixture reactivity, despite the fact that laminar propagation velocity decreases strongly with increasing pressure. The turbulent flame speed increases from $\sim 5.7 \text{ ms}^{-1}$ to $\sim 10.7 \text{ ms}^{-1}$ as the pressure increases.

References

- [1] S.A. Filatyev, J.F. Driscoll, C.D. Carter, J.M. Donbar, Measured properties of turbulent premixed Flames for model assessment, including burning velocities, stretch rates, and surface densities, *Combust. Flame* 141 (2005) 1-21.
- [2] A.Cuoci, A. Frassoldati, T. Faravelli, E. Ranzi, A computational tool for the detailed kinetic modeling of laminar flames: application to $\text{C}_2\text{H}_4/\text{CH}_4$ coflow flames, *Combust. Flame* 160 (2013) 870-886.
- [3] M. Klein, A. Sadiki, J. Janicka, A digital filter based generation of inflow data for spatially developing direct numerical or large eddy simulations, *J. Comput. Phys.* 186 (2003) 652-665.
- [4] <http://creckmodeling.chem.polimi.it/index.php/menu-kinetics/menu-kinetics-detailed-mechanisms/menu-kinetics-c1-c3-mechanism>
- [5] T.J. Poinso, S.K. Lele: Boundary Conditions for Direct Simulations of Compressible Viscous Flow, *J. Comput. Phys.* 101 (1992) 104-129.
- [6] J.C. Sutherland, C.A. Kennedy, Improved boundary conditions for viscous, reacting, compressible Flows, *J. Comput. Phys.* 191 (2003) 502-524.

- [7] D. Cecere, E. Giacomazzi, N.M.S. Arcidiacono, F.R. Picchia, Direct numerical simulation of a turbulent lean premixed CH₄/H₂-Air slot flame, *Combust. Flame* 165 (2016) 384-401.
- [8] D. Cecere, E. Giacomazzi, An immersed boundary method for Large Eddy Simulation of compressible flows using a staggered-grid approach, *Comput. Methods Appl. Mech. Engrg.* 280 (2014) 1-27.
- [9] S. Bougrine, S. Richard, A. Nicolle, D. Veynante, Numerical study of laminar flame properties of diluted methane-hydrogen-air flames at high pressure and temperature using detailed chemistry, *Int J Hydrogen Energy* 36 (2011) 12035-12047.
- [10] H. Kobayashi, T. Kawahata, K. Seyama, T. Fujimari, J.S. Kim, *Proc. Combust. Inst.* 29 (2009) 1793-1800.
- [11] N. Bouvet, F. Halter and C. Chauveau, Y. Yoon, On the effective Lewis number formulations for lean hydrogen/hydrocarbon/air mixtures, *Int J Hydrogen Energy* 38 (2013) 5949-5960.
- [12] B. Savard, G. Blanquart, An a priori model for the effective species Lewis numbers in premixed turbulent flames, *Combust. Flame* 161 (2014) 1547-1557.
- [13] K. Harstad, J. Bellan, The Lewis number under supercritical conditions, *Int. J. Heat and Mass Transfer*, 42, (1999) 961-970.
- [14] E. Giacomazzi, D. Cecere, F.R. Picchia, N.M. Arcidiacono, Approaching the Numerical Simulation of Trans- and Super- Critical Flows, *European Combustion Meeting 2017*, 18-21 April, Dubrovnik.

DEFINITION OF A FIGURE OF MERIT FOR THE OPTIMIZATION OF ENEA NAI DEVICE

Romolo Remetti¹, Giada Gandolfo^{1*}, Luigi Lepore¹, Nadia Cherubini²

¹*SAPIENZA University of Roma, Department of Basic and Applied Sciences for Engineering, via Scarpa 14, Roma 00161, Italy*

²*ENEA, Italian National Agency for New Technologies, Energy and Sustainable Economic Development, C.R. Casaccia, via Anguillarese 301, Roma 00123, Italy*

ABSTRACT. In the frame of Chemical, Biological, Radiological, and Nuclear defense European activities, the ENEA, the Italian National Agency for New Technologies, Energy and Sustainable Economic Development, is proposing the Neutron Active Interrogation system (NAI), a device designed to find transuranic-based Radioactive Dispersal Devices hidden inside suspected packages. It is based on Differential Die-Away time Analysis, an active neutron technique targeted in revealing the presence of fissile material through detection of induced fission neutrons. Several Monte Carlo simulations, carried out by MCNPX code, and the development of ad-hoc design methods, have led to the realization of a first prototype characterized by easy transportability, light weight, and real-time response. First results have shown device's capability to detect gram quantities of fissile materials.

1 Introduction

Since September 2013, ENEA, the Italian National Agency for New Technologies, Energy and Sustainable Economic Development, was involved in the EDEN (End-user DEMO for cbrNe) Demonstration Project within the European framework [1], whose primary target has been to face the CBRNE risks in EU Member States through research, technological development of new tools, and related experimental demonstrations.

At ENEA Casaccia Research Center, the Nuclear Material Characterization and Radioactive Waste Management Laboratory is proposing the Neutron Active Interrogation system (NAI) as a convenient technical solution to find transuranic-based RDDs hidden inside suspected packages.

NAI uses a remotely controlled neutron active interrogation stage for detecting fissile and fertile materials potentially combined with explosives. Its main goal is being able to detect even low quantities (i.e. some grams) of fissile material thanks to the Differential Die-Away time Analysis [2-8], a neutron interrogation technique targeted in revealing the presence of fissile material through detection of induced fission neutrons.

Operative constraints ask for easy transportation, carrying, quick deploying into field scenarios, and fast operability. Reliable responses about the presence of nuclear threats have to be obtained within few seconds.

2 Materials and methods

The NAI device is based on the Differential Die Away time Analysis (DDAA) technique optimized for small quantities of fissile materials.

DDAA involves a fast neutron source, a moderator around the sample suspected of containing fissile material, and a ^3He neutron detectors array surrounded by cadmium sheets.

The interrogation technique can be summarized as follows: 1) the source emits an appropriate flux of fast neutrons (interrogation neutrons), 2) neutrons slow down in the moderator, 3) thermal neutrons induce fissions on fissile materials, 4) both scattered interrogation neutrons, and newly-produced induced fission neutrons may be collected by the detectors array.

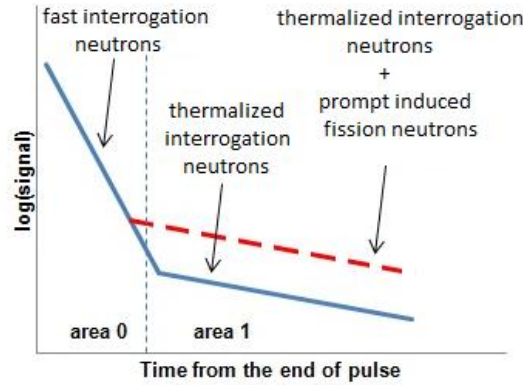


Fig.1: Theoretical DDAA expected measured signal

The expected measured signal is shown in Fig.1. Such trends can be explained as follows: i) fast interrogation neutrons are characterized by a certain die-away time as shown in area 0; ii) if fissile material is not present (solid curve) the signal in area 1 is produced by thermalized interrogation neutrons that have a die-away time some orders of magnitude bigger than fast neutrons' one (this signal is called hereafter "background signal"); iii) if fissile material is present (dashed curve) the signal in area 1 is produced by the sum of thermalized interrogation neutrons and prompt induced fission neutrons, characterized by the same die-away time; iv) the difference between the two curves is appreciable thanks to cadmium sheets surrounding the detection system, that reduce of several order of magnitude the signal of thermalized interrogation neutrons; v) the more is the fissile mass, the more is the difference between the two curves.

The device optimization is based on the simulation of several possible experimental setups in order to identify the better configuration. The starting point of the study is the experimental geometry used by K. A. Jordan et al. shown in fig.5 of ref. [9]. Different layouts have been compared using the mathematical criterion shown below.

Fig. 1 shows, in log scale, a typical trend of the signal vs. time. It is possible to approximate this curve with two straight lines: one due to signal coming from the source (thermalized interrogation neutrons), and the other one due to signal coming from the sum of background and prompt induced fission neutrons.

Both straight lines are determined selecting the region of the most likely linearity (in log scale), considering for each curve an appropriate row of N data $(t_i, y_i \pm \sigma_i)$. All transition regions are neglected.

Considering the set of N data $(t_i, y_i \pm \sigma_i)$, a least squares regression line is obtained as follows:

$$y = A + Bt$$

where:

$$A = \frac{S_{tt} \cdot S_y - S_t \cdot S_{ty}}{S \cdot S_{tt} - S_t \cdot S_t} \quad B = \frac{S \cdot S_{ty} - S_t \cdot S_y}{S \cdot S_{tt} - S_t \cdot S_t}$$

$$S_t = \sum_{i=1}^N \frac{t_i}{\sigma_i^2} \quad S_y = \sum_{i=1}^N \frac{y_i}{\sigma_i^2} \quad S_{tt} = \sum_{i=1}^N \frac{t_i^2}{\sigma_i^2} \quad S_{ty} = \sum_{i=1}^N \frac{t_i \cdot y_i}{\sigma_i^2} \quad S = \sum_{i=1}^N \frac{1}{\sigma_i^2}$$

The parameters A and B are affected by uncertainty; it is possible to calculate σ_A and σ_B using the propagation of statistical errors:

$$\sigma_A^2 = \sum_{i=1}^N \left(\frac{\partial A}{\partial y_i} \right)^2 \cdot \sigma_i^2 \quad \sigma_B^2 = \sum_{i=1}^N \left(\frac{\partial B}{\partial y_i} \right)^2 \cdot \sigma_i^2$$

$$\Delta A = \sigma_A = \sqrt{\frac{S_{tt}}{S_{tt} \cdot S - S_t^2}} \quad \Delta B = \sigma_B = \sqrt{\frac{S}{S_{tt} \cdot S - S_t^2}}$$

After the definition of both regression lines, the intersection time is calculated. It corresponds to the instant when slope changes.

$$t' = \frac{A_1 - A_2}{B_2 - B_1} \quad \Delta t' = t' \cdot \left(\frac{\Delta(A_1) + \Delta(A_2)}{A_1 - A_2} + \frac{\Delta(B_1) + \Delta(B_2)}{B_2 - B_1} \right)$$

Passing to the exponential form,

$$y_1' = 10^{A_1 + B_1 t} \quad y_2' = 10^{A_2 + B_2 t}$$

y_1' approximates the background signal, y_2' approximates the signal with fissile material in the sample.

Having fixed the duration t_m of the measurement, it is possible to define C_1 , the counts corresponding to the background, and C_2 , the counts corresponding to the case in which fissile material is present.

$$C_1 = \int_{t'}^{t'+t_m} y_1' dt \quad C_2 = \int_{t'}^{t'+t_m} y_2' dt$$

The net counts C are obtained for difference.

$$C = \frac{1}{\ln 10} \left[\frac{10^{A_2 + B_2(t'+t_m)} - 10^{A_2 + B_2 t'}}{B_2} - \frac{10^{A_1 + B_1(t'+t_m)} - 10^{A_1 + B_1 t'}}{B_1} \right]$$

The uncertainty is given by ΔC .

$$\Delta C = \left| \frac{\partial C}{\partial A_1} \right| \cdot \Delta A_1 + \left| \frac{\partial C}{\partial A_2} \right| \cdot \Delta A_2 + \left| \frac{\partial C}{\partial B_1} \right| \cdot \Delta B_1 + \left| \frac{\partial C}{\partial B_2} \right| \cdot \Delta B_2 + \left| \frac{\partial C}{\partial t'} \right| \cdot \Delta t'$$

In order to take into consideration the uncertainty associated to the evaluation of the C value, it is also possible to define a proper figure of merit, FOM, in the following form:

$$FOM = \frac{1}{\sqrt{nps}} \frac{C_2 - C_1}{|\Delta C_1| + |\Delta C_2|}$$

Where $1/\sqrt{nps}$ is a factor that makes the simulation result independent from the number of simulated source particles (nps) [10]; in this way, the comparison between simulations with different nps becomes possible.

From the previous considerations, it results that the FOM is a quantitative parameter that characterizes the quality of configuration: the higher is the FOM, the more appropriate is the analyzed geometry in order to implement experimentally the DDAA.

3 Simulation results

Several simulations have been carried out in order to optimize the NAI experimental setup according to the required performances.

Fixing the same value for the mass of moderator (about 106 kg), the relative positions between the device components influence the quality of the response. Fig.2 reports the sequential MCNPX trials for the DDAA optimization for the measurement of small volume samples.

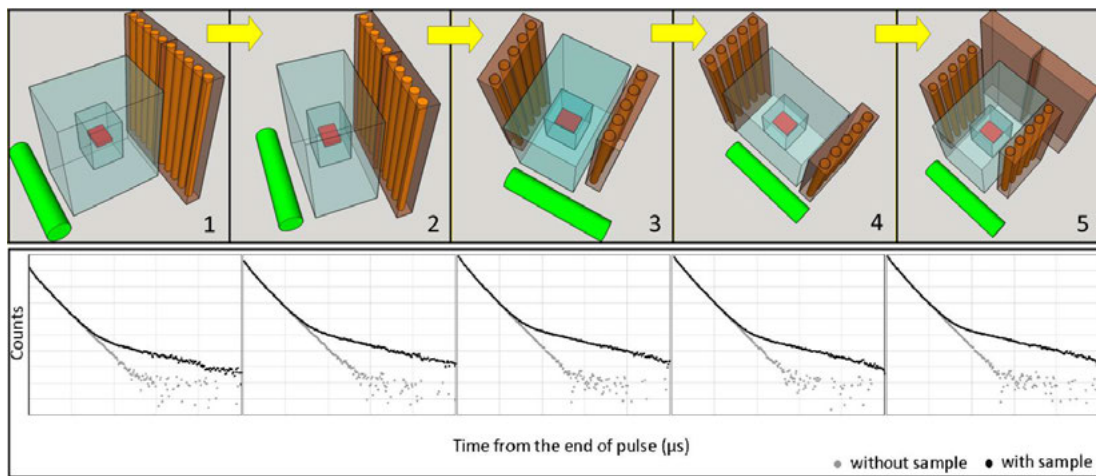


Fig.2: Sequential MCNPX trials for the DDAA optimization with a fixed value for the mass of moderator. In green the neutron generator, in transparent blue the moderating structure around the sample to be measured (red), in orange the ^3He tubes embedded into a polyethylene structure (gray).

The five possible setups shown in Fig. 2 have been simulated into MCNPX. The code outputs the time behavior of $^3\text{He}(n,p)^3\text{H}$ reactions recorded by ^3He tubes. The elaboration of resulting data generates the DDAA curves shown in Fig. 2, in which grey curve represents the case in which the cavity into the moderator is empty, and the black curve represents the case in which the sample containing fissile material is present. Observing the curves, it is possible to state that the setup 1 is the worst, because the discrimination between the two curves is the least efficient. On the other hand, setups 3 and 5 seem to be the best, enhancing the difference between the two curves. This statement is confirmed by the successive elaboration of simulation results through the mathematical method described previously.

From the elaboration of simulated data, the following results, in terms of the FOM, are produced:

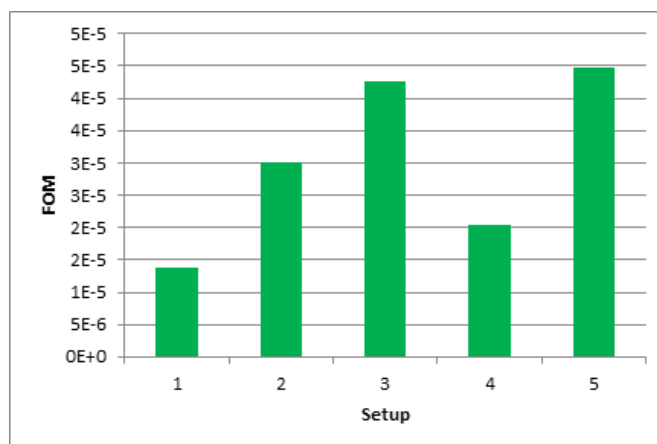


Fig.3: FOM produced by the elaboration of simulated data for the five possible configurations shown in fig.2

As a general result, it is recommended:

- to reduce the moderator bulk inserted between the sample and the detectors, because the less it is, the higher is the detection efficiency (referring to Fig. 2, setup 2 is better than 1, and setup 3 is better than 4);
- to reduce the moderator bulk inserted between the sample and the neutron source, because the less is the mass, the higher is the neutron flux on the sample (obviously, an appropriate thickness of moderator has to be maintained because the slower are the neutrons, the higher is the probability to induce thermal fissions);
- to realize a sample cavity, because when the detectors surround the sample, the detection efficiency is the highest; moreover, this corresponds to the most efficient discrimination between interrogation and induced fission neutrons (referring to Fig. 2, setup 5 is the best among the others).

Further simulations have been carried out to optimize the minimum moderator mass, in order to lower the weight of the device, thus allowing better transportability. In particular, 30 kg moderator reduction was assayed and a prototype has been tested on the field in a live demo open to the public in the framework of EDEN Project Demonstration RN4.1 and RN4.2, occurred on 29th and 30th September 2015 at ENEA Frascati Research Centre in Rome [11].

3 Conclusions

The ENEA NAI device is a tool designed to improve CBRNE resilience capacity of EU Member States. In particular, NAI is built to uncover radioactive and nuclear threats also in the form of RDDs, the so-called “dirty bombs”. The DDAA laboratory technique has been transposed to field scenarios, designing a configuration capable in giving a real-time response about the presence of fissile materials inside a suspected package.

The design of the device has been carried out thanks to several simulations with the aim of optimizing the experimental setup according to the required performances.

The development of a mathematical criterion, based on the definition of a figure of merit, has allowed the design of a transportable system, light in weight, with a real-time response, able to provide a positive detection of fissile material in the case of a sample containing about 2 g of ²³⁵U hidden in a package.

The computing resources and the related technical support used for this work have been provided by CRESCO/ENEAGRID High Performance Computing infrastructure and the staff [12].

CRESCO/ENEAGRID High Performance Computing infrastructure is funded by ENEA, the Italian National Agency for New Technologies, Energy and Sustainable Economic Development, and by Italian and European Research Programmes; see <http://www.cresco.enea.it/english> for more information.

The simulations ran on CRESCO4 cluster. The number of simulated source particles for each possible layout was 2×10^{10} . Each simulation required a CPU time of about 3×10^5 s.

References

- [1] <https://www.eden-security-fp7.eu/#close>, last accessed: 22 May 2017
- [2] Caldwell, J.T.; Kunz, W.E.; Atencio, J.D. Apparatus and Method for Quantitative Assay of Generic Transuranic Wastes from Nuclear Reactors. Patent US4483816. 1984
- [3] Jordan, K.A., Gozani, T., Pulsed neutron differential die away analysis for detection of nuclear materials, *Nucl. Instrum. Methods Phys. Res. B*, 2007, 261, 365-368
- [4] Menlove, H.O., Menlove, S.H., Tobin, S.J., Fissile and fertile nuclear material measurements using a new differential die-away self-interrogation technique, *Nucl. Instrum. Methods Phys. Res. A* 2009, 602, 588-593.
- [5] Henzl, V., Swinhoe, M.T., Tobin, S.J., Menlove, H.O., Measurement of the Multiplication of a Spent Fuel Assembly with the Differential Die-away Method Within the Scope of the Next Generation Safeguards Initiative Spent Fuel Project," *Journal of Nuclear Materials Management* 2012, 40:3, 61-69
- [6] Belian, A., Menlove, H.O., Swinhoe, M.T., and Tobin, S.J., New Design of the Differential Die-away Self-interrogation Instrument for Spent Fuel Assay, *Journal of Nuclear Materials Management* 2012, 40:3, 58-60
- [7] Kaplan, A.C., Henzl, V., Menlove, H.O., Swinhoe, M.T., Belian, A.P., Flaska, M., Pozzi, S.A., Determination of total plutonium content in spent nuclear fuel assemblies with the differential die-away self-interrogation instrument. *Nucl. Instrum. Methods Phys. Res. A* 2014, 764, 347-351
- [8] Kaplan, A.C., Henzl, V., Menlove, H.O., Swinhoe, M.T., Belian, A.P., Flaska, M., Pozzi, S.A., Determination of spent nuclear fuel assembly multiplication with the differential die-away self-interrogation instrument, *Nucl. Instrum. Methods Phys. Res. A* 2014, 757, 20-27
- [9] Jordan, K.A.; Gozani, T.; Vujic, J. Differential die-away analysis system response modeling and detector design. *Nucl. Instrum. Methods Phys. Res. A* 2008, 589, 436-444.
- [10] Briesmeister, J.F., Editor, MCNP—A General Purpose Monte Carlo Code for Neutron and Photon Transport; LA-12625-M, Los Alamos National Laboratory, Los Alamos, New Mexico, November 1993.
- [11] Cherubini, N., Dodaro, A., Gandolfo, G., Lepore, L., Marzo, G.A., Piccinelli, E., Remetti, R., Field Prototype of the ENEA Neutron Active Interrogation Device for the Detection of Dirty Bombs. *Challenges* 2016, 7(2), 17; <http://dx.doi.org/10.3390/challe7020017>
- [12] Giovanni Ponti, "The role of medium size facilities in the HPC ecosystem: the case of the new CRESCO4 cluster integrated in the ENEAGRID infrastructure," in 2014 International Conference on High Performance Computing and Simulation, pp. 1030-1033.

STRUCTURE OF METAL OXIDE NANOCLUSTERS FROM AB-INITIO COMPUTATION

Roberto Grena^{1,2}

¹*C.R. ENEA Casaccia, via Anguillarese 301, Rome, Italy*

²*SPCTS, rue Atlantis 12, Limoges, France*

ABSTRACT. Ab-initio methods are valuable tools when studying the structure of very small nanoclusters (up to some hundreds of atoms). Small nanoclusters are often quite far from the crystal bulk structure and they cannot be studied as bulk pieces with ordered crystal structure; neither bulk/surface models can be applied under a certain size. Moreover, the environment is so different from the bulk crystal that empirical potentials built in usual environments can easily fail. The presented activity is aimed to understand the structure of metal dioxide nanoclusters, their behaviour in different environments (e.g., when they are used as additives in nanofluids) and the tendency to form ordered or disordered structures.

1 Introduction

The determination of the structure of very small nanoclusters is a challenging problem, since the structure is often quite far from the known crystal bulk structure, and under a certain size no bulk or bulk/surface model can be used to accurately describe the structure. On the other side, with a number of atoms of the order of some hundreds it is impossible to explore systematically the phase space to find an equilibrium structure from scratch. It is also likely that structures will change depending on the synthesis process, on the environment [1] and on the aging of the sample. The aim of the activity described in the present report is to obtain informations about the structure of very small (diameter < 2 nm) metal dioxide nanoclusters. Many of such materials (such as TiO₂ or ZrO₂) have strong technological importance, and current synthesis techniques allow to produce extremely small clusters whose properties are important to assess.

Two main aspects were investigated: how to obtain a plausible description of the properties of the global minimum, and how to assess the dynamical structure of the cluster in different environment. Various techniques are employed, such as standard minimization tools (BFGS), Car-Parrinello (CP) and Born-Oppenheimer (BO) molecular dynamics.

2 Computational techniques and required resources

2.1 General description of the computations

A starting point for the computations are the experimental informations about the clusters. However, they are often very incomplete: it is possible to assess the size, the general shape (spherical/ovoidal), and to obtain incomplete information on the structure from scattering, such as the PDF (Pair Distribution Function). From the PDF, one can find which bulk structure is more similar to the cluster

structure, if there is any. For larger clusters, usually the PDF is enough to univocally identify the crystal structure of the bulk of the cluster, and only the surface rearrangement should be studied; a complete description of the cluster structure is often achieved. Unfortunately, this is not the case when small clusters are considered. The PDF obtained can be quite far from the crystalline structure. In this case, among the polymorphs of the crystal, the structure with a PDF that is locally most similar to the cluster PDF should be selected, identifying peaks and small-distance features typical of the crystal. If such a structure is found, a piece of bulk crystal is cut with approximately the same size and shape of the cluster to study. This is used as starting configuration for the structure optimization. If the PDF appears quite far from all the crystal structures, e.g., due to a strong tendency to disorder, the only possibility is to consider all the possible polymorphs of the crystal and repeat the analysis starting from different initial configurations.

In order to find a plausible energy minimum, a bit of disorder is introduced to break the initial symmetry of the cluster, and an initial relaxation is performed. Such a minimum will likely be only a local minimum, near to the crystal structure. In order to explore the phase space, annealing and quenching are performed, heating the cluster to high temperatures and then cooling it down to obtain a new starting point for the minimization. Of course, a full exploration of the phase space is impossible, but informations such as the tendency to disorder and general properties of the global minimum can be found by comparing the different local minima. In particular, it can happen that, after the first cycles, the structure becomes quite stable for the annealing, obtaining in the following quenching structures near in geometry and energy: in such a case, it is likely that the found structure is near to the equilibrium structure.

The obtained structures can then be used to compute a theoretical PDF, to be compared to the experimental results. Even if the informations given by the experimental PDF alone is far from complete, a good agreement with the PDF of a theoretically found minimum is a strong evidence that the equilibrium structure has been found.

The structures obtained from annealing and quenching are static minima, i.e., they are (local) equilibrium structures for the completely isolated cluster at temperature $T = 0$ K. However, in real clusters two factors affect strongly the structure: environment and temperature. The first factor can be studied statically, hypothesizing a mechanism of interaction of the cluster with molecules of the environment (e.g. chemisorption of dissociated water, [1]) and computing minima when the interaction is introduced (e.g. placing H^+ and OH^- groups bound to the surface). The second aspect require a dynamical simulation, that should be performed with molecular dynamics. A simulation for a sufficient long time (> 10 ps) allows to observe directly the structural changes due to temperatures, and to compute an average PDF that is likely to be found when experiments are made at quite high temperatures. Moreover, the frequencies of vibration of the cluster can be extracted from the dynamics.

Molecular dynamics can be employed also in interaction with an environment, e.g., observing the dynamical effect of hot molten nitrates on a ceramic nanocluster. The interaction with the environment and the structural changes it induces can be studied in temperature.

2.2 Technical details

All the computations are ab-initio, based on Density Functional Theory (DFT) in Kohn-Sham formulation (KS) [2,3]. The software Quantum Espresso is used [4]. The software adopt a plane waves – pseudopotential approach. The chosen functional was the Perdew-Burke-Ernzerhof functional (PBE) [5]. Pseudopotentials of both ultrasoft [6] and norm-conserving [7] types are used, depending on the material: pseudopotentials were selected by testing them on the crystal, computing the crystal size and bulk modulus and selecting the pseudopotentials that better reproduce the experimental data. Metals considered in the various computations are Ti, Zr, Ce, Hf and Sn. Moreover, Oxygen is required to form the dioxide; computations of the behaviour of a nanocluster in

molten Sodium nitrate was also performed, so Na and N atoms were required too. Norm-conserving pseudopotentials were used for Ce, Hf, Sn, while Ultrasoft pseudopotentials were used for O, Ti, Zr, N, Na. For each computation, the cutoff on the energy of the plane waves was found with a convergence test and resulted usually quite high, due to the presence of a small-core atom as O and to the localized nature of the bonds.

Two different class of clusters were considered, one with a diameter around 1.2-1.3 nm (130-150 atoms) and one with a diameter around 2 nm (300-350 atoms). The smaller systems of course allowed more refinements in the computations.

The initial relaxation, and the annealing-and-quenching procedures, were all performed using Car-Parrinello (CP) molecular dynamics [8] as a relaxation tool, since direct optimization methods failed to converge on such large systems when the starting point was far from the minimum; this was true even for the smaller clusters. However, smaller clusters allowed a refining of the minima using “traditional” (non-CP) DFT and a quasi-Newton (BFGS) minimization method. So, this further refinement was applied to the smaller cluster when looking for the minima.

In the dynamical simulations, Born-Oppenheimer method (BO) was used for the isolated smaller clusters, with a time step of 20 au (around 0.5 fs). The method was not applicable to larger cluster or to clusters in an environment, for convergence problems. In these cases, CP was used, with a time step of 2 au (about 0.05 fs).

2.3 Resources

Computations are performed using Cresco3 or Cresco4 system, preferably the latter. The number of cores required is usually 256 (or 288 in the case of Cresco3). An annealing/quenching cycle require from 30 to 50 runs of 24 hours, depending on the disorder of the final structure (highly disordered structures require longer times). Due to the long computation time, the search of multiple minima was limited to 4 minima.

Dynamical computations with BO method on smaller clusters allowed to simulate about 0.15 ps of time with a 24 hours run; CP method applied to the cluster immersed in molten nitrates allowed to simulate roughly the same time each day. So, the collection of an adequate time for the analysis (10 ps) require about 70 runs. Additional work for the initial relaxation should be considered, especially for the immersed cluster.

3 Studied systems

In this section, the computations made will be shortly reviewed.

Structural analysis of MO₂ clusters with a diametre around 2 nm

Annealing-and-quenching, with the method discussed above, of clusters of dioxide of 5 differemnt metals: Ti, Zr, Hf, Ce and Sn. The choice of the metals was made in order to analyze the widest possible range of materials with different properties (bulk typical crystal structures, electronegativity, ionic radius, allowed oxidation numbers) and the property that most interested to study was the tendency to assume crystal-like or disordered structures.

Polymorphism of TiO₂ clusters

Some evidence that TiO₂ can assume different structures, and not only the widely accepted anatase-like structure, was theoretically investigated on small (138 atoms) and “large” (342 atoms) clusters, with the annealing-and-quenching method starting from different bulk structures.

Dynamics of a small isolated ZrO₂ cluster

BO dynamics of a small (129 atoms) cluster of ZrO₂ was investigated, simulating its behaviour for a time of 10 ps at a temperature of 500 K.

Dynamics of a small ZrO₂ cluster immersed in molten nitrate

The behaviour of a small (129 atoms) cluster of ZrO₂ was simulated when it was immersed in liquid NaNO₃, in order to reproduce the behaviour of a nanoparticle in a nanofluid. Aspects to study were: the structural changes induced by the molten salt, the stability and the possible bounds between the salt ions and the cluster surface.

Acknowledgements

This work is made in collaboration with the Science des Procédés Céramiques et de Traitements de Surface (SPCTS) of Limoges, which supplies experimental results and PDFs computations.

The computing resources and the related technical support used for this work have been provided by CRESCO/ENEAGRID High Performance Computing infrastructure and its staff [9]. CRESCO/ENEAGRID High Performance Computing infrastructure is funded by ENEA, the Italian National Agency for New Technologies, Energy and Sustainable Economic Development and by Italian and European research programmes, see <http://www.cresco.enea.it/english> for information.

References

- [1] R. Grena et al. Stabilization Effect of Surface Impurities on the Structure of Ultrasmall ZrO₂ Nanoparticles: An Ab-Initio Study. *Journal of Physical Chemistry C* **119**, pp. 15618-15626, (2015).
- [2] P. Hohenberg and W. Kohn. Inhomogeneous electron gas. *Physical Review* **136**, pp. B864-871, (1964).
- [3] W. Kohn and L.J. Sham. Self-consistent equations including exchange and correlation effects. *Physical Review* **140**, pp. A1133-1138, (1965).
- [4] P. Giannozzi et al. QUANTUM ESPRESSO: a modular and open-source software project for quantum simulations of materials. *Journal of Physics: Condensed Matter* **21**, 395502, (2009).
- [5] J.P. Perdew, K. Burke, M. Ernzerhof. Generalized Gradient Approximation Made Simple. *Physical Review Letters* **77**, pp. 3865–3868, (1995).
- [6] D. Vanderbilt. Soft self-consistent pseudopotentials in a generalized eigenvalue formalism. *Physical Review B* **41**, pp. 7892-7895, (1990).
- [7] N. Troullier and J.L. Martins. Efficient pseudopotentials for plane-wave calculations. *Physical Review B* **43**, pp. 1993 – 2006, (1996).
- [8] R. Car and M. Parrinello. Unified Approach for Molecular Dynamics and Density-Functional Theory. *Physical Review Letters* **55**, pp. 2471-2474, (1985).
- [9] G. Ponti et al. The role of medium size facilities in the HPC ecosystem: the case of the new CRESCO4 cluster integrated in the ENEAGRID infrastructure. *Proceedings of the 2014 International Conference on High Performance Computing and Simulation, HPCS 2014*, 6903807, pp. 1030-1033.

SMAGORINSKY DYNAMIC MODEL FOR LARGE-EDDY SIMULATION OF TURBULENCE

Giacomo Rossi^{1*}, Donato Cecere², Eugenio Giacomazzi², Nunzio M. S. Arcidiacono²,
Franca Rita Picchia² and Bernardo Favini¹

¹*Sapienza University, Mechanical and Aerospace Engineering Department, Via Eudossiana 18, 00184, Rome, Italy*

²*ENEA, Process and Energy Systems Engineering Laboratory, Via Anguillarese 301, 00123, S. M. di Galeria (Rome), Italy*

ABSTRACT. The Germano dynamic improvement of the Smagorinsky subgrid turbulence model is successfully validated by means of the comparison between experimental data and numerical results obtained through the HearT numerical code on the backward facing step test.

1 Introduction

The Smagorinsky model [1] is the progenitor of most subgrid-scale stress models: unresolved momentum fluxes are expressed according to the Boussinesq assumption

$$\tau_{ij} - \frac{\delta_{ij}}{3}\tau_{kk} = -\mu_T \left(\frac{\partial \bar{u}_i}{\partial x_j} + \frac{\partial \bar{u}_j}{\partial x_i} \right) = -2\mu_T \bar{S}_{ij} \quad (1)$$

where μ_T is a subgrid scale viscosity, modelled via dimensional analysis as

$$\mu_T = C_s^2 \bar{\Delta}^{4/3} l_T^{2/3} |\bar{S}| \quad (2)$$

where l_T is the turbulence integral length scale, C_s is a model constant and \bar{S} the resolved shear stress. If the integral scale is assumed to be of the order of the grid size $l_T \simeq \Delta$, the eddy viscosity equation can be simplified as

$$\mu_T = (C_s \bar{\Delta})^2 |\bar{S}| \quad (3)$$

where the Smagorinsky constant C_s is real, so the model is absolutely dissipative. The value of C_s can be evaluated as

$$C_s \simeq \frac{1}{\pi} \left(\frac{2}{3C_K} \right)^{3/4} \quad (4)$$

that for a Kolmogorov constant $C_K \simeq 1.4$ yields $C_s \simeq 0.18$. For a lower value of Smagorinsky constant ($C_s = 0.1$) this model behaves very well for isotropic turbulence, free-shear flows and channel flow (with a damping function at the wall): near solid boundaries, indeed, the Smagorinsky model is too dissipative and therefore the length scale is typically modified by means of the Van Driest damping

*Corresponding author. E-mail: giacomo.rossi@uniroma1.it.

function, accounting for the reduced growth of the small scales near walls. Hence, the eddy viscosity can be rewritten as

$$\mu_T = \left[C_s \bar{\Delta} \left(1 - e^{-y^+/25} \right) \right] |\bar{S}| \quad (5)$$

2 Germano Turbulent Dynamic Model

The dynamic procedure developed by Germano aims to compute models' constants during the computation, rather than imposing them a priori. This is accomplished by defining a test filter (for the computed field) whose width $\widetilde{\Delta}$ is larger than the grid filter Δ : $\widetilde{\Delta} = \alpha \Delta$, with typically $\alpha = 2$.

The Smagorinsky model is here taken as an example to show how the dynamic procedure works. The subgrid-scale tensor of the double filtered field \widehat{u} is

$$\widehat{\tau}_{ij}^{\text{SGS}} = \widehat{u_i u_j} - \widehat{u}_i \widehat{u}_j \quad (6)$$

The resolved turbulent stress corresponding to the test filter applied to the field \widetilde{u} is

$$\mathcal{L}_{ij} = \widetilde{u_i u_j} - \widetilde{u}_i \widetilde{u}_j \quad (7)$$

The quantities $\widehat{\tau}_{ij}^{\text{SGS}}$, $\widetilde{\tau}_{ij}^{\text{SGS}}$ and \mathcal{L}_{ij} are related by the algebraic relation (Germano's identity) [2]

$$\mathcal{L}_{ij} = \widehat{\tau}_{ij}^{\text{SGS}} - \widetilde{\tau}_{ij}^{\text{SGS}} \quad (8)$$

In this equation $\widehat{\tau}_{ij}^{\text{SGS}}$ and $\widetilde{\tau}_{ij}^{\text{SGS}}$ have to be modelled while \mathcal{L}_{ij} can be explicitly calculated by applying the test filter to the LES results.

Assuming that an eddy-viscosity model is used to parameterize both subgrid and subtest stresses implies

$$\widetilde{\tau}_{ij}^{\text{SGS}} - \frac{1}{3} \widetilde{\tau}_{ll}^{\text{SGS}} \delta_{ij} = 2\widetilde{\mathcal{A}}_{ij} C \quad \text{and} \quad \widehat{\tau}_{ij}^{\text{SGS}} - \frac{1}{3} \widehat{\tau}_{ll}^{\text{SGS}} \delta_{ij} = 2\mathcal{B}_{ij} C \quad (9)$$

Substituting (9) in (8), it follows

$$\mathcal{L}_{ij} - \frac{1}{3} \mathcal{L}_{ll} \delta_{ij} = 2\mathcal{B}_{ij} C - 2\widetilde{\mathcal{A}}_{ij} C \quad (10)$$

In order to obtain C , it can be removed from the filtering as if it were constant, leading to

$$\mathcal{L}_{ij} - \frac{1}{3} \mathcal{L}_{ll} \delta_{ij} = 2C M_{ij} \quad (11)$$

Now all terms of (11) can be determined with the aid of \overline{u} : there are however five independent equations for only one variable C , so the problem is overdetermined. The coefficient can be determined via a least square approach to calculate the value that "best satisfies" the system (11):

$$C = \frac{1}{2} \frac{\mathcal{L}_{ij} M_{ij}}{M_{ij}^2} \quad (12)$$

However, the analysis of DNS and experimental data revealed that C field predicted by (12) varies strongly in space and contains a significant fraction of negative values, with a variance which may be

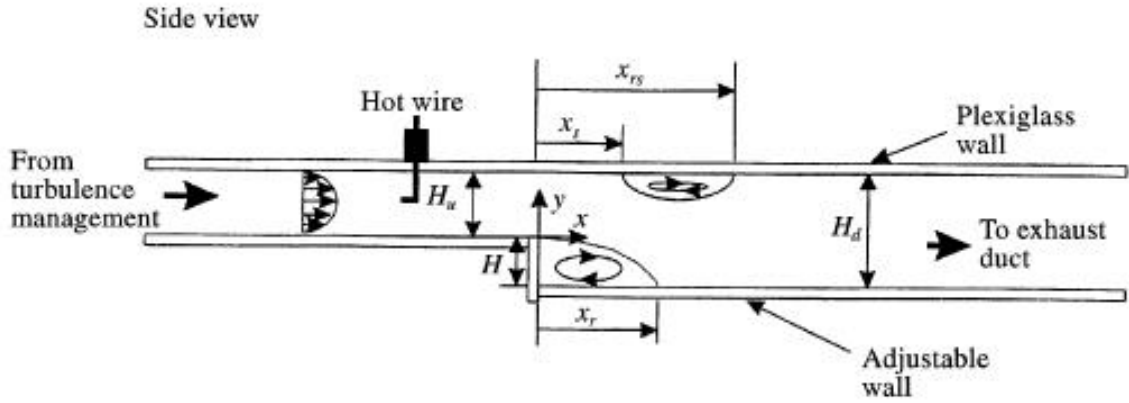


Figure 1: Backward facing step configuration [5]

Table 1: Simulation Setup

Step height (H)	1.27 cm
Inlet height (H_u)	$8H$
Tunnel span (D)	$12H$
Total grid points	23 148 600
Minimum grid space	3.197×10^{-1} mm
Inlet velocity	44.2 m s^{-1}
Jet Reynolds number ($Re_{jet} = UH/\nu$)	5000
Freestream Mach number (M)	0.128
Wall boundary layer thickness (δ_{BL})	1.9 cm

ten times higher than the square mean: so the removal of C from the filtering operation is not really justified and very large negative values of the eddy viscosity are a destabilizing process in a numerical simulation.

The trick often adopted to avoid this consists in averaging both numerators and denominators of (12) over space and/or time: averaging over direction of flow homogeneity is a popular choice to obtain good results.

3 Numerical Test: Backward Facing Step

The Backward Facing Step [3, 4] is a widely used benchmark problem to evaluate the performance of turbulence models in the prediction of separated flows. The fluid flows with an average velocity U in a channel, then it enters into a wider channel characterised by a step of height H as shown in Fig. 1, H_u and H_d being the channel heights upstream and downstream of the step, respectively. After the flow separates at the step, the flow reattaches to the lower wall at a distance x_r .

For this case a lot of experimental data are available [6, 7], as averaged and rms streamwise and spanwise velocities, at different distances from the step; in particular, the measures take place at the following abscissas: -5.08 cm, 1.27 cm, 5.08 cm, 7.62 cm and 12.7 cm, with the step edge placed at 0 cm.

Figures 2-3 compare experimental data (symbols) and HeaRT (Heat Release and Turbulence) results (lines): in the graph, streamwise and spanwise velocities have black colour, while their rms fluctuations have green color.

Very good agreement between experimental and numerical data is achieved far from the walls. Differences near the walls is probably due to the poor resolution of the computational grid into the shear layer. It is observed that no van Driest damping function is implemented in the HeaRT code, demanding this effect to the dynamic calculation of the Smagorinsky constant.

4 Concluding Remarks

The Germano dynamic procedure applied to the Smagorinsky subgrid turbulence model, permits to compute the model' constants during the numerical simulation, rather than imposing them a priori. In this manner it is possible to obtain a better representation of the small scales viscous dissipation with a moderate computational overhead.

References

- [1] J. Smagorinsky. GENERAL CIRCULATION EXPERIMENTS WITH THE PRIMITIVE EQUATIONS. *Monthly Weather Review*, 91(3):99–164, March 1963.
- [2] Massimo Germano, Ugo Piomelli, Parviz Moin, and William H. Cabot. A dynamic subgrid-scale eddy viscosity model. *Physics of Fluids A: Fluid Dynamics*, 3(7):1760, July 1991.
- [3] B. F. Armaly, F. Durst, J. C. F. Pereira, and B. Schönung. Experimental and theoretical investigation of backward-facing step flow. *Journal of Fluid Mechanics*, 127(-1):473, apr 2006.
- [4] D. M. Driver and H. L. Seegmiller. Features of a reattaching turbulent shear layer in divergent channel flow. *AIAA Journal*, 23(2):163–171, feb 1985.
- [5] T. Lee and D. Mateescu. Experimental and Numerical Investigation OF 2-D Backward-Facing Step Flow. *Journal of Fluids and Structures*, 12(6):703–716, aug 1998.
- [6] Langley Research Center. http://turbmodels.larc.nasa.gov/backstep_val.html.
- [7] Ercofac Classic Database. http://cfd.mace.manchester.ac.uk/cgi-bin/cfd/db/prpage.cgi?31&DNS&database/cases/case31/Case_data&database/cases/case31&cas31_head.html&cas31_desc.html&cas31_meth.html&cas31_data.html&cas31_refs.html&cas31_rsol.html&1&0&0&0.

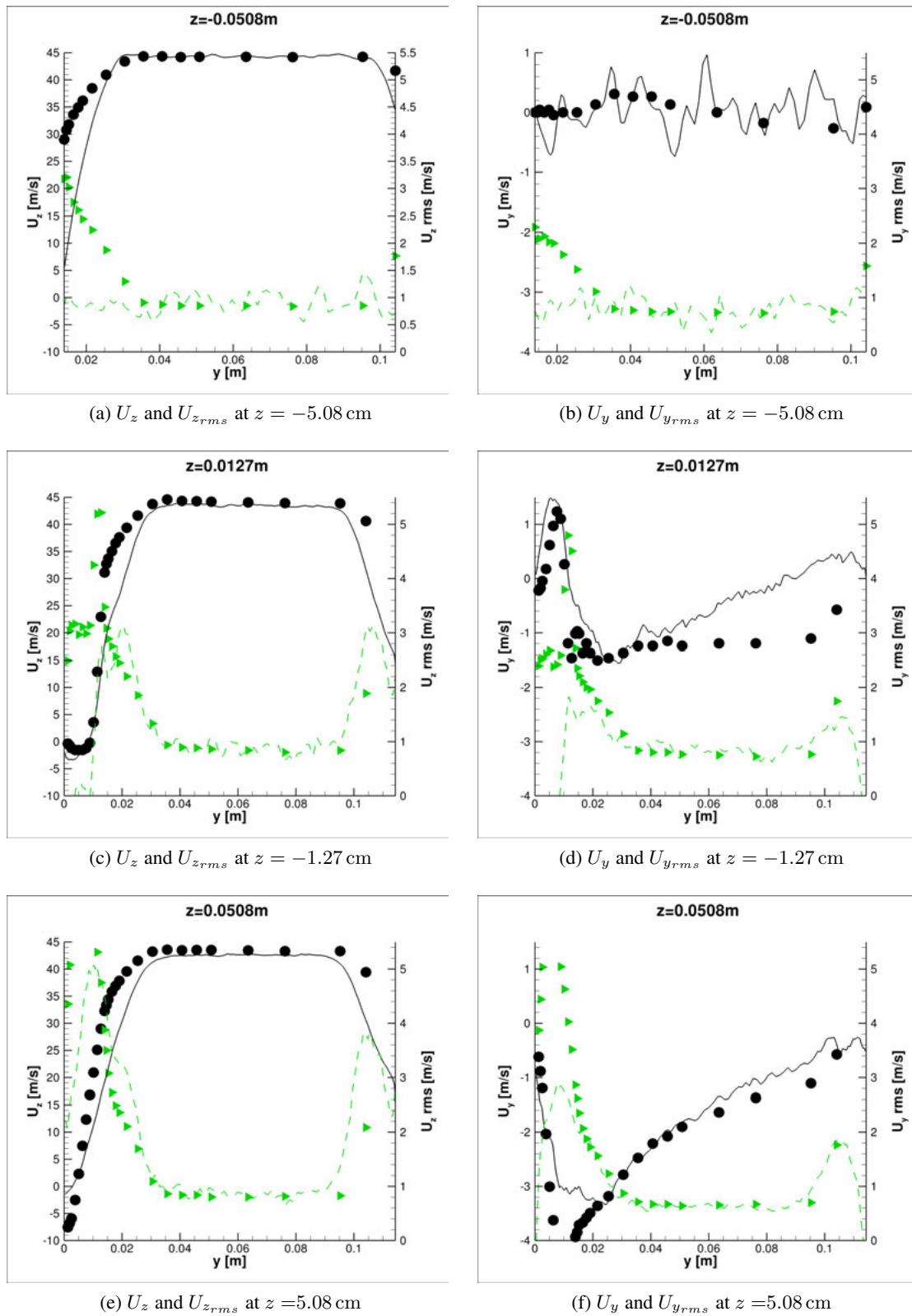


Figure 2: Streamwise and crosswise average velocity (black lines and symbols) and their rms fluctuations (green lines and symbols).

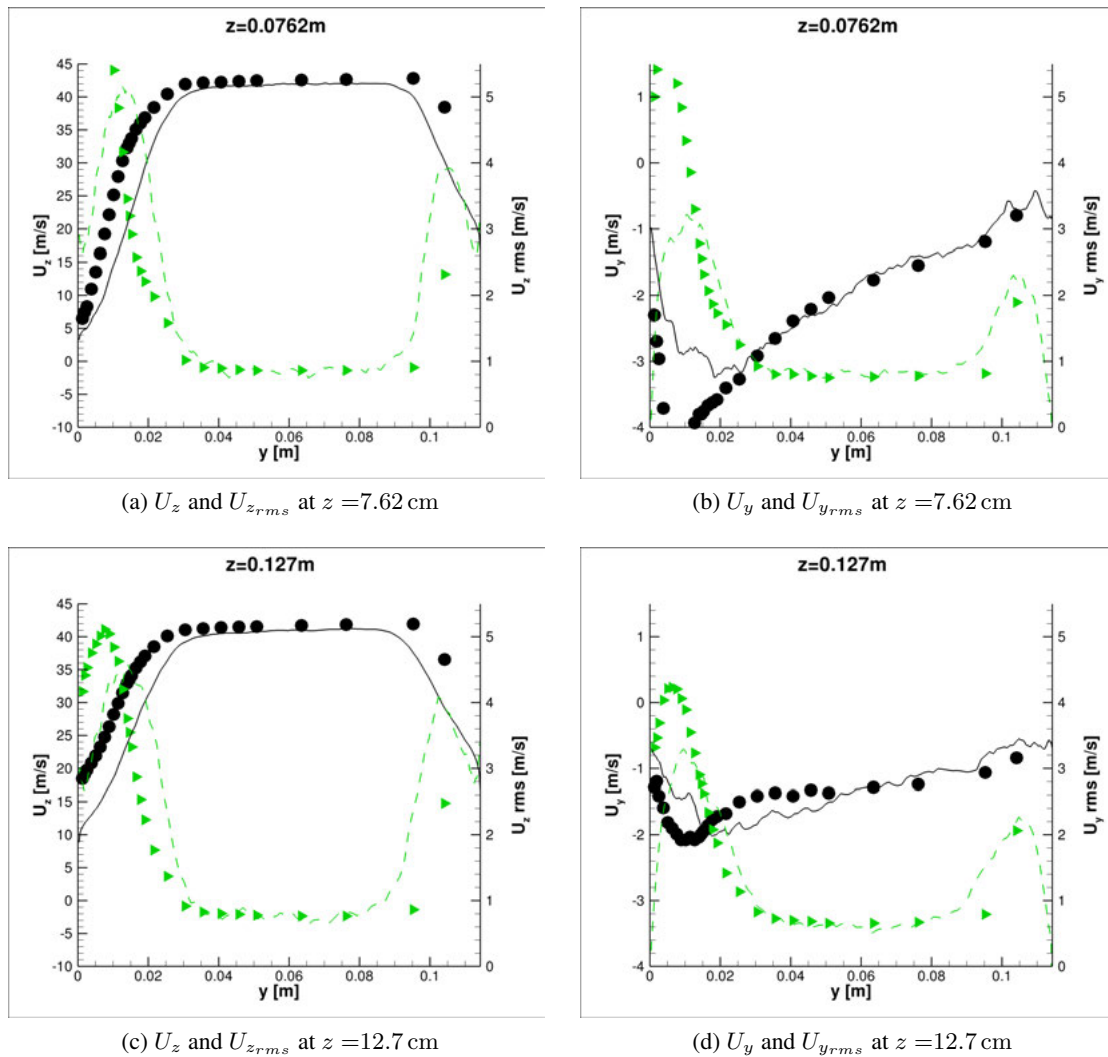


Figure 3: Streamwise and crosswise average velocity (black lines and symbols) and their rms fluctuations (green lines and symbols).

CHARACTERIZATION OF MCL1 INHIBITION VIA FAST SWITCHING DOUBLE ANNIHILATION TECHNOLOGY ON THE CRESCO3 CLUSTER

Piero Procacci^{1*}

Dipartimento di Chimica, Università di Firenze, Via della Lastruccia 3, I-50019 Sesto Fiorentino, Italy

ABSTRACT. In this report we present the MPI performances of the ORAC molecular dynamics code on the CRESCO3 cluster for the Fast Switching Double Annihilation method in the determination of drug-receptor dissociation free energies. We also present some preliminary FS-DAM results on the inhibition of the Myeloid Cell Leukemia 1 (MCL1) protein using new potent specific inhibitors. MCL1 is a key apoptosis regulator and its selective inhibition can be of great importance in cancer therapy.

1 Introduction

In the recent years, thanks to the constant support of the CRESCO infrastructure, we developed a new massively parallel technology for the computation of the dissociation free energies in drug-receptor systems, described at the atomistic level. The method, termed Fast Switching Double Annihilation (FS-DAM) and thoroughly described in Refs[1, 2, 3, 4, 5], is based on a combination of Replica Exchange with Solute Tempering technique (REST) and non equilibrium (NE) alchemical approach. In contrast to the mainstream equilibrium alchemical protocols such as FEP/REST[6], in the NE alchemical approach, the equilibrium sampling is required only at the starting fully coupled bound and bulk states (attainable using conventional enhanced sampling simulation methods such as REST), thus eliminating altogether the need for the optimization of the so-called thermodynamic length along the alchemical coordinate as in equilibrium FEP or Thermodynamic Integration studies.[7] In FS-DAM, the dissociation free energies are estimated from the distributions of the NE works[8] obtained by launching fast and independent annihilation trajectories (originated from the configurations harvested in the REST stage) of the bound ligand and of the ligand in bulk solvent. Most importantly, unlike in FEP, the confidence level in FS-DAM predictions (assuming no error from the force field), a crucial quantity in a industrial approach, can be determined very reliably using standard bootstrap analysis on the collection of the NE works. FS-DAM, implemented in our in-house ORAC code[5], is particularly suited for non uniform memory access (NUMA) multi-core architectures such as the CRESCOx clusters, relying on a weak scaling parallelism for REST and NE technologies on the MPI level and enforcing an OpenMP layer for the strong scaling parallelization of the bonded and non bonded forces within a single shared memory access compute node.

In this report we examine the performances of FS-DAM on the MPI level as evaluated on the CRESCO3 cluster using the ORAC OpenMP/MPI hybrid code. We also present some important preliminary results on the inhibition of the apoptosis regulator Myeloid Cell Leukemia 1 protein (MCL1) by a potent recently discovered[9] indole-amide compound.

*Corresponding author. E-mail: procacci@unifi.it.

2 MPI performance of the FS-DAM on CRESCO3

OpenMP tests for the ORAC (intranode shared memory) have been thoroughly discussed in Ref. [5, 10]. Here we present the performance of the code for the MPI layer only in order to assess the internode communications overhead in the FS-DAM approach.

As described elsewhere,[5, 10] for each ligand-receptor pair, the computation of the alchemical annihilation free energy via FS-DAM involves two computational steps:

i) the acquisition of a Boltzmann sampling of the fully coupled state (the complex and the ligand in bulk) using Replica Exchange Simulation with solute tempering (hereinafter **REST**). For such stage, a simulation time on the target state from few to few tens of ns is acquired by running concurrent multiple REST batteries in parallel, for a total simulation time of the order of the microsecond.

ii) the fast switching annihilation of the ligand in the complex and in bulk solvent in a swarm of independent non equilibrium trajectories (hereinafter **FS-NE**), typically lasting from few tens to few hundreds of picoseconds for a total simulation time of the order of the microsecond. The selected ligand-

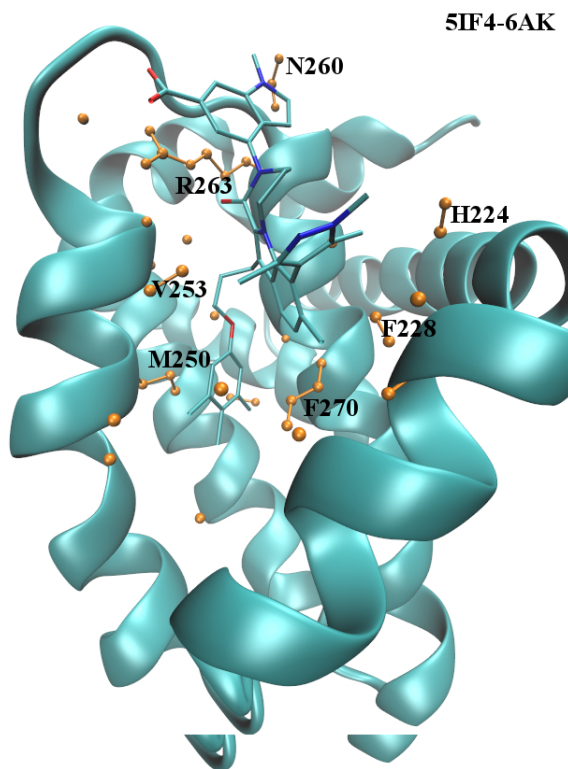


Figure 1: The MCL1-6AK complex [pdb id code 5if4] : The ribbon structure is the MCL1 protein. The 6AK indole ligand is depicted in the bond/stick representation. MCL1 atoms within 4.0 Å of the inhibitor are represented in ball and stick (orange color) along with residue specification (one letter code). Residue numbering is that of the pdb file 5if4.

receptor complex in this report, provided in the PDB file 5if4[9], is the Myeloid Cell Leukemia 1 (MCL1) protein in complex with a potent indole-amide inhibitor (indicated with 6AK). The complex is reported in Figure 2, where we show the main ligand-residue contacts that are involved in binding. The force field for the atomistic description of the ligand-receptor system is a combination of the AMBER99SB force field[11] for the protein, GAFF[6] for the 6AK ligand, and the TIP3 model[12] for the solvating water.

For the simulations of any kind, periodic boundary conditions are used while temperature and pressure are kept constant at 300 K and 1 Atm standardly using a Nosé thermostat and a Parrinello-Rahman Lagrangian, respectively.

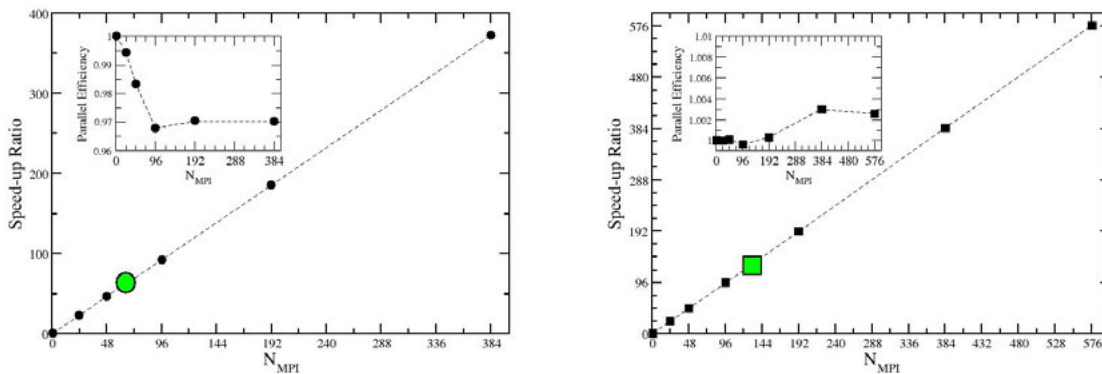


Figure 2: Left panel; Performance tests for the REST computational stage; the symbol in green corresponds to the interpolated speed up ratio for a typical value of 64 MPI instances (assuming 6-8 threads on the OpenMP layer). Right panel: Performance tests for the and FS-NE computational stage. The symbol in green corresponds to the interpolated speed up ratio for a typical value of 128 MPI instances (assuming 3-6 OpenMP threads).

In the Figures 1 and 2, we report the speed up ratio and parallel efficiency, *referred to the MPI layer only*, obtained for the MCL1-6AK protein in complex with an indole-amide inhibitor, a system of 11175 atoms) on the CRESCO3 HPC system. For the REST stage (see Figure 1), we run a REM simulation lasting 1.545 ps. Simulations were run (using in all cases one OpenMP thread per trajectories) with 1, 24,48,86,192 and 384 replicas (i.e. MPI processes) for a corresponding total simulation time of 1.545, 37.08, 74.16, 148.32, 296.64 and 593.28 picoseconds. All REST tests were done in an elapsed time ranging from 270.9 seconds (1 replica) to 279.2 seconds (384 replicas).

For FS-NE (see Figure 2), we launched NE trajectories lasting 0.6 ps. FS-NE parallel simulations were done producing 1, 24, 48, 96, 192, 384 and 576 independent non communicating trajectories, for a total simulation time of 0.6, 14.4, 28.8, 57.6, 115.2, 230.4 and 345.6 picoseconds. All FS-NE tests were done in an elapsed time ranging from 119.8 to 120.2 seconds. The performances on the MPI level are practically ideal for both the REST and FS-NE computational stages, in a wide range including 48 (REST) and 128 (FS-NE) processors as required in the MCL1 project. While, expectedly, the embarrassingly parallel FS-NE computation exhibits no loss whatsoever of parallel efficiency (see the inset plot in Figure 2), in the REST computation a minor efficiency loss can be barely appreciated with the 384 replicas simulation running at 97% of parallel efficiency (see the inset plot in Figure 1). This moderate efficient loss in REST is due the communication overhead during replica exchange attempts. These are normally implemented each 15 fs (i.e. 103 attempts in total in the test) for all contiguous pairs of replicas and involve a `MPI_SEND / MPI_RECEIVE` couple of three double precision numbers (the REST scale factors) followed by an `MPI_BARRIER` on all MPI processes.

3 Dissociation Free energy of the MCL1-6AK complex via FS-DAM

The REST stage for the MCL1-6AK and the 6AK in bulk solvent, featuring about 11000 and 3000 atoms simulated for a total time of 20 ns in four eight-replicas batteries (according to the scaling protocol described in Ref [5, 10]) were computed on CRESCO3 (288 cores, 48 on the MPI layer and six on the OpenMP) in 48 and 13 wall clock hours, respectively, producing about 216/480 configurations sampled at 300 K and P=1 Atm every 10 ps. From these initial configurations of the bound ad bulk state, we started the FS-NE stage, by launching in parallel blocks of 48 NE ligand annihilation trajectories in the same thermodynamic condition, each engaging 6 cores on the OpenMP layer for a total of 288 cores jobs on the CRESCO3 facility. The FS-NE stage on the whole collection of 216(complex) and 480 (bulk) starting states and using different annihilation times (from 90 ps to 720 ps), was completed in about two wall clock days.

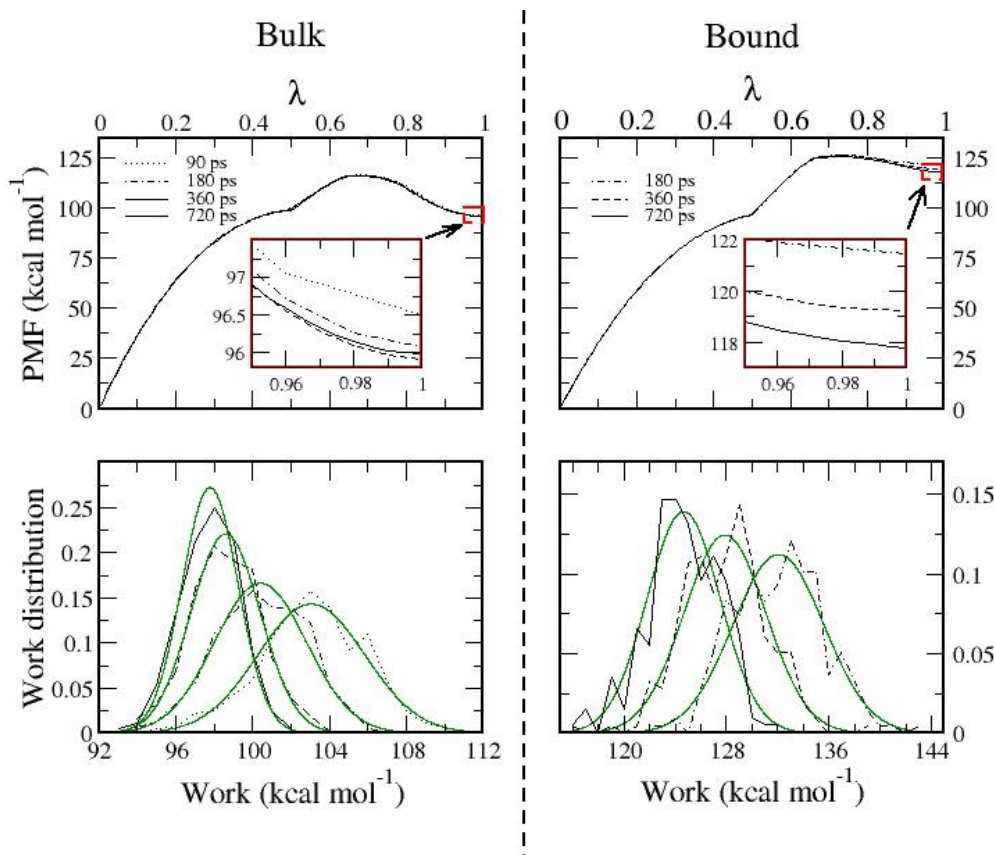


Figure 3: Upper panels: PMF for the annihilation of the ligand in bulk (left) and in the complex(right) obtained using different annihilation rates. The insets are a zoom of the PMF in the final stages $\lambda \simeq 1$ of the alchemical parameter λ Lower panel: Work distributions computed at various annihilation rate for the ligand in bulk (left) and in the complex (right). The corresponding Gaussian distributions, evaluated using the first two moments of the collection of 480 and 216 FS-NE works (unbound and bound state respectively), are shown in green color.

As discussed in Ref. [3, 4], the ligand annihilation free energy (in bulk and complex) along the alchemical path was computed using the first two moments (mean μ and variance σ) of the NE work distribution,

assumed to be normal, i.e.

$$\Delta G(\lambda) = \mu(\lambda) - \frac{\beta\sigma(\lambda)^2}{2} \quad 0 \leq \lambda \leq 1. \quad (1)$$

where λ is the alchemical parameter with $\lambda = 0$ and $\lambda = 1$ indicating the fully coupled and fully decoupled ligand state, respectively. We stress that, in case of Gaussian distribution, Eq. 1 is a manifestation of the Crooks theorem[13] and as such is an *exact* equation.

In Figure 3 (bottom panels), we show the final annihilation work distributions evaluated at $\lambda = 1$ for the A6K decoupled ligand using various annihilation rate in bulk and in the complex. The corresponding superimposed normal distributions computed using the first two moments $\mu(1)$ and $\sigma(1)$ are also shown in the Figure. In all cases, the Gaussian assumption appears to be fully justified. Further evidence comes from the calculation of higher moments of the distributions (kurtosis and skewness, data not shown) that are zero within statistical (bootstrap) error in all cases. In the same Figure 3 (upper panels), we show the annihilation free energy $\Delta G(\lambda)$ or Potential of Mean Force (PMF) for the unbound state (ligand in bulk) and for the bound state (ligand in the complex) for various annihilation times ranging from 90 to 720 ps (unbound state) and from 180 to 720 ps (bound state). Figure 3 represents a spectacular demonstration of the validity of the Crooks theorem, Eq. 1 and of the Gaussian assumption. As prescribed by the Crooks and Jarzynski theorems[13, 14], the invariance of the PMF to changes in the NE annihilation rate is observed at any λ within statistical (bootstrap) error for the annihilation of the ligand in bulk. For the annihilation of the ligand in the complex, the dissipation $W_{\text{diss}} = \beta\sigma^2/2$, is significantly larger and a bias error[15] of $B = \beta\sigma^2/(2N_w)$ is observed for λ approaching to 1 (fully decoupled state). The λ annihilation protocol is, for all rates, such that for $0 \leq \lambda \leq 0.5$ the ligand-environment electrostatic interactions are switched off, while for $0.5 < \lambda \leq 1$, the ligand-environment Lennard-Jones interactions potential is brought to zero.

The differences between the two PMFs, for the the annihilation of the ligand in the complex and in bulk, provides important information on the nature of the binding in the 6AK-MCL1 system. Such difference is shown in Figure 4 (duration of the NE 720 ps for both bound and unbound systems) and shows that the electrostatic interactions slightly disfavors binding while a gain is observed in the dispersive repulsive (cavity) part. A similar trend was observed also in other cases.[4, 5]

Finally, the dissociation free energy of the 6AK ligand in the MCL1 system is given by the difference between the annihilation free energies at the alchemical end point $\lambda = 1$, i.e. $\Delta G_0 = \Delta G_b(1) - \Delta G_u(1)$. The actual value of the ΔG_0 must be corrected[3] for a standard state dependent volume term, $RT \ln(V_{\text{site}}/V_0)$ with V_0 being the standard state volume, and possibly by a bias error.[15] The binding site volume, V_{site} , can be estimated from the fluctuation of the center of mass distances between ligand and receptor in the REST equilibrium stage of the complex. In the Table 1, data are summarized.

Annihilation time (ps)	ΔG_b	ΔG_u	$RT \ln(V_{\text{site}}/V_0)$	Bias[15]	ΔG_0
90	-	96.55 ± 0.54	-	-	-
180	121.34 ± 1.12	95.58 ± 0.44	-2.48 ± 0.1	-1.56	21.7 ± 1.6
360	119.19 ± 1.02	95.88 ± 0.23	-2.48 ± 0.1	-1.02	19.8 ± 1.3
720	117.66 ± 1.01	95.95 ± 0.16	-2.48 ± 0.1	-0.67	18.6 ± 1.2

Table 1: Annihilation free energies [ΔG_u (unbound ligand) and ΔG_b (bound ligand)], volume[3] and bias [15] corrections and standard dissociation free energies ΔG_0 for the 6AK-MCL1 complex. Reported errors have been evaluated by bootstrap analysis. All energy values are in kcal/mol. The experimental dissociation free energy for the 6AK-MCL1 complex[9] is below the theoretical limit in the given experimental condition[9] for competitive binding assay and is termed to be of ‘‘picomolar order’’ and is estimated to be $\Delta G_{\text{exp}} \geq 13$ kcal/mol.

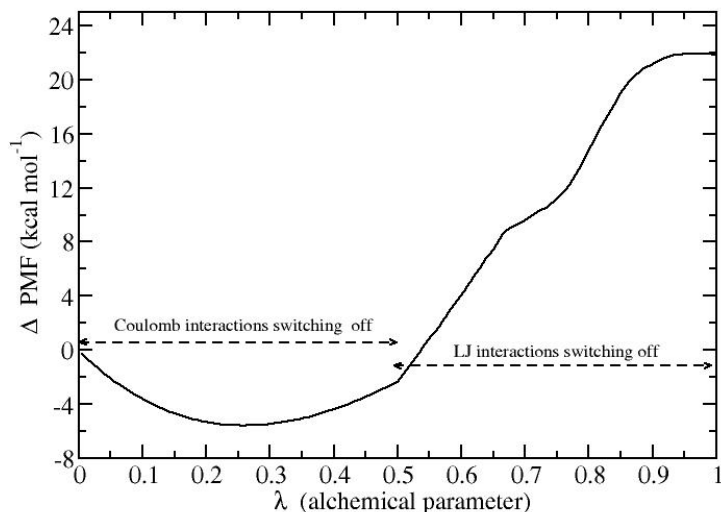


Figure 4: Difference between the PMF of the ligand in the complex and in bulk along the alchemical coordinate. The final value $\Delta\text{PMF}(\lambda = 1)$ represent the MCL1-6AK dissociation free energy (except for a standard state volume correction)

4 Conclusion

Using extensive tests on the CRESCO3 facility, we have shown that the ORAC molecular dynamics code exhibits essentially a linear scaling for thermodynamic parallelism (Replica Exchange and Fast Switching Non Equilibrium technologies) when implemented on the MPI layer. We have computed, using the FS-DAM technology, the dissociation constant of the MCL1-6AK constant, confirming the potency of the inhibitor versus the apoptosis regulator MCL1, with important implication in cancer therapy. A full paper on the MCL1 inhibition is in currently in preparation.

References

- [1] Piero Procacci and Chiara Cardelli. Fast switching alchemical transformations in molecular dynamics simulations. *J. Chem. Theory Comput.*, 10:2813–2823, 2014.
- [2] Robert B. Sandberg, Martina Banchelli, Carlo Guardiani, Stefano Menichetti, Gabriella Caminati, and Piero Procacci. Efficient nonequilibrium method for binding free energy calculations in molecular dynamics simulations. *J. Chem. Theory Comput.*, 11(2):423–435, 2015.
- [3] Piero Procacci. I. dissociation free energies of drug-receptor systems via non-equilibrium alchemical simulations: a theoretical framework. *Phys. Chem. Chem. Phys.*, 18:14991–15004, 2016.
- [4] Francesca Nerattini, Riccardo Chelli, and Piero Procacci. Ii. dissociation free energies in drug-receptor systems via nonequilibrium alchemical simulations: application to the fk506-related immunophilin ligands. *Phys. Chem. Chem. Phys.*, 18:15005–15018, 2016.
- [5] Piero Procacci. Hybrid mpi/openmp implementation of the orac molecular dynamics program for

- generalized ensemble and fast switching alchemical simulations. *J. Chem. Inf. Model.*, 56(6):1117–1121, 2016.
- [6] Lingle Wang, Yujie Wu, Yuqing Deng, Byungchan Kim, Levi Pierce, Goran Krilov, Dmitry Lupyan, Shaughnessy Robinson, Markus K. Dahlgren, Jeremy Greenwood, Donna L. Romero, Craig Masse, Jennifer L. Knight, Thomas Steinbrecher, Thijs Beuming, Wolfgang Damm, Ed Harder, Woody Sherman, Mark Brewer, Ron Wester, Mark Murcko, Leah Frye, Ramy Farid, Teng Lin, David L. Mobley, William L. Jorgensen, Bruce J. Berne, Richard A. Friesner, and Robert Abel. Accurate and reliable prediction of relative ligand binding potency in prospective drug discovery by way of a modern free-energy calculation protocol and force field. *J. Am. Chem. Soc.*, 137(7):2695–2703, 2015.
- [7] Levi N. Naden and Michael R. Shirts. Linear basis function approach to efficient alchemical free energy calculations. 2. inserting and deleting particles with coulombic interactions. *J. Chem. Theory Comput.*, 2015.
- [8] Piero Procacci. Unbiased free energy estimates in fast nonequilibrium transformations using gaussian mixtures. *J. Chem. Phys.*, 142(15):154117, 2015.
- [9] Taekyu Lee, Zhiguo Bian, Bin Zhao, Leah J. Hogdal, John L. Sensintaffar, Craig M. Goodwin, Johannes Belmar, Subrata Shaw, James C. Tarr, Nagarathanam Veerasamy, Shannon M. Matulis, Brian Koss, Melissa A. Fischer, Allison L. Arnold, DeMarco V. Camper, Carrie F. Browning, Olivia W. Rossanese, Amit Budhraj, Joseph Opferman, Lawrence H. Boise, Michael R. Savona, Anthony Letai, Edward T. Olejniczak, and Stephen W. Fesik. Discovery and biological characterization of potent myeloid cell leukemia-1 inhibitors. *FEBS Letters*, 591(1):240–251, 2017.
- [10] Piero Procacci. *High Performance Computing on CRESCO infrastructure: research activities and results 2015*, chapter Fast switching alchemical simulations: a non equilibrium approach for drug discovery projects on parallel platforms. Giovanni Ponti, ENEA, DTE-ICT-HPC, CR Portici, 2016.
- [11] Romelia Salomon-Ferrer, David A. Case, and Ross C. Walker. An overview of the amber biomolecular simulation package. *Wiley Interdisciplinary Reviews: Computational Molecular Science*, 3(2):198–210, 2013.
- [12] W. L. Jorgensen, J. Chandrasekhar, J.D. Madura, R.W. Impey, and M.L. Klein. Comparison of simple potential functions for simulating liquid water. *J. Chem. Phys.*, 79:926–935, 1983.
- [13] G. E. Crooks. Nonequilibrium measurements of free energy differences for microscopically reversible markovian systems. *J. Stat. Phys.*, 90:1481–1487, 1998.
- [14] C. Jarzynski. Nonequilibrium equality for free energy differences. *Phys. Rev. Lett.*, 78:2690–2693, 1997.
- [15] Jeff Gore, Felix Ritort, and Carlos Bustamante. Bias and error in estimates of equilibrium free-energy differences from nonequilibrium measurements. *Proc. Natnl. Acad. Sci. USA*, 100(22):12564–12569, 2003.

DPPC BIOMEMBRANE SOLUBILIZATION BY TRITON TX-100: A COMPUTATIONAL STUDY.

A. Pizzirusso^{1*}, A. De Nicola¹, G. J. A. Sevink², A. Correa³, M. Cascella⁴, T. Kawakatsu⁵, M. Rocco⁶, Y. Zhao⁷, M. Celino⁸ and G. Milano¹

¹ *Salerno University, Department of Chemistry and Biology "Adolfo Zambelli", 84084, Via Giovanni Paolo II, 132, Fisciano (SA), Italy.*

² *Leiden Institute of Chemistry, Leiden University, P. O. Box 9502, 2300 RA Leiden, The Netherlands.*

³ *Department of Chemical Science, Federico II University of Naples, Via Cinthia, Complesso Monte S. Angelo, 80126 Napoli, Italy.*

⁴ *Department of Chemistry and Hylleraas Centre for Quantum Molecular Sciences, University of Oslo, Sem Saeland Svei 26, 0371 Oslo, Norway.*

⁵ *Department of Physics, Tohoku University, Aoba, Aramaki, Aoba-ku, Sendai 980-8578, Japan.*

⁶ *Biopolimeri e Proteomica, Ospedale Policlinico San Martino, Largo R. Benzi 10 I-16132, Genova, Italy.*

⁷ *Dalian Minzu University, Institute of Nano-Photonics, School of Physics and Materials Engineering, 116600, Dalian, China.*

⁸ *ENEA, C.R. Casaccia, Via Anguillarese 301, I-00123 Roma, Italy.*

ABSTRACT. We examine at molecular level the solubilization mechanism of lipid membrane in presence of Triton TX-100. Our aim is to investigate, by means of hybrid Molecular Dynamics - Self Consistence Field Computer Simulation, the Three Stage model proposed in literature. Flat DPPC lipid bilayers and curved vesicles have been investigated at different concentration of TX-100 detergent employing Coarse Grained (CG) models. In particular, in flat lipid surfaces the detergent repartition is almost absent, following the pathway of the slow solubilization membrane mechanism. The high curvature surfaces, instead, promotes a membrane rupture following the pathway of the fast solubilization proposed in a generalization of the Three Stage Model.

1 Introduction

The project is focused on innovative Molecular Dynamics (MD) simulations, based on hybrid particle-field representation called Molecular Dynamics-Self Consistent Field (MD-SCF) [1, 5],

*Corresponding author. E-mail: apizzirusso@unisa.it.

of DPPC membranes solubilization in presence of Triton TX-100 as detergent. The solubilization of lipid bilayers is a complex mechanism that particularly depends on the type and concentration of the detergent. For this purpose we used a common anionic surfactant, TX-100, at concentrations both lower and close to the experimental TX-100/DPPC saturation ratio ($R_e^{sat} = 0.44$) and close to the TX-100/DPPC solubilization ratio ($R_e^{sol} = 1.0$). One of the most known mechanisms to explain the solubilization process is the three-stage model proposed by Helenius and Simons [2]. A generalization of the Three Stage Model is proposed by Lichtenberg and coworkers [4], with two possible modifications of the original model related to the slow and fast solubilization, that take place according to the curvature of the membrane. In agreement with this experimental evidence [4], we found two different solubilization mechanisms by means of MD-SCF Simulations, depending on a fast (in presence of curved vesicles) or slow (in presence of flat bilayer) detergent repartitions.

For obtaining accessible simulation times to understand the different solubilization pathways, we opt thus for CRESCO supercomputing resources.

2 Simulation Details: MD-SCF Approach

The main feature of the hybrid MD-SCF approach is that the calculation of intermolecular non-bonded forces and potentials, representing the most computationally demanding part of MD simulations, can be substituted by a calculation of external potentials dependent on the local density (at position \mathbf{r}) [5]. According to the idea of SCF theory, a multi-body problem, such as molecular motion, can be reduced to a problem of deriving the partition function of a single molecule in an external potential $V(\mathbf{r})$ and to obtain a convenient expression of $V(\mathbf{r})$ and its derivatives.

In the framework of SCF theory, a molecule is regarded to be interacting with the surrounding molecules through a mean field, rather than direct interactions among the molecules. Assuming that the density dependent interaction potential W , where each species is specified by the index K , takes the form:

$$W[(\phi_k(\mathbf{r}))] = \int d\mathbf{r} \left(\frac{K_B T}{2} \sum_{KK'} \chi_{KK'} \phi_K(\mathbf{r}) \phi_{K'}(\mathbf{r}) + \frac{1}{2\kappa} \left(\sum_K \phi_k(\mathbf{r}) - \phi_0 \right)^2 \right) \quad (1)$$

where $\phi_K(r)$ is the coarse-grained density of species K at position r and $\chi_{KK'}$ are the mean field parameters for the interaction of a particle of type K with the density fields due to particles of type K' . It can be shown using the so-called saddle point approximation that the external potential is given by:

$$V_K(\mathbf{r}) = \frac{\delta W[(\phi_k(\mathbf{r}))]}{\delta \phi_K(\mathbf{r})} = K_B T \sum_{K'} \chi_{KK'} \phi_{K'}(\mathbf{r}) + \frac{1}{\kappa} \left(\sum_K \phi_k(\mathbf{r}) - \phi_0 \right) \quad (2)$$

To connect the particle and field models for the proposed hybrid MD-SCF scheme, it is necessary to obtain a smooth coarse-grained density function directly from the particle positions. Such function can be obtained using a mesh-based approach, which must also be able to give

Table 1: Flat Bilayer Systems.

TX-100/DPPC	No. of Particles	DPPC	Water	TX-100	Density (kg/m^3)	Box Size (nm^3)	Time (μs)
0.43 (R)	301500	3500	237000	1500	1120.03	33.64x33.64x26.95	3.0
0.43 (U)	301500	3500	237000	1500	1033.68	37.88x37.88x23.03	6.8
1.0 (R)	302500	2500	235000	2500	1137.22	33.76x33.76x26.03	5.2
1.0 (U)	302500	2500	235000	2500	1057.56	29.86x29.86x35.78	4.7

the density derivatives required to calculate the forces acting on molecules. The derivation of eq. 2 and the implementation of this approach are reported elsewhere [1, 5].

All simulations reported in the present report have been performed by using the parallel version of OCCAM MD code [7].

We used a CG models based on the Martini force-field for both phospholipid DPPC and TX-100 [6] able to match some experimental behavior. In particular, in our recent work [3] the CG model of TX-100, Martini based, has been validated to reproduce the experimental area/molecule in mixed TX-100/DPPC mono and bilayers.

3 Simulation Results

In Table 1 and Table 2 the composition of each simulated system, and relative information about systems size and simulation times, are reported both for flat membranes (bilayer) and for curved ones (vesicles). In particular, for the flat bilayer systems (Table 2) two different initial conditions have been considered: one with TX-100 equally and randomly distributed between the two layers of the membrane (R), and one with TX-100 inserted in only one layer (U). For the curved bilayers (spherical vesicles, see Table 2) instead, four different systems have been considered: The label W indicates that TX-100 is initially distributed in the water phase, while the label S indicates a symmetric distribution of TX-100 between the inner and outer layer of a vesicle. Furthermore the labels O and I are referring to an asymmetric distribution of TX-100 in the outer and inner layers of a vesicle, respectively.

Although we have a wide range of systems available, they present only two different pathways for solubilization depending on the curvature of the chosen system. These are thus a slow solubilization for the flat bilayer with surface distortions (see Figure 1A where the formation of a budding phenomenon is visible), resulting in a micellization on its surface. While a rapid solubilization followed by a rapid distribution of TX-100 within the two leaflets in the case of the curved bilayer is observed. Starting from a perfectly spherical vesicle ($t = 0\mu s$), it starts to increase in the asphericity (less than $t \simeq 1\mu s$, see Figure 1B), and to cause the pores (less than $t \simeq 2\mu s$, see Fig.1C), with TX-100 distributed in correspondence of the most positive curved surface areas (*i. e.* in the outer layer). A $t > 3\mu s$ the vesicle is completely solubilized by TX-100 and it lose its original shape.

We have proved that two different membrane solubilization pathways occur when lipid surfaces have a different curvature. While strongly curved membranes allow fast repartition of detergents between the two leaflets of the membrane, flat membranes fall in a regime of very slow detergent repartition rates. The description of the Membrane Solubilization phenomena with a

Table 2: Vesicle systems.

TX-100/DPPC	No. of Particles	DPPC	Water	TX-100	Density (kg/m^3)	Box Size (nm^3)	Time (μs)
0.10 (W)	195524	877	183680	88	1053.26	28x28x28	4.5
0.10 (S)	195524	797	184760	80	1054.32	28x28x28	4.5
0.10 (I)	195524	797	184760	80	1054.32	28x28x28	4.8
0.10 (O)	195524	797	184760	80	1054.32	28x28x28	4.8
0.43 (W)	195524	877	179345	377	1043.31	28x28x28	5.7
0.43 (S)	195524	613	184208	264	1049.80	28x28x28	4.5
0.43 (I)	195524	613	184208	264	1049.80	28x28x28	4.8
0.43 (O)	195524	613	184208	264	1049.80	28x28x28	4.8
1.0 (W)	195524	877	171845	877	1026.10	28x28x28	4.5
1.0 (S)	195524	439	183686	438	1045.52	28x28x28	4.5
1.0 (I)	195524	439	183686	438	1045.52	28x28x28	4.8
1.0 (O)	195524	439	183686	438	1045.52	28x28x28	4.8

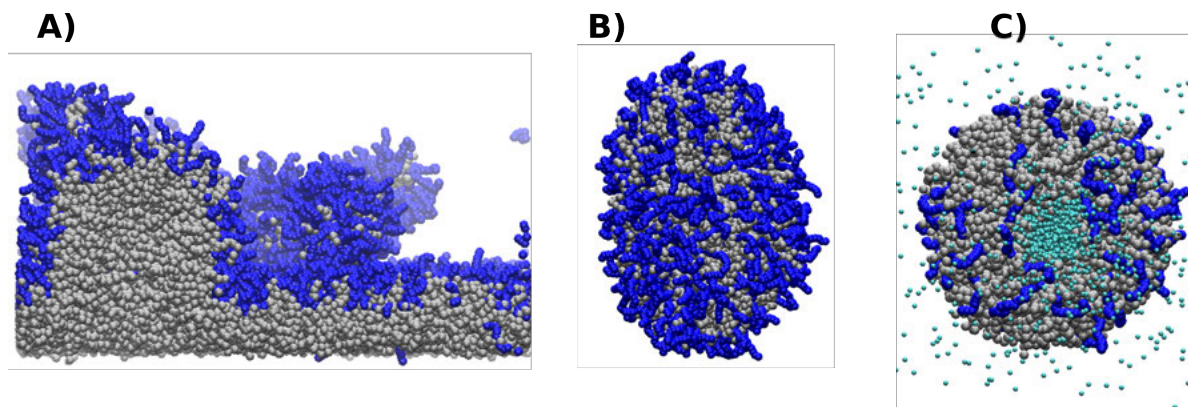


Figure 1: Some snapshots that highlight the solubilization mechanism at molecular level both for flat bilayer (A) and for curved bilayer (B, C). The TX-100 molecules are reported in dark blue, while DPPC molecules are indicated in gray. In C) The water molecules inside the vesicle are also reported and coloured in cyano.

molecular level of resolution, was possible thanks to the CRESCO Supercomputing resources, and for this purpose we used 64 and/or 96 CPUs on the cresco queue cresco4_16h24 for each simulation run. This computational study on the membrane solubilization by using MD-SCF approach has recently produced a publication on *Phys. Chem. Chem. Phys.* Journal, in which we thank the HPC team of Enea (<http://www.enea.it>) for using the ENEA-GRID and the HPC facilities CRESCO (<http://www.cresco.enea.it>) in Portici.

References

- [1] De Nicola A., Zhao Y., Kawakatsu T., Roccatano D., and Milano G. *J. Chem. Theory Comput.*, 7:2947–2962, 2011.
- [2] Helenius A. and Simons K. *Biochim. Biophys. Acta*, 415:29–79, 1975.
- [3] Pizzirusso A., De Nicola A., and Milano G. *J. Phys. Chem. B*, 120:3821–3832, 2016.
- [4] Lichtenberg D., Ahyayauch H., and Goni F. M. *Biophys. J.*, 105:289–299, 2013.
- [5] Milano G. and Kawakatsu T. *J. Chem. Phys.*, 130:214106, 2009.
- [6] Marrink S. J., Risselada H. J., Yefimov S., Tieleman D. P., and de Vries A. H. *J. Phys. Chem. B*, 111:7812–7824, 2007.
- [7] Zhao Y., De Nicola A., Kawakatsu T., and Milano G. *J. Comput. Chem.*, 33:868–880, 2012.

VARIANT DISCOVERY FOR *Triticum durum* VARIETY IDENTIFICATION

Giuseppe Aprea^{1*}, Alessia Fiore¹, Patrizia Pallara¹, Giovanni Giuliano¹

¹*Italian National Agency for New Technologies, Energy and Sustainable Development (ENEA) Casaccia Research Center, Via Anguillarese 301, 00123 Roma, Italy.*

ABSTRACT. In this report we describe how we generated candidates variants to characterize *Triticum durum* varieties samples.

1 Reference transcriptome assembly

The Iden.Pr.eP.T project (PON 2007-2013) aims to yield methods for identification of typical farming products. In this context, here we describe how we generated several sets of variants to identify 5 *Triticum durum* varieties from Sicilian farms: Core, Irìde, Mimmo, Saragolla and Simeto. In order to generate the candidate variants, a reference transcriptome is needed. The Cappelli variety was chosen for this purpose. All variants obtained later have the Cappelli *Triticum durum* transcriptome as reference.

1.1 Rna-seq data

Triticum durum Cappelli samples from different tissues were collected and RNA libraries were prepared and sequenced. Adapters removal and quality trimming with cutadapt ([5]) and trimmomatic ([1]) were done first. Available data, before and after cleaning, is shown in table 1.

1.2 Assembly

The cleaned libraries were then assembled using Trinity software ([2]). The assembled transcripts have been filtered to extract all unique isoforms longer than 400 nucleotides. The final metrics are shown in 2.

2 Variants detection

Once the reference transcriptome was ready we proceeded with variant detection for the 5 varieties. All variants were then delivered to the project partners to be used to set up SNP array assays for variety identification.

*Corresponding author. E-mail: giuseppe.aprea@gmail.com.

Table 1: Illumina paired ends data.

Species	Tissue	Paired ends [Raw]	Bases [Raw]	Paired ends [Cleaned]	%	Bases [Cleaned]	%
<i>Triticum durum</i> Cappelli	Etiolated buds	3.889.392	1.309.824.449	3.116.296	80,12%	854.680.437	65,25%
	Root	4.850.936	2.101.069.198	3.442.521	70,97%	1.082.573.612	51,52%
	Stem	4.317.793	1.432.515.355	3.538.476	81,95%	974.954.597	68,06%
	Leaves	4.527.531	1.710.278.586	3.224.243	71,21%	946.685.718	55,35%
	Awn	5.894.133	2.004.794.614	4.408.396	74,79%	1.197.403.623	59,73%
	Milk development stage grain	3.771.823	1.742.989.227	2.877.065	76,28%	890.565.897	51,09%
	Dough development stage grain	5.123.225	2.292.319.455	3.720.707	72,62%	1.165.870.187	50,86%

Table 2: Assembly metrics.

N longer transcripts	68.281
Cumulated length	45.758.737
Mean length	670
Minimum length	400
Maximum length	6442
N50	662

2.1 RNA-seq data

Grain tissue samples from all the varieties were collected and RNA libraries were prepared and sequenced. Adapters removal and quality trimming with cutadapt ([5]) and trimmomatic ([1]) were done first. Available data, before and after cleaning, is shown in table 3.

2.2 Variants discovery

In order to detect nucleotide variants for the 5 varieties we used the following pipeline for each sample cleaned library:

- reads mapping to the Cappelli transcriptome with bowtie2 ([3]);
- realignment and quality scores adjustment with the Broads GATK ([6]);
- variant calling with Samtools ([4]);

We detected 307.113 variants (280.402 SNPs and 26.711 INDELS). Only a very few of them were unique (see table 4).

Table 3: Illumina paired ends data.

Species	Tissue	Paired ends [Raw]	Bases [Raw]	Paired ends [Cleaned]	%	Bases [Cleaned]	%
<i>Triticum durum</i> Core	grain	1.390.568	371.764.320	995.325	71,58%	237.849.496	63,98%
<i>Triticum durum</i> Iride		2.718.183	745.636.355	1.999.171	73,55%	491.054.153	65,86%
<i>Triticum durum</i> Mimmo		1.316.794	356.684.004	905.140	68,74%	219.192.101	61,45%
<i>Triticum durum</i> Saragolla		590.262	166.313.097	405.524	68,70%	101.628.096	61,11%
<i>Triticum durum</i> Simeto		1.393.205	373.395.487	958.244	68,78%	228.736.798	61,26%

Table 4: Unique variants.

Species	Unique Variants
Core	4
Iride	6
Mimmo	2
Saragolla	7
Simeto	40

3 Final remarks

Cappelli *Triticum durum* transcriptome was assembled yielding $\sim 70,000$ long ($\geq 400nt$) transcripts with N50 length of 662nt. Using this transcriptome as reference, 307.113 variants (280.402 SNPs and 26.711 INDELS) were detected for 5 *Triticum durum* varieties (Core, Iride, Mimmo, Saragolla and Simeto). These data have been made available to the Iden.Pr.eP.T project partners to develop SNP arrays assay to identify them.

4 Acknowledgements

References

- [1] Anthony M. Bolger, Marc Lohse, and Bjoern Usadel. Trimmomatic: A flexible trimmer for Illumina sequence data. *Bioinformatics*, 30(15):2114–2120, aug 2014.
- [2] Manfred G Grabherr, Brian J Haas, Moran Yassour, Joshua Z Levin, Dawn A Thompson, Ido Amit, Xian Adiconis, Lin Fan, Raktima Raychowdhury, Qiandong Zeng, Zehua Chen, Evan Mauceli, Nir Hacohen, Andreas Gnirke, Nicholas Rhind, Federica di Palma, Bruce W Birren, Chad Nusbaum, Kerstin Lindblad-Toh, Nir Friedman, and Aviv Regev. Full-length transcriptome assembly from RNA-Seq data without a reference genome. *Nature biotechnology*, 29(7):644–52, 2011.

- [3] Ben Langmead and Steven L Salzberg. Fast gapped-read alignment with Bowtie 2. *Nature methods*, 9(4):357–359, 2012.
- [4] Heng Li, Bob Handsaker, Alec Wysoker, Tim Fennell, Jue Ruan, Nils Homer, Gabor Marth, Goncalo Abecasis, Richard Durbin, and Others. The sequence alignment/map format and SAM-tools. *Bioinformatics*, 25(16):2078–2079, 2009.
- [5] Marcel Martin. Cutadapt removes adapter sequences from high-throughput sequencing reads. *EM-Bnet.journal*, 17(1):pp. 10–12, 2011.
- [6] Aaron Mckenna, Matthew Hanna, Eric Banks, Andrey Sivachenko, Kristian Cibulskis, Andrew Kernytsky, Kiran Garimella, David Altshuler, Stacey Gabriel, Mark Daly, and Mark a Depristo. The Genome Analysis Toolkit : A MapReduce framework for analyzing next-generation DNA sequencing data The Genome Analysis Toolkit : A MapReduce framework for analyzing next-generation DNA sequencing data. *Genome Research*, 2010.

MOLECULAR DYNAMICS SIMULATIONS OF PEPTIDE-TiO₂ INTERFACES

Marco Polimeni¹, Loukas Petridis², Jeremy C. Smith² and Caterina Arcangeli^{3*}

¹*Lund University, Theoretical Chemistry Department, P.O. Box 11111, SE-22100, Lund, Sweden¹*

²*Center for Molecular Biophysics, Oak Ridge National Laboratory, P.O. Box 2008, Oak Ridge, Tennessee, 37830 USA*

³*ENEA, Italian National Agency for New Technologies and Sustainable Economic Development, R.C. Casaccia, Via Anguillarese, 301 00123 Rome, Italy*

ABSTRACT. In this report, part of the results published by Polimeni *et al.* [1] will be presented. The results were obtained by using molecular dynamics (MD) simulations in order to investigate the dynamics at the interface between a specific peptide sequence and a TiO₂ anatase surface. Some of these simulations were performed on the CRESCO platform.

1 Introduction

Understanding the molecular level mechanisms occurring at bioinorganic interfaces is of critical importance for the development and design of new bio-derived material [2]. Among peptide sequences able to selectively bind inorganic materials, the RKLPDA (Arg–Lys–Leu–Pro–Asp–Ala) has been demonstrated to show a peculiar adhesion to titanium surfaces [3]. Experimental mutational analysis [3], supported by previous MD simulations of the RKLPDA-TiO₂ rutile interface [4-6], have indicated that the recognition of the substrate is mainly driven by electrostatic interactions. The simulations were mainly focused on the adsorbed state [4-6], without considering the dynamical adsorption process occurring at the interface. Here we report the dynamical processes occurring at the interface between the peptide and a TiO₂ anatase surface as obtained by performing multiple MD simulations [2]. In our simulations we observe a diffusion of the peptide from the bulk water phase towards the TiO₂ surface. The peptide anchors to the surface by the recognition of water layers at the interface *via* the charged groups of its side-chains. During the simulations the peptide samples a number of anchored and dissociated states. Such behaviour is in agreement with the weak bound of the synthetic peptide to Ti, as obtained by the experimental data [7].

2 Computational Methods

Several simulations in which the peptide was placed at different initial distances from the surface were performed. The interfaces, composed of the TiO₂ anatase surface and the peptide, were solvated by water molecules and 100mM of NaCl to neutralize the system. Simulations were performed with the GROMACS 4.5.5 package [8], using the OPLS-AA force field implemented with the Lennard-Jones and Coulomb parameters for Ti and O atoms [9,10]. The SPC/E force field was used for water

¹ Corresponding author. E-mail: caterina.arcangeli@enea.it.

model [11]. Periodic boundary conditions were applied. The systems were energy minimized and equilibrated for 200 ps. Unrestrained MD were carried out in NVT ensemble. During the simulations, the inorganic surface was kept frozen. Table I summarizes some details of the simulations and lengths of the trajectories.

Table 1: Simulation details and MD simulations carried out

Simulation details	
Temperature	300K [12]
Dielectric constant	1
Integration time step	2 fs
Long-range electrostatic force	PME method [13]
Short-range electrostatic and van der Waals cutoff	1 nm
Peptide-surface initial distance	Length of simulations
0.15 nm	100 ns
0.25 nm	100 ns
0.40 nm	300 ns

3 Results and Discussion

We have investigated the dynamical processes occurring at the interface by placing the peptide at different initial distances from the surface, namely 0.15 nm, 0.25 nm, 0.4 nm. We have monitored the diffusion of the peptide and the minimum distances from the TiO₂ surface to the whole peptide as a function of simulation time for the three different MD simulations (Fig. 1). When the peptide is initially placed close to the surface (0.15 nm, red line), we observe that it remains at an average minimum distance of about 0.23 nm (see Fig. 4, lower plot). This distance is maintained throughout the simulation (100 ns). When the peptide is initially placed at longer distances from the surface (0.25 and 0.4 nm, green and black lines) we observe a rapid diffusion of the peptide towards the interface. The peptide remains at an average minimum distance of about 0.35 nm from the surface. Afterwards, the peptide samples different states of transient association and dissociation from the surface. Such behaviour is in agreement with the experimentally observed weak bound of the synthetic minTBP-1 peptide to Ti ($K_d=13.2 \mu\text{M}$) [7]. Only when the minTBP-1 is multivalently fused to several proteins, acting as protein framework to maximize the affinity and selectivity of the peptide, a strong affinity to Ti ($K_d=3.82 \text{ nM}$) [7] seems to be guaranteed. On the basis of these experimental evidences, it is not surprising that in our simulations the peptide do not show a strong binding with the surface around which it transiently associate and dissociate.

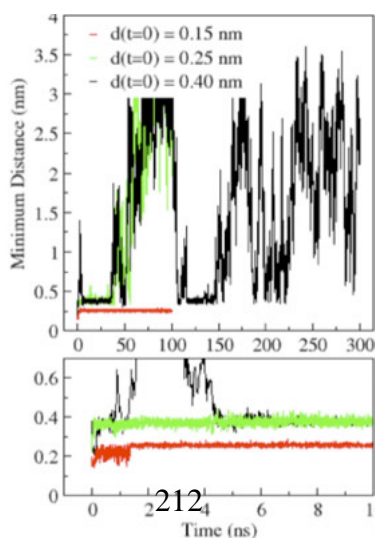


Fig.1: The peptide-surface minimum distances as a function of simulation time (upper plot) and of the first 10 ns of simulation (lower plot) for the three different MD simulations in which the initial peptide-surface distances were 0.15 (red line), 0.25 (green line), and 0.4 nm (black line).

A pictorial view of the dynamical processes occurring at the interface is shown in Figure 2. The positively charged groups of the Arg and Lys side chains ($-\text{NH}_2^+$) and the negative group of the Asp side chain ($-\text{COO}^-$) are responsible for the contacts established at the interface in all the simulations.

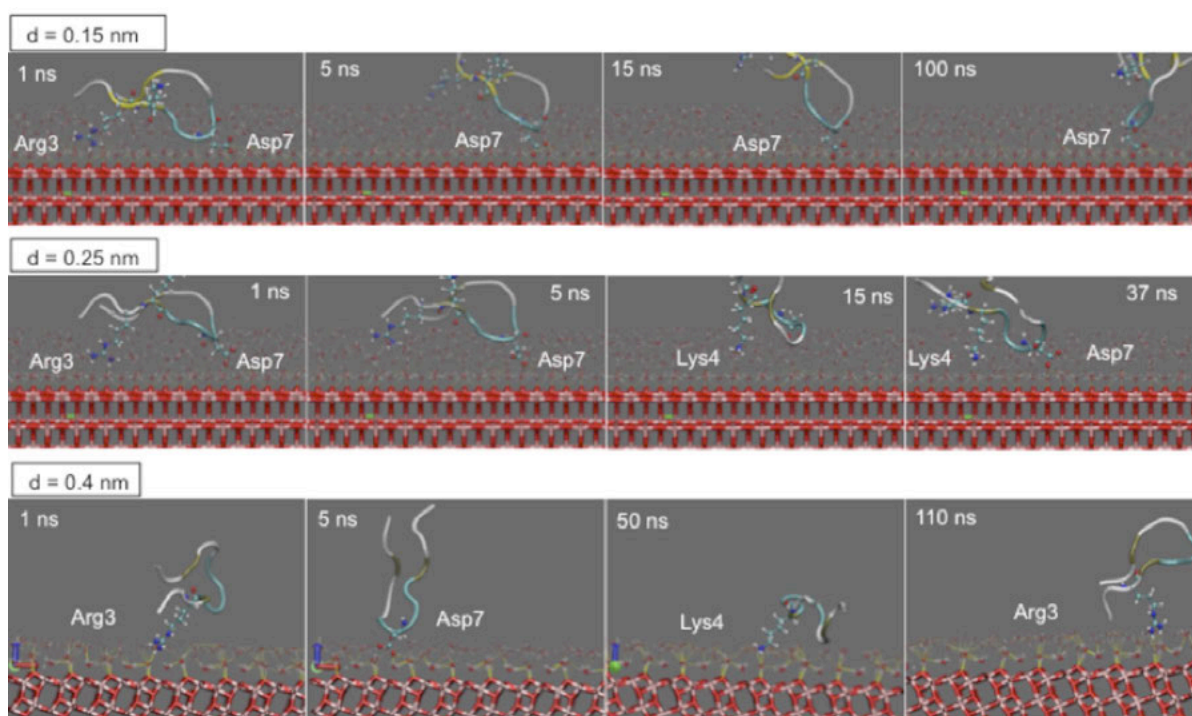


Fig.2: Simulation snapshots taken at selected times of the 0.15, 0.25 and 0.4 nm MD trajectories. The peptide backbone is shown as a ribbon. The Arg3, Lys4 and Asp7 residues are represented by the CPK model. Only a limited number of water molecules (< 0.9 nm from the TiO_2 surface) are displayed for clarity .

As illustrated in all the snapshots of Fig. 2, a layer of water molecules adjacent to the surface prevents the peptide from interacting directly with the surface. We calculated how the water molecules distribute around the surface by calculating the average number of O and H atoms of water molecules as a function of z-distance from Ti atoms of surface (Fig. 3). The profile shows two structured water layers around the surface. The first water layer is characterized by one peak at 0.22

nm and a second one at 0.29 nm corresponding to the O (black line) and H atoms (brown line), respectively. The second water layer is characterized by one peak at 0.36 nm (O atoms) and another peak placed at 0.42 nm (H atoms). At longer distances, the average number of water molecules remains roughly constant and no preferential orientation of water molecules is found (bulk water). Figure 3 shows also the distribution profiles of the atoms of Arg3, Lys4 and Asp7 as a function of the z-distance from the Ti atoms for the $d(t=0)=0.15, 0.25$ and 0.4 nm MD simulations. The first peak of the Asp7 atoms of the $d(t=0)=0.15$ nm simulation (Figure 3(b), yellow line) is observed at a value (0.21 nm) which is in proximity of the first water layer. This finding suggests that the negatively charged group of Asp7 forms a strong bond with the hydrogen atoms of the first water layer. At larger initial distances from the surface (Figure 3(c, d)), all the atoms of Asp7 (yellow line) are located in the second water layer (peak at 0.42 nm). Arg3 (blue line) and Lys4 (turquoise line) residues do not seem to play a fundamental role in the interaction process at the interface.

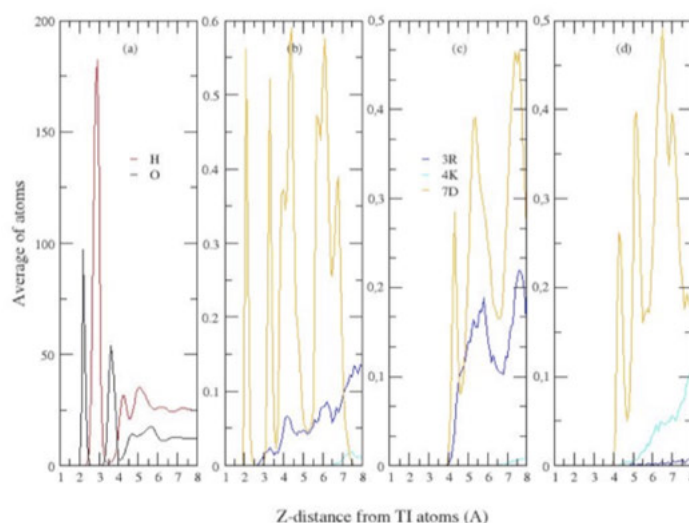


Fig.3: The average number of O (black line) and H (red line) atoms of the water molecules within 0.8 nm from the Ti atoms of the surface, (a). The average number of all atoms of Arg3 (blue line), Lys4 (turquoise line) and Asp7 (yellow line) within 0.8 nm from the Ti atoms of the surface as observed for the 0.15 nm (b), 0.25 nm (c) and 0.4 nm (d) MD simulations.

3 Conclusions

Our simulations suggest that the recognition mechanism is characterized initially by diffusion of the peptide from the bulk water phase towards the TiO₂ surface. There are two layers of structured water at the interface through which the peptide interacts with the TiO₂ surface. We have found that, in agreement with previous experimental and computational work [3-6], the protein-surface recognition is driven by electrostatic interactions. In particular, the interaction of the negatively charged group of Asp residue with the first water layer appears strong enough to anchor the peptide to the surface for the whole simulation time. In contrast when the peptide anchors to the surface by the second water layer, it samples both dissociated and anchored states.

Acknowledgement

We acknowledge the ENEA-HPC team for supporting our computational activities in the ENEAGRID infrastructure and on the CRESCO high performance platform. ORNL is managed by UT-Battelle, LLC for the U.S. Department of Energy under Contract DE-AC05-00OR22725.

References

- [1] Polimeni M.; Petridis L.; Smith J. C.; Arcangeli C. “Dynamics at a Peptide-TiO₂ Anatase (101) Interface”. *J. Phys. Chem B*, **2017** DOI 10.1021/acs.jpcc.7b04707.
- [2] Costa, D. ; Garrain, P. ; Baaden, M. “Understanding Small Biomolecule-Biomaterial Interactions: A Review Of Fundamental Theoretical And Experimental Approaches For Biomolecule Interactions With Inorganic Surfaces”. *J. Biomed. Mater. Res., Part A* **2013**, 101A, 1210-1222.
- [3] Sano, K.-I.; Shiba, K. “A Hexapeptide Motif That Electrostatically Binds To The Surface Of Titanium”. *J. Am. Chem. Soc* **2003**, 125, 14234-14235
- [4] Skelton, A. A.; Liang, T.; Walsh, T. R. “Interplay Of Sequence, Conformation, And Binding At The Peptide-Titania Interface As Mediated By Water”. *ACS Appl. Mater. Interfaces* **2009**, 1 1482-1491.
- [5] Schneider, J.; Ciacchi, L. C. “Specific Material Recognition By Small Peptides Mediated By The Interfacial Solvent Structure”. *J. Am. Chem. Soc.* **2012**, 134, 2407-2413.
- [6] Arcangeli, C.; Borriello, I.; Gianese, G.; Celino, M.; Morales, P. “Organic Functionalization Of Metal Oxide Surfaces: An Atomic Scale Modelling Approach”. *Nanosci. Nanotechnol. Lett.* **2013**, 5, 1147-1154.
- [7] Sano, K.-I.; Ajima, K.; Iwahori, K.; Yudasaka, M.; Iijima, S.; Yamashita, I.; Shiba, K. “Endowing A Ferritin-Like Cage Protein With High Affinity And Selectivity For Certain Inorganic Materials”. *Small* **2005**, 1, 826-32.
- [8] Van Der Spoel, D.; Lindahl, E.; Hess, B.; Groenhof, G.; Mark, A. E.; Berendsen, H. J. “GROMACS: Fast, Flexible, And Free”. *J. Comput. Chem.* **2005**, 26, 1701-1718
- [9] Kang, Y.; Li, X.; Tu, Y.; Wang, Q. “On The Mechanism Of Protein Adsorption Onto Hydroxylated And Nonhydroxylated TiO₂ Surfaces”. *J. Phys. Chem.* **2010**, 2, 14496-14502.
- [10] Predota, M.; Bandura, A. V.; Cummings, P. T.; Kubicki, J. D.; Wesolowski, D. J.; Chialvo, A. A.; Machesky, M. L. “Electric Double Layer At The Rutile (110) Surface. 1 Structure Of Surfaces And Interfacial Water From Molecular Dynamics By Use Of Ab Initio Potentials”. *J. Phys. Chem. B* **2004**, 108, 12049-12060
- [11] Berendsen, H. J. C.; Grigera, J. R.; Straatsma, T. P. “The Missing Term In Effective Pair Potentials”. *J. Chem. Phys.* **1987**, 91, 6269-6271.
- [12] Berendsen, H. J. C.; Postma, J. P. M.; van Gunsteren, W. F.; Di Nola, A.; Haak, J. R. “MD With Coupling To An External Bath”. *J. Chem. Phys.* **1984**, 81, 3684-3690.
- [13] Essman, U.; Perela, L.; Berkowitz, M. L.; Darden, T.; Lee, H.; Pederson, L. G. “A Smooth Particle Mesh Ewald Method”. *J. Chem. Phys.* **1995**, 103, 8577-8592.

MATERIALS FOR ENERGY IN THE FRAMEWORK OF THE EUROPEAN CENTRE OF EXCELLENCE EoCoE

M. Celino¹, S. Giusepponi¹, M. Gusso¹, U. Aeberhard², A. Walker³, S. Islam³,
D. Borgis⁴, X. Blase⁴, M. Salanne⁴, M. Burbano⁴
T. Deutsch⁵, L. Genovese⁵, M. Athenes⁵, M. Levesque⁵, P. Pochet⁵

¹ ENEA, Italy, ² Forschungszentrum Jülich, Germany, ³ University of Bath, United Kingdom,
⁴ CNRS, France, ⁵ CEA, France

ABSTRACT. Materials discovery for energy applications by using numerical and modeling techniques is a challenging tasks that needs the exploitation of the ever increasing power of high performance computing platforms. Not only hardware is needed but also focussed expertises and state of the art software packages. To this end the EoCoE European Centre of Excellence has been established to allow sinergies in the field of modeling for energy applications. Materials for energy pillar (Workpackage WP3) of EoCoE is developing models and software in three energy applications: PV, batteries and supercapacitors. In order to improve the industrial impact, application lines are also developed which provide new numerical tools both for modeling and numerical characterizations.

1 Introduction

The European Energy oriented Centre of Excellence in computing applications (EoCoE, pronounced Echo [1]) was created with the goal of tapping the huge potential offered by the rapidly advancing High Performance Computing (HPC) infrastructure to foster and accelerate the European transition to a reliable low-carbon energy ecosystem. EoCoE is organised around a central Franco-German hub coordinating a pan-European network, assembling twenty-one partners from a total of eight countries, all strongly engaged in both the HPC and energy fields. The central hub manages one of the most important HPC platform in Europe and it is coordinated with the HPC installations of the other partners, ENEA Cresco is one of them. The Franco-German hub manages one of the most powerful supercomputer in Europe Thematically EoCoE is composed of four domain pillars, each addressing a specific research community in sustainable energy: Energy Meteorology, as a means to predict variability of solar and wind energy production; Energy Materials, dedicated to photovoltaic cells, batteries and super capacitors for energy storage; Energy Hydrology, as a vector for thermal or kinetic energies associated with geothermal and hydropower respectively; and Fusion for Energy, geared to electricity plants as a long-term sustainable energy source. The thematic pillars are connected via a strong transversal basis specialising in the high-end computing demands of scientific and industrial research, with HPC-related expertise in numerical methods, applied mathematics, and advanced programming methods and tools for Exascale. The EoCoE project is guided by four high-level objectives: 1) to enable scientific breakthroughs in the Energy domain by redesigning existing codes used for energy-related applications; 2) to develop cutting-edge mathematical, numerical and computational methods and tools; 3) to adapt service activities (outputs of the first two objectives) to public laboratories, industries and SMEs, including training activities for reducing the skill gap; 4) to foster HPC and the Energy-oriented scientific and industrial communities ecosystem.

Several EoCoE-owned applications have been benchmarked and their performance improved to the extent that they are already opening up new modelling possibilities in their respective energy domains. At the same time, EoCoE has fostered a growing competence in the development of efficient mathematical libraries and tools push codes performance toward exascale. Having established a highly effective internal network combining HPC and Energy modelling expertise, EoCoE offers this know-how to external public and commercial clients through its web service page [2], while forging strategic alliances with major European stakeholders.

2 Materials for energy

The main objectives of Materials for Energy workpackage (WP3) of EoCoE are: to provide an organized set of computational routines for morphology, electronic structure and transport properties of energy-related materials for PV, batteries and supercapacitors; to set up a screening methodology for designing materials for PV, rechargeable batteries and supercapacitors with optimal energy conversion and storage capabilities; to demonstrate the usability of the infrastructure to address challenging open problems in the field of energy focussing on their atomic scale origin. To fulfil the WP objectives three application lines have been set up. An application line is a WP3 transversal activity that composes the available numerical methods and models to better address a full characterization of a technological application (in this project PV, batteries and supercapacitors). The development of the application line approach will allow to extend this methodology to other energy technologies. In the following a very brief sketch of the Materials for Energy workpackage.

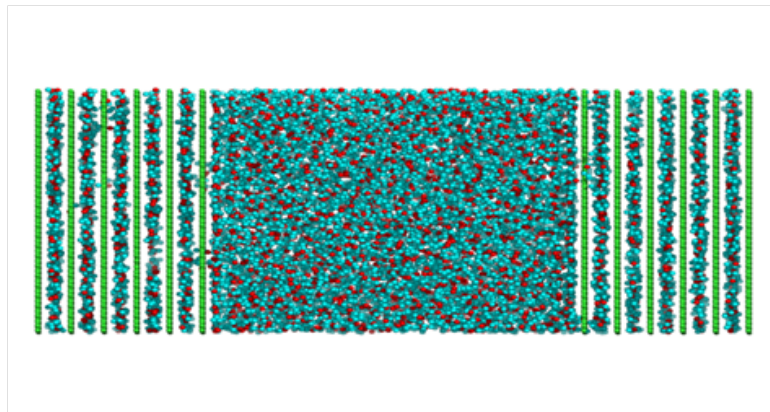


Figure 1: Simulation cell of a BMIM-PF6 ionic liquid surrounded by nanoporous graphene electrodes. Color scheme; blue: 3-site BMIM+ molecules, red: single-site PF-6 molecules, green: carbon electrode atoms.

3 Inorganic photovoltaic

An ENEA – Jülich collaboration, supported by the computational expertise available in the Center of Excellence EoCoE, has designed a new procedure to model the Silicon heterojunction solar cell from the atomic-scale material properties to the macroscopic device characteristics [3]. The atomic scale configurations have been designed by performing highly accurate quantum simulations by using the ab-initio electronic structure packages and exploiting the computational power of both ENEA

CRESCO and Jülich HPC platforms . Both the optimization of the numerical codes and the right design of the model material allow for upscaling of the performance for the simulation of large interfaces. This approach opens the way to the simulation of very large interfaces fully exploiting the power of HPC infrastructures. A step further toward the complete characterization of the solar cell is given by the implementation of a massively parallel Discontinuous Galerkin Maxwell solver for light propagation and absorption that uses data structures defined by Jülich. The efficient parallelization on supercomputers allows to model light trapping architectures in silicon heterojunction solar cells with realistic multi-scale textures for anti-reflection and light incoupling. Moreover, the in-house developed NEGF code PVnegf is adapted to the simulation of hole flow across the Si heterointerface. This includes in a first stage the complex scattering processes for photogeneration and relaxation of charge carriers in Si. Next, a phenomenological defect channel will be added. Finally, connection will be made to the realistic electronic structure via use of a localized orbital basis (Wannier formalism) [4].

4 Supercapacitors and batteries

Batteries and supercapacitors play complementary roles in the field of energy storage. While the former are characterized by large energy densities, which makes them suitable for many applications such as in electric vehicles, supercapacitors show better power densities and are therefore used when fast charges/discharges are needed. Both devices would highly benefit for a better understanding of the atomic structure of the solid materials and of the liquid electrolytes which are involved.

We focused on the family of LLZO solid electrolytes for Li-ion batteries and on the study of nanoporous carbon-based electrodes for supercapacitors. Conventional lithium-ion batteries rely on unstable liquid-organic polymer electrolytes, which pose practical limitations in terms of ammobility, miniaturization, and safe disposal. A possible solution is to replace liquid electrolytes with inorganic ceramics that are electrochemically stable and nonflammable. The $\text{Li}_7\text{La}_3\text{Zr}_2\text{O}_{12}$ (LLZO) garnet is the most studied member of this family, and can be considered prototypical. The Metalwalls code (CEA) is used to simulate both pure and doped LLZO models.

The optimization of carbon-based supercapacitors is of fundamental importance for electrical energy storage. In order to achieve supercapacitors high-performance, it is necessary to understand the molecular mechanism of adsorption of ions inside the pores of the carbon electrodes. With the purpose to increase the energy per unit of volume, we analyzed systems consisting of perforated graphene, which allows the diffusion of the ions between the sheets and provides us with fast charging and discharging rates, and an ionic liquid electrolyte [5, 6]. In this simulation it is possible to maintain the electrodes at constant potential by allowing the charge of the carbons of the electrode to fluctuate at each time step, which is essential to obtain a realistic behavior of the ionic liquid/electrode interface (Fig. 1).

5 Perovskite

The need for an accurate ab initio description of the electronic and optical properties of the active part of organic and hybrid systems in perovskite solar cells is compelling. The long term stability of hybrid organic-inorganic perovskites (HOIP), APbI_3 , where A is an organic cation, is a barrier to commercialization of perovskite solar cells. Recently, a mixture of formamidinium ($\text{H}_2\text{NCH}_2\text{NH}_2^+$, FA), methylammonium (CH_3NH_3^+ , MA), cesium (Cs^+), rubidium (Rb^+) cations in the A position of the HOIP has been shown to exhibit improved thermodynamic and photo-stability, crystal quality

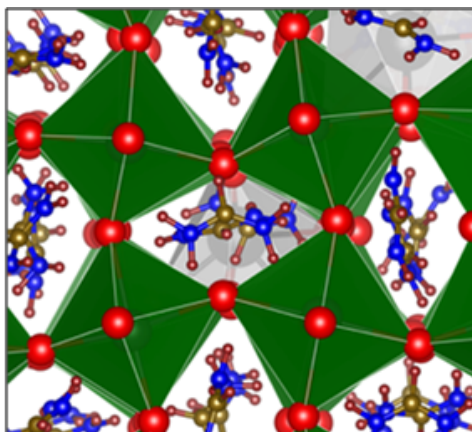


Figure 2: Crystal structure of $\text{CH}_3\text{NH}_3\text{PbX}_3$ perovskites ($X=\text{I}, \text{Br}$ and/or Cl). The methylammonium cation (CH_3NH_3^+) is surrounded by PbX_6 octahedra. Red spheres are I^- ions, and the molecules in the centre of each cell are FA cations made of H,C, N atoms.

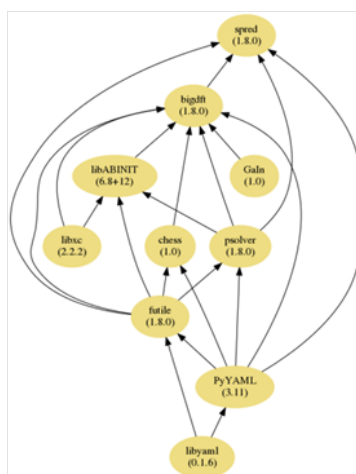


Figure 3: Scheme of the BigDFT modularity. Modularity of the numerical codes improves the sharing of codes, their management, their maintainability and their optimization for HPC platforms.

and electronic properties. Performing ab initio molecular dynamics simulations, the University of Bath has predicted dynamical structure-property relations of these recently synthesized mixed A-cation perovskites (Fig. 2) [7]. As the cations move, bonds between the I and Pb ions change as the cell distorts to accommodate the FA cation motion. Bond changes affect the electronic structure of the cell so alter charge recombination rates. The real-space formulation of coupled electronic-atomic structure provides electron and hole hopping rates required for the mesoscale analysis.

6 Numerical tools

Several numerical tools are developed in order to perform large scale characterizations to compute physical quantities of interest for real applications:

- **Methods for supercapacitor characterization, code interfacing (CNRS).** Thanks to code developments and optimizations in EoCoE, MDFT code is now able to tackle the large dimensions of the supercapacitors model used by Metawalls. The external potential corresponding to the constant charge electrodes of Metalwalls is now implemented in MDFT. For the MDFT theory, the sole input to fully characterize the solvent is the spatial and angular dependent direct correlation function of the bulk, homogeneous, solvent.
- **Development and porting of methods for force-field parametrization (CEA).** Development and porting of methods via charge analysis to facilitate the parametrization of the force fields using DFT. This will be applied to organic ions and also to batteries (interaction between graphite-like electrode and the electrolyte). The linear scaling version of BigDFT builds an optimized localized atom-centered basis set for each atom expressed on Daubechies wavelets basis sets. A charge analysis, which is the natural way to compare with polarizable force fields, is now allowed.
- **Methods to characterize oPV (CEA).** A validation scheme devoted to provide reference electronic properties data on few hundred atom systems (e.g. a dopant with its first shell of neighbors) has been set-up, combining state-of-the-art many-body perturbation theory for finite size systems (the GW and Bethe-Salpeter formalisms, as implemented in the FIESTA package), with an accurate micro-electrostatic approach (the MESCAL package) allowing to account for the electrostatic and polarization effects generated by the environment. The goal is to validate, with one of the most accurate methodology for systems of that size, the larger scale approaches that will be used in production modes on the atomic scale structures [9].
- **Estimating free energies in Monte Carlo simulations: systematic variance reduction through conditioning.** The calculation of the free energy as a function of an external parameter is an important task of molecular simulation. In materials science for example it gives access to the conditions of phase coexistence, to the equilibrium concentrations of point defects and to the mobility of these defects. A method for calculating free energy based on a conditioning procedure over the external parameter considered like an additional coordinate has been implemented [8]. It allows computing free energy barriers for the migration of defects and carriers in kinetic Monte Carlo methods.
- **Boosting KMC simulations of the migration of defects.** The computational efficiency of Kinetic Monte Carlo (KMC) simulations is notoriously limited by the kinetic trapping of the simulated trajectories within low energy basins. To overcome kinetic trapping two extensions to the factorized KMC code have been developed. Algorithmic development will continue in collaboration with EDF in the code LaKiMoCa. The algorithm is applied to speed up the KMC simulation of charged carriers in oPV materials and in electrolytes.
- **Modularity with BigDFT.** Modularity is a cornerstone to share codes, improving them in the field of HPC and also simplify the maintainability of the code. So BigDFT has been split into different parts. In collaboration with E-CAM and its ESL (Electronic Structure Library), CEA participate to some modules [10]. The libconv library is developed by using the BOAST tool (metaprogramming optimization).

References

- [1] More information on the website www.eocoe.eu

- [2] More information on the website www.eocoe.eu/services
- [3] U.Aeberhard et al. *Journal of Green Engineering* 5, 11-32 (2016).
- [4] U.Aeberhard, *J of Computational Electronics* 15, 1219-1232 (2016).
- [5] M.Burbano, D.Carlier, F.Boucher, B.J.Morgan, M.Salanne. *Phys. Rev. Lett.* 116, 135901 (2016).
- [6] R.Burt, K.Breitsprecher, B.Daffos, P-L.Taberna, P.Simon, G.Birkett, X.S.Zhao, C.Holm, M.Salanne, *J. Chem. Chem. Lett.* 7, 4015 (2016).
- [7] G.Richardson, S.E.J.O'Kane, R.G.Niemann, T.A.Peltola, J.M.Foster, P.J.Cameron, A.B.Walker. *Energy & Environmental Science* 9 1476 (2016).
- [8] M.Athnes and P.Terrier. *J. of Chemical Physics* 146, 194101 (2017).
- [9] I.Duchemin, D.Jacquemin, X.Blase. *J Chem Phys* 144, 164106, (2016).
- [10] L.E.Ratcliff, S.Mohr, G.Huhs, T.Deutsch, M.Masella, L.Genovese. *WIREs Comput Mol Sci* 2017.

CAVITY DESIGN FOR A CYCLOTRON AUTO-RESONANCE MASER (CARM) RADIATION AT HIGH FREQUENCY

Silvio Ceccuzzi¹, Giuseppe Dattoli¹, Emanuele Di Palma^{1*}, Gian Luca Ravera¹, Elio Sabia¹
and Ivan Spassovsky¹

¹ *Enea C.R. Frascati, Via E. Fermi 45, 00044 Frascati(Roma), Italy*

ABSTRACT. The design of a self-sustainable fusion plants, like DEMO tokamak reactor, demands for a high wall-plug efficiency ($\sim 30\%$) of the electron cyclotron resonance heating (ECRH) and electron cyclotron current drive (ECCD) systems. The development of a microwave tube satisfying these efficiency requirements and providing high output power ($\sim 1MW$) at a high frequency ($\sim 250 GHz$) is a challenging task that is hard to be accomplished using the currently available technologies and design tools. A promising powerful source of microwave radiation for ECRH and ECCD is the Cyclotron Auto-Resonance Maser (CARM) oscillator which a Bragg-type cavity. In order to reach the desired efficiency an accurate cavity design, guided by a robust beam-wave interaction model, is necessary. The design of a cavity with a length around half thousand times the wavelength under investigation imposes severe constraints, in terms of CPU times and RAM, hardly met by any of the existing commercially available Particle in Cell (PIC) codes. We have envisaged at ENEA FRASCATI the following procedures for the cavity design: development of a model based on semi-analytical scaling formulae, suitable for the definition of the working point, which will be followed by a full 3D analysis for the cavity optimization for a complex geometry. The paper contains an account of the design strategy developed so far.

1 Introduction

A major objective to be pursued in the design of future fusion plants is the decrease of re-circulated power, which draws a special attention to the wall-plug efficiency of the electron cyclotron resonance heating (ECRH) and electron cyclotron current drive (ECCD) systems commonly referred to as EC *H&CD*. The conceptual study for a self-sustainable demonstrator reactor (DEMO) foresees for the current drive systems an efficiency larger than 30% [1]. Such requirement is critical for the current electron cyclotron systems, where the microwave generators play the major role in impairing a sufficient wall-plug efficiency.

Furthermore, a microwave tube that meets the DEMO requirements, i.e., is able to provide high continuous-wave power of the order of (1 MW) at high frequency (250 GHz) is far beyond the boundary of the currently available technologies. Nowadays, the scientific community is devoting a special effort to extend the frequency range operation of the gyrotron (the most mature technology in the field of mm-wave tubes) beyond 200 GHz.

Within the ENEA fusion and nuclear safety department, a task force has been established in September 2016 for the development of a Cyclotron Auto-Resonance Maser (CARM) oscillator device, able to meet the requirements of future electron cyclotron heating and current drive systems in reactor-relevant

*Corresponding author. E-mail: emanuele.dipalma@enea.it.

fusion machines like DEMO[2]. This means the realization of a continuous-wave high-power (1 MW) mm-wave (> 200 GHz) source with high efficiency and reliability, which represents an outstanding physical and technical challenge that no vacuum tube has won yet. As long-term goal, ENEA aims at a 250 GHz, 1 MW CARM oscillator, being a type of source based on the Doppler upshifted interaction between a circular waveguide mode and a mildly relativistic electron beam in a highly oversized Bragg resonator allowing a consistent reduction of the static magnetic field in the interaction cavity too.

The design of the CARM cavity, composed by a short smooth cylindrical waveguide section delimited by two Bragg reflectors, is a challenging task, aimed at realizing the conditions to select the right operational mode and to limit the growth of the competing modes. The most urging problem when dealing with the chosen cavity configurations is the competition between the selected operating code mode and the neighboring parasitic (spurious) modes.

Therefore, the radio frequency circuit design must be supported by a numerical model allowing to accurately simulate the intra-cavity beam wave interaction. The large length of the full resonator (80 cm) compared to the wavelength under investigation impairs the effectiveness of a classical PIC code, based on the discretization of the Maxwell equations, due to the huge amount of computer memory and CPU time required by the resulting mesh sizes.

The main idea to solve the problem is based on the derivation of the semi-analytical formula and scaling law, that allow to optimize the cavity design with a manageable tools before to run the full 3D simulation[3, 4, 5]. The reliability of that formulae have been supported by a commercial PIC code (CST Microwave Studio[®]) simulation whose parallel version, working whit Graphics Processing Unit (GPU), has been installed on CRESCO HPC facilities. In case of a CARM amplifier, namely the simplest geometry without Bragg reflectors, experimental data from the Massachusetts Institute of Technology (MIT) [6] have been compared with semi-analytical formulae, our homemade 1D code (GRAAL), the commercial PIC code by CST Microwave Studio and the CSPOT code by MIT. Measurements are overlapped with predicted curves in Fig.1 showing a reasonable agreement among the simulation tools.

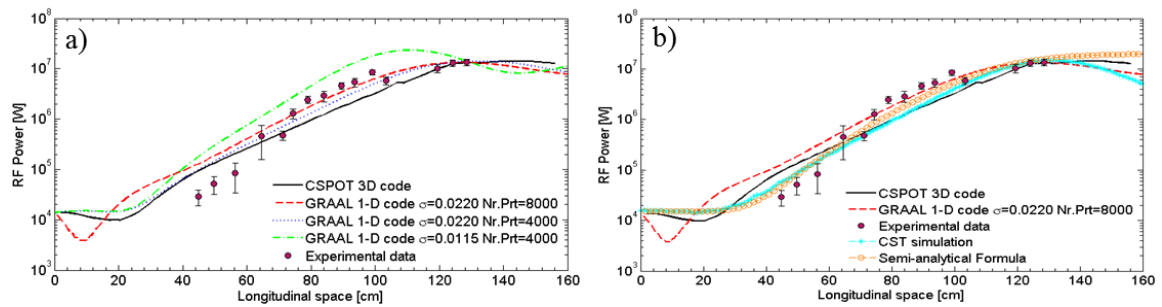


Figure 1: Experimental results of a 35-GHz CARM amplifier from MIT compared with: a) the CSPOT code by MIT and the homemade GRAAL code (varying σ , the velocity spread of the beam particles, and the number of particles (Nr. Prt.) used in the simulation) and b) the PIC commercial code by CST Microwave Studio and the semi-analytical formulae.

Furthermore, starting from an amplifier at low frequency (35 GHz) we moved to an oscillator configuration by reducing the interaction length and putting two Bragg reflectors at the end of the smooth cylindrical section. The beam-wave interaction of the oscillator has been simulated using CST Microwave Studio on CRESCO ENEAGRID with one GPU. In Fig. 2 the simulation results put in evidence the right resonance of the RF circuit at the 35 GHz.

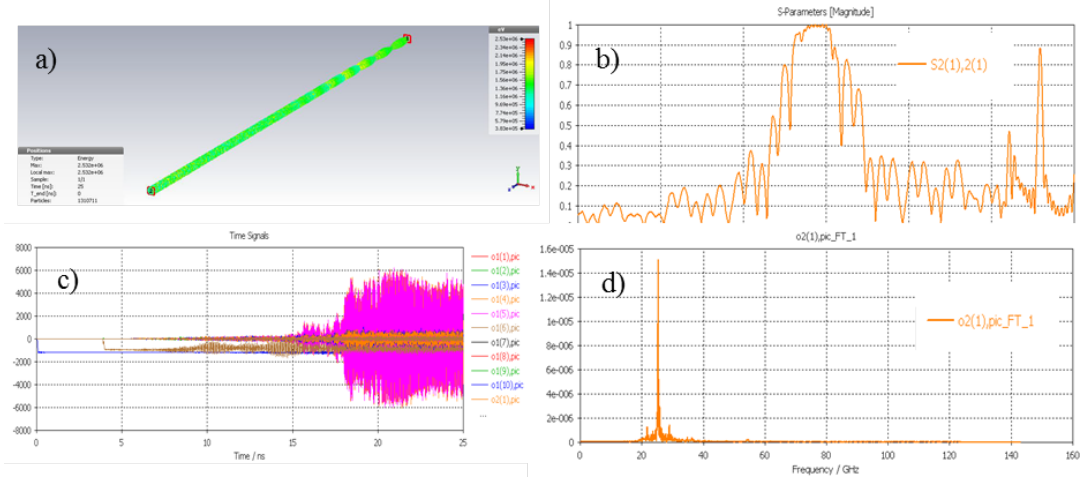


Figure 2: Simulation of a CARM oscillator at 35 GHz exciting the TE_{11} mode with a particles beam source at port 1 having: 128 A of current, the relativistic factor γ value equal to 3.96 and the pitch value equal to 0.27; reporting in: a) the particle preview trajectory, b) the scattering parameter S_{21} , c) the output signals at port 2 and d) the Fast Fourier Transform of the TE_{11} mode signal at port 2

2 CARM simulations at high frequency

The computational requirement of a PIC simulation for a CARM oscillator at 250 GHz is beyond the resources in our ENEAGRID in term of the GPU cards.

We have therefore developed a semi-analytical model of the beam wave interaction derived by linearizing the Vlasov equation. The obtained results put in evidence the dangerous behavior of the beam-wave interaction with gyrotronic modes near the cut-off at the frequency range $62 \div 88 GHz$ being the associated growth rate of the gyrotron mode greater than the CARM mode interaction.

Taking in mind that the Bragg resonate only at the 250 GHz in a narrowed band, a CST simulation has been performed considering a smooth cylindrical section (without Braggs) at 90 GHz in order to select the most dangerous mode with a significant growing of the output signal. Fig.3 reports the simulation results of a particles electron beam (with beam current and voltage of 8 A and 600 kV respectively) interacting with the waveguide modes of a smooth cylindrical cavity (with the radius of 7.5 mm and the length of 13 cm).

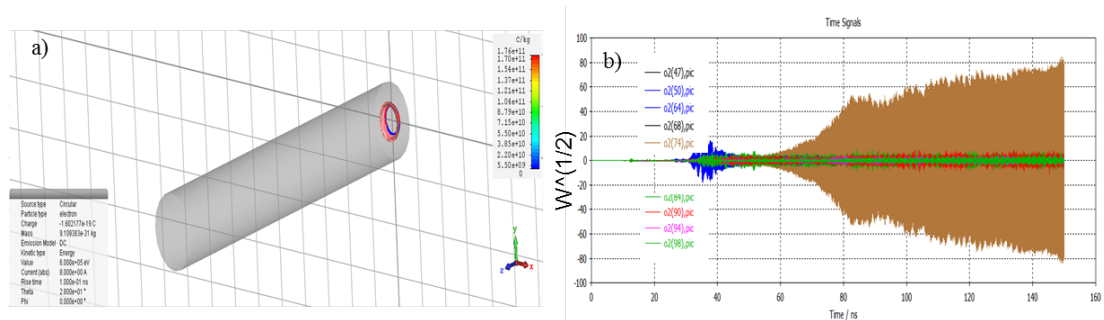


Figure 3: PIC simulation results on CRESCO ENEAGRID with two GPUs (a) the geometry design with the particles electron beam (b) the most significant output modes signal excited by the beam at low frequency, the worst in brown is related to the mode TM_{42}

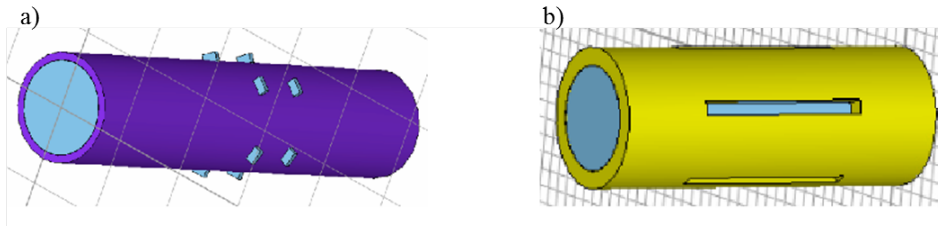


Figure 4: Circular waveguide with transversal (a) and longitudinal (b) slots. Light blue identifies vacuum parts, while other colours are used to indicate metals

The only way to limit the parasitic modes growth at low frequency is to delete them by modifying the cavity mode structure, which can be achieved by providing appropriate cuts on the waveguide. An important step forward in the design of the ENEA CARM has been accomplished thanks to the possibility of running full-wave simulations of circular waveguides with either transversal or longitudinal slots as depicted in Fig. 4. Some CARM experiments in the past have been impaired by the excitation of gyrotron modes, namely, waveguide modes intersecting the beam line very close to their cutoff frequency. The most dangerous gyrotron mode of the ENEA CARM is the TM_{42} (see Fig.3), whose propagation can be impeded by providing waveguide walls with transversal slots. On the other hand, longitudinal slots mostly affect transverse electric modes and can be designed to select a single polarization of the working mode as well as to damp modes with azimuthal index different from the one of the operational mode. Some outcomes of preliminary optimizations carried out for slotted waveguides are reported in Fig. 5. For the case of transversal slots, the behavior of a waveguide section

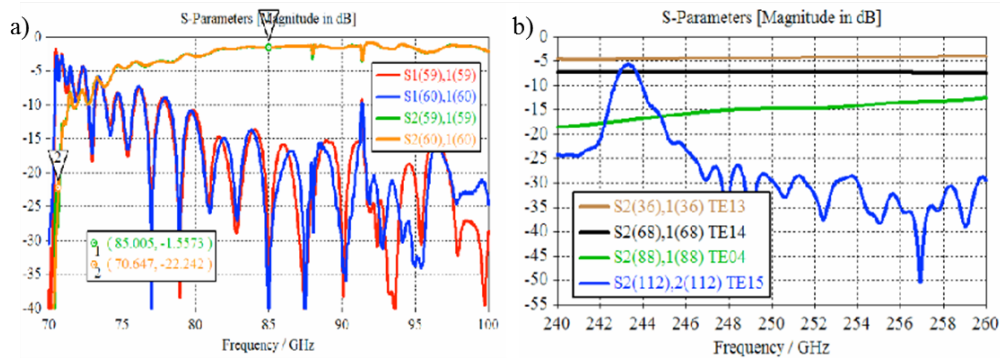


Figure 5: (a) Main scattering parameters across the ENEA CARM cavity with 5 rings of 8 transversal slots: both polarization of the TM_{42} , i.e., mode numbers $nn = 59$ and 60 , are impaired when transmitted ($S2(nn),1(nn)$); adjacent rings are rotated of 22.5 degrees. (b) Main transmission parameters of some unwanted modes in a circular waveguide with internal radius of 2.92 mm and 5 longitudinal slots.

is studied around the frequency where the dispersion curve of the TM_{42} mode intersects the beam line. This frequency is lower than the operational frequency of the ENEA CARM, leading to a reasonable computation time if relevant waveguide section is simulated by means of two GPUs TESLA K40m 2×10 in CRESCO. When moving to 250 GHz, the computational load increases significantly; therefore a waveguide with smaller diameter has been simulated. Despite this geometry differs from the actual cavity, it equally provides a meaningful, though preliminary, assessment of the effects of longitudinal slots on unwanted modes

3 Conclusions

The electromagnetic simulation of a such CARM cavity for RF generation at high frequency by means of the most advanced numerical tools is far beyond the computational resources of an ordinary workstation. The parallelization of a calculation task is mandatory to handle around 130 millions of cells, required to adequately mesh the geometry, as well as about 400 modes above cutoff at the working frequency. For the modeling and simulation of the components, the ENEA CARM task force mainly relies on CST Studio Suite, i.e., a commercial software equipped with efficient time domain solvers that can be parallelized over GPUs. Calculations employing up to two GPUs have been recently run within the CRESCO/ENEAGRID High Performance Computing infrastructure, allowing unprecedented simulation capability and significant advancements of the CARM project. However, to simulate the full Bragg cavity at high frequency on CRESCO ENEAGRID we need at least 4 GPUs.

References

- [1] H. Zhom, “*On the Minimum Size of DEMO*”, *Fusion Sci. Technol.*, vol. 58(2), pp. 613-624, Oct. 2010.
- [2] ENEA CARM Design Team, “*A 250 GHz Radio Frequency CARM Source for Plasma Fusion*”, *website:www.enea.it/it/pubblicazioni/pdf-volumi/v2016-cdr-carm.pdf*, volumi Enea, ISBN:978-88-8286-339-5, pp. 1-154, 2016.
- [3] G. Dattoli, P.L. Ottaviani, and S. Pagnutti, “*Booklet for FEL Design: A Collection of Practical Formulae*”, Frascati, Italy, Edizioni Scientifiche Frascati, 2007.
- [4] E. Di Palma, E. Sabia, G. Dattoli, S. Licciardi, I. Spassovsky, “*Cyclotron auto resonance maser and free electron laser devices: a unified point of view*”, *Journal of Plasma Physics*, 83(1), pp. 905830102, Feb. 2017.
- [5] S. Ceccuzzi, G. Dattoli, E. Di Palma, A. Doria, E. Sabia and I. Spassovsky, “*The High Gain Integral Equation for CARM-FEL Devices*”, *IEEE J. Quantum Elect.*, vol. 51(7), pp. 1-9, Jul. 2015.
- [6] C. Chen, S. Wurtele, “*Linear and non linear theory of cyclotron autoresonance masers with multiple waveguide modes*”, *Phys. Fluids B*, vol.3, pp.2133, Apr. 1991.

FIRST PRINCIPLES STUDIES OF MATERIALS FOR ENERGY CONVERSION AND STORAGE

Michele Pavone*, Ana B. Muñoz-García and Eduardo Schiavo

¹University of Naples “Federico II”, Department of Chemical Sciences, via Cintia 26, 80126, Naples, Italy

ABSTRACT. In this contribution we report the works done on CRESCO during the year 2016. Three works have been published in the field of energy conversion and storage and one on the theoretical investigation of a reaction mechanism. The following sections highlight the main results of these works and provide an overview on the calculations done.

1 Computational design of cobalt-free mixed proton-electron conductors for solid oxide electrochemical cells

Proton-conducting solid-oxide electrolyzer and fuel cells (PC-SOECs/FCs) are intermediate temperature clean devices for H_2 evolution and conversion. The major difficulty in the development of such electrode materials is to find efficient mixed proton-electron conductors (MPIECs), with also effective catalytic activity toward oxygen reduction and evolution reactions (ORR/OER). We applied first principles methods to design new perovskite-oxides MPEC based on the known $BaZrO_3$ PC ceramic. We studied the substitution of Zr atoms with Mn and Fe. A 25% substitution of Fe or Mn is found to be enough to obtain electronic structural features that can enable electric conductivity. Different distributions of the Fe and Mn atoms were studied and are showed on the left in Figure 1. [1]

We also investigated other relevant processes for MPEC-based electrodes, such as hydration, proton migration, and ORR/OER electrocatalysis. For the latter we used the computational hydrogen electrode method developed by Nørskov et al. [2]

For the investigation of the electronic properties of BZO, BZF and BZM materials and for the characterization of ORR/OER intermediates we used spin-polarized Kohn-Sham DFT with the *Vienna Ab initio Simulation Package* (VASP, version 5.3.5)[3]. We applied the generalized-gradient approximation (GGA) exchange-correlation density functional of Perdew, Burke and Ernzerhof (PBE)[4]. To amend for the well-known self interaction error in DFT, we used the effective GGA+U approach within the rotationally invariant formulation of Dudarev [5] as implemented in VASP. The core electrons of each element are described by projected augmented-wave (PAW) potentials. We used plane waves basis sets with 800eV kinetic energy cut-off and a $4 \times 4 \times 4$ Γ centered k-point mesh. The climbing-image nudged elastic band (CI-NEB) method has been used to locate minimum energy paths (MEPs) for proton migration and the corresponding barrier heights

We found that the substitution of Zr with both Fe and Mn gives promising electrodes. With our investigation we were also able to discriminate the effect of the two transition metal substitutions. Fe provides better electronic features and electrocatalytic activities, whereas Mn allows for better hydration and proton migration.

*Corresponding author. E-mail: michele.pavone@unina.it.

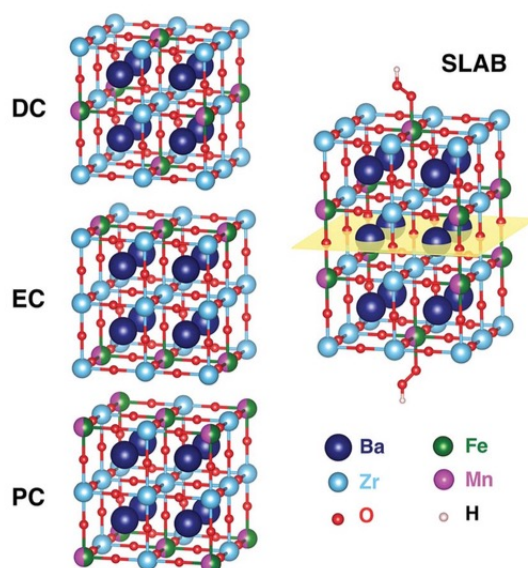


Figure 1: Left: BZF/BZM structural models with diagonal (DC), edge (EC) and plane (PC) relative distributions of the two Fe/Mn atoms in the 40-atom supercells. Right: 7-layer slab used for surface calculations (with OOH adsorbates on Fe/Mn sites). The symmetry plane on the central layer is highlighted.

2 K-doped $Sr_2Fe_{1.5}Mo_{0.5}O_{6-\delta}$ predicted as a bifunctional catalyst for air electrodes in proton conducting solid oxide electrochemical cells

Perovskite oxides are promising electrodes for ORR and OER, but is difficult for a single material to catalyze both reactions efficiently. We used first principles methods to investigate the K-doped $Sr_2Fe_{1.5}Mo_{0.5}O_{6-\delta}$ mixed proton-electron conducting oxide. In this work we showed that aliovalent doping tunes the electronic features to be optimal for the ORR and lattice expansion-driven surface reconstruction stabilizes the key *OOH intermediate for the OER. The resulting ORR/OER overpotentials are very low ($\sim 0.5V$), suggesting the application of this material as an air electrode in reversible solid oxide electrochemical cells.[6]

A computational set up similar to the one used for the work reported in Section 1 was used: PBE+U, VASP 5.3.5, 600 eV plane waves cut off and a $4 \times 4 \times 1$ Γ -centred k-point mesh.

We characterized the intermediates of ORR and OER on the (001) surface of SFMO and KSFMO. We considered all the possible non-equivalent sites on the surface. We also considered the oxygen-deficient surface: the formation of vacancies has been directly correlated with the OER/ORR activity in many transition metal oxides. Among the active sites investigated there is one (named K6 in the paper) that was found to be active for both OER and ORR with overpotential values comparable to those of known well-performing catalysts. Figure 2 shows the OER and ORR profiles on this site.

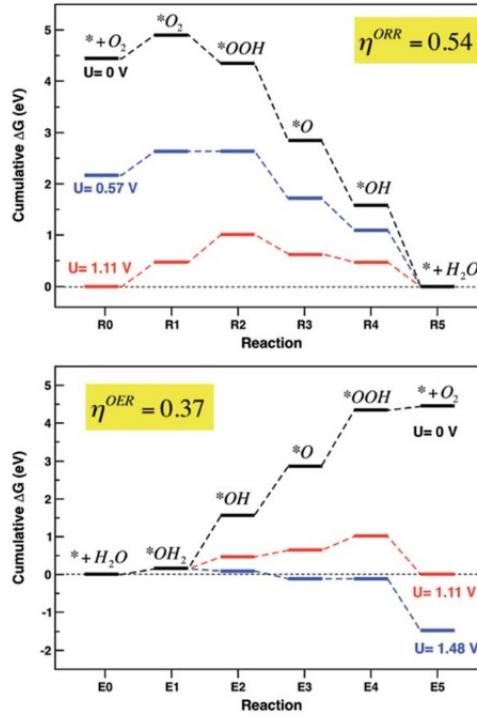


Figure 2: Cumulative free energy reaction steps of the ORR (top) and OER (bottom) at $U = 0$ V (black line), 1.11 V (red line) and U_{ONSET} (blue line) for the K6 site; the corresponding overpotentials are highlighted in yellow.

3 Unveiling the controversial mechanism of reversible Na storage in TiO_2 nanotube arrays: Amorphous versus anatase TiO_2

TiO_2 nanostructures represent a suitable choice as anode materials in Na-ion batteries (NiBs) thanks to their inherent safety, low cost, and structural stability. In recent years, various mechanistic hypotheses have been proposed for the reversible insertion of sodium ions in the TiO_2 structure. Interestingly, when tested as binder- and conducting additive-free electrodes in laboratory-scale sodium cells, amorphous and crystalline (anatase) TiO_2 nanotubular arrays exhibit peculiar and intrinsically different electrochemical responses. In particular, after the initial electrochemical activation, anatase TiO_2 shows excellent rate capability and very stable long-term cycling performance with larger specific capacities, and thus a clearly superior response compared with the amorphous counterpart. To obtain deeper insight, the insertion of sodium ions in the TiO_2 bulk phases is systematically modeled by density functional theory calculations. We performed DFT calculations of Na^+ insertion in the TiO_2 bulk phases. The amorphous and anatase phases were modeled using 96-atom supercells (Figure 3).[7] A total of 14 different insertion sites for a single Na ion could be identified in the model of the amorphous phase. For each of these sites, we computed the insertion energy in as:

$$E_{ins} = E_{TiO_2:Na} - E_{TiO_2} - E_{Na} \quad (1)$$

The amorphous phase contains several highly favorable insertion sites for accommodating Na ions.

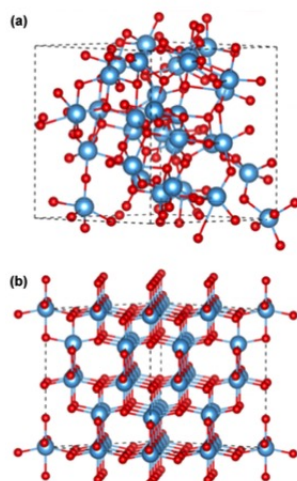


Figure 3: Structural models of the TiO₂ bulk phases: 96-atom supercell of (a) amorphous and (b) anatase TiO₂. Color code: Ti (light-blue) O (red).

These sites can also act as traps for the Na ions, which can screen the external electrostatic field. Nevertheless, the anatase crystal structure is much more stable upon cycling because the insertion of new Na ions does not perturb it. The channels directed along the (010) direction offer a favorable path for sodium ion diffusion and the insertion energies are not affected by the proximity of other Na ions in adjacent sites, thus ensuring the long-term reliability of the anatase-based systems.

4 Experimental and Theoretical Investigation on the Catalytic Generation of Environmentally Persistent Free Radicals from Benzene

Environmentally persistent free radicals (EPFRs) are toxic products deriving from incomplete combustion and are able to generate DNA damage and pulmonary dysfunction. They are formed on particulate matter through interaction with aromatic hydrocarbons, catalyzed by transition metal oxides, and produce reactive oxygen species (ROS) in aquatic media. The processes are already described for substituted aromatic molecules, but not for unsubstituted aromatic systems, such as benzene. In this article we report on the reaction of benzene with molecular oxygen in the presence of Cu_xO/SiO_2 , suggesting a mechanism based on cluster and periodic computational models. [8]

Cluster calculations were run with the *Gaussian 09* program. Optimized geometries and harmonic vibrational frequencies of reactants, intermediates, and products were calculated using DFT with the hybrid functional B3-LYP and a 6-311G** basis set. For Si and Cu the LanL2 effective core potential and the related LanL2DZ basis set were used. In the periodic calculations we used PBE+U with the VASP code (version 5.3.5) Figure 4 reports the reaction path investigated both on the cluster and on the Cu_2O (111) surface.

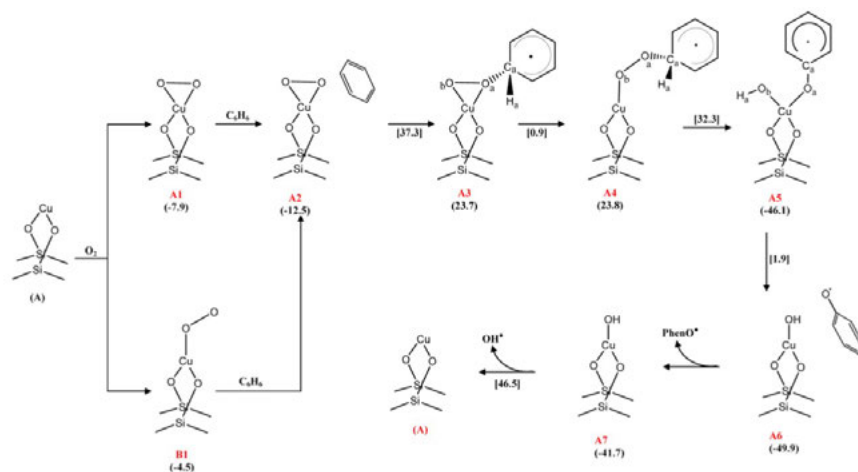


Figure 4: Mechanism of benzene hydroxylation activated by $[\text{Cu}(\text{Si}_4\text{O}_{12}\text{H}_6)]_1$ catalyst: we report the reaction scheme, the relative electron energies of intermediates with respect to separate reagents (round parentheses), and the activation energies (square parentheses). Reported energies include zero-point energy corrections.

References

- [1] Ana Belen Munoz-Garcia, Mariarosaria Tuccillo, and Michele Pavone. Computational design of cobalt-free mixed proton-electron conductors for solid oxide electrochemical cells. *J. Mater. Chem. A*, 5:11825–11833, 2017.
- [2] J. K. Nørskov, J. Rossmeisl, A. Logadottir, L. Lindqvist, J. R. Kitchin, T. Bligaard, and H. Jónsson. Origin of the overpotential for oxygen reduction at a fuel-cell cathode. *The Journal of Physical Chemistry B*, 108(46):17886–17892, 2004.
- [3] G. Kresse and J. Furthmüller. Efficiency of ab-initio total energy calculations for metals and semiconductors using a plane-wave basis set. *Computational Materials Science*, 6(1):15–50, 1996.
- [4] John P. Perdew, Kieron Burke, and Matthias Ernzerhof. Generalized gradient approximation made simple. *Physical Review Letters*, 77(18):3865–3868, 1996.
- [5] S. L. Dudarev, G. A. Botton, S. Y. Savrasov, C. J. Humphreys, and A. P. Sutton. Electron-energy-loss spectra and the structural stability of nickel oxide: An lsda+u study. *Phys. Rev. B*, 57:1505–1509, Jan 1998.
- [6] Ana B. Munoz-Garcia and Michele Pavone. K-doped $\text{sr}_2\text{fe}_{1.5}\text{mo}_{0.5}\text{o}_6$ -delta predicted as a bifunctional catalyst for air electrodes in proton-conducting solid oxide electrochemical cells. *J. Mater. Chem. A*, 5:12735–12739, 2017.
- [7] Federico Bella, Ana B. Muñoz-García, Giuseppina Meligrana, Andrea Lamberti, Matteo Destro, Michele Pavone, and Claudio Gerbaldi. Unveiling the controversial mechanism of reversible Na storage in TiO_2 nanotube arrays: Amorphous versus anatase TiO_2 . *Nano Research*, 10(8):2891–2903, Aug 2017.
- [8] Massimiliano D'Arienzo, Livio Gamba, Franca Morazzoni, Ugo Cosentino, Claudio Greco, Marina Lasagni, Demetrio Pitea, Giorgio Moro, Cinzia Cepek, Valeria Butera, Emilia Sicilia, Nino Russo,

Ana B. Muoz-Garca, and Michele Pavone. Experimental and theoretical investigation on the catalytic generation of environmentally persistent free radicals from benzene. *The Journal of Physical Chemistry C*, 121(17):9381–9393, 2017.

Role of the Sub-surface Vacancy in the amino-acids adsorption on the (101) Anatase TiO₂ surface: A first principles study

L. Maggi^{1*}, F. Gala², G. Zollo²

¹*IAS-5/INM-9 Computational Biomedicine Division- Forschungszentrum Jülich, Jülich, Germany*

²*Dipartimento di Scienze di Base e Applicate per l'Ingegneria, Università di Roma "La Sapienza," Via A. Scarpa 14-16, 00161 Rome, Italy*

ABSTRACT. In last years the simultaneous enhancement of both technological experimental instrument and the computational resources to investigate the nano-scale world, allowed the scientists to lead new kind of applications depending on the particular interactions between organic/inorganic compounds. In particular there is a new wide area of investigation regarding the functionalization of metal-oxide surfaces with biological matter, in order to develop new kind of sensor and generally nano-devices able to implement or supply part of currently science fields. In this work we shall give a first interpretation of possible selective interaction between some amino acids and Anatase (101) surface. These amino acids can be addressed as the potential responsible of the interaction between physiological peptides which in turn have the particular properties of interact both with biological matter (DNA, cells, proteins etc.) and inorganic material. This work reports the results of first-principles computational studies of two different amino acids on a substrate of titanium oxide surface in presence of an intrinsic defect and water. The amino acids chosen for the adsorption simulations are supposed to be responsible for the adhesion process of biological peptides and inorganic surfaces; thus the understanding of the processes involved in the adsorption of amino acids and the physical reasons that may eventually explain the selectivity of such phenomena is of fundamental importance.

1 Introduction

Here we have performed an ab-initio Density Functional Theory (DFT) calculation in order to evaluate the adsorption energy of two amino-acids on the (101) Anatase TiO₂ surface in presence of an intrinsic defect, in particular an oxygen vacancy located in a sub-surface layer. It has been shown the Anatase is the most stable phase at the nanometer scale [1] and the 101 plane is the most energetically favorable in such system as well [2]. Moreover in order to simulate as much as possible a "real" surface we introduced a sub-surface oxygen vacancy which has been proved by experimental and computational studies to be a quite common defect in such surface [3]. Water could play always a crucial role in every physic-chemical process that occurs in a biological environment thus, in order to calculate biomolecule adsorption energy, It is not feasible to avoid a previous study on the water adsorption on the same surface. This study has been carried out calculating the adsorption energy of different adsorption water molecules configurations. The most energetically favorable has been chosen to perform the amino-acids adsorption energy calculations. Finally we performed the adsorption energy calculations for two amino-acids, Lysine and Arginine. These studies have been done in both "dry" and "hydrated" configurations.

2 Vacancy Formation Energy Calculation

The system from which we started is a 108-atoms Anatase TiO₂ slab where the 101 plane is directed towards the positive z-axis direction. The super-cell has the dimension of 10.42 X 11.23 X 31.00 Å³. The thickness of the slab is about 10 Å. According to previous computational study [3] the oxygen vacancy has been located in a site belonging to a sub-surface layer of this slab (Fig. 1). All the calculations have been performed within the DFT-GGA scheme using the PBE (Perdew-Burke-Ernzerhof) formula for the exchange-correlation functional as implemented in Quantum Espresso package [8] Ultra-soft pseudo-potential have been used and the cut-off energy values were set to 60 Ry for the kinetic energy and to 400 Ry for the electronic density. All the calculations have been performed using two low-symmetry k- points in the irreducible Brillouin zone. The ground state configuration has been achieved after a full relaxation using the BFGS quasi-newtonian algorithm until the residual forces were less than 0.003 eV/Å. Both the standard GGA and the GGA+U functional were employed for this study. The Hubbard U was set to 3.3 eV according to previous computational study on this particular surface [4]. The Vacancy Formation

Energy has been calculated using the following:

$$E_{\text{form}} = E_{\text{slab}} - E_{\text{slab+def}} + E_{\text{O}_2}/2$$

Where $E_{\text{slab+def}}$ and E_{slab} are the energy of the slab in presence and without the defect respectively and $E_{\text{O}_2}/2$ half the energy of oxygen molecule. The difference between the GGA and GGA+U functional is not negligible (see Table 1), and in principle is not possible to assess which method yields a more realistic result. Anyway the spin DOS calculations lead to conclude that the GGA+U should be chosen in order to perform such calculation. Indeed the latter predicts the last two occupied electronic states lying below the conduction band, depicting TiO₂ as insulator as it really is. Instead the GGA functional put these states in the conduction band. In the GGA+U they are localized on surface and on a bulk Titanium atoms as shown in the Fig. 1.

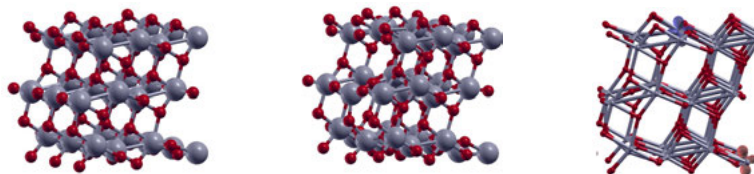


Figure 1: TiO₂ slab without the oxygen vacancy (left); TiO₂ slab without with the oxygen vacancy (center); The localization of the last two electronic states calculated with the GGA+U functional (right). The iso-value used for this spin density plot is ± 0.04

	GGA	GGA+U
E_{form} (eV)	5.07	4.46

Table 1: Formation Energy for the Oxygen vacancy calculated with GGA and the GGA+U functional

3 Water Adsorption Energy Calculation

The water adsorption has been carried out comparing once more the results obtained by GGA+U and GGA functional. Moreover a long-range interaction term has been included in energy functional. The A-(101) TiO₂ surface has six different adsorption sites for water molecules. However according to Ref. 5 in presence of an oxygen vacancy they are not equivalent. The site shown in Fig. 2 indeed presents a larger adsorption energy. In the framework of GGA+U functional is easy to understand this fact as one of the electronic states localized on the same Titanium atom where the water adsorption takes place [5] (see Table 2). The adsorption energies per water molecule were calculated using the formula:

$$E_{\text{ads}} = (E_t - E_{\text{slab}} - n E_{\text{H}_2\text{O}}) / n$$

Where E_t is the total energy of the system (slab + waters), E_{slab} is the energy of the slab in presence of the defect, $E_{\text{H}_2\text{O}}$ is the energy of water molecule and n is the number of adsorbed molecules.

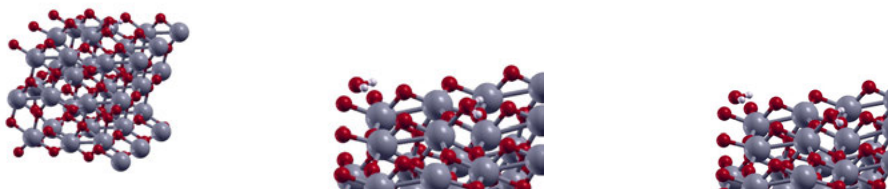


Figure 2: The first water adsorption site (left). Two different configurations for the two-adsorbed water molecules systems (center and right)

In order to get closer to a biological environment we studied the adsorption of two water molecules. Keeping the first one in the most stable site there are only two possible configurations in which the molecules could be arranged. The first one provides the two molecules in two sites in the same row side by side and the second one is placed behind the first water to the right or to the left the vacancy site (see Fig. 2). The first configuration shows larger adsorption energy, so this is the configuration used for the further calculation of amino-acids adsorption.

		GGA+U	GGA
$E_{\text{ads}(1\text{H}_2\text{O})}$	(eV)	-1.28	-1.11
$E_{\text{ads}(2\text{H}_2\text{O})(\text{conf } 1)}$	(eV)	-0.90	-0.85
$E_{\text{ads}(2\text{H}_2\text{O})(\text{conf } 2)}$	(eV)	-0.80	-0.78

Table 2: Adsorption Energy per water molecule calculated with GGA and GGA+U for the one-water adsorbed system and the two water-adsorbed systems

Although we have shown the GGA+U might produce more “realistic” scenario, however this method is computationally very expensive. For this reason before proceeding we calculated some quantities, for the slab with one and two adsorbed waters, in order to evaluate the error one commits using a standard GGA functional instead of GGA+U. The quantities are:

$$\epsilon_n = \frac{\int_{\Gamma} n_{Hubb} - n_o d\mathbf{r}}{\int_{\Gamma} n_{Hubb} d\mathbf{r}} \times 100 \quad \epsilon_V = \frac{\int_{\Gamma} V_{Hubb} - V_o d\mathbf{r}}{\int_{\Gamma} V_{Hubb} d\mathbf{r}} \times 100$$

Where n_{Hubb} and n_o are the electron density calculated with GGA+U and GGA respectively and V_{Hubb} and V_o are electrostatic potential calculated with GGA+U and GGA respectively. ϵ_V and ϵ_n quantify the difference in the electron density and electrostatic potential and they have been calculated in region above the surface where the adsorption most likely takes place. Another calculated quantity was the Atomic Displacement (AD):

$$AD = \frac{\sum_i^N |r_i^{Hubb} - r_i^o|}{N}$$

Where r_i^{Hubb} and r_i^o are the position of the i -th atom in the system with GGA+U and GGA respectively and N are the number of atoms. The AD quantifies the geometrical difference between the systems. The table below shows the values of these three quantities, as these values are very small it is feasible to avoid the calculation of Hubbard correction since it will increase enormously the computational costs leading to very similar results anyway.

	ϵ_n (%)	ϵ_V (%)	AD (Å)
1H ₂ O-system	5.5	2.4	0.8
2H ₂ O-system	7.5	2.6	1.0

Table 3: The three quantities previously defined for the one and two adsorbed water molecules systems

4 Amino-Acids Adsorption

The adsorption energies for the Lysine and for the Arginine have been calculated in both “dry” and “hydrated” configuration. Because both the amino-acids are positively charged in environment at pH 7 we simulated them in this protonated state so after a full minimization calculation using a charged cell a counter ion has been introduced achieving a neutral cell. Finally a self-consistent calculation has been performed in order to calculate the energy of the system. This choice has been adopted to avoid the well-known total error due to charged super-cells [6]. The adsorption energy has been calculated using the following:

$$E_{\text{ads}} = E_t - E_{\text{slab}} - E_{\text{amino}+(H_2O)+\text{ion}}$$

Where E_t is as usual the total energy of the system, E_{slab} is the energy of the slab with the adsorbed waters on it and $E_{\text{amino}+(H_2O)+\text{ion}}$ is the energy of the amino acids with the water shell (when it is present) and the counter ion.

5 Dry Amino-Acids Adsorption

5.2 Lysine

We chose two different initial configurations for the energy calculation of the lysine. One of this provides the $-\text{NH}_3$ of the amino-acids side chain between the two adsorbed molecules the other one instead provides this group above one of the molecule. These two initial configurations lead two different final configurations (Fig. 3). In the first final configuration Lysine interacts directly with the surface unlike the second one where the amino-acids adsorption is mediated by the water via hydrogen bonds. The error introduced by avoiding the Hubbard Correction could be more

predominant in the first configuration leading to a not negligible discrepancy between the calculated energies (see Table 4).

5.2 Arginine

Only one initial configuration has been chosen for the Arginine. The final configuration provides the amino-acids makes two hydrogen bond with the adsorbed water.

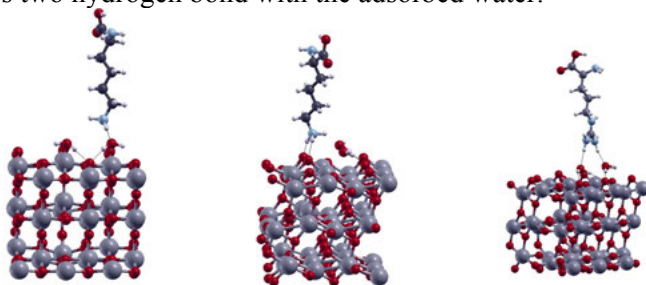


Figure 3: The final configurations of the dry Lysine (left and center) and Arginine (right)

6 Hydrated Amino-Acids Adsorption

The water shell surround the two amino-acids is the result of Classical Molecular dynamics simulation runs. Despite the fact it is made by a lot of water molecules just few of them mediate the adsorption of the amino-acids with the surface, thus a first minimization run has been performed to identify which of them interacts with the biomolecules and then a second run was performed to calculate the energies.

6.1 Lysine

Likewise the dry configurations two different initial configurations for the Lysine has been chosen. They lead to two different final configurations. In the first the adsorption is mediated by the second layer waters only belonging to the water shell that make bonds directly with the surface. In the second one the adsorption is mediated by the second layer water molecules that make bonds with the adsorbed water molecule on the surface.

6.2 Arginine

The adsorption of the Arginine is mediated by the water molecules belonging to the water shell which makes hydrogen bonds with the adsorbed water molecules on the surface itself. The calculated energies are summarized in the table below.

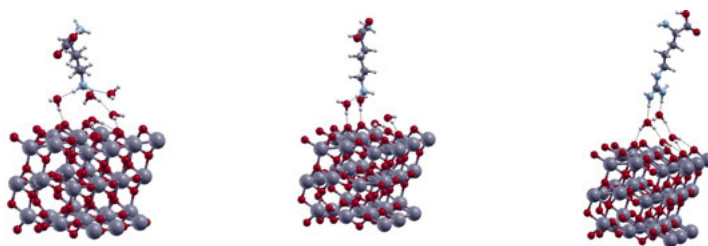


Figure 4: The final configuration of hydrated Lysine (left and center) and Arginine (right)

	Arginine	Lysine	
		Conf.1	Conf. 2
Dry Configuration (eV)	-2.20	-3.11	-2.52
Hydrated Configuration (eV)	-2.29	-2.67	-2.56

Table 4: Final Adsorption Energy of dry and hydrated amino-acids

7 Discussion and Conclusion

In this study has been shown how the presence of a sub-surface oxygen vacancy may improve the amino acid adhesion with the respect to the slab without defect [7]. This might due to the localization of an electron in the first layer of the surface which could increase the electrostatic attraction between surface and the amino-acids. From the table above should be noticed the shorter adsorption energy of the Arginine both in the dry and the hydrated configuration might be due to the fact that the steric hindrance of the latter doesn't allow it to get closer to the surface and It is less affected by the electrostatic attraction and long-range interaction as well. In the case

of the hydrated amino acids the adsorption occurs via the second layer of waters, which are not adsorbed on the surface, and these in turn form H-bonds with the adsorbed water molecule of the surface or with a surface oxygen directly. The arginine is placed above the second water layer so get further from the surface. The first and the second lysine starting configuration provide instead a quite different final configuration. In both the final configurations the lysine seems to place "among" the second water layer rather than above the waters. As discussed previously the less steric hindrance due to the Lysine's ending group allows the amino acid to get closer to the surface so the long-range interaction and the electrostatic potential contribute to yield a larger adsorption energy. Finally the adsorption energies for the lysine in the second configuration and for the arginine becomes slightly larger in the hydrated case with respect to the dry case. This behavior is unexpected because the second water shell should be shield the long-range interactions and the attractive electrostatic potential produced by the surface, leading to smaller adsorption energies. However, on the other hand, the number of hydrogen bonds in the hydrated configurations increases with respect to the dry configurations for both the amino-acids. The waters belonging to the second shell, indeed, both in the arginine and in the lysine case form extra bonds with the surface. This contribution leads to a larger adsorption energy and thus the competition between the shielding due to the second water shell and the formation of the "extra" hydrogen-bonds yields a slightly larger adsorption energy. The competition between these two effects doesn't take place in the first lysine configuration where the second water shell doesn't form new hydrogen bonds with the surface. The adsorption energy for this configuration, indeed, is considerably smaller in the hydrated case.

In conclusion the A-(101) TiO₂ shows an high affinity for both the amino-acids and moreover such a surface seems to be selective between the two examined amino acids, the lysine in particular shows a larger adsorption energy than the arginine adsorption energy. Finally the study of this adsorption phenomenon could be further developed using for instance enhanced sampling Molecular Dynamics Techniques, like Metadynamics, in order to explore different thermodynamic stable states as the adsorption and the desorption states, including the temperature effect and all the necessary water molecules to reproduce the biological environment.

References

- [1] Oskam G, Nellore A,tesi Penn R L and Searson P 2003 J. Phys. Chem. B 107 1734
- [2] Y. Gao and S. A. Elder, Mater Lett. 44, 228 2000.
- [3] *Hongzhi Cheng and Annabella Selloni. Energetics and diffusion of intrinsic surface and subsurface defects on anatase TiO₂ (101). The Journal of chemical physics, 131(5):054703, 2009.*
- [4] *Giuseppe Mattioli, Paola Alippi, Francesco Filippone, Ruggero Caminiti, and Aldo Amore Bonapasta. Deep versus shallow behavior of intrinsic defects in rutile and anatase tio2 polymorphs. The Journal of Physical Chemistry C, 114(49):21694–21704, 2010.*
- [5] *Yunbin He, Antonio Tilocca, Olga Dulub, Annabella Selloni, and Ulrike Diebold. Local ordering and electronic signatures of submonolayer water on anatase tio2 (101). Nature materials, 8(7):585–589, 2009.*
- [6] *G Makov and MC Payne. Periodic boundary conditions in ab initio calculations. Physical Review B, 51(7):4014, 1995.*
- [7] *Lorenzo Agosta, Giuseppe Zollo, Caterina Arcangeli, Francesco Buono- core, Fabrizio Gala, and Massimo Celino. Water driven adsorption of amino acids on the (101) anatase tio 2 surface: an ab initio study. Phys- ical Chemistry Chemical Physics, 17(3):1556–1561, 2015.*
- [8] *QUANTUM ESPRESSO: a modular and open-source software project for quantum simulations of materials Paolo Giannozzi et al 2009 J. Phys.: Condens. Matter 21*

LES OF HEAT TRANSFER IN AN ASYMMETRIC RIB-ROUGHENED DUCT: INFLUENCE OF ROTATION

Domenico Borello^{1*}, Alessandro Salvagni¹ and Franco Rispoli¹

¹*Sapienza Università di Roma, Dip. Ing. Mecc. E Aerosp., Via Eudossiana, 18, 00184 Roma, Italy*¹

ABSTRACT. We report on an LES study of effects of destabilising rotation on heat transfer over a ribbed surface in a rectangular duct at $Re = 15000$. The duct bottom wall, ribbed by flow-normal, equally-spaced square sectioned ribs, was uniformly heated (except for the ribs) by a constant heat flux. The duct was rotated with angular velocity corresponding to the rotation number of 0.3, around an axis parallel to the ribs in counterclockwise direction destabilising the ribbed-wall adjacent flow. These well-resolved LES gave some new insight into the rotation effects on flow and heat transfer providing information that are not easily accessible to experiments. An attempt was made to identify the heat transfer effects due to the rotation-induced modifications of the secondary motion, and the direct effects on the turbulence statistics, especially the budgets of the temperature variance and turbulent heat flux. It turned out that the former is predominant in the recirculation zone, whereas the latter prevails just after it.

1 Introduction

This paper reports on LES of heat transfer on a configuration that reproduces the experiments of Mayo et al. (2015). In their work, several measurements were done changing the rotation rate and Reynolds number, aiming at finding a correlation between heat transfer rate and rotation number. However they were not able to find any correlation despite a large amount of information collected. Here we analyse the whole configuration, providing additional information in zones not accessible to experimental analysis. In particular we analyse Reynolds fluxes and their budgets to extract information that can give useful insight to reconstruct the whole heat transfer mechanism in the duct. Computational details and validation of LES and post-processing tools used for the budget analysis are presented in the next sections, referring to a simple test cases, for which DNS results were available (Kasagi et al., 1992). Then, analysis of heat transfer in the current configuration is carried out. Finally, some conclusion are drawn.

2 Flow and computational details

The heat transfer in a rotating rib-roughened duct is investigated by means of Large Eddy Simulation (LES), using Smagorinsky model with the dynamic calculation of the Smagorinsky constant. Along one duct wall, equally spaced ribs, oriented perpendicular to the flow direction, are distributed. Periodic boundary conditions were set at inlet and outlet section. The other boundaries are treated as no-slip, walls are set as adiabatic except for the

¹ Corresponding author. E-mail: first.author@first.institution.

ribbed surface where a constant heat flux (equal to $433:44\text{W}=\text{m}^2$) was imposed. As in a periodic domain the heat flux can never be damped, a sink term in the energy equation (Γ , product of the velocity normal to the periodic surfaces and the temperature gradient) was inserted as suggested by Patankar et al. (1977) to control the temperature growth.

The bulk Reynolds number (based on hydraulic diameter D_h and bulk velocity U_0) is 15000 while the Prandtl number is assumed equal to 0:71. Effect of duct rotation on heat transfer was evaluated for the case of anti-clockwise rotation direction of the duct, at a Rotational number $Ro = D_h * U_0 / 0:3$, the ribbed wall being the pressure (destabilising) side.

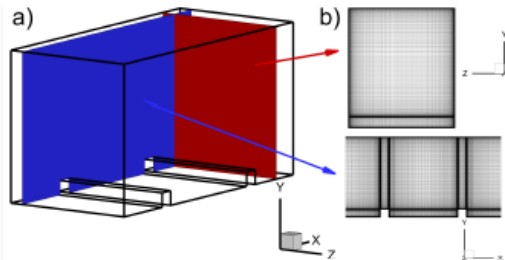


Figure 1: Computational domain: a) sketch of the domain; b) grid details (Borello et al., 2015b).

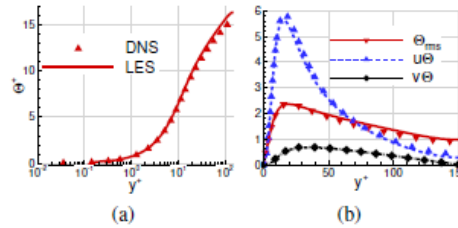


Figure 2: a) Temperature and b) second moment statistics of temperature. Symbols: DNS of Kasagi et al. (1992).

In the rotating case, the turbulent structures were longer than the space between two successive ribs. Therefore, the computing domain extends for twice the rib-to-rib distance. The domain is discretised using a 17:6M block-structured hexahedral grid (figure 1-b). The minimum distance between the cells centres and the solid walls was maintained sufficiently small to achieve values of y^+ smaller than 0:5 in more than 97% of the computational grid. The dimensionless time step was set to 10^{-4} in order to obtain a CFL number below 0:3. The non-dimensionalized governing equations were solved by means of the well validate in-house unstructured finite-volume computational code T-FlowS (Borello et al., 2015a,c). In the rotating frame of reference, influence of the Coriolis and the centrifugal forces has to be considered. Nevertheless, centrifugal force becomes important only when density gradients are relatively high and the buoyancy number exceed a threshold value (i.e. a strong heat transfer is considered). As discussed in Mayo et al. (2015), here the buoyancy number is small enough and then centrifugal force can be treated as a potential term in the momentum equation, and included into the pressure term. A second-order accurate CDS scheme is used for discretizing the convective terms. Second-order time discretisation scheme is employed. A fully coupled solution of the Navier-Stokes system is obtained using the SIMPLE scheme, while the Preconditioned BiCG solver is adopted for the solution of the algebraic linearized equation system. Convergence threshold was set equal to 10^{-8} for the BiCG solver and 10^{-6} for the SIMPLE scheme. Time-averaged results were obtained by performing 28:9 and 22 flow through times (FTT) for the non rotating and rotating case respectively. It is important to point out that energy equation was activated starting from a fully developed “cold” solution (without considering heat transfer). It was firstly solved keeping constant the flow field (velocity and pressure), to reduce its residuals, and then 3 FTT were performed before starting to collect statistics. The symmetry with respect to the mid-span plane was considered to further average the results.

3 Preliminary assessment

Thermal LES and time-averaging tools for computing Reynolds Fluxes budgets were validated against DNS data of stationary channel flow at $Re = 5650$ and $Re_\tau = 150$ (Kasagi et al., 1992). The

grid ($2\pi \times \pi \times 2$) consists of $48 \times 72 \times 48$ hexahedral cells. Wall cell height was chosen to achieve a y^+ of 0:2. The maximum Δy^+ at the centre of the channel is 12, having 12 cells in the $y^+ < 10$ region. Dimensions of the cells in the streamwise and spanwise directions, in wall coordinate, are respectively 25 and 12:5. According to Kasagi et al. (1992), fixed temperature condition were imposed at the wall. With this condition, the temperature gradient at the wall is constant and the dimensionless γ is 1.

Figure 2 shows good agreement between LES and DNS, especially close to the wall. For the channel simulation, both a constant value of turbulent Prandtl number and the polynomial expression of Kays et al. (2012) were used. Since there was not difference in the statistics, we chose to use for all LES computations a constant value of Pr_t (0:9). Good agreement was obtained for temperature and Reynolds fluxes due to a proper estimation of terms of the equation for $\theta \theta$ and $u_i \theta$.

LES is able to reproduce budget terms in the Reynolds Fluxes equations (figure 3), except for dissipation terms, which depends on small scales that are modelled in LES. Dissipation is obtained by summing up the balancing term (the sum of all the other terms of the equation). For temperature covariance ($\theta \theta$) and streamwise heat flux ($u \theta$) the production is balanced by dissipation away from the wall ($y^+ > 50$), while the pressure gradient redistributes energy from streamwise to vertical heat flux, and for the last one it is balanced by the production term (note the different scales in the three cases).

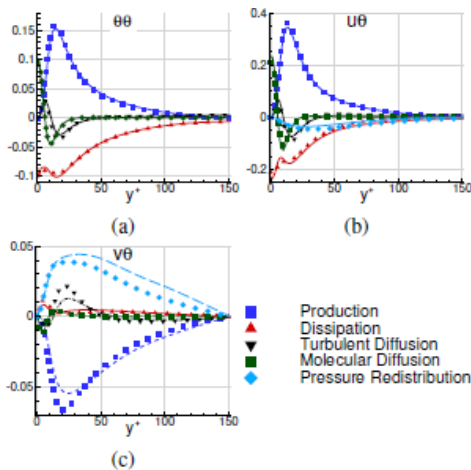


Figure 3: Budget of a) temperature covariance, b) streamwise turbulent heat flux, c) normal to wall turbulent heat flux. Symbols: DNS of Kasagi et al. (1992).

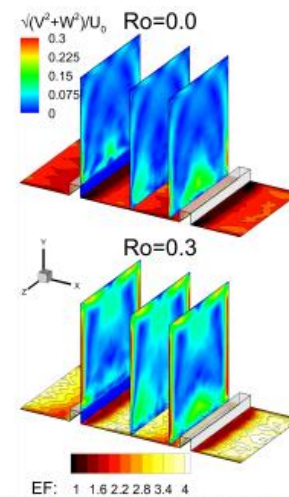


Figure 4: Averaged distribution of secondary motions and enhancement factor.

4 Main results

The flow field was analysed and discussed in Borello et al. (2015b) and not reported here for sake of brevity. The assessment of the quality of the results was performed by considering the enhancement factor (EF) defined as the ratio between the Nusselt number and the Nusselt number from the Dittus-Boelter correlation for a pipe flow (Nu_0): $EF = Nu/Nu_0$; $Nu = hD_h/k$; $Nu_0 = 0.023 Re^{0.8} Pr^{0.4}$

Table 1: Enhancement factor. Experiments from Mayo et al. (2015)

Case	LCD	LES
$Ro=0.0$	2.5	2.16
$Ro=-0.3$	3.1	3.06

Table 1 shows the comparison of the surface averaged enhancement factor for the two cases here investigated. As argued in Borello et al. (2015b), in the rotating case, the overall EF increases due to the presence of large convective motions that increase turbulence and promote heat removal from the solid wall. The agreement with the experimental data is satisfactory and however in the measurement uncertainty range indicated in Mayo et al. (2015). The rotation increases the magnitude of the secondary flows (see figure 4). In particular, the Coriolis force acts exerting an acceleration in y direction that is proportional to the x -component of velocity. Such velocity is maximum at the duct symmetry plane ($z/h = 4.68$) and zero at the lateral walls. Then, the overall result is that a secondary flow towards the ribbed wall is generated close to the symmetry plane, while near the lateral walls the flow is ascending. Interestingly, the rib causes the flow to develop a positive y -velocity to cross the obstacle, and this is sufficient to destroy the secondary vortex generated by the Coriolis force.

Conclusions

The heat transfer in a stationary and rotating rib roughened duct was analysed by means of LES. In the rotating case the heat removal was found to be higher due to the higher “level of turbulence”, enhanced by rib-induced and Coriolis-induced secondary flows. In particular two main ways of enhancing were found: 1. The increasing of secondary motions, due to rib induced flow and promoted by the rotation, which increases hot/cold gas mixing; 2. The increasing of velocity and temperature fluctuations, which promotes turbulent heat transfer.

References

- Borello, D., Anielli, D., Rispoli, F., Salvagni, A., and Venturini, P. (2015a). Unsteady CFD analysis of erosion mechanism in the coolant channels of a rotating gas turbine blade. In ASME Turbo Expo 2015: Turbine Technical Conference and Exposition
- Borello, D., Salvagni, A., and Hanjalić, K. (2015b). Effects of rotation on flow in an asymmetric rib-roughened duct: LES study. *International Journal of Heat and Fluid Flow*, 55:104–119.
- Borello, D., Salvagni, A., Rispoli, F., and Hanjalić, K. (2015c). LES of the flow in a rotating rib-roughened duct. In *Direct and Large-Eddy Simulation IX*, pages 283–288. Springer.
- Casarsa, L. and Arts, T. (2005). Experimental investigation of the aerothermal performance of a high blockage rib-roughened cooling channel. *Journal of turbomachinery*, 127(3):580–588.
- Han, J.-C., Dutta, S., and Ekkad, S. (2012). *Gas turbine heat transfer and cooling technology*. CRC Press.
- Kasagi, N., Tomita, Y., and Kuroda, A. (1992). Direct numerical simulation of passive scalar field in a turbulent channel flow. *Journal of heat transfer*, 114(3):598–606.
- Kays, W. M., Crawford, M. E., and Weigand, B. (2012). *Convective heat and mass transfer*. Tata McGraw-Hill
- Mayo, I., Arts, T., El-Habib, A., and Parres, B. (2015). Twodimensional heat transfer distribution of a rotating ribbed channel at different Reynolds numbers. *Journal of Turbomachinery*, 137(3):031002.
- Murata, A. and Mochizuki, S. (2003). Effect of crosssectional aspect ratio on turbulent heat transfer in an orthogonally rotating rectangular duct with angled rib turbulators. *International Journal of Heat and Mass Transfer*, 46(16):3119–3133.
- Narasimhamurthy, V. D. and Andersson, H. I. (2015). Turbulence statistics in a rotating ribbed channel. *International Journal of Heat and Fluid Flow*, 51:29–41.
- Patankar, S., Liu, C., and Sparrow, E. (1977). Fully developed flow and heat transfer in ducts having streamwise periodic variations of cross-sectional area. *Journal of Heat Transfer*, 99(2):180–186.
- Saravanamuttoo, H. I. H., Rogers, G. F. C., and Cohen, H. (2001). *Gas turbine theory*. Pearson Education.
- Tafti, D. (2005). Evaluating the role of subgrid stress modelling in a ribbed duct for the internal cooling of turbine blades. *International Journal of Heat and Fluid Flow*, 26(1):92–104.
- Visscher, J., Andersson, H. I., Barri, M., Didelle, H., Viboud, S., Sous, D., and Sommeria, J. (2011). A new set-up for PIV measurements in rotating turbulent duct flows. *Flow Measurement and Instrumentation*, 22(1):71–80.

SOLEEDGE2D-EIRENE simulations of the reference scenario of the M15-20 JET experiment

G. Rubino^a

^a ENEA C.R. Frascati, via E. Fermi 45 – 00044, Frascati (Rome), Italy

Abstract

The advanced magnetic configurations can represent a possible solution in the framework of the power exhaust issue. The numerical modelling is then a crucial aspect in order to predict the Scrape off Layer plasma conditions. In this context, the new SOLEEDGE2D-EIRENE code represents a promising tools since of the difficulties encountered by the largely validated 2D edge codes EDGE2D-EIRENE and SOLPS. In this work we present a validation of the SOLEEDGE2D-EIRENE code performed by comparing the obtained numerical results and the one of EDGE2D-EIRENE simulating a JET discharge. In particular, we focus on outer target quantities and we show the necessity to define proper diffusion coefficients in order to get similar results.

1 Introduction

The “Fusion Electricity - A roadmap to the realisation of fusion energy“[1] report published by EFDA in 2012 has recognized the “Heat-exhaust issue“ as one of the major problem towards the realization of a future fusion power plant. The large amount of power conducted and convected from the main plasma towards the divertor targets concentrates on a relative small surface area leading to extremely high thermal loads onto the target plates. Furthermore, high particle and neutron fluence in a reactor sets up a stronger limit to the allowable heat fluxes, below 5-10 MW/m² in stationary conditions. In order to mitigate the risk that the ITER baseline solution, based on Single Null Divertor (SND) with W divertor plates, will not extrapolate to a Demonstration fusion power plant (DEMO), the EUROfusion is currently assessing alternative solutions to take into account; in particular, a dedicated Work Packages of the 2014-2018 EUROfusion work plan, i.e. WPD TT1, deals with the assessment of alternative divertor geometries. Possible proposed solutions are the so called advanced magnetic configurations: X-Divertor (XD), Super-X divertor (SXD) and the Snowflake divertor (SF).

The numerical modeling is therefore essential to study the possible benefit deriving from the different proposed configurations and to better understand the physical processes able to alleviate the power exhaust issue. Several 2D edge codes are currently available in the fusion community. However, the most used and largely validated codes, i.e. EDGE2D-EIRENE and SOLPS, are not able to treat the advanced configurations due to the presence of a second null point. In this work a new numerical tool has been used, i.e. SOLEEDGE2D-EIRENE[2]. This code is primarily based on the Braginskii’s equation[3] for the description of the plasma species, whereas the Monte Carlo code EIRENE is used to track the neutral particle trajectories. A different numerical scheme is adopted to treat the transport equations; in particular, a penalization technique is used to implement the boundary conditions. The magnetic-field-aligned computational grid includes the plasma and extends into the plasma facing components (PFCs). A mask function is used to differentiate the plasma from the PFCs and, by forcing the solution in the wall domain through extra terms in the balance equations, the boundary conditions at the plasma-wall interfaces are recovered.

This characteristic gives a high flexibility to SOLEEDGE2D-EIRENE. Indeed, since the vessel shape is defined by the mask function matrix, this code is able to treat complex divertor and wall geometries and, thanks to the features of the mesh generator, it is able to manage complex magnetic configurations, as the SF divertor. In addition, since the mesh extends up to the wall, the codes is

able to directly evaluate the effect of the first wall on SOL plasma conditions.

The SOLEDGE2D-EIRENE code and the mesh generator have been installed on the HPC CRESCO facilities and an initial validation phase has been performed. A preliminary predictive study on the reference scenario of the JET experiment M15-20 has been performed. The results obtained with SOLEDGE2D-EIRENE has been compared with the numerical results in [4], where the EDGE2D-EIRENE[5] code has been used to predict the SOL plasma conditions in the experiment.

2 SOLEDGE2D-EIRENE setup

The aim M15-20 JET experimental campaign is the assessment of the effect of the flux expansion on the radiative divertor performance. Three different equilibria are discussed in [6] and has been designed starting from the JPN # 81472 @ $t=9s$; in particular, semi-horizontal configurations are modified below the X-point. For the validation phase performed in this work we have used the reference equilibrium, while the two high flux expansion cases (HFE) has not been taken into account.

As a first step in the analysis, we have considered an H-mode pure deuterium plasma even though the experiment is based on Nitrogen seeded discharges. This choice is dictated by the need to define the set of input parameters for the SOLEDGE2D-EIRENE simulations. The main input and boundary conditions used in the simulations refers to [4]. The input power crossing the separatrix is set to 8 MW. This value is obtained by considering the predicted input power during inter-ELM phase where the core radiation and the rate of change of the pedestal stored energy is subtracted from the total heating power. The Deuterium puff is located in the High field side (HFS) region and it has been adjusted to get the same outer midplane electron density $n_{e,OMP}$ as in [4].

Since of the presence of the internal transport barrier related to the H-mode, the cross field transport coefficients of particle, D_p , and electron and ion energy, respectively χ_e and χ_i , above the X-point vary along the radius, while the value in the divertor region has been set constant and equal $D=0.64 \text{ m}^2/\text{s}$ and $\chi_e = \chi_i = 1 \text{ m}^2/\text{s}$. Finally, we focus our analysis on the outer divertor, since the cross-field drifts have not been included in the simulations due to numerical instabilities.

3 Results

Initially, the transport coefficients in the main SOL, that is in the SOL region above the X-point, has been set equal to the one used in the EDGE2D-EIRENE simulations in [4]. Figure 1 shows the profile of D_p and χ_e (and χ_i) as a function of the radial distance from the separatrix measured at the equatorial plane. As can be seen, the internal transport barrier is reproduced by the sharp decrease in the transport coefficients near the separatrix.

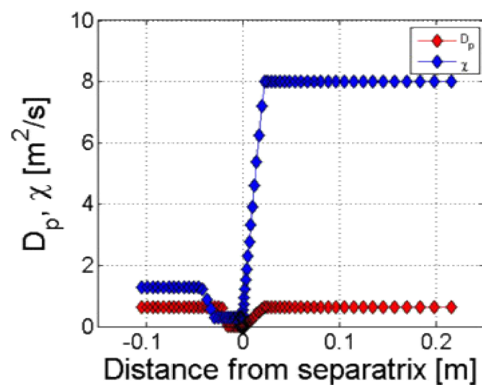


Figure 1: Diffusion coefficients D_p and χ initially used in the simulations. The presence of the internal transport barrier is simulated by a sharp decrease in the diffusion coefficients near the separatrix.

Once stationary conditions have been reached, the results obtained with SOLEDGE-EIRENE has been compared with the one obtained with EDGE2D-EIRENE. Figure 2 shows the results in terms of electron density and temperature on the outer target. As can be seen, the two calculations have given different profiles both in terms of density and temperature. Especially, the profiles calculated in SOLEDGE2D-EIRENE were higher than the corresponding one obtained with EDGE2D-EIRENE. In addition, the temperature peak obtained in SOLEDGE2D-EIRENE was shifted with respect to the one EDGE2D-EIRENE and the profiles was braoder. An analysis of the data have shown that this behavior was related to the different upstream profiles obtained in the two calculations. Indeed, even if we have got the same separatrix density and we have imposed the same transport coefficients, the profile of the density was much broader in case of SOLEDGE2D-EIRENE; in turn, this has directly affected the SOL conditions and the outer target density profile. Likewise, the upstream temperature profile obtained with SOLEDGE2D-EIRENE was higher than the one of EDGE2D-EIRENE. This difference had a strong effect on the temperature profile along the SOL since the high temperature in the former case have modified the ionisation distribution which was more concentrated near the target plates in SOLEDGE2D-EIRENE calculations, while the neutrals were ionized in the all the divertor chamber in EDGE2D-EIRENE case.

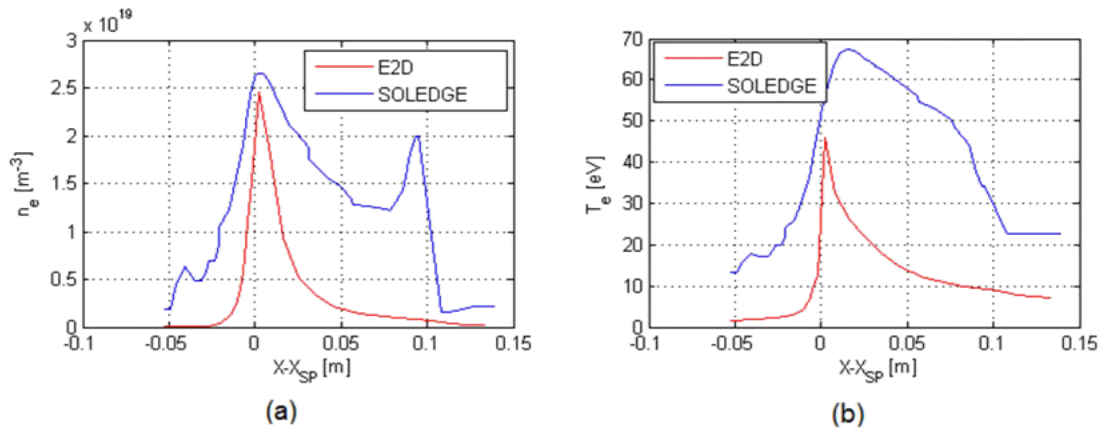


Figura 2: (a) Electron density and (b) temperature profiles on the outer target as a function of the distance from the outer strike point. The profiles obtained with SOLEDGE2D-EIRENE are higher and broader than the one obtained with EDGE2D-EIRENE.

Therefore, in order to get similar results in terms of density and temperature profiles, we have performed a redefinition of the transport coefficients. We have used two different approaches. The first one is based on the “autofit” function implemented in SOLEDGE2D-EIRENE. In this case, the upstream profiles of electron and ions temperature and density are given to the code, which iteratively solves the equations by changing the radial profiles to approach the desired one. However, numerical instability have arisen, which either have led to simulation crashes or drastically have increased the computational time. As a consequence, we have decided to manually adjust the transport coefficients to approach the EDGE2D-EIRENE upstream profiles as much as possible. Clearly, this second approach represents a high computational demanding method and a trade-off between the obtained results and computational time was needed.

Figure 3(a) shows the imposed transport profiles obtained by progressively changing the upstream value of D_p and χ . We can observe that the plateau of χ in the main SOL has been increased from 8 to 10 m^2/s , while reducing the radial range for the raising. On the contrary, the radial range defining the internal barrier has been increased. This choice has been motivated from the need to reduce the separatrix temperature. As the change in D_p is concerned, radial step in the main SOL is reduced as well, while the plateau into the core region has been increased in order to get a more flat core density profile, as in [4].

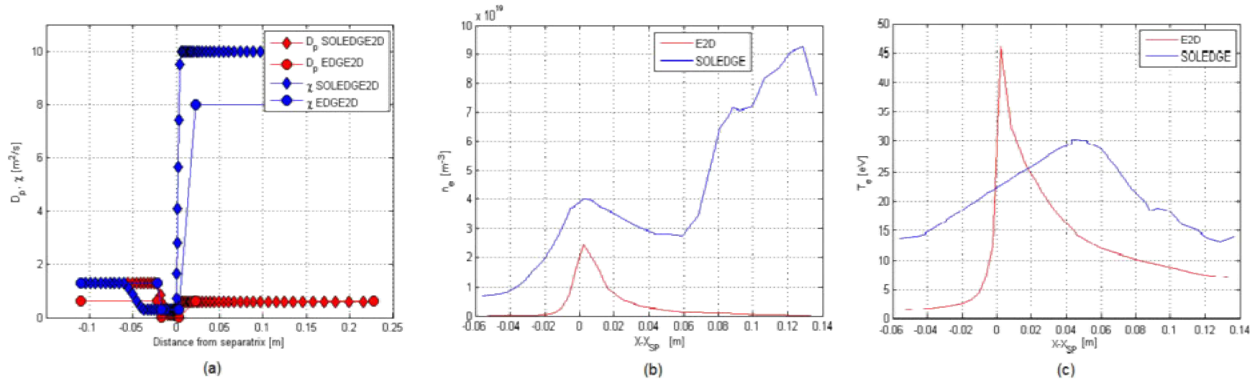


Figure 3: Radial profile of the diffusion coefficient D_p (red) and χ (blue). (b) The electron density and (c) temperature profiles on the outer target as function of the distance from the strike point are shown.

The results in terms of target profiles for the electron density and temperature are shown in figure 3 (b) and (c), respectively. Although the redefinition of the transport coefficient has allowed to obtain closer upstream profiles, the target one have shown difference. The target electron temperature is reduced compared to the one in figure 2 (c), but the peak is shifted towards the far SOL. This behaviour is related from one hand to the decrease in the upstream temperature and on the other hand on the higher value of χ in figure 1. The target electron density obtained with SOLEDGE2D-EIRENE was similar to the previous one, but have shown a sharp increase in the far SOL. The reason for this behaviour is under investigation, but can be probably related to the lower target temperature which have changed the ionisation distribution.

4 Conclusions

The feature of the SOLEDGE2D-EIRENE to deal with complex geometries represents an important possibility in the numerical modelling of the advanced magnetic configurations. The analysis of the different effects that can help in solving the power exhaust issue can be performed by means of this promising tool. However, a validation phase is necessary in order to assess the reliability of the code. In this work, we have shown that a definition of the input parameters is needed by comparing the results of the calculation with the numerical results of the EDGE2D-EIRENE code. In particular, we have shown the effect of a change in the diffusion coefficients, especially the effect on target quantities. The next step in the analysis is clearly the direct comparison of the numerical results with the experimental data, which represents the most important phase in the code validation.

References

- [1] EFDA. Fusion Electricity - A roadmap to the realisation of fusion energy, 2012.
- [4] H .Bufferand et al. , J. Nucl. Mater. 438 (2013) S445-S448.
- [3] S.I. Braginskii, Rev. Plasma Phys. V1, 205 (1965).
- [4] B.Viola et al., Nuclear Materials and Energy, 2017, <http://dx.doi.org/10.1016/j.nme.2017.07.004>
- [5] R. Simonini, et al., Contrib. Plasma Phys. 34 (1994) 368-373.
- [5] Calabro, G., Albanese, R., Ambrosino, R., Ariola, M., Crisanti, F., De Tommasi, G., et al. (2016). Divertor configuration with two nearby poloidal field nulls: modelling and experiments for EAST and JET tokamaks, in: Proc of the 22nd International Conference on Plasma Surface Interactions in Controlled Fusion Devices (PSI 22), Rome.

ENEA
Promotion and Communication Service

www.enea.it

Printed at the ENEA Technographic Laboratory – Frascati

November 2017